Rispler, Adrian Roberto
Ph. D. 1999

This thesis has been accepted for the award of the degree in the Faculty of Engineering

ANALYSIS AND OPTIMISATION OF HIGHLY LOADED JOINTS

Adrian Roberto Rispler B.E. (Aero) Hons.

A thesis submitted in fulfilment of the requirements for the degree of Doctor of Philosophy

Department of Aeronautical Engineering
The University of Sydney

July 1998

ABSTRACT

The goals of this dissertation were to investigate methods of increasing the efficiency of highly loaded aircraft type joints. The thesis can be divided into five main sections. The first section provides some background to the type of joints that can be found on an aircraft. A brief literature review of optimisation methods is also presented in this section. The section is completed with some theoretical background to be employed in subsequent Chapters.

The second section deals with the structural optimisation of bonded joints. Following a brief review of previous research conducted in this field, different optimisation methods are presented and employed in the shape optimisation of the adherends of bonded joints. A heuristic method known as ESO (Evolutionary Structural Optimisation Method) is described. In summary, the method is based on finite element analysis and consists in discarding the unstressed material of a loaded structure in an incremental stepwise fashion. Applications of this method to achieve minimisation of maximum peak stresses in the adhesive follow. In one case, ESO was applied to the shaping of adherends and on the other case to the shaping of an adhesive fillet. In the shape optimisation of adherends, only the portion of adherend within the overlap region is allowed to evolve. Large reductions of peak stresses at the tip of the adhesive were achieved for both single and double lap joints. This is followed by the shape optimisation of adhesive fillets to minimise the stress concentration at the tip of the adhesive. Thus the adherend shape remains unchanged throughout the optimisation process. This method was also successful in achieving significant reductions on peak stresses within the adhesive fillet.

Also in the second section, a modification of the ESO method is introduced for the optimisation of composite pin-loaded joints. This is preceded by presenting the different failure modes commonly found in composite materials and a survey of different methodologies which are currently available to the designer for the reduction of peak stresses

on pin-loaded joints. The modified approach proposed, consists of changing the finite element's property of highly stressed elements around a loaded hole in a stepwise fashion, allowing the formation of an insert. This insert provides a localised plastic zone, which reduces the stress concentration on the composite material providing stress relief. The application of this new method to the optimisation of pin-loaded joints resulted in a large reduction in stress concentration around loaded holes. The prediction of stress concentration reductions around loaded holes was correlated by mechanical testing, employing photoelastic analysis to determine full strain fields in the vicinity of the loaded hole. The correlation was very successful both in terms of magnitude and patterns of full strain field, proving the potential of this new method. The method was then applied to multiple load cases and on two holes in a series or in a parallel configuration.

The third section of the thesis deals with the analysis of T-joints used also in marine structures. Experimental studies were conducted employing different filler types at the resin rich area normally found in web/flange intersections. Also, the flange and web thicknesses of T-joints were varied to assess the influence of geometrical parameters on pull-out strength. Finite element analysis was conducted to correlate the no-insert configuration with the thinnest web. Different types of analysis were employed to study this situation. The most accurate failure prediction was achieved with a two-dimensional orthotropic plane strain analysis employing the actual geometry of the plies (as measured by an electronic microscope). Stiffness and failure initiation zone were also accurately predicted using this analysis.

Section four deals with the analysis, design, manufacturing and testing of an aircraft composite hinge. Composite hinges were manufactured of thermoplastic and thermoset materials and tested to failure. Thermoplastic hinges achieved a larger failure load when compared to thermoset hinges. The failure mode was, in all instances, by delamination.

Finally, the fifth section presents conclusions from the different investigations performed on bonded joints, pin-loaded joints, T-joints and the design and testing of a composite hinge. This is followed by recommendations for future work.

ACKNOWLEDGEMENT

I wish to express my sincere thanks to my supervisor, Professor Grant Steven, who guided and supported me throughout the course of my research. A thank you is also extended to my associate supervisor, Dr. Lyiong Tong, for sharing his wealth of knowledge in the structural analysis of joints through numerous technical discussions. A sincere thank you is also extended to Dr. Osvaldo Querin, for his assistance and guidance with the software coding and implementation of the modifications required for the running of the Evolutionary Structural Optimisation Method.

I would also like to acknowledge the contribution of Gabriel Gudas and Michael Baker for their assistance with the fabrication of test panels and for their guidance into the manufacturing of composite hinges and of Radu Turcanu, for his assistance with the setting-up of the data acquisition system. Thanks are also extended to John Raju, Stuart Dutton and Assoc. Professor Don Kelly for their support and guidance on behalf of the Cooperative Research Centre for Advanced Composite Structures (CRC-ACS), whose scholarship allowed me to perform this research.

To my parents, Alfredo and Diana, for their full selfless support and encouragement showed to me, I would like to extend my immense appreciation and gratefulness.

Finally and most importantly, to my beloved wife Yvonne, for her understanding and unlimited support and for giving up all those hours that we missed of being together, and to my three year old son Aaron Ryan for giving me the inspiration to complete my research, I wish to tell them THANK YOU.

Adrian R. Rispler

July 1998

TABLE OF CONTENTS

CHAPTER

CHAPTER 1

INTRODUCTION

1.1 Aircraft structures and materials

The basic functions of an aircraft's structure are to transmit and withstand applied loads. The structure provides with an aerodynamic shape and protects payload and systems from the environment in which the aircraft operates. The requirements of carrying large payloads, while providing the aerodynamic shape needed in order to achieve the desired performance, results in thin shell structures being used extensively throughout the aircraft. Longitudinal stiffening members and transverse frames are employed to support the shell structure to enable it to resist applied and induced loads without buckling. These structures are called semi-monocoque.

The construction of an aircraft is usually divided into a number of sub-assemblies. Examples of these sub-assemblies include: nose, outer wing, centre section, wing tip, elevator, centre fuselage, rear fuselage, etc. Each one of this sub-assemblies are in turn subdivided into minor assemblies such as ribs, spars, stringers, etc.

Wing sections usually consist of numerous spars, ribs and skin. One of the functions of the rib is to maintain the shape of the cross-section dictated by the aerodynamic requirements of the aircraft. The rib structure provides distribution to the aerodynamic pressure loads and concentrated loads (such as the load due to the engine weight) into the structure. These ribs also redistribute stress around discontinuities such as inspection panels, etc. Ribs can be lightly or heavily loaded depending on their spanwise position in the wing and if they are required to transmit large concentrated loads such as those from the undercarriage or engines thrust. Hinge reactions from ailerons and flaps need also be reacted by ribs.

Aerodynamic forces are transmitted into ribs and stringers by the wing skin. Shear stresses developed in the skin and spar webs resist shear and torsional loads. Bending and axial loads are reacted by skin and stringers. Fuselage structures perform similar functions to those on the wing. Although the aerodynamic forces on the fuselage are low in comparison to those experienced by the wing, the fuselage supports large concentrated loads coming from the wing, undercarriage, tailplane reactions, etc.

Most of the minor assemblies are attached into sub-assemblies whether by riveting or adhesively bonding the different components. For example, the skin is usually riveted to the rib flanges and longitudinal stiffeners. Where the load to be transmitted is high, (eg. wing attachment to fuselage) the joining method generally used is mechanically fastening by bolts. Furthermore, when a need arises for components to be disassembled, mechanically fastened joints are also used. This, together with practical limitations on component size imposed by manufacturing processes, inspection requirements and repairs, means that the presence of load carrying joints (adhesively bonded or mechanically fastened) are inevitable in large structures.

Highly loaded joints can be found throughout an aircraft. In particular, hinge reactions from ailerons, flaps, spoiler and other moving surfaces need to be transferred to the surrounding structures. This transfer of load occurs through joints. Load transfer can occur in shear, compression, tension or a combination of these transfer modes. Joints in marine structures can also be highly loaded. Examples of joints with high load transfer are deck-to-bulkhead and shell-to-bulkhead joints. In these joints, load transfer occurs out-of-plane. On aircraft structures, out-of-plane joints can be found in integrally composite spars and on hinge/spar connections.

Aluminium alloys are still the most widely used alloys in commercial jet transport design, although titanium, high strength steel, and composites have made slow but steady inroads in their usage [1]. Consistent progress has been made with the various structural materials in increasing strength as well as toughness properties. Application of advanced composites to civil aircraft has generally lagged behind military use because cost is a more important consideration and safety is a more critical concern [2]. Nevertheless, composite

materials usage in aerospace applications has been increased during the last decades as a result of a need for improved performance.

A potential for greater weight savings, coupled with new production techniques aimed at reducing production costs and greater accuracy in the analysis of composite structures, should result in an increased use of composite materials for primary structures. In order to take full advantage of composite materials, two steps are essential. Firstly, the need to establish sound design techniques which account for all possible failure modes in composite materials. The second step is the need for optimising composite designs to achieve minimum weight structures without any reduction in strength.

The increasing scarcity of raw materials and a rapid depletion of conventional energy sources is being translated into a demand for lightweight, efficient and low cost structures [3]. This demand for more efficient structures requires the structural engineer to consider using the available materials in an optimum way. One can not overstate the future importance of structural optimisation methods in achieving increased performance, by reducing weight (particularly in aircraft structures) and reducing stress concentrations, through efficient redistribution of available material. To ignore this, would be to overlook the increased use of optimisation software in the aerospace, naval, automotive and high-tech industries.

Although much of the use of optimisation software is at a research and development level, engineers have begun to use optimisation techniques for applications. For example, SAAB and FFA (Aeronautical Research Institute of Sweden) developed in conjunction with ALFGAM Optimeering AB the OPTSYS system which integrates design and analysis for optimisation of industrial designs [4]. Dornier has tested OPTIMA, an optimisation software produced by the University of Stuttgart. Optimisation of composite structures has become a field of its own right. Today, thicknesses and fibre orientations are possible design variables.

In these current times, where reduction of costs are required by the largest commercial aircraft manufacturers and increased competition is on the rise between suppliers, the need for the Australian aerospace industry to more cleverly design and manufacture parts has also

increased. In this context, the CRC-ACS (Cooperative Research Centre for Advance Composite Structures) aims at advancing the development of composite structures by performing research on different areas critical to the Australian industry.

The following section provides a more detailed research scope on which this dissertation is based.

1.2 Research Scope

In the past two decades, the design of composites joints has attracted considerable attention. The largest contributions to these efforts have come from the aerospace industry. Much of these efforts were founded on experimental test programs that were conducted to provide with data for particular design requirements. Only limited amount of work has been produced in the optimisation of joints, with most of it concentrating in providing design guidelines to aid the structural engineer in his design efforts. Literature surveys covering research in the areas of bonded, bolted and out-of-plane joints are presented in Chapters 3, 4 & 9 respectively.

In shape optimisation, the objective is usually to minimise the maximum stress by reshaping an internal or external boundary. The joining of two or more structural components generally produce stress concentrations which reduce the efficiency of the overall structure. A number of design and analysis cycles are often required for the selection of a satisfactory joint design. These cycles generally rely on trial and error methods. An aim of this dissertation was to apply the Evolutionary Structural Optimisation (ESO) method to the design of adhesively bonded joints. As the method progressively removes elements while providing a history of stresses throughout the evolutionary process, the guess work is taken out of the design loop. The shape optimisation process was applied to bonded joints as a min-max problem to minimise the stress concentration in the adhesive. This was achieved in the case of single and double lap-joints by shaping the profile of adherends. For the minimisation of stresses in the

adhesive layer on reverse tapered joints, the profile of the adhesive fillet was optimised by employing ESO.

The behaviour of composite laminates with stress concentrations, in particular bolted and pin-loaded joints, is of great interest in design because of the resulting reduction in strength and fatigue life of joints. The reduction in fatigue life occurs mainly due to damage growth around these stress concentrations. The literature survey, presented in Chapter 4, shows a large number of approaches investigated by different researchers in dealing with stress concentration reduction around loaded holes. Since the preferred mode of failure in bolted and pin-loaded joints is bearing, most of the approaches attempt to increase the bearing strength of joints. Apart from the commonly used approaches in highly loaded joints of local thickening and the addition of $\pm$ 45° plies around loaded holes, more recent methods such as laminate tailoring [5], the use of elliptic shape bolts [6], and the bonding of circular metallic inserts in loaded holes [7-9], have been pursued. Optimum fibre placement to increase bearing strength was studied by Crothers et. al. [10]. A study on the optimum shape for a pin-loaded hole was also pursued by Lee [11]. Another aim of this dissertation was to develop a new methodology for the minimisation of stress concentrations in pin-loaded joints based on modifying the shape of a metallic insert bonded in a loaded hole. A further aim, was to achieve this by developing a new concept within the heuristic optimality criteria method ESO. In pursuing these goals, it was found that the assumptions on load distributions could affect the optimum shape of the inserts. This prompted a study on load distribution assumptions around pin-loaded holes and their effect on the optimum shapes of metallic inserts. An investigation on the effect of joint geometry and insert material on the optimum shape of inserts is also presented. Furthermore, the new optimisation method was then applied to a multiple load case problem and to multiple holes in series and in parallel. Another important aim was to validate the optimisation method by testing pin-loaded joints and achieving stress concentration reductions at the composite interface to match those ones obtained by finite element analysis.

The manufacturing of the pin-loaded composite specimens prompted an investigation on issues related in particular to the cutting of complex shapes in composite materials. The

acquisition of detailed stress/strain information exactly at the interface is not a simple task. Different methods were reviewed resulting in small strain gauges being initially trialed right at the interface between composite and metallic insert. Due to the need of full strain field information for an accurate validation of the proposed optimisation method, a photoelastic technique was finally employed.

When components need to be joined perpendicular to each other, the load needs to be transferred in an out-of-plane mode. Laminated composites, generally lack of reinforcing fibres across plies. This often results in low out-of-plane strength due to resin dominated failures. An added stress concentration factor due to local geometry changes at the intersection of both components to be joined, and residual stresses present in the joint after manufacturing can decrease the joint efficiency considerably. An aim of this dissertation was to investigate experimentally the possibilities of increasing pull-out strength in out-of-plane joints by placing differently shaped composite inserts in the resin rich area normally encountered in T-type joints. To better understand the load transfer mechanisms in these type of joints, out-of-plane joints need to be characterised and a failure prediction capability needs to be established. A further aim of this dissertation was to explore the validity of normal failure theories such as Tsai-Wu, etc., normally based on classical lamination theory as failure prediction tools for out-of-plane joints. The aim is then to devise a valid strategy to firstly predict the load transfer and stiffness in T-type joints, followed by a strategy to predict failure loads, failure modes and location of failure initiation. The emphasis is on predicting initiation of failure rather than its progression, as this approach should be more useful for design purposes.

The use of composites into the area of highly loaded structures is presently quite limited. The additional aim of this dissertation was to extend the use of composites into this area by designing, manufacturing and testing of a control surface hinge fitting. The composite fitting was to be comparable in robustness and durability to the aluminium fitting it aimed to replace. An innovative design concept for hinges and hard points in thick composites was a further aim of this work together with the implementation of the fitting using liquid moulding and dry preform technology. The final aim of the work was to validate the design concept and

implementation of the part by conducting a static structural test with the most severe design load case available. Some of the work performed on the experimental investigation of increasing pull-out strength was also employed during the design and manufacture of the proposed composite hinges.

1.3 Joints

Joints are said to be the most important part on a structure, particularly where composite parts are concerned. Hart-Smith [12], advocates that the correct sequence for designing composite structures is to first locate and size the joints in fibres optimised for that role, and then fill the gaps in between. Because of their ductile nature and well-established design procedures for the sizing of joints, an accurate stress analysis is often not required for metals.

Two basic techniques are available to the designer to join composite components, adhesive bonding and mechanical fastening. There are several types of adhesive joint configurations used for joining composite components. The simplest and most frequently used configurations are the single and double-lap joint. Other configurations employed include, double butt-strap joint, double-scarf joint, stepped joints, reverse tapered joints, etc. Since the matrix of composite laminates can be weaker than structural adhesives currently used, failure can occur in the form of delamination on the components to be joined instead of on the adhesive layer. The type of failure on bonded joints will generally depend on the stacking sequence, joint geometry, type of loading and type of adhesive material employed. Adhesively bonded joints transmit shear very efficiently but are very weak in peel. Thus it is important for the designer to ensure that the load is transferred mainly in shear and that direct or induced peel stresses are minimised.

Mechanical fastening is usually by ways of riveting or bolts. The load is usually transmitted in single or double shear. Failure modes are similar to those experienced in metal structures but differ significantly in the mechanisms by which damage initiates. Joint

geometry, laminate thickness, lay-up, stacking sequence and type of loading influence both failure loads and modes.

1.4 Methods of structural optimisation

The structural design for minimum weight or minimum material has been one of the main objectives for structural engineers. Early research performed on numerical structural optimisation was focused almost entirely on parametric optimisation or the sizing of design variables. Parameters such as plate thickness and cross sectional areas of bars were normally considered as design variables. The acceptance of finite element analysis as a design tool together with the availability of high performance computers and improved optimisation algorithms has seen the integration of finite element analysis and mathematical programming methods to form a complete structural design system. An early comprehensive compilation of structural optimisation techniques and mathematical programming techniques was published by Schmit [13] in 1960. During the 1970's, a set of techniques called approximation concepts were developed to carry out the structural optimisation problems while using mathematical programming methods in a more cost-effective way [14]. These techniques transform a problem statement involving a large number of implicit functions to a sequence of a relatively small number of approximate problems incorporating explicit functions. A detailed work on mathematical programming techniques and their application to structural optimisation problems can be found in the work of Haftka et. al. [3].

Although optimisation employing mathematical programming techniques have become much more efficient in the last 15 years due to improvements in algorithms used in the search engines [15], their use is not simple and complex problems are also quite expensive to run. Furthermore, these methods are more applicable and effective for the sizing of design variables rather than for shape or topology optimisation problems in which the geometry of the finite element model changes throughout the optimisation process. The difficulties which are present in shape optimisation and that are not encountered on sizing optimisation are mostly found in two broad areas [16]. Firstly and as mentioned previously, the continuous

change of the finite element model hinders the accuracy of the finite element analysis throughout the optimisation process. Secondly, it is more costly to obtain good sensitivity derivatives with respect to shape design variables than with respect to sizing design variables. One of the available methods for optimising the shape of components using mathematical programming techniques is the shape basis vector method [17]. This method is quite convenient to "fine-tune" shapes rather than evolving radical shapes [18] and essentially consists of relating the old and new shapes through a simple linear function. A group of design variables is called a shape basis vector. These vectors describe the allowable shape changes and contain information on how and how much a shape may vary during the optimisation process. Several methods are available to generate shape basis vectors. A detailed description of these methods can be found in the MSC/ NASTRAN manual by Moore [17].

An excellent survey of issues concerning to the sizing of shape design variables in the solving of optimisation problems employing mathematical programming techniques can be found in the work by Haftka et. al. [16].

Another area of research in which the current mathematical programming techniques are not cost-effective is the area of topology optimisation. Topology optimisation has currently two important areas of research [19]. The first area is called layout optimisation in which the optimal topology together with the geometry and sizes of members is optimised concurrently. The second area of research is termed generalised shape optimisation. This area of research involves the simultaneous selection of the shape of external and internal boundaries and the topology of the internal boundaries. An ever-increasing amount of research activities is currently being directed towards alternative optimisation methods which deal with topology and shape optimisation. This will eventually result in structural optimisation becoming more widely available to engineers and scientists by simplifying and making less costly and more reliable the overall optimisation process.

Several classes of methods of structural optimisation are proving useful in this emerging role [20]. These powerful class of methods are generically grouped together with the title

Optimality Criteria (OC) [21]. Optimality criteria methods consist of two complementary ingredients [3]. The first ingredient is the provision of the optimality criteria, which can be based on rigorous mathematical statements or based on an intuitive approach such as achieving a fully stressed design. The second ingredient is the algorithm employed to resize the structure in order to satisfy the optimality criterion. Other methods known as heuristic optimality criteria are known to achieve practical results efficiently. One of such technique is known as the Homogenization Method, pioneered by Bendsøe [22, 23]. This method has proven to be successful in generating optimum topologies for continuum structures by treating element densities as design variables. The Homogenization Method concurrently optimises the topology of the structure and the microstructure of the material that forms it. That is, the shape optimisation problem is converted into a material redistribution problem. This problem is then solved using mathematical programming techniques with sequential quadratic programming used to determine the optimal material distribution. Since the density distribution is to be optimised, the resulting density distribution needs to be post-processed to extract the final/optimum shape.

Another heuristic optimality criteria method is known as the Simulated Biological Growth method. This method; which was pioneered by Mattheck [24, 25]; simulates numerically the growth mechanism of trees by copying the self-optimisation of living trees which always grow into shapes of constant surface stresses. Although the Biological Growth method is only applicable to the shape optimisation of parts, the method has been extended to cover topology optimisation by adding a routine similar to the Homogenization Method called SKO-method (Soft Kill Option) [26, 27]. The Biological Growth technique uses an artifice whereby stress at the surface being shape optimised is converted to temperature and the surface allowed to move outwards (swell), if the stress is high, or inwards (shrink) if the stress is low. The motion is achieved by the thermal expansion equivalent of the artificial temperature. Several iterations are generally needed.

In 1992, another heuristic optimality criteria method known as Evolutionary Structural Optimisation (ESO) method, was developed by Xie and Steven [28-31]. The ESO method is based on slowly removing understressed thus inefficient material in an evolutionary style

from the structure to achieve a more fully stressed design. Initially, benchmark tests were performed on ESO to validate the methodology [28-31]. Once the method was successfully benchmarked, it was applied to a vast number of dissimilar problems. Following the initial testing, ESO was also extended to structures with multiple load cases, Xie et. al. [32], multiple constraints, Steven et. al. [33] and dynamic problems Steven et. al. [34]. The ESO method has been subsequently applied to the design of aircraft patch repairs, Steven et. al. [35], the design of metal inserts in composite joints, Rispler et. al. [36, 37], the shape optimisation of adherends and adhesive fillets in single and double lap-joints, Rispler et. al. [37, 38], and the shape optimisation of cutouts in composite material, Falzon et. al. [39]. The optimality criterion of ESO was also modified to incorporate stiffness constraints, Chu et. al. [40], buckling, Manickarajah et. al. [41] and non-linear structural behaviour, Querin et. al. [42]. A more complete list of capabilities of the ESO method can be found in the work by Querin [43].

It is interesting to note that the ESO method does in theory what the experimental stress concentration minimisation process by employing the photoelastic method [44-46] does in practice. That is, in the photoelastic stress minimisation method, the initial design is studied in the photoelastic apparatus to determine low fringe areas close to high stress concentration areas. With the aid of a scraping device, material is removed gradually from the low fringe density areas of interest. Visual feedback is then employed by the operator to remove surface material to achieve reductions in stress concentrations.

1.5 The Cooperative Research Centre for Advanced Composite Structures (CRC-ACS)

The CRC-ACS was established in 1991 by the Australian Government with the objective of providing a greater interaction between industry and academia in order to advance the development of composite technology in the Australian aerospace industry. The operations of the centre were divided into different research areas to address various aspects

critical to the industry. Such aspects included the design, testing and manufacturing of composite structures.

One of these programs (Program 2.4), focussed on providing a mathematical basis and tools for design, validation and testing of highly loaded joints. This program was designed to complement work carried out under the task on primary structures. The CRC-ACS program was subdivided into five closely related sub-tasks:

1) To develop a validated procedure for the design of highly loaded joints (bolted or bonded) in thick-skin components.

2) To develop innovative design procedures for such joints, including the effects of metal inserts.

3) To develop an improved methodology for the determination of materials design allowables and "knock-down" factors.

4) To develop an optimisation capability for joint design based on existing optimisation programs.

5) To investigate the design and manufacture of highly loaded composite hinges.

These sub-tasks highlight the areas of interest of the CRC-ACS. Although this dissertation addresses some of the areas of concern described above, a large portion of the research conducted departed significantly from those areas and has originated solely on the author of this dissertation.

1.6 Thesis Lay-out

This dissertation deals with the analysis and optimisation of highly loaded joints. The thesis is arranged into twelve chapters in this manuscript. It starts by introducing in this current chapter typical aircraft structures, type of loadings, materials commonly used in the

aerospace industry and how they are assembled together. A brief introduction on the importance of highly loaded joints in aircraft structures and on the optimisation of structures in general follows. The research scope of this dissertation is then presented followed by a brief summary of selected methods of structural optimisation including both mathematical programming techniques and heuristic approaches. The significance of the CRC-ACS in developing strategic advantages for the Australian aerospace industry is then discussed. Chapter 1 concludes with the arrangement of the work presented in this dissertation.

In Chapter Two, theory dealing with orthotropic laminates and optimisation theory is covered. Within the optimisation theory section, classical numerical techniques and a mathematical representation of the Evolutionary Structural Optimisation method ESO are explained.

Chapter Three deals with the optimisation of adhesively bonded joints. Advantages and disadvantages in employing bonded joints and a brief description on joint types and their analysis are initially discussed. This is followed by existing research found in the literature where the optimisation of bonded joints was attempted. An optimisation of a single lap joint employing the shape basis vector technique follows. The concept behind the Evolutionary Structural Optimisation method and its benchmarking is followed by several applications of this heuristic approach to the shape optimisation of bonded joints.

In Chapter Four, the optimisation of pin loaded joints is discussed. Firstly, the different failure modes and methods for improving bearing strength are presented. A more recent method to increase bearing strength by placing metallic inserts in loaded holes is then introduced. In the original definition of the ESO method, plates could only be deleted. This Chapter shows a modification to the original approach whereby plates had their property changed to correspond to that of a different material with the effect of redistributing large stresses around loaded holes. This original concept is then employed to minimise maximum stresses at the composite interface of loaded holes, in single and multiple hole configurations and with one or two load cases, by switching material from composite to aluminium as the evolutionary process unfolds.

Manufacturing details regarding the production of pin-loaded joint specimens discussed in Chapter Four, including panel geometry, lay-up, cure cycles and production of inserts and cut-outs are discussed in Chapter Five.

Description of test set-ups, fixtures and techniques to measure critical strains at the composite interface for the pin-loaded joints discussed in Chapters Four and Five are presented in Chapter Six. The photoelastic technique is discussed in detail in this chapter.

Discussions of all test results from pin-loaded joints are covered in Chapter Seven. Failure loads from the first batch test results with w/d=4 (width over diameter ratio) are correlated to values obtained with the aid of "BOLT" (bolted joints failure analysis code). Correlation of the second batch test results with w/d=11.5 is presented pictorially in the form of maximum shear strain contours comparing the photoelastic pattern/magnitude with that obtained from the finite element analysis of the pin-loaded joints tested.

In Chapter Eight, the experimental evaluation of composite T-joints is presented. The different configurations tested are introduced together with manufacturing details and test set-up. This is followed by the discussion of test results and a conclusion on the effect of placing inserts on resin rich areas in out-of-plane joints.

Chapter Nine presents a detailed failure analysis of composite T-joints. In particular, a T-joint without insert is analysed comprehensively. Different failure criterions are considered and a conclusion is made as to the efficacy of current failure theories for the accurate prediction of failure loads and modes. The required detail of modelling to achieve accurate results and good correlation with test results is further presented.

The design of a composite hinge is presented in Chapter Ten. The calculation of the critical load case is presented and the existing aluminium hinge design is analysed with the aid of finite element analysis. The design process employed to arrive to the proposed

composite hinge design follows. A 2D and 3D finite element analysis of the proposed design completes the chapter.

In Chapter Eleven, the testing program on the composite hinges designed is presented. Firstly, manufacturing details for both the thermoset and thermoplastic hinges is given together with the test set-up employed. An analysis of test results for both types of hinges follows. The effect of ply drop-off at web/flange intersection on the thermoplastic hinge is also presented. The chapter concludes with an assessment of manufacturing cost and a comparison of test results for the different hinges.

Finally, Chapter Twelve gives the conclusion to this dissertation, detailing the work done and the goals achieved. Recommendations for future work are also given.

1.7 References

[1] Davis, R. A., "*Jet Transport Design Progress 1954 to the future*", lecture presented at the International Aerospace Congress, Sydney, Australia, February 25-27, 1997.

[2] Schwartz, M. M., "*Composite Materials Handbook*", McGraw-Hill Book Company.

[3] Haftka, R. T., Gurdal, Z., "*Elements of Structural Optimization*", 3rd edition, Kluwer Academic Publishers, 1993.

[4] Esping, B., Romell, O., "*Structural Optimization using OASIS-ALADDIN System*", NATO/DFG Advanced Study Institute, Berchtesgaden, Germany, September, 1991.

[5] Eisenmann, J. R., Leonhardt, J. L., "Improving Composite Bolted Joint Efficiency by Laminate Tailoring", Joining of Composite Materials, *ASTM STP-749*, K.T. Edward, Ed., American Society for Testing and Materials, pp. 117-130, 1981.

[6] Wang, J. T., Lotts, C. G., Davis, D. D. Jr., "Analysis of Bolt-Loaded Elliptical Holes in Laminated Composite Joints", *Journal of Reinforced Plastics and Composites*, Vol. 12, pp 128-138, February 1993.

[7] Nilsson, S., "Increasing Strength of Graphite/Epoxy Bolted Joints by Introducing an Adhesively Bonded Metallic Insert", *Journal of Composite Materials*, Vol. 2, pp. 642-650, 1989.

[8] Herrera-Franco, P. J., Cloud, G. L., " Strain-Relief for Composite Fasteners-An Experimental Study", *Journal of Composite Materials*, Vol. 26, pp. 751-768, 1992.

[9] Mirabella L., Galea, S. C., " An Experimental Investigation into the use of Inserts to enhance the static performance of thin composite bolted lap joints", *Proceedings of ICCM-11*, Vol. 6, pp 148-157, Gold Coast, Australia, July 14-18, 1997.

[10] Crothers, P.J., Drechsler, K., Feltin, D., Herszberg, I., Bannister, M., " The Design and Application of Tailored Fibre Placement", *Proceedings of ICCM11*, Gold Coast, Australia, Vol. 1, pp 600-610, 14^{th}-18^{th} July 1997.

[11] Lee, M. S., "*Shape Optimization of a hole in symmetric laminates*", PhD Thesis, University of Michigan, U.S.A, 1987.

[12] Hart-Smith, L. J., "Joints", Engineered Materials Handbook on Composites, *ASM International*, Vol. 11, pp. 479-494.

[13] Schmit, L. A., "Structural Design by Systematic Synthesis", *Proceedings* 2^{nd} *Conference on Electronic Computation*, ASCE, New York, 1960.

[14] Miura, H., MSC/NASTRAN, "*Handbook for Structural Optimization*", MSC/NASTRAN Ver. 66, The MacNeal-Schwendler Corporation, December, 1988.

[15] Vanderplaats, G. N., "*Numerical Optimization Techniques for Engineering Design: with Application*", McGraw-Hill, New York, 1984.

[16] Haftka, R. T., Grandhi, R. V., "Structural shape optimisation: a survey", *Computer Methods in Applied Mechanics and Engineering*, Vol. 57, pp. 91-106, 1986.

[17] Moore, G. J., "*MSC/NASTRAN Design Sensitivity and Optimization – User's Guide*", The MacNeal-Schwendler Corporation, 1994.

[18] Zhu, C., Dhanasekar, M., Hagaman, B., "Application of Shape Basis Vector to the Optimisation of Rail Sections", *Proceedings of The Australasian Conference on Structural Optimisation*, ACSO '98, pp. 451-458, Oxbridge Press, Victoria, Australia, February 11-13, 1998.

[19] Rozvany, G. I. N., "Topology Optimization of Multipurpouse Structures", *Proceedings of The Australasian Conference on Structural Optimisation*, ACSO '98, pp. 31-41, Oxbridge Press, Victoria, Australia, February 11-13, 1998.

[20] Steven, G. P., "SORGA Structural Optimisation Notes Number 1", http://www.ae.su.oz.au/wwwdocs/note1.html, Department of Aeronautical Engineering, University of Sydney, NSW, 2006, Australia, January, 1998.

[21] Rozvany, G. I. N., "*Structural Design via Optimality Criteria*", Kluwer Academic Publishers, Dordrecht, 1989.

[22] Bendsøe, M. P., "*Optimization of Structural Topology, Shape, and Material*", Springer, Heidelberg, 1995.

[23] Bendsoe, M. P., Kikuchi, N., "Generating optimal toplogies in structural design using a homogenisation method", *Computational Methods In Applied Mechanical Engineering*, Vol. 71, pp. 197-224, 1988.

[24] Mattheck, C., Burkhardt, S., "A New Method of Structural Shape Optimisation Based on Biological Growth", *International Journal of Fatigue*, Vol. 12, No. 3, pp. 185-190, 1990.

[25] Mattheck, C., Moldenhauer, H., "An Intelligent Cad-Method based on Biological Growth", *Fatigue Fract. Engineering Material Structures*, Vol. 13, No. 1, pp. 41-51, 1990.

[26] Baumgartner, A., Harezheim, L., Mattheck, C., "SKO: Soft Kill Option. The biological way to find an optimum structure topology", *International Journal of Fatigue*, Vol. 14, No. 6, pp. 387-393, 1992.

[27] Walther, F., Mattheck, C.," Local Stiffening and Sustaining of Shell and Plate Structures by SKO and CAO", *Proceedings of the World Congress on Optimal Design of Structural Systems*, Vol. 1, pp. 181-188, 1993.

[28] Xie, Y. M., Steven, G. P., "Shape and layout optimisation via an evolutionary procedure", *Proceedings of the International Conference on Computational Engineering Science*, Hong Kong University of Science and Technology, Hong Kong, December, 17-22, 1992.

[29] Xie, Y. M., Steven, G. P., " A simple evolutionary procedure for structural optimisation", *Computers and Structures*, Vol. 49, No. 5, pp. 885-896, 1993.

[30] Steven, G. P., Xie, Y. M., "Evolutionary structural optimisation with FEA", *Computational Mechanics*, Vol. 1, pp. 27-34, August, 1993.

[31] Xie, Y. M., Steven, G. P., "*Evolutionary Structural Optimization*", Springer-Verlag, London, 1997.

[32] Xie, Y. M., Steven, G. P., "Optimal design of multiple load case structures using an evolutionary procedure", *Engineering Computations*, Vol. 11, pp. 295-302, 1994.

[33] Steven, G. P., Querin, O. M., Xie, Y. M., "Multiple constrain environments for evolutionary structural optimisation", *Proceedings of the First World Congress on Structural and Multidisciplinary Optimization*, Pergamon, Oxford, pp. 213-218, Goslar, Germany, June, 1995.

[34] Steven, G. P., Xie, Y. M.," Evolutionary Structural Optimization applied to problems in structural dynamics", *3rd World Congress on Computational Mechanics*, Chiba, Japan, paper H2-2, 1994.

[35] Steven, G. P., Querin, O. M., Xie, Y. M., "Analysis of Aircraft Patch Repairs Using ESO", *Proceedings of the Second Pacific International Conference on Aerospace Science and Technology*, Melbourne, Australia, pp. 683-688, March, 20-23, 1995.

[36] Rispler, A. R., Steven, G. P., "Shape Optimisation of Metallic Inserts in Composite Bolted Joints", *Proceedings of the Second Pacific International Conference on Aerospace Science & Technology*, Melbourne, Australia, Vol. 1, pp. 225-230, March, 20-23, 1995.

[37] Rispler, A. R., Steven, G. P., "Optimisation of Highly Loaded Joints", *Proceedings of the 20th Congress of the International Council of the Aeronautical Sciences*, Sorrento, Italy, Volume 1, pp. 160-166, September 8-13, 1996.

[38] Rispler, A. R., Steven, G. P., Tong, L., Wisnom, M., "Shape Optimisation of Adhesive Fillets", submitted to the *International Journal of Adhesion and Adhesives*.

[39] Falzon, B. G., Steven, G. P., Xie, Y. M.,"Shape optimization of interior cutouts in composite materials", *Structural Optimization*, Vol. 11, pp. 43-49, 1996.

[40] Chu, D. N., Xie, Y. M., Steven, G. P., "Evolutionary Structural Optimization for problemswith stiffness constraints", *Finite Element in Analysis and Design*, Vol. 21, pp. 239-251, 1996.

[41] Manickarajah, D., Xie, Y. M., Steven, G. P., "A simple method for the optimisation of columns, frames and plates against buckling", *Structural Stability and Design*, A. A Balkema Publishers, Rotterdam, pp. 175-180, October, 1995.

[42] Querin, O. M., Steven, G. P., Xie, Y. M., "Topology optimisation of structures with material and geometric non-linearities", *Proceedings of the 6th AIAA/USAF/NASA/ISSMO Symposium on Multidisciplinary Analysis and Optimization*, Bellevue, Washington, U.S.A, AIAA-96-4116-CP, pp. 1812-1818, September, 4-6, 1996.

[43] Querin, O. M., "*Evolutionary Structural Optimisation: Stress Based Formulation and Implementation*", PhD Thesis, Department of Aeronautical Engineering, University of Sydney, Australia, April, 1997.

[44] Durelli, A. J., Rajaia, K., "Optimum hole shapes in finite plates under uniaxial load, ASME, *Journal of Applied Mechanics*, Vol. 46, pp. 691-695, 1979.

[45] Durelli, A. J., Rajaia, K., "Minimising stress with photoelasticity", *Machine Design*, Vol. 53, No. 28, pp. 125-130, 1981.

[46] Heywood, R. B., "*Photoelasticity for Designers*", Pergamon, Oxford, 1969.

CHAPTER 2

THEORETICAL CONSIDERATIONS

2.1 Introduction

This Chapter provides a description of the analysis employed in this work. The basic lamination theory is described briefly together with the derivation of orthotropic properties as employed in Chapter 9 (Failure analysis of T-joints). This is followed by a brief summary of the mathematical representation of the evolutionary structural optimisation method [1] employed in Chapters 3 & 4.

2.2 Basic Lamination Theory

A lamina or ply is an arrangement of unidirectional fibres in a matrix. The lamina is an orthotropic material where the principal material axis is determined by the direction of the fibres. Stacks of laminae with various orientations form a laminate and are generally called a lay-up. To simplify the analysis and due to the different plies having different orientations, laminates are analysed using a common fixed system of coordinates (x,y,z) as shown in Figure 2.1.

Composite material can be analysed at different levels and on different scales. At the constituent level parameters such as fibre diameter have to be considered. Micromechanics studies the interaction of fibres and matrices at the microscopic level. At the lamina level, the unidirectional lamina is usually considered as a quasi homogeneous anisotropic material with individual average stiffness and strength properties [3]. The analysis in this case is called macromechanics. At the laminate level the macroscopic analysis is employed in conjunction with lamination theory to predict both stiffness and strength as a function of lamina properties

and lay-up. Finally, at the structure level, finite element methods coupled to lamination theory are usually employed to determine the overall behaviour and state of stresses in each lamina forming the component.

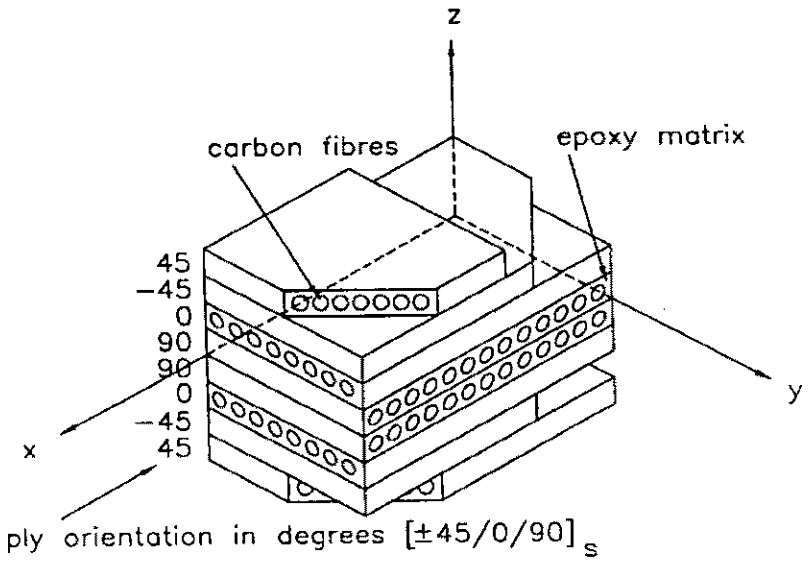

Figure 2.1: Laminate reference coordinate system [2]

The following notation (refer to Figure 2.2) is used throughout this work to characterise unidirectional ply's properties:

E_1, E_2, E_3 = Young's moduli along the principal ply directions

G_{12}, G_{23}, G_{13} = Shear moduli in 1-2, 2-3, and 1-3 planes respectively (equivalent to their reciprocals)

$\upsilon_{12}, \upsilon_{23}, \upsilon_{13}$ = Poisson's ratios in different planes

X_{1T}, X_{2T}, X_{3T} = Tensile strengths along the principal ply directions

X_{1C}, X_{2C}, X_{3C} = Compressive strengths along the principal ply directions

X_{12}, X_{23}, X_{13} = Shear strengths in 1-2, 2-3, and 1-3 planes respectively (equivalent to their reciprocals)

$\alpha_1, \alpha_2, \alpha_3$ = Coefficients of thermal expansion

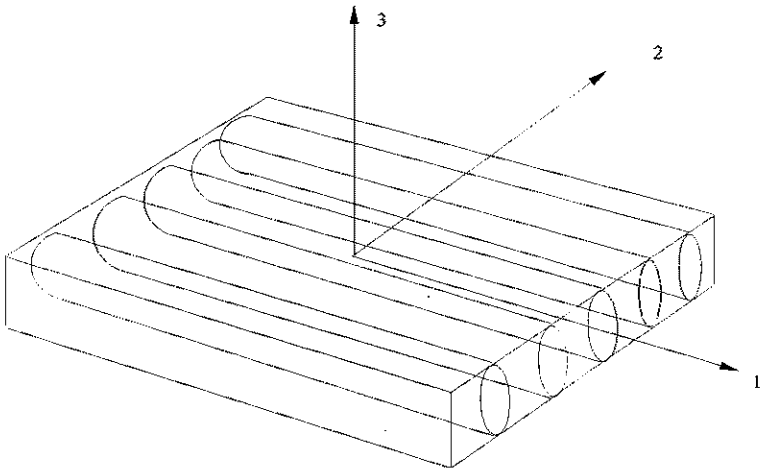

Figure 2.2: Lamina coordinate system

2.2.1 Orthotropic material with transverse isotropy

The analysis of composite T-joints performed in Chapter 9, considers the individual laminae wich conform the laminate as an orthotropic material with transverse isotropy. A transverse isotropic material is an orthotropic material in which at every point there is a plane where the mechanical properties are the same in all directions. Figure 2.3 depicts a typical unidirectional lamina with fibres packed in imperfect hexagonal array's which can be considered as transversely isotropic. In this Figure, the plane of isotropy is normal to the fibres (2-3).

The stress-strain relationship for a transversely isotropic material is characterised by only five independent elastic constants as shown in Equations 2.1 & 2.2 [3].

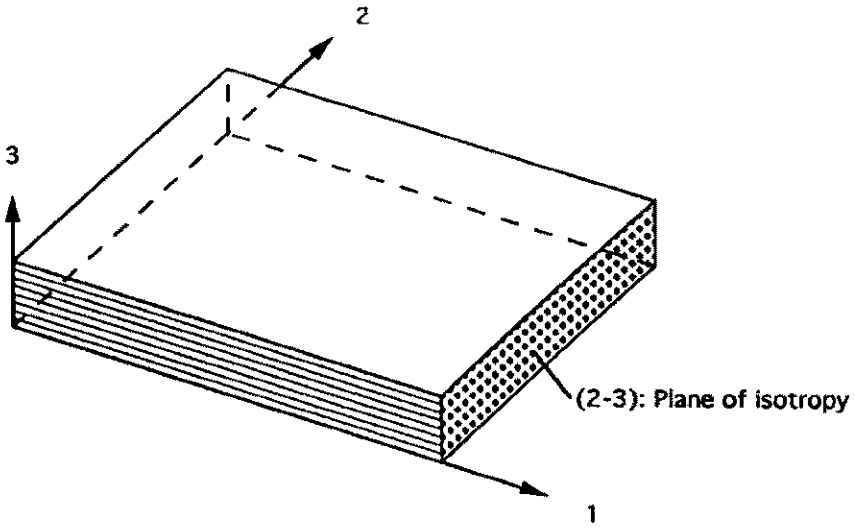

Figure 2.3: Orthotropic material with transverse isotropy [3]

$$\begin{bmatrix}\sigma_1\\ \sigma_2\\ \sigma_3\\ \tau_4\\ \tau_5\\ \tau_6\end{bmatrix} = \begin{bmatrix} C_{11} & C_{12} & C_{12} & 0 & 0 & 0\\ C_{12} & C_{22} & C_{23} & 0 & 0 & 0\\ C_{12} & C_{23} & C_{22} & 0 & 0 & 0\\ 0 & 0 & 0 & \frac{C_{22}-C_{23}}{2} & 0 & 0\\ 0 & 0 & 0 & 0 & C_{55} & 0\\ 0 & 0 & 0 & 0 & 0 & C_{55}\end{bmatrix} \begin{bmatrix}\varepsilon_1\\ \varepsilon_2\\ \varepsilon_3\\ \gamma_4\\ \gamma_5\\ \gamma_6\end{bmatrix} \tag{2.1}$$

$$\begin{bmatrix}\varepsilon_1\\ \varepsilon_2\\ \varepsilon_3\\ \gamma_4\\ \gamma_5\\ \gamma_6\end{bmatrix} = \begin{bmatrix} S_{11} & S_{12} & S_{12} & 0 & 0 & 0\\ S_{12} & S_{22} & S_{23} & 0 & 0 & 0\\ S_{12} & S_{23} & S_{22} & 0 & 0 & 0\\ 0 & 0 & 0 & 2(S_{22}-S_{23}) & 0 & 0\\ 0 & 0 & 0 & 0 & S_{55} & 0\\ 0 & 0 & 0 & 0 & 0 & S_{55}\end{bmatrix} \begin{bmatrix}\sigma_1\\ \sigma_2\\ \sigma_3\\ \tau_4\\ \tau_5\\ \tau_6\end{bmatrix} \tag{2.2}$$

The same relations can be expressed in terms of engineering constants as shown in Equation 2.3. The relations between mathematical and engineering constants are obtained by

conducting imaginary elementary experiments [3]. The relations between compliances S_{ij} and engineering constants follows:

$$\begin{bmatrix} \varepsilon_1 \\ \varepsilon_2 \\ \varepsilon_3 \\ \gamma_4 \\ \gamma_5 \\ \gamma_6 \end{bmatrix} = \begin{bmatrix} \frac{1}{E_1} & -\frac{\upsilon_{21}}{E_2} & -\frac{\upsilon_{31}}{E_3} & 0 & 0 & 0 \\ -\frac{\upsilon_{12}}{E_1} & \frac{1}{E_2} & -\frac{\upsilon_{32}}{E_3} & 0 & 0 & 0 \\ -\frac{\upsilon_{13}}{E_1} & -\frac{\upsilon_{23}}{E_2} & \frac{1}{E_3} & 0 & 0 & 0 \\ 0 & 0 & 0 & \frac{1}{G_{23}} & 0 & 0 \\ 0 & 0 & 0 & 0 & \frac{1}{G_{13}} & 0 \\ 0 & 0 & 0 & 0 & 0 & \frac{1}{G_{12}} \end{bmatrix} \begin{bmatrix} \sigma_1 \\ \sigma_2 \\ \sigma_3 \\ \tau_4 \\ \tau_5 \\ \tau_6 \end{bmatrix} \tag{2.3}$$

From the symmetry of the compliance matrix in Equation 2.2 and by equating those terms with Equation 2.3, the following relations are obtained:

$$\frac{\upsilon_{12}}{E_1} = \frac{\upsilon_{21}}{E_2}$$

$$\frac{\upsilon_{13}}{E_1} = \frac{\upsilon_{31}}{E_3} \tag{2.4}$$

$$\frac{\upsilon_{23}}{E_2} = \frac{\upsilon_{32}}{E_3}$$

The finite element analysis work requires the input of stiffnesses C_{ij} in order to calculate the state of stresses at each element. To obtain the relationship between these stiffnesses and the engineering constants, the compliance matrix $[S_{ij}]$ need to be inverted and the stiffnesses C_{ij} need to be expressed as a function of the compliances as follows:

$$C_{11} = \frac{S_{22}S_{33} - S_{23}^2}{S}$$

$$C_{22} = \frac{S_{33}S_{11} - S_{13}^2}{S}$$

$$C_{33} = \frac{S_{11}S_{22} - S_{12}^2}{S} \qquad \textbf{(2.5)}$$

$$C_{12} = \frac{S_{13}S_{23} - S_{12}S_{33}}{S}$$

$$C_{23} = \frac{S_{12}S_{13} - S_{23}S_{11}}{S}$$

$$C_{13} = \frac{S_{12}S_{23} - S_{13}S_{22}}{S}$$

$$C_{44} = \frac{1}{S_{44}}, \quad C_{55} = \frac{1}{S_{55}}, \; C_{66} = \frac{1}{S_{66}}$$

where the determinant S is given by the following expression:

$$\mathrm{S} = \begin{vmatrix} S_{11} & S_{12} & S_{13} \\ S_{12} & S_{22} & S_{23} \\ S_{12} & S_{23} & S_{33} \end{vmatrix} \qquad \textbf{(2.6)}$$

The relations between S_{ij} and the engineering constants are then substituted in Equation 2.6 to obtain:

$$C_{11} = \frac{1 - \upsilon_{23}\upsilon_{32}}{E_2 E_3 \Delta}$$

$$C_{22} = \frac{1 - \upsilon_{13}\upsilon_{31}}{E_1 E_3 \Delta}$$

$$C_{33} = \frac{1 - \upsilon_{12}\upsilon_{21}}{E_1 E_2 \Delta} \tag{2.7}$$

$$C_{12} = \frac{\upsilon_{21} + \upsilon_{31}\upsilon_{23}}{E_2 E_3 \Delta} = \frac{\upsilon_{12} + \upsilon_{13}\upsilon_{32}}{E_1 E_3 \Delta}$$

$$C_{23} = \frac{\upsilon_{32} + \upsilon_{12}\upsilon_{31}}{E_1 E_3 \Delta} = \frac{\upsilon_{23} + \upsilon_{21}\upsilon_{13}}{E_1 E_2 \Delta}$$

$$C_{13} = \frac{\upsilon_{13} + \upsilon_{12}\upsilon_{23}}{E_1 E_2 \Delta} = \frac{\upsilon_{31} + \upsilon_{21}\upsilon_{32}}{E_2 E_3 \Delta}$$

$$C_{44} = G_{23}, \qquad C_{55} = G_{13}, \quad C_{66} = G_{12}$$

where,

$$\Delta = \frac{1}{E_1 E_2 E_3} \begin{vmatrix} 1 & -\upsilon_{21} & -\upsilon_{31} \\ -\upsilon_{12} & 1 & -\upsilon_{32} \\ -\upsilon_{13} & -\upsilon_{23} & 1 \end{vmatrix} \tag{2.8}$$

For transversely isotropic materials such as the ones employed on the T-joint analysis where the 2-3 plane is the plane of isotropy, Equation 2.8 is further simplified by employing the following assumptions:

$$E_2 = E_3, \qquad G_{12} = G_{13}, \qquad \upsilon_{12} = \upsilon_{13} \tag{2.9}$$

A more detailed derivation of the above equations can be found in Daniel et. al. [3].

2.2.2 Analysis of thin composite laminates

The assumption of plane stress is often employed in the analysis of thin composite structures. The following assumptions [4] are made with reference to Figure 2.4:

(a) The thickness, t, is much smaller than a & b.

(b) The deformations u, v, w are small in comparison to t.

(c) The in-plane strains ε_x, ε_y, ε_{xy} are small compared to unity.

(d) Non-linear terms of stress resultants and plate slopes are maintained to account for in-plane stress effects.

(e) Interlaminar strains ε_{zx}, ε_{zy}, ε_z are negligible.

(f) The in-plane displacements u and v are linear functions of the z-axis.

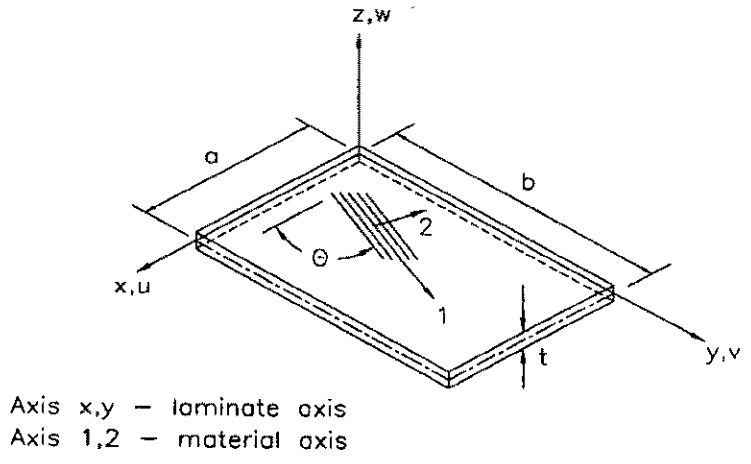

Figure 2.4: Laminate geometry [2]

The stress-strain relationship for a thin composite material under plane stress assumptions is characterised by only four independent elastic constants as shown in Equations 2.10 & 2.11 [3,5].

$$\begin{bmatrix}\sigma_1\\ \sigma_2\\ \tau_6\end{bmatrix}=\begin{bmatrix}Q_{11} & Q_{12} & 0\\ Q_{12} & Q_{22} & 0\\ 0 & 0 & Q_{66}\end{bmatrix}\begin{bmatrix}\varepsilon_1\\ \varepsilon_2\\ \gamma_6\end{bmatrix} \tag{2.10}$$

$$\begin{bmatrix}\varepsilon_1\\ \varepsilon_2\\ \gamma_6\end{bmatrix}=\begin{bmatrix}S_{11} & S_{12} & 0\\ S_{12} & S_{22} & 0\\ 0 & 0 & S_{66}\end{bmatrix}\begin{bmatrix}\sigma_1\\ \sigma_2\\ \tau_6\end{bmatrix} \tag{2.11}$$

Equation 2.11 can be expressed in terms of engineering constants by using the following relationships between compliances S_{ij} and engineering constants:

$$\begin{aligned} S_{11} &= \frac{1}{E_1}\\ S_{22} &= \frac{1}{E_2}\\ S_{12} &= -\frac{\upsilon_{12}}{E_1} = -\frac{\upsilon_{21}}{E_2}\\ S_{66} &= \frac{1}{G_{12}} \end{aligned} \tag{2.12}$$

Similarly Equation 2.10 can be expressed in terms of engineering constants by using the following relationships between stiffnesses and engineering constants:

$$\begin{aligned} Q_{11} &= \frac{E_1}{1-\upsilon_{12}\upsilon_{21}}\\ Q_{22} &= \frac{E_2}{1-\upsilon_{12}\upsilon_{21}}\\ Q_{12} &= \frac{\upsilon_{21}E_1}{1-\upsilon_{12}\upsilon_{21}} = \frac{\upsilon_{12}E_2}{1-\upsilon_{12}\upsilon_{21}}\\ Q_{66} &= G_{12} \end{aligned} \tag{2.13}$$

The 66 subscript used in Equations 2.10-2.13 is a result of compacting the tensor relationship (6x6 matrix). The 3, 4, 5 subscripts are not needed since no stress is generated through the ply's thickness as a result of assumption (a) in this section. A more detailed derivation of the above equations can be found in Whitney et. al. [5].

In the bending/extension case, the constitutive equation for a thin laminated plate may be derived as follows:

$$\begin{bmatrix} N \\ M \end{bmatrix} = \begin{bmatrix} A & B \\ B & D \end{bmatrix} \begin{bmatrix} \varepsilon \\ K \end{bmatrix} \tag{2.14}$$

where $\{N\}=\{N_x \quad N_y \quad N_{xy}\}$ have dimensions of force per unit length, $\{M\}=\{M_x \quad M_y \quad M_{xy}\}$ are the moment resultants per unit length, [A] represents the laminate extensional stiffness matrix, [D] represents the laminate bending stiffness matrix, [B] characterises the laminate bending/extension coupling matrix and [ε] and [K] represent the strains and curvatures of the deformed plate respectively. The different matrices are characterised in more detail by the following expressions:

By definition, the stress and moment resultants are given by:

$$\begin{aligned} [Nx, \quad Ny, \quad Nxy] &= \int_{-\frac{t}{2}}^{\frac{t}{2}} \left[\sigma_x^{(k)}, \sigma_y^{(k)}, \sigma_{xy}^{(k)}\right] dz \\ [Mx, \quad My, \quad Mxy] &= \int_{-\frac{t}{2}}^{\frac{t}{2}} \left[\sigma_x^{(k)}, \sigma_y^{(k)}, \sigma_{xy}^{(k)}\right] \mathrm{z}\, dz \end{aligned} \tag{2.15}$$

where the superscripted (k) refers to the k^{th} layer of the laminate. The laminate stiffness matrix [A] is defined as:

$$A_{ij} = \sum \left(Q_{ij}\right)_k \left(h_k - h_{k-1}\right) \tag{2.16}$$

And the laminate bending stiffness matrix [D] is defined as:

$$D_{ij} = \sum \left(Q_{ij}\right)_k \left(h_k^3 - h_{k-1}^3\right) \tag{2.17}$$

The laminate bending/extension coupling matrix [B] is defined as:

$$B_{ij} = \sum \left(Q_{ij}\right)_k \left(h_k^2 - h_{k-1}^2\right) \tag{2.18}$$

where h represents the distance from the k^{th} ply to the midplane and the numbering of plies starts from the bottom up. That is, ply 1 would be the outer ply on the laminate.

The above matrices, are expressed as a function of the transformed reduced stiffness Q_{ij} which is defined in terms of the stiffness matrix terms of the stress-strain relation for a unidirectional lamina $\overline{Q_{ij}}$, obtained from the generalised form of Hooke's Law:

$$\begin{aligned}
Q_{11} &= \overline{Q_{11}}\cos^4\theta + \overline{Q_{22}}\sin^4\theta + 2\left(\overline{Q_{12}} + 2\overline{Q_{66}}\right)\cos^2\theta\sin^2\theta \\
Q_{22} &= \overline{Q_{11}}\sin^4\theta + \overline{Q_{22}}\cos^4\theta + 2\left(\overline{Q_{12}} + 2\overline{Q_{66}}\right)\cos^2\theta\sin^2\theta \\
Q_{12} &= \overline{Q_{11}}\cos^2\theta\sin^2\theta + \overline{Q_{22}}\cos^2\theta\sin^2\theta + \overline{Q_{12}}\left(\cos^4\theta + \sin^4\theta\right) - 4\overline{Q_{66}}\sin^2\theta\cos^2\theta \\
Q_{16} &= \overline{Q_{11}}\cos^3\theta\sin\theta - \overline{Q_{22}}\cos\theta\sin^3\theta + \overline{Q_{12}}\left(\cos\theta\sin^3\theta - \cos^3\theta\sin\theta\right) + 2\overline{Q_{66}}\left(\cos\theta\sin^3\theta - \cos^3\theta\sin\theta\right) \\
Q_{26} &= \overline{Q_{11}}\cos\theta\sin^3\theta - \overline{Q_{22}}\cos^3\theta\sin\theta + \overline{Q_{12}}\left(\cos^3\theta\sin\theta - \cos\theta\sin^3\theta\right) + 2\overline{Q_{66}}\left(\cos^3\theta\sin\theta - \cos\theta\sin^3\theta\right) \\
Q_{66} &= \overline{Q_{11}}\cos^2\theta\sin^2\theta + \overline{Q_{22}}\cos^2\theta\sin^2\theta - 2\overline{Q_{12}}\cos^2\theta\sin^2\theta + \overline{Q_{66}}\left(\cos^2\theta - \sin^2\theta\right)^2
\end{aligned} \tag{2.19}$$

Finally, the strains and curvatures of the deformed plate are related to the mid-plane in-plane displacements *u*, *v* and *w* (see Figure 2.4) by:

$$\begin{aligned} \varepsilon_x &= \varepsilon_x^o - zk_x \\ \varepsilon_y &= \varepsilon_y^o - zk_y \\ \varepsilon_{xy} &= \varepsilon_{xy}^o - zk_{xy} \end{aligned} \tag{2.20}$$

where the superscript o denotes mid-plane properties and the individual terms can be expressed as:

$$\begin{aligned} \varepsilon_x^o &= \frac{\partial u}{\partial x}, \quad \varepsilon_y^o = \frac{\partial v}{\partial y}, \quad \varepsilon_{xy}^o = \frac{\partial v}{\partial x} + \frac{\partial u}{\partial y} \\ \mathrm{k}_x &= \frac{\partial^2 w}{\partial x^2}, \quad \mathrm{k}_y = \frac{\partial^2 w}{\partial y^2}, \quad \mathrm{k}_{xy} = 2\frac{\partial^2 w}{\partial x \partial y} \end{aligned} \tag{2.21}$$

Details of the above formulations may be found in the work by Tsai [6].

2.3 Optimisation methods

The currently employed structural optimisation methods can be broadly classed in two groups: those ones based on mathematical programming techniques also called gradient based methods and the Heuristic based methods.

Gradient based methods search for an optimum solution by using derivatives of the objective function and constraints. Design variables are usually modified to achieve this optimum solution. These variables can be continuous or discrete depending on the problem to be solved. Generally, continuous variables are employed as it is simpler to solve a problem with such variables. Furthermore, the solution obtained can always be adjusted to the closest integer solution without a significant effect on structural response [7]. The drawbacks of these types of methods lies in that the choice of design variables has a large influence on the solution obtained. Therefore, it is critical to identify the effect of variations of design variables on the objective function prior to the application of structural optimisation methods.

The heuristic based methods apply an intuitive approach to the optimisation problem. In general such methods are not mathematically intensive and are based on practical and fast techniques that are likely to lead to an optimum solution. Therefore, heuristic methods do not guarantee to find an optimum solution but determine the best solution possible given the constraints (time). Computer Aided Shape-Optimisation (CAO) is one example of an heuristic approach. This method was devised by Mattheck et. al. [8] and is based on observations of the natural growth of trees. It simulates numerically the growth mechanism of trees by copying the self-optimisation of living trees which always grow into shapes of constant surface stresses. The goal behind the concept is to achieve a state of constant Von Mises stress in the structure. A Biological Growth technique is employed coupled with finite element analysis whereby stress at the surface being shape optimised is converted to temperature and the surface allowed to move outwards (swell), if the stress is high, or inwards (shrink) if the stress is low. This process is repeated several times until the surface of the finite element model is on a state of constant Von Mises stress.

2.3.1 Gradient based methods

Most of these methods employ numerical search techniques. The design variables are usually modified in a stepwise fashion to improve the value of the objective function, or to reduce the violation of the imposed constraints. The process is terminated when no further progress can be made on either values or when the progress is too slow (objective function is reaching an asymptote). In some cases no constraints are prescribed. For these cases, the differential calculus method achieves the optimum solution most efficiently.

When constraints are set on the optimisation problem, optimality can be checked using for example Kuhn Tucker's approach or the Lagrangean approach. These approaches are based on differential calculus methods. Alternative methods for constraint optimisation problems to using differential calculus methods are known as search methods. Linear Programming and Integer-Linear Programming approaches are considered search methods.

Only the Integer-Linear Programming approach will be presented in detail in the next section due to its similarity to the Evolutionary Structural Optimisation method (ESO) employed in this dissertation. The reader is referred to the work by Haftka [7] for a detail description and the mathematical representation of the remaining methods mentioned above.

2.3.1.1 Integer-Linear Programming (ILP)

Problems based on calculus and linear programming techniques assume a positive and continuous solution vector $x=(x_1,x_2,...,x_n)$. Therefore, the optimum solution can take up any value of the design variables between their lower and upper bound. In some cases, design variables need to be discrete values. For example, if one is optimising the cross-section of a beam and desires to manufacture it, it would be more appropriate and economic to limit the cross-section to one commercially available. The solving of such a problem is achieved by employing a branch of mathematical programming known as *integer-linear programming* [9]. This type of problem can be characterised as follows:

Minimise $$f(x) = c^T x \tag{2.22}$$

Subject to $$Ax = b \tag{2.23}$$

$$x_i \in X_i = \{d_{i1}, d_{i2}, ..., d_{il}\}, \quad i \in I_d$$

where

I_d is a set of design variables that can only take discrete values

X_i is a set of allowable discrete values

Integer-Linear Programming problems can also have design variables with binary decision making processes {0,1}. As mentioned previously, it is possible in some instances to adjust the values obtained from continuous problem to the nearest integer in order to obtain the integer solution [7]. However, in some cases the approximation may lie outside the

feasible region, for example violating some of the imposed constraints. Thus this solution would be unfeasible. To avoid this possible error, an algorithm known as Branch-and-Bound algorithm can be employed [9]. The most appropiate and robust algorithm to solve an ESO type problem is by using a modification of the branch and bound algorithm [1].

2.3.1.2 Homogenisation Method

This method developed by Bendsoe [10], was the first in introducing the possibility of optimising both the topology of the structure and the microstructure of the material that constitutes the structure simultaneously. To achieve this, classical quadratic programming techniques are employed to minimise the compliance of the structure which is represented by finite elements. Each one of these elements is composed of a composite material with microvoids with the density being able to take up any value in the interval {0, 1}. Material densities of each element are the design variables (continuous variables). Furthermore, the density of each finite element is controlled with geometric variables which determine the material and its microstructure. The Homogenisation method can be characterised as follows:

$$\textbf{Minimise} \qquad l(u)$$

$$\textbf{Subject to} \qquad a_e(u,v) = l(v) \quad \text{for all } v \in U \tag{2.24}$$

where:

$$l(u) = \int_{\Omega} fud\Omega + \int_{T} tudT \quad \text{is the load linear form} \tag{2.25}$$

f are the body loads

and t are the surface tractions

and $a_e(u,v)$ represents the internal virtual work of an elastic body at the equilibrium u and for an arbitrary virtual displacement v:

$$a_e(u,v) = \int_{\Omega} E_{ijkl}(D)\varepsilon_{ij}(u)\varepsilon_{kl}(v)\, d\Omega \tag{2.26}$$

where:

$$\varepsilon_{ij} = \frac{1}{2}\left(\frac{\partial u_i}{\partial x_i}\right) + \left(\frac{\partial u_j}{\partial x_j}\right) \qquad \text{are the linearised strains} \tag{2.27}$$

U is the space of kinematically admissible displacement fields

E_{ijkl} is the rigidity tensor dependent on the design variables

This problem can be solved by employing for example the Sequential Linear or Non-linear Programming techniques.

2.4 Mathematical representation of the Evolutionary Structural Optimisation Method

The ESO method consists of the progressive removal of low stressed elements from a structure until an optimum is reached. As a result of removing these low stressed elements, the design converges to a fully stressed structure.

Querin [1] has observed similarities between the Integer-Linear Programming (ILP) method and ESO. He has classed ESO as a subset of the ILP method and has observed the following differences between them:

1) Inequality constraint functions are not bounded by a finite number
2) Inequality constraints change as the evolutionary process unfolds

The following mathematical representation of ESO (Equations 2.28-2.30) applies to discretised finite element structures.

Minimise

$$f(x) = \frac{\sum_{i=1}^{n} x_i \sigma_{VM_i} \bullet V_i}{FL} \tag{2.28}$$

Subject to

$$\sum_{i=1}^{n} x_i \left[[K]^i \{u\}^i - \{F_0\}^i - \{F_b\}^i - \{F_s\}^i \right] - \{P\} = 0 \tag{2.29}$$

$$x_e \left(x_e \cdot \sigma_{VM_{ee}} - RR \cdot \sigma_{VM_{Max}} \right) \geq 0 \tag{2.30}$$

$$x_e \in X_e = \{0,1\}, \qquad e \in E$$

where:

Eq. (2.29)	is the equality constraint and finite element formulation
Eq. (2.30)	is the ESO inequality constraint
V_i	is the volume of the i^{th} element of discretised structure
F	is the resultant applied load to the structure
L	is a nominal length for the structure
σ_i	is the Von Mises stress in the i^{th} element of discretised structure
E	is the set of discrete elements that make up the original FE mesh
X_e	is a set of allowable discrete values
n	is the number of elements in the structure
x_e	is the ESO multiplies

The minimisation of Equation 2.28 is generally true for all problems in which there is a change in volume as the evolutionary process evolves. In the case of the original problem treated in Chapter 4 (Optimisation of pin-loaded joints) whereby the volume of the structure

remains constant throughout the optimisation process the objective of the problem is to minimise the maximum Von Mises stress in the composite structure. That is, it is acceptable to obtain a larger maximum Von Mises stress in other areas of the joint (non–composite, ie insert material) to achieve the overall objective of minimising maximum stresses in the composite material. In other words the minimisation of Equation 2.28 is not the objective of min-max problems where the total volume of the structure remains unaltered.

2.5 References

[1] Querin, O. M., "*Evolutionary Structural Optimisation: Stress Based Formulation and Implementation*", PhD Thesis, Department of Aeronautical Engineering, University of Sydney, Australia, April, 1997.

[2] Falzon, B. G.,"*An Investigation into the Buckling and Postbuckling Behaviour of Hat-stiffened Composite Panels*", PhD Thesis, Department of Aeronautical Engineering, University of Sydney, Australia, December, 1995.

[3] Daniel, I. M., Ishai, O., "*Engineering Mechanics of Composite Materials*", Oxford University Press, 1994.

[4] Whitney, J., "*Structural Analysis of Laminated Anisotropic Plates*", Technomic Publishing Co., Inc., Lancaster, Pennsylvania, 1987.

[5] Whitney, J. M., Daniel, I. M., Pipes, R. B., "*Experimental Mechanics of Fibre Reinforced Composite Materials*", Soc. Expt. Stress Analysis Monograph 4, Prentice-Hall, 1982.

[6] Tsai, S. W., "*Composites Design*", 4th Edition, Think Composites, Dayton, 1988.

[7] Haftka, R. T., Gurdal, Z., "*Elements of Structural Optimization*", 3rd edition, Kluwer Academic Publishers, 1993.

[8] Mattheck, C., Burkhardt, S., "A new method of structural shape optimization based on biological growth", *International Journal of Fatigue*, Vol. 12, No. 3, pp. 185-190, 1990.

[9] Beale, E. M. L., "*Introduction to optimization*", John Wiley & Sons, 1988.

[10] Bendsoe, M. P., "*Optimization of structural topology, shape and material*", Springer, Berlin, 1995.

CHAPTER 3

SHAPE OPTIMISATION OF ADHESIVELY BONDED JOINTS

3.1 Introduction

Almost every designed structure requires component members to be connected. The designer must then decide from alternatives ranging from mechanical fasteners such as screws and rivets to bonding. The main disadvantages of mechanical connections are that they do not distribute the load uniformly, thus resulting in large local stresses. Joining the members adhesively can often significantly reduce this problem [1]. For aircraft, some of the advantages over mechanically fastened or integrally machined structures were identified by Alner [2]:

(a) Weight savings between 5% to 25% can be achieved depending whether the members are structural or non-structural (flaps, control surfaces, etc.)

(b) A smooth exterior finish can be achieved. This is of particular importance in high performance aircraft.

(c) Sealing of pressurised cabins and integral fuel tanks is simplified since good structural adhesives are highly resistant to air and fuel leakage.

(d) Production costs are reduced, since the cost of the bonding process is independant of the total area to be joined.

(e) Bonding generally increases fatigue life by eliminating the stress concentrations normally present in riveted structures.

Summarising, light, stiff and economic structures may be obtained by adhesively bonding structural members. Another advantage of adhesive bonding is that it enables dissimilar

materials to be joined, even in the case where one of the materials is non-metallic [3]. A major application of bonding is therefore, the joining of composite materials.

The adhesives that are used in the aircraft industry are generally the epoxy resins. This is due to their strength, versatility and excellent adhesion to a variety of surfaces. Furthermore, epoxy adhesives possess important characteristics such as high specific adhesion to metals, high cohesive strength within the glue line, low shrinkage when cured and low creep when compared to thermoplastics. They also act as effective barriers to heat and electric current and are moisture resistant. Their main disadvantages are toxicity when not cured, low shelf-life and a moderate to high cost [4].

Despite the many advantages mentioned above, the use of adhesives as a method of joining structural members is still limited. The main problems that have tended to limit their use are difficulties in predicting strength and optimising joint geometry to achieve the desired strength and reliability. Other difficulties in employing bonded joints are the variability of cure and the quality assurance or integrity of the joint.

3.1.1 Structural bonded joints

A structural joint is defined as a particular segment of structure which functions as a load transfer medium from one or more structural member to adjacent members. Adhesively bonded joints are most efficient while transferring load in shear. In peel, their strength is unsatisfactory. Due to this shortcoming, it is considered good design practice to arrange the joint to transfer the load in shear and minimise any induced or direct peel stresses. Design of bonded joints thus requires knowledge of shear and peel stress distributions in the bond line and adherends, available through stress analysis. Bonded joints should always be stronger than the individual adherends they are joining. Lap joints are often found throughout the aircraft and are a significant item in the design process for structural integrity. Different types of joints are employed depending on the loading conditions and materials employed. Figure 3.1 shows the most commonly used arrangements in bonding adherends.

Where the adherends are thin and the load is low, adherends with uniform thickness tend to be used. On the other hand, where adherends are thick and loading is high, stepped lap joints or tapered adherends are utilised.

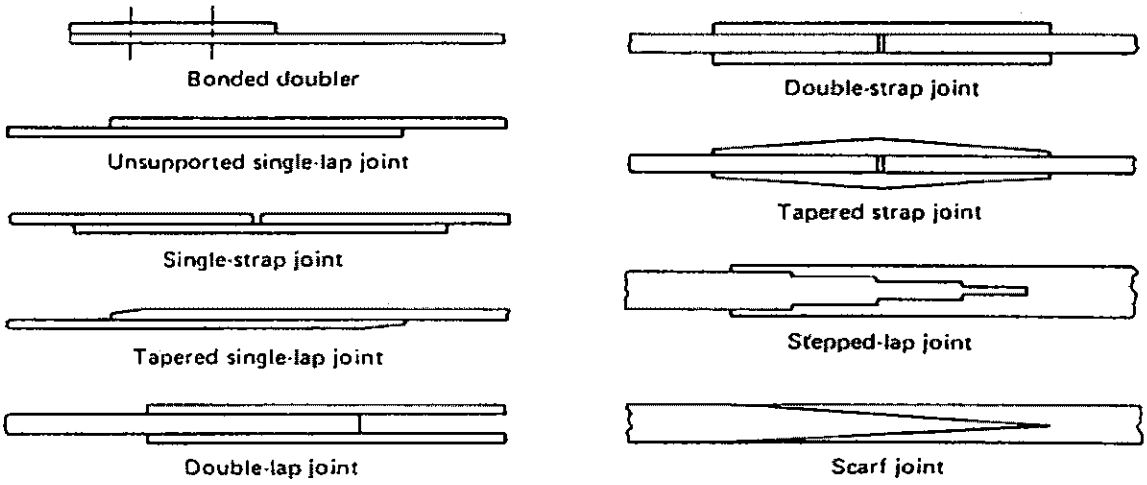

Figure 3.1: Types of adhesively bonded joints [5]

The single lap joint under longitudinal tension is often used to demonstrate the accuracy of theories for calculating stresses in adhesively bonded joints. Elastic stress distribution in this type of joints was originally studied by Volkersen [6]. His analysis assumed that the adhesive was linear elastic with deformation occurring only in shear. His assumptions concluded in predicting a decrease in shear stress concentration in the adhesive layer for increasing adherend stiffness or the thickness of the adhesive layer. A decrease in adhesive shear modulus and overlap length also resulted in a decrease in stress concentration.

The importance of peel stresses in adhesively bonded joints was firstly introduced by Goland and Reissner [7]. They showed that bending of the adherends due to the eccentricity of the applied tensile load produces significant peel stress perpendicular to the plane of the adhesive film. They employed simple approximations to calculate the bending moment and shear force at the ends of the joint as functions of the applied tension. Some of the assumptions in the Goland and Reissner theory follow: adhesive shear and peel

stresses are constant through the adhesive thickness, direct stresses (parallel to the adherends) in the adhesive are negligible, adherend and adhesives are linear elastic and the adhesive thickness is ignored.

Both theories have shortcomings due to the assumptions they employ. While Volkersen's theory neglects the flexibility of the adhesive, the theory by Goland and Reissner ignores the transverse flexibility of the adherend sheets. Furthermore, stress boundary conditions at joint edges are not satisfied in either theory.

Some time after these two theories became widely known, much work has been published with simplifications and modifications to either theory. Research based on experimental work was also published extensively. A comprehensive literature survey on bonded joints can be found in the work by Ellis [8]. Some of the landmarks in the analysis of bonded joints are briefly presented in the following paragraphs.

Kutscha and Hofer [9] found that in single lap joints with dissimilar adherend thicknesses, the maximum shear stress occurs where the load enters the joint from the thinner adherend.

The application of the finite element method to bonded joint analysis was initially employed by the mid-sixties. In particular, Wolley and Carver [10] were the first to apply the finite element method to single lap joints, assuming plane stress conditions. The work analysed the effect of the Young's Moduli ratios and geometries on the peel and shear stress distributions.

Adams and Peppiatt [11] started an investigation on the accuracy of Goland and Reissner's approach in 1973. In their work, they showed that Poissons ratio strains in the adherends of a single lap joint induce transverse stresses in the adhesive and adherends. Effect of bending was neglected and the adhesive was modelled as an infinite number of shear springs (ie. peel stresses were ignored). In other work, they included the adhesive fillet in their analysis. A triangular fillet was modelled as opposed to the commonly used assumption of a square adhesive fillet. A reduction on the maximum shear stress of 70 % was obtained by modelling the adhesive fillet as a triangle.

Hart-Smith [12] improved on the Goland and Reissner's approach by incorporating a third free-body diagram for the adherend outside the joint in addition to the two free-body diagrams from each of the upper and lower halves of the joint. Imposing additional boundary conditions involving displacements and their first derivatives solved the additional unknowns. A closed form analytical method is generally employed by Hart-Smith to analyse relatively simple bonded joints. For more complex joints, he employs iterative solutions on a digital computer. In his analysis, he accounts for adhesive plasticity by using an elastic-plastic shear stress model. Adherend stiffness imbalance and adherend thermal mismatch are also accounted for in his approach. The elastic-plastic theory employed by Hart-Smith predicts an increase in joint strength when compared to the linear elastic analysis usually employed.

Analyses by Hart-Smith are similar to those ones presented on the Engineering Sciences Data Unit (E.S.D.U.) [13]. In both cases, adhesives are modelled as elastic-plastic materials. These close-form type analyses are the most widely available and have been considered to be sufficiently accurate and effective to be employed by industry.

3.1.2 Research on shape optimisation of bonded joints

Joints are sources of stress concentrations which diminish the overall efficiency of a structure. In strength critical components it becomes imperative to reduce these stress concentration factors so as to increase structural efficiency. Stress concentrations in bonded joints arise from abrupt changes in adherend/adhesive thicknesses and from differences in elastic moduli [6]. Limited work can be found to date in the use of FEA optimisation on adhesively bonded joints. Groth and Nordlund [14] studied optimum shapes of adherends with the intention of minimising the Tsai-Hill factor (objective function) along the adhesive overlap. The Tsai-Hill yield criterion is a general form of the Von Mises yield hypothesis for non-isotropic materials. Joint types included in the analysis were single-lap, double-lap, double-strap and a console bonded to a rigid wall. The adherends for both the single and double-lap joints had to be pre-profiled so that the mesh distortions would not make the analysis unfeasible. Furthermore, slave and master

variables were employed to enforce anti-symmetry for the single lap joint case. Finally, explicit linear constraints had to be employed to ensure that the finite element mesh did not fail during the optimisation process. The optimum shape found for the adherends of single lap joints by Groth et. al. consisted in double tapered adherends with a flat region in between both tapers.

Ojalvo [15], studied a procedure to minimise elastic shear stress concentrations in adhesive lap joints. The procedure consisted of employing an inverse method which imposes a desired shear stress distribution and then determines the required adherend shapes to achieve it. The objective function in this case was based on shear stresses, thus the solution obtained by this method needed to be checked to determine the actual shear and peel stresses in the joint. Optimum adherend shapes presented for both single and double lap joints are single curvature tapers.

Lerchenthal [16]; employing some simplifying assumptions; succeeded in determining the shape of adherends which produce as far as possible a uniform shear stress distribution in the direction of the glue line. Photoelastic techniques were employed to verify shear stresses in the glue line.

Cherry and Harrison [17], postulated that the objective to obtain an optimum single lap joint should be that of achieving a uniform shear stress along the overlap length. A closed form solution was employed to this effect resulting in a uniformly tapered joint.

Two different optimisation methods were evaluated for the shape optimisation of adherends and adhesive fillets in an attempt to correlate optimum shapes achieved by employing different approaches. The first method considered, is known as the shape basis vector technique [18]. This method employs approximation concepts and mathematical programming techniques to achieve optimum shapes of structures given a design objective and constraints. A brief description of the shape basis vector method and the difficulties experienced with its implementation is given on the next section. The second method presented in this chapter is referred to as the "evolutionary structural optimisation method" or ESO [19-20]. A commercial version of this software called EVOLVE [21] has been released to the market by its developers. This method does not require any mathematical

formulations or the reinforcing of constraints. It also does not require the use of an objective function. The ESO method is broadly classified as a heuristic optimality criteria method.

After assessing both shape optimisation methods, the ESO method was chosen to reshape the adherends in bonded joints to obtain fully stressed adherends. Although no explicit objective is required, the goal was to minimise the peak stresses at the end of the overlaps. The same method was also applied to optimise the shape of adhesive fillets found in tabs of tensile test specimens in which the adherends were titanium and T800 unidirectional tape.

3.2 Shape basis vector technique

As mentioned on Chapter 1, a variety of optimisation methods have been developed during the last few decades. The shape basis vector (SBV) approach is a fairly recent method which employs mathematical programming techniques for shape optimisation of parts. This method has been adopted by the finite element analysis code MSC/NASTRAN within their optimisation solution sequence (SOL 200) [18]. This module allows the geometry of the design model to be varied to improve a design objective (e.g minimum weight) while satisfying various design constraints (e.g maximum stress). The variation of geometry is achieved in MSC/NASTRAN by changing the locations of nodes. The coordinates of these nodes are controlled by design variables while their movement is represented by shape design variables. A shape basis vector is a group of design variables. This vector contains information on the magnitude and direction of shape variation. In a finite element model, the geometric shape is expressed in terms of node coordinates. The following equations outline the relationship between the new and old geometry:

$$\{R\}^{new} = \{R\}^{old} + \sum_{i=1}^{n} \left(X_i^{new} - X_i^{old}\right)\{T_i\} \qquad (3.1)$$

$$\{\Delta R\} = \sum_{i=1}^{n} \Delta X_i \{T_i\} \qquad (3.2)$$

where:

{R}	= nodes coordinates
{T}	= shape basis vector
X_i	= design variable
n	= number of design variables
new	= at end of design cycle
old	= at beginning of design cycle

Equation (3.1), shows that the new shape is linearly dependant on a combination of the shape basis vector and the *old* shape. The shape basis vectors are generated within the MSC/NASTRAN environment. Four methods are available to generate SBV's. A brief description of these methods follows:

a) *Manual Grid variation method (MGV):* This is the most tedious method since it requires the input of every single direction and magnitude of node coordinate change. Although this method is very general, it is very time consuming without the aid of a pre-processor. Furthermore, this method often results in mesh distortion problems due to the fact that the SBV's are not updated in between design cycles.

b) *Direct input of shapes (DIS):* In this method, an auxiliary model (FEM) provides externally generated vectors which are then used to define shape basis vectors. The auxiliary model has the same geometry but different loads and constraints. Its advantage is the easy generation of SBV's. The disadvantages include the need of running a model beforehand to generate the SBV's and the lack of updated shape basis vectors in between design cycles causing mesh distortion.

c) *Geometric boundary shapes (GBS):* This method allows the creation of SBV's using only the boundary of the structure. Shape variations can be defined manually or with a

geometry-based pre-processor. The advantages of this method is that directions and magnitudes of node variations need only be defined for the boundaries and that the SBV's are updated in between design cycles reducing the chance of mesh distortion. The main disadvantage is the fact that a considerable number of directions and magnitudes of node variations might still need to be generated.

d) *Analytic boundary shapes (ABS):* This method is similar to the GBS method described above with the difference that shape variations do not need to be defined manually or even with the help of a pre-processor. Instead, an auxiliary model is constructed by the designer over the boundaries of the structure that are to be changed. For example, a series of bar elements can be generated at the edge of plate elements. The designer constraints and loads the auxiliary model independently from the main model to generate a shape variation over the boundary. The code then interpolates these variations to the interior of the structure thus generating shape basis vectors. The advantages of this method are its generality and the fact that no pre or post-processor is required. In addition, SBV's are updated in between design cycles. A possible disadvantage is the creativity required by the designer in generating adequate SBV's by choosing loads and boundary conditions for the auxiliary model relevant to the problem at hand.

The design variables are usually linked to a basic variable set. The constraints are grouped into regions and from each region only constraints which violate a "threshold" constraint are selected. A modified feasible direction algorithm is employed for searching the optimal solution which best meets the constraints. This process is iterated until all the constraints are satisfied or when the violated constraints can not be reduced further.

The shape optimisation of adherends in bonded joints was attempted by employing the ABS method for the generation of SBV's. The design objective was chosen to be the minimisation of the Tsai-Hill factor shown in equation (3.3). The Tsai-Hill yield criterion is a general form of the Von Mises yield hypothesis. Yielding is said to occur when the TSAI value is greater or equal to 1. The notation employed in this equation is described in Chapter 2. The reason for choosing this objective function was the goal of correlating the

optimum shape obtained from the shape basis vector approach to that obtained by Groth et. al. [14] with the optimisation code OASIS-ALADDIN.

$$TSAI = \left(\left(\frac{\sigma_1}{X_{1T}} \right)^2 + \left(\frac{\sigma_2}{X_{2T}} \right)^2 - \frac{1}{RHO} \frac{\sigma_1 \sigma_2}{X_{1T} X_{2T}} + \left(\frac{\tau}{X_{12}} \right)^2 \right)^{\frac{1}{2}} \quad \textbf{(3.3)}$$

This function allows different weights to be given to stress component depending on their influence. That is, values of X_{1T}, X_{2T}, X_{12} and RHO can be given different values to make the objective function being dominated for example by the shear stress. RHO is a non-dimensional factor. When this factor equals 1, the coupling of the direct and peel stresses has some weight on the TSAI value. On the other hand, when RHO is assigned a large magnitude, the effect of the coupling between the direct and peel stresses on the TSAI value is negligible. The definition of the remaining values can be found in Chapter 2. For the single lap-joint analysis (see Figure 3.5 for geometry and constraints), the following yield stresses were used for the adhesive layer:

X_{1T} = 2 MPa
X_{2T}= 2 MPa
X_{12} = 1.01 MPa
RHO = 10000

Details regarding the finite element analysis, material properties and loading are given in Section 3.4.1. For the analysis of single lap joint failures, both peel and shear stresses are significantly important. The starting geometry was chosen to be square ended adherends so as to be able to obtain an equivalent comparison with the analysis run employing the heuristic approach ESO. Figure 3.2 depicts the finite element model mesh corresponding to the starting model. A coarse mesh was employed in order to minimise mesh distortion problems during the optimisation runs. The shape basis vectors were generated using an auxiliary boundary model. This model was generated by creating a group of bar elements on the boundary of the upper adherend along the length of the adhesive overlap. The auxiliary model was then loaded independently by placing a force at

the end of the group of bar elements with boundary conditions corresponding to a cantilever beam. The design variables (node coordinates) along the adhesive overlap corresponding to the bottom adherend were related to their anti-symmetric design variables of the upper adherend to reduce computational effort.

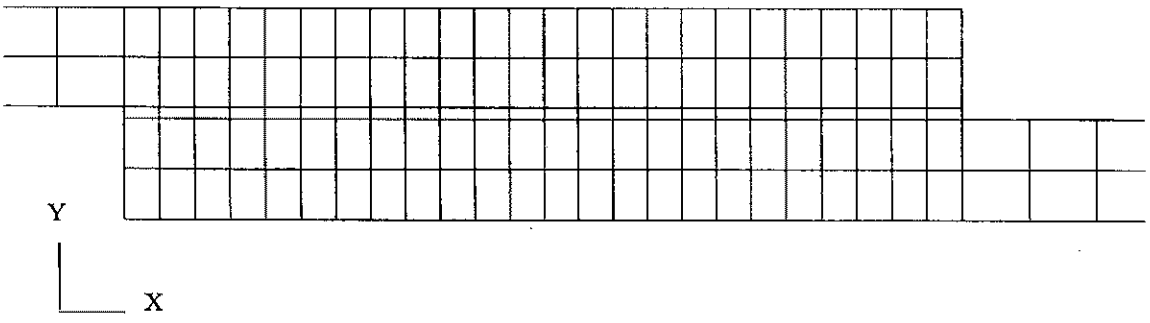

Figure 3.2: Mesh of starting finite element model

Initially the optimisation was performed on four node elements. The result after the first design iteration was not encouraging. The finite element analysis could not be solved after the design variables (node coordinates of the upper and lower adherend along the adhesive overlap) were modified. The new coordinates assigned to the design variables resulted in an extremely distorted mesh with skewed and tapered elements well beyond the default allowable for these parameters. Essentially, the elements; in particular those close to the end of the overlap; had severe shape distortion resulting in ill-conditioning of the stiffness matrix. In an attempt to restrict the mesh distortion, the auxiliary model which determines the SBV's was modified by generating different loads together with boundary conditions corresponding to simply supported beams. The type of element was also changed to eight node elements and the mesh refined locally at the tip of the adherends.

Unfortunately, the mesh distortion was only marginally reduced. It was then decided to modify the starting design by generating a new model with a single taper on both upper and lower adherend. The mesh corresponding to the single taper model is shown in Figure 3.3. A similar approach was followed by Groth et. al., where it was found that the design variables corresponding to the adherends; along the overlap length; needed to be assigned

explicit linear constraints to ensure that the finite element mesh did not fail during the optimisation process. Although the pre-profiling of the adherends removed all problems related to mesh distortion, no significant gain in stress reduction was achieved. Furthermore, the shape of the adherends did not vary apart from small coordinate variations close to the tip of the adhesive. That is, the optimum design converged to a single taper adherend, which is the known result.

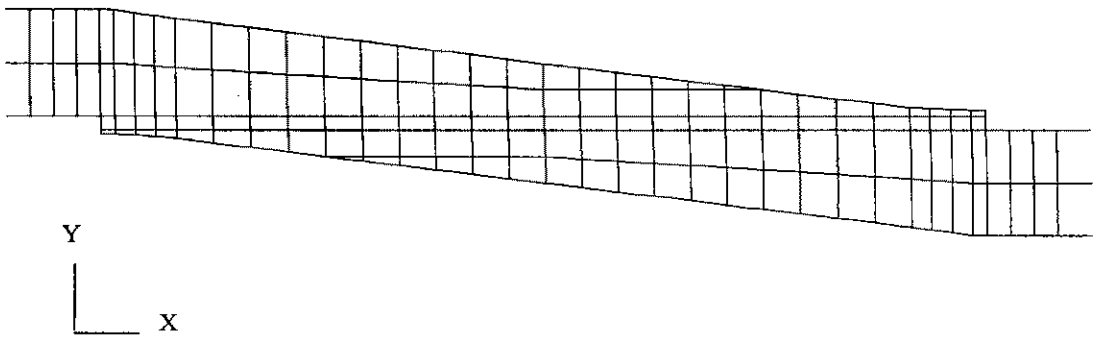

Figure 3.3: Mesh of single taper finite element model

The results obtained from the shape basis vector approach show that this technique is only appropiate for "fine-tuning" existing designs and that radical shape changes can not be expected without the use of an automatic mesh generator. The regeneration of a model by fully re-meshing the structure once the optimisation code detects severe mesh distortion could solve problems similar to the one attempted in this section.

3.3 Evolutionary Structural Optimisation

3.3.1 Concept and Methodology

A simple Evolutionary Structural Optimisation procedure [19,20] developed by G.P. Steven and Y.M. Xie has been employed for the optimisation of adhesively bonded joints

by shaping the adherend profiles to reduce peak stresses at the end of the overlaps. The ESO method consists basically of removing the low stressed part of the material progressively from the structure.

Firstly, a finite element analysis of the desired structure is performed and the stress distribution found. A plate stress file is then set-up and using some criterion for rejection, here called a Rejection Criterion (RC), such as the Von Mises stress, the low stressed material is removed. For example, elements which have a Von Mises stress lower than a Rejection Ratio (RR) times the maximum Von Mises stress in the structure are deleted. The finite element analysis and rejection cycle are then repeated until a steady state (s.s) is reached. An Evolution Rate (ER) is then introduced and added to the current RR until another steady state is reached. This process is repeated until the desired optimum is reached, for example, till all stress levels are 20 % of the maximum in the whole structure. A flowchart showing the methodology of EVOLVE; the commercial version of ESO; is shown in Figure 3.4.

The benchmarking of the EVOLVE method has been carried out in several papers presented by the developers [19-23]. The optimisation problems benchmarked include an optimal two-bar frame, a Michel type structure and an MBB beam (designed to carry the fuselage floor in an Airbus carrier). The solutions obtained with EVOLVE for the above problems are compared with Suzuki et. al. [24], Hemp [25] and Rasmussen et al. [26] respectively. In all cases, the comparison between the two corresponding solutions indicates a very similar topology. Additional examples of the capabilities of the developed software EVOLVE which employs the heuristic optimality criteria method ESO can be found in the work by Querin et. al. and Querin [21, 23]. These include non-linear solutions, three-dimensional problems and optimisation of beam structures.

A new development within ESO is the bidirectional evolutionary structural optimisation (BESO) method which allows elements of a structure to be either added or removed [1].

[1] Examiner queried possibility of recovering deleted elements. The following reference has been added post-examination. Ref. [33]

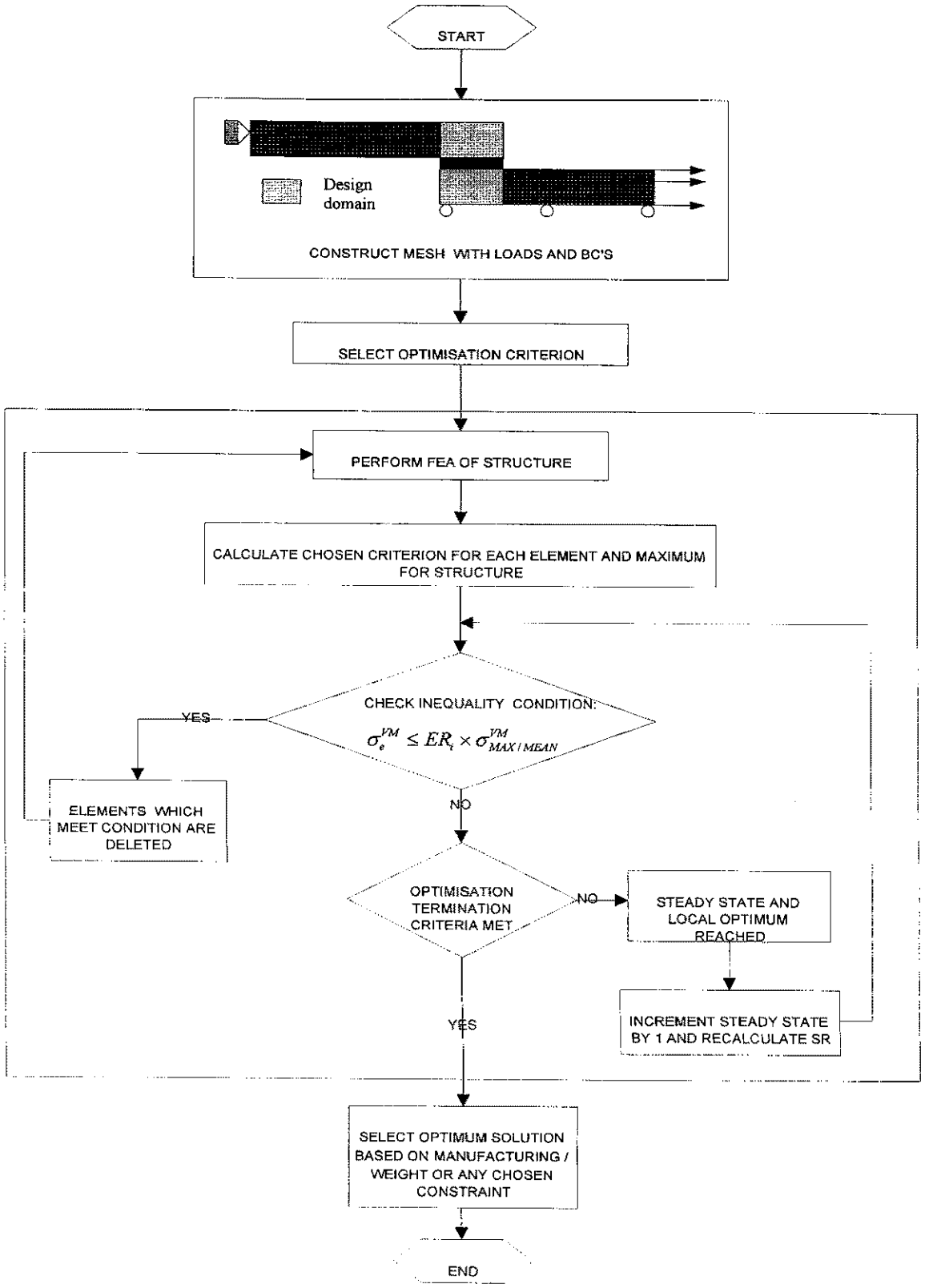

Figure 3.4: EVOLVE / ESO Flowchart

3.4 Shape Optimisation of adherends in single and double lap joints

The evolutionary structural optimisation method described in the preceding sections was applied to both single (SLJ) and double lap joints (DLJ). As mentioned previously, this method consists essentially in deleting the lowly stressed elements from the joint progressively. This should lead to fully stressed adherends which in turn re-distribute the stresses to the adhesive interface more evenly thus minimising the peak peel stresses normally found in this type of joints. In the cases presented, the overlap length and adhesive thickness were set as constants and only the adherends along the overlap were allowed to evolve. A single element across the adhesive layer was employed.

Typically, the selection of an adequate joint requires a number of design and analysis cycles which rely heavily on the trial and error method. The ESO method relies, for the cases presented, on iterative FEA and progressive removal of elements which takes the guess work out of the design loop. The objectives in both cases are to minimise the maximum stresses in the adhesives.

The shape of the adherends (SLJ) correlates very well to that obtained with a different optimisation program [14].

3.4.1 Finite Element Analysis and Optimisation results

The dimensions of the joint together with the loading and kinematic constraints are shown in Figure 3.5. A plane strain analysis with QUAD4 elements was employed. The load corresponded to a nominal shear stress in the adhesive of 1 Mpa and the materials had the following properties: aluminium adherends (E=70000 Mpa,υ=0.3); epoxy adhesive (E=2000 MPa, υ=0.3). The geometrical non-linearity present in single lap joints is not accounted for in the analysis. The starting models had square ended adherends with only one element across the adhesive thickness. A coarse mesh with 1383 QUAD4 elements and 8 TRI3 (3 node triangular) elements was initially employed to determine whether the size of the elements would affect the overall shape of the adherends. It was found that although the overall shape did not vary significantly when finer meshes were employed,

the curvature of the adherends taper slightly changed. Furthermore, the finer mesh provides more points at the edge of the adherends from which a spline could be constructed. The finer mesh model consisted of 7909 QUAD4 elements and 8 TRI3 elements.

The evolution criteria employed for the optimisation of adherend shapes in both single and double lap-joints was the Von Mises stress. The software allows the nomination of non-design properties for areas of the joint for which no elements are allowed to be deleted. The only area from which material could be removed was above/below the adhesive overlap length. Furthermore, an optimisation parameter which ensures that only plates with at least one free edge can be removed at any time was employed so as to obtain a feasible solution. Without this parameter, an adherend with holes could be obtained.

The optimum adherend shape (SLJ) is shown in Figure 3.6. The optimum rejection ratio was found to be RR=13.1 %, yielding a reduction in peel stress at the end of the overlap of approximately 36 %. The evolutionary rate was set to ER=0.1.The maximum shear stress increased by only 2 % and its peak was shifted inwards to the joint by one element (0.2mm). Groth et. al. [14]; in their optimisation work; obtained a very similar shape of adherends as depicted in Figure 3.7.

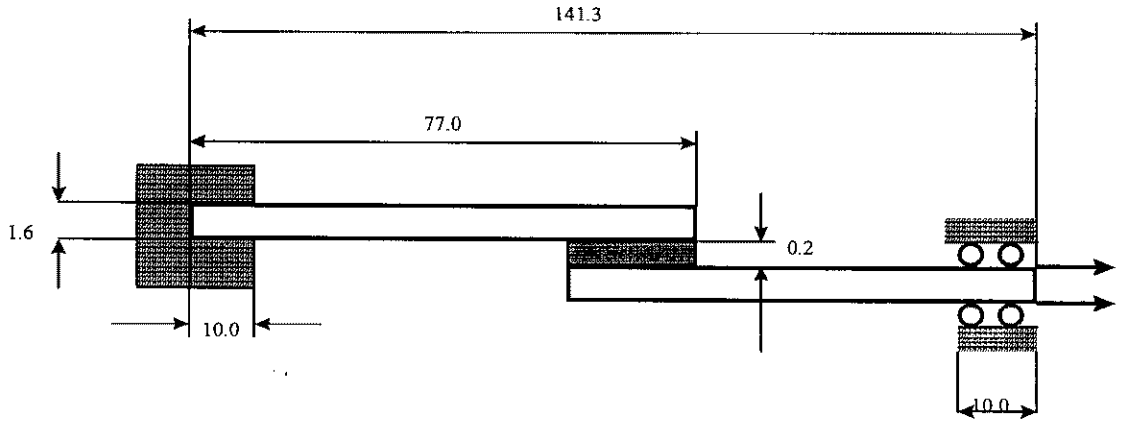

Figure 3.5: Geometry and boundary conditions of SLJ

The running time was approximately 12 hours in a 486-DX33 processor with 16 Mb RAM. To obtain the optimum rejection ratio, the different design cycles were initially run independently and the stresses along the overlap compared for each cycle. Due to the large post-processing time required to assess the optimum solution for min-max problems, a monitoring property was introduced in EVOLVE. This reduced the post-processing time for this type of problems significantly as the elements for which stresses are required, can be specified as a post-processing property number. The only stresses, which are available through this post-processing facility, are the stresses corresponding to the driving criterion. That is, if the driving criterion is the Von Mises stress, this stress will be output for all elements whose property was specified and for every steady state to a file. This file contains the desired property numbers and the stresses (specified as driving criterion) at each steady state. Furthermore, a maximum or mean stress vs iteration or s.s number can be generated within the EVOLVE post-processing facility to quickly determine the overall trends in stress profiles as the analysis progresses.

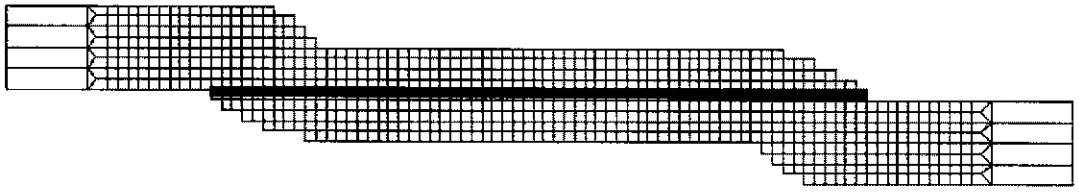

Figure 3.6: Optimum adherend profiling along overlap (ESO, Single Lap Joint)

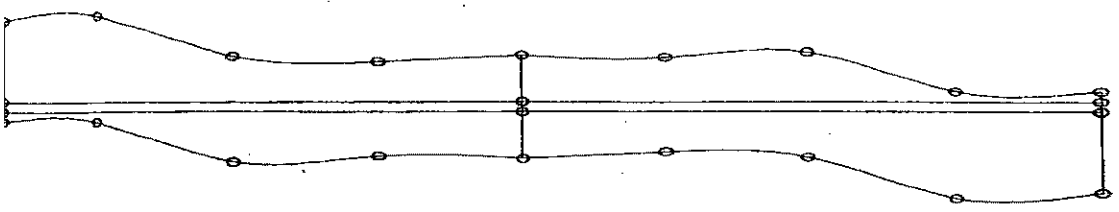

Figure 3.7: Optimum adherend profiling along overlap, Ref. [14]

The shear and peel stress distributions vs overlap length for both original and optimised model are shown in Figure 3.8 & 3.9 respectively.

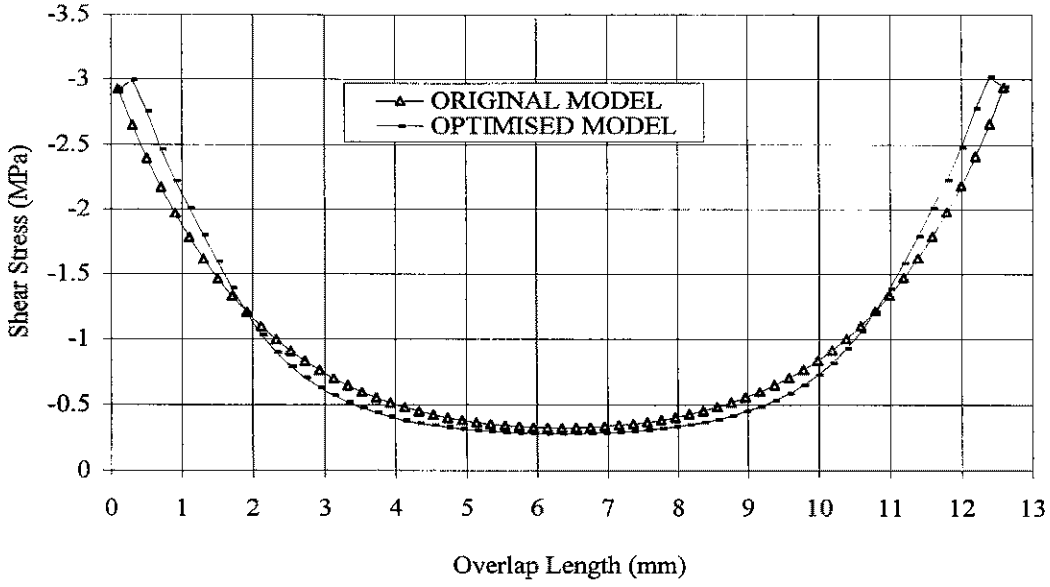

Figure 3.8: Shear stress distribution (SLJ)

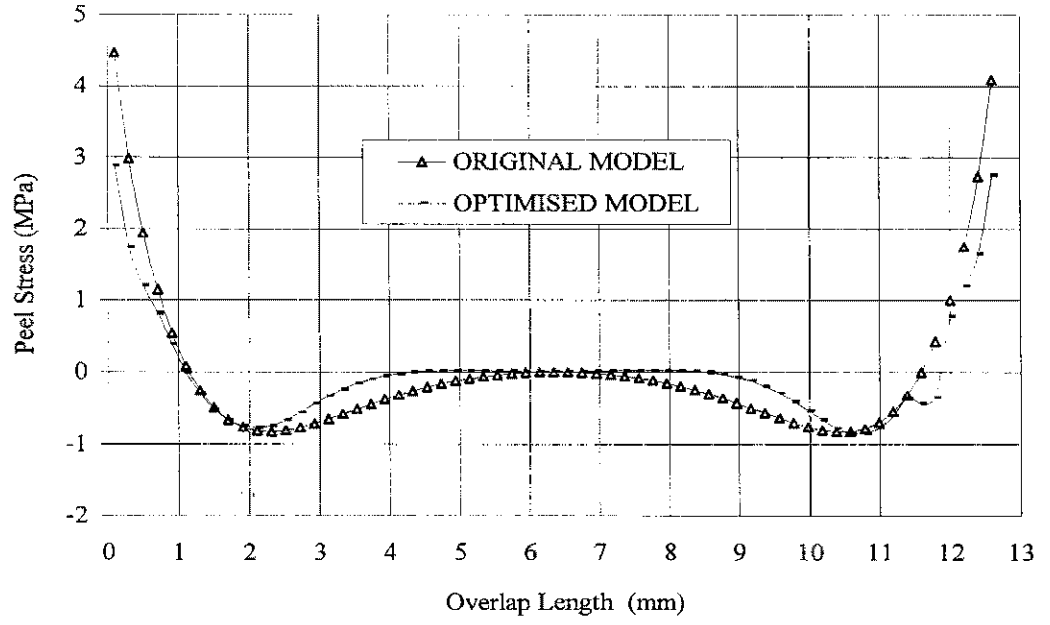

Figure 3.9: Peel stress distribution (SLJ)

In order to obtain a more defined shape of the adherend profiles and to assess the influence of size of element on the optimum adherend shape, a refined mesh model was run. The refined mesh model was created by un-evolving the optimum solution obtained from the coarse mesh model by 10 steady states and subdividing each element along the overlap region in 9 elements (3x3). This model was employed as the starting geometry for the optimisation run. The optimum adherend shape (SLJ) resulting from running the refined mesh model is shown in Figure 3.10.

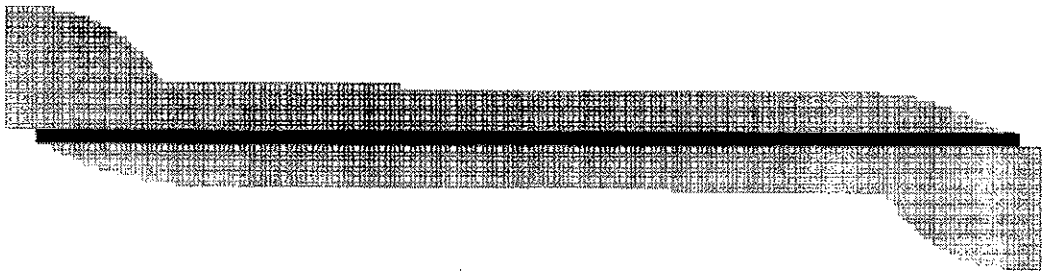

Figure 3.10: Optimum adherend profile (SLJ- refined mesh model)

Although both optimum adherend shapes obtained from the refined model and the coarse mesh model are very similar, the former illustrates more clearly the convexity of the adherend at the end of the overlap. Furthermore, the flat centre section of the upper and lower adherends is reduced by the presence of a small step (1 element in height) on the refined mesh model. The DLJ model was similar to the SLJ model, but with different boundary conditions as shown in Figure 3.11.

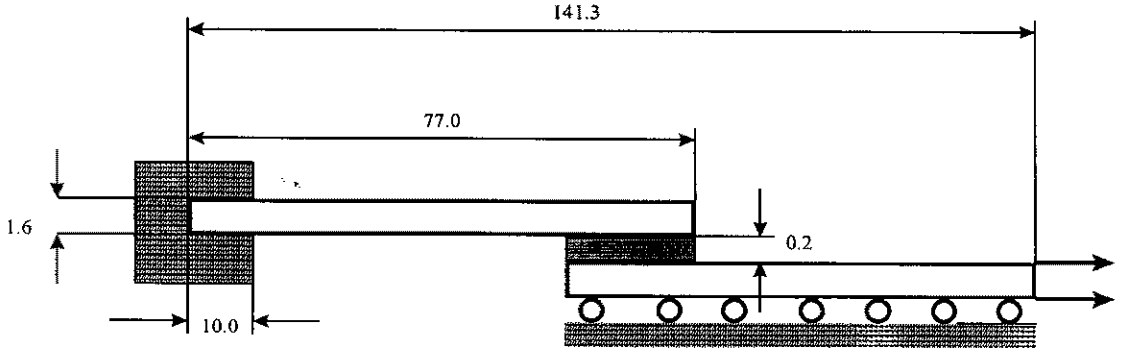

Figure 3.11: Boundary conditions for DLJ

For the DLJ a reduction in peel and shear stress of 17 % and 8 % respectively was achieved with a RR=16.4 %. In the DLJ case, only the upper adherend was allowed to evolve so as to keep boundary conditions due to symmetry. The optimum adherend shape (DLJ) is shown in Figure 3.12. The running time for the evolutionary process to converge to an optimum solution was of 3.5 hours in a 486-DX33 processor with 16 Mb RAM.

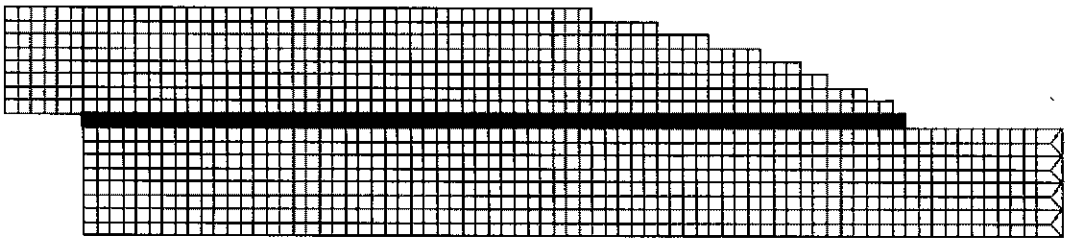

Figure 3.12: Optimum adherend profiling along overlap (Double Lap Joint)

The plotting of the shear and peel stresses of original and optimised model vs overlap length is shown in Figures 3.13 & 3.14 respectively. The sharp drop in shear stress magnitude shown in Figure 3.13 at the tip of the adhesive occurs as a result of the adherend element above the adhesive tip being removed.

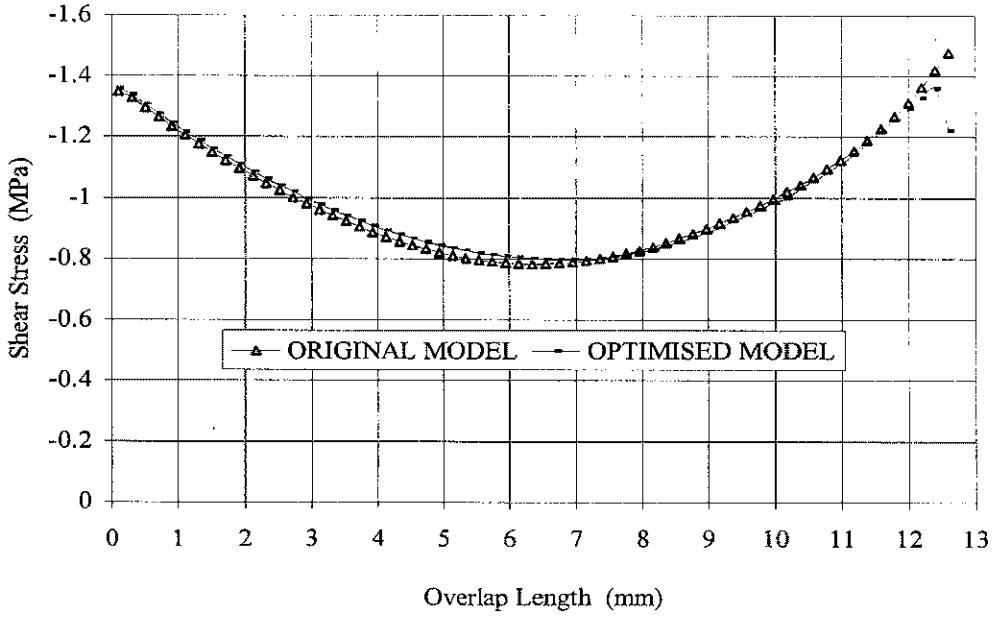

Figure 3.13: Shear stress distribution (DLJ)

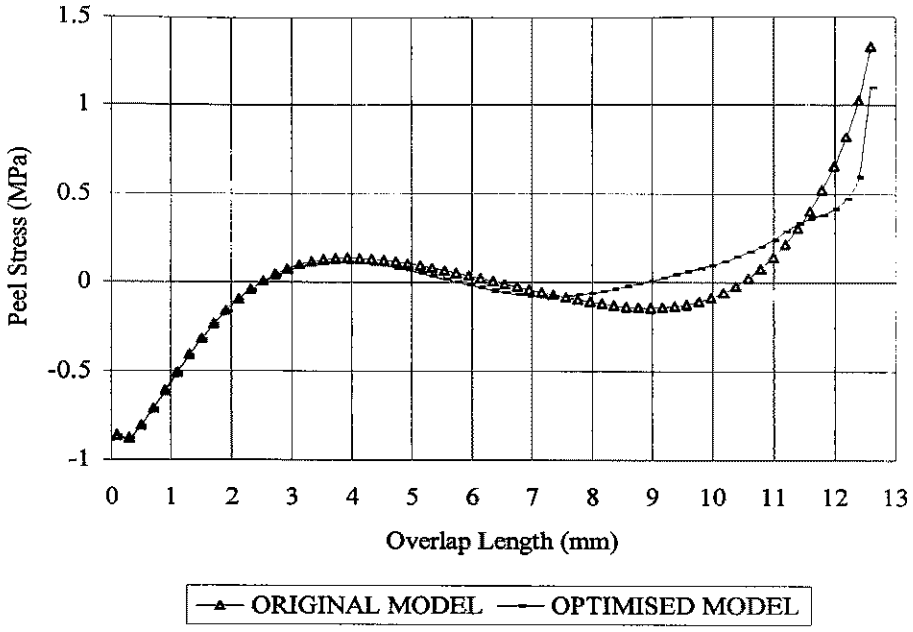

Figure 3.14: Peel stress distribution (DLJ)

Similarly to the refinement of the single lap joint model, the optimum upper adherend shape for the double lap joint analysis was un-evolved and re-analysed. The optimum adherend shape (DLJ) resulting from running the refined mesh model is shown in Figure 3.15. A larger extent of the convex curvature on the optimised upper adherend can be noted on the refined mesh model when comparing it to the coarse mesh model. While the shape of the upper adherend remains straight up to two thirds of the overlap length on the coarse model, on the refined model the flat region only extends up to half the overlap length. This results in a less steeper taper for the refined mesh model.

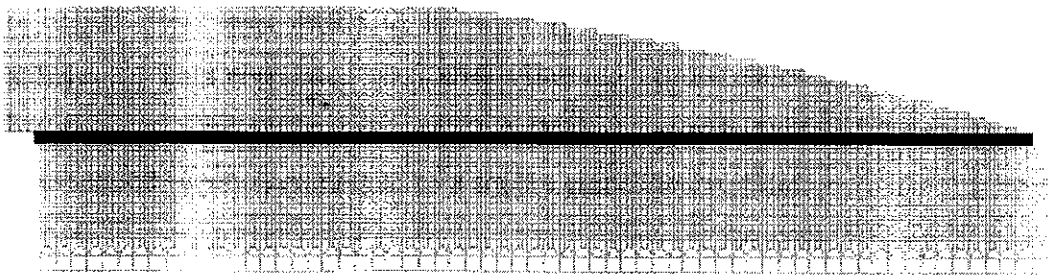

Figure 3.15: Optimum adherend profile (DLJ- refined mesh model)

3.4.2 Discussion

Most work on optimisation of bonded joints has tried to achieve a uniform shear stress distribution along the overlap [15-17]. In practice, a uniform shear stress distribution is not desirable due to creep considerations [27]. In single lap joints, the most critical stresses are the peel stresses which are induced by the eccentricity of the load path. Similarly, the double lap joint also suffers from peel stress concentrations, but in this case the peak shear stresses are also important. The reason for this is that the double lap joint does not suffer from large bending moments in the adherend which are the main cause of peel stresses at the end of the overlap. The method presented in the preceding Section and by Rispler et. al. [28], aims at reducing the maximum adhesive peak stresses at the end of the overlap. The results indicate that the methodology was successful in reducing critical stresses in both the single and double lap joint configurations. The achieved reductions in peak peel stresses in the SLJ and shear and peel stresses in the DLJ should ultimately lead to an increase in joint strength by reducing the stress concentrations causing failure initiation.

3.5 Shape Optimisation of Adhesive Fillets

3.5.1 Introduction

The effect of spew fillet size has been studied by Adams et. al. [11]. The effect of the size was studied by assuming a 45° fillet and changing its size. The magnitude of principal stresses obtained from such analysis showed a large difference when compared to results obtained from analysis which assume the adhesive to have a square edge. The highest principal stress was found to lie adjacent to the tip of the unloaded adherend (upper adherend). This correlated well with observed failure characteristics during testing. The inclusion of a triangular spew (45°) decreased the magnitude of the maximum principal stress by 40 % when compared to a square end adhesive fillet.

Crocombe et. al. [29] included the effect of additional parameters such as material and geometric properties. In their analysis, the stress distribution across the adhesive

thickness was not assumed constant. Their results for a lap joint with a spew fillet indicate that the averaged maximum adhesive stress increased with decreasing modulus ratio (increasing adhesive stiffness) up to a limiting value, after which they decreased again. Variations of overlap length, adhesive thickness and adherend thickness was also included in their analysis.

A program analysing the sensitivity of stress distribution of bonded joints to manufacturing irregularity and variability was carried out in an attempt to gain better understanding of the factors affecting joint strength [30]. The factors identified in such research are mainly related to the geometry of the spew fillet. The experimental fillet geometry depicted in Figure 3.16 was identified as being present in most of the manufactured joints.

The parameters which appear to be common along spew fillets obtained, are the long run-out of epoxy onto the surface of the CFRP (carbon fibre reinforced plastic) central adherend and the presence of a horizontal 'plateau' butting against the end tab tip (upper adherend) [30].

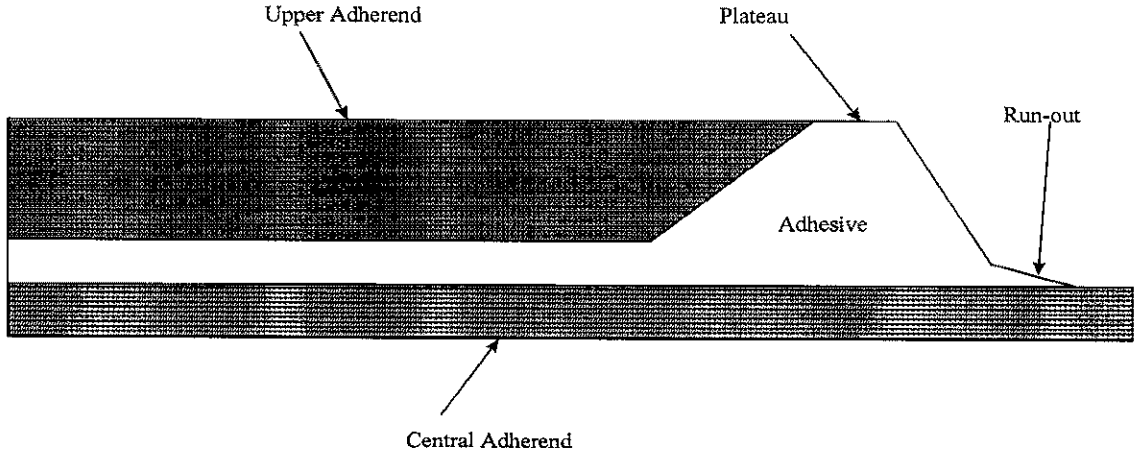

Figure 3.16: Schematic of experimental fillet geometry

The research also looked at reducing the maximum principal stresses in the adhesive fillet by varying its geometry [30]. The aim of reducing these stresses was that the failure initiation area during testing was identified as being at the adhesive near the adhesive/upper adherend tip interface. Different geometries of adhesive fillets were analysed and compared to the baseline design. These geometries were chosen based on a full finite element analysis of a manufactured joint with the experimental fillet geometry shown in Figure 3.16 and on test results. The exact dimensions of the chosen fillet were measured using a magnification microscope with x, y and z crosshairs.

The goal of the collaborative research performed at the University of Sydney was to minimise the maximum principal stresses on the adhesive fillet found in tabs of tensile test specimens with reverse taper by applying structural optimisation methods. This should ultimately increase the joint strength. The objective function was chosen from analysing the peak stresses at each material and comparing them to their allowables. Furthermore, the peak epoxy stress was identified to be the main cause of failure by crack initiation [30]. Although peel stresses in the CFRP adherend can result in failure of the joint by delamination, these stresses were only critical for square ended adhesive fillets.

3.5.2 Finite Element Analysis

Two different cases were analysed. In all joints, the central adherend was CFRP. The first case analyses the optimum fillet shape where the material of the upper adherend is CFRP. The second one consists in an adhesive joint with the upper adherend being made of titanium. Within this case, another model was studied with different adhesive properties (Young's Modulus). In all cases, the starting model corresponded to a square fillet profile.

The mesh employed for the three different models analysed was exactly the same. The geometry of the adherends and adhesive is shown in Figure 3.17. Double lap shear (DLS) boundary conditions were employed (Figure 3.18). Some distorted elements near the upper adherend tip were present due to an extremely fine taper. Orthotropic material properties for the unidirectional tape T800 were calculated from given material data. The

analysis was performed under plain strain assumptions and employed four noded elements with orthotropic properties. Furthermore, the analysis was linear static. As mentioned in Reference [30], the use of a linear static analysis should be valid due to the failure mode being crack initiation controlled. The loading applied to the model was 1 GPa in tension and 100° C cooldown on all nodes. The cooldown temperature aims at including the effect of residual thermal stresses due to cure shrinkage.

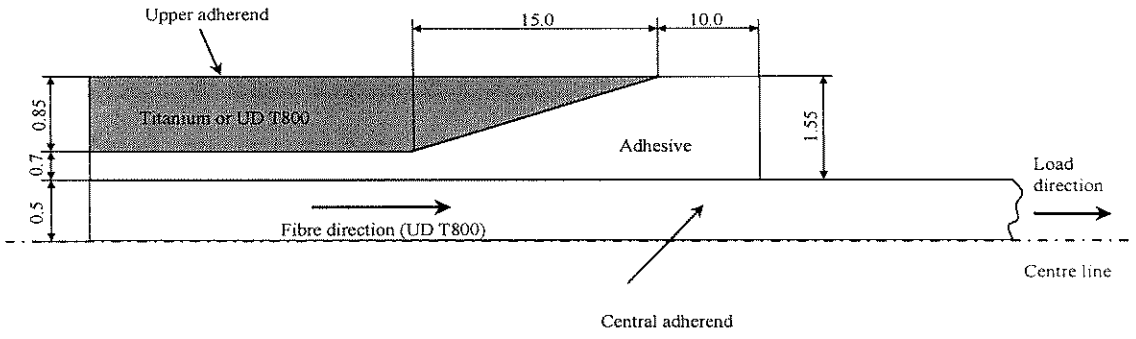

Figure 3.17: Adherend and adhesive geometry

The material properties used for the different models are listed on Table 3.1 while material allowables are given in Table 3.2. The values quoted for the different material were obtained from Reference [30]. The notation is as follows:

1= fibre direction 2= through-thickness 3= in-plane transverse

Table 3.1: Material properties

Material	E_1 (GPa)	E_2 (GPa)	E_3 (GPa)	υ_{xy}	υ_{zx}	CTE_x (με/°C)	CTE_y (με/°C)	CTE_z (με/°C)
UD T800	175	10	10	.27	.0154	-0.9	27	27
Titanium	110	110	110	.29	.29	9	9	9
Epoxy adhesive	*5	*5	*5	.38	.38	60	60	60

Note: * The Young's Modulus of the adhesive was varied in some models to assess the influence of adhesive stiffness on both maximum stresses and optimum fillet shape.

Table 3.2: Material allowables

Material	σ_{max} (VM) (MPa)	σ_{max} princ. Tension / Compression (MPa)	σmax_1 (GPa)	σmax_2 (MPa)	σmax_3 (MPa)
UD T800	n/a	n/a	2.7	50	50
Titanium	1000	n/a	n/a	n/a	n/a
Epoxy Adhesive	n/a	40 / 52	n/a	n/a	n/a

3.5.3 Optimisation Techniques

The EVOLVE code was employed to optimise the shape of the adhesive fillet. The driving criterion for all models was the mean maximum principal stress on the structure. The only material which was allowed to evolve was the adhesive. The adherends were selected as non-design properties. The evolutionary rate was selected to be 0.1 %. This was found to be necessary as with higher evolutionary rates, too many elements would be deleted from the structure between steady states.

Within the two cases analysed (different upper adherend materials), two different optimisation techniques were employed. The first one allowed the optimisation code to consider the stresses of all elements in the model to derive the driving criterion (Average Maximum Principal Stress). This technique will be referred to in this Chapter as the Classical Evolutionary Technique. The second technique consisted in employing the passive element capability of EVOLVE. The passive element approach allows for the selection of desired properties from which the stresses are calculated. Essentially, as the objective is to minimise stresses in the adhesive, the adherend properties are selected as passive so that the stresses calculated for elements within the adherends do not influence the driving criterion. This approach also simplifies the post-processing significantly. This technique will be referred to in this Chapter as the Passive Evolutionary Technique

In the Classical Evolutionary Technique, three properties were selected to monitor the maximum principal stresses during the optimisation process. These properties are shown in a schematic (Figure 3.18) of the starting model (square ended adhesive fillet shape, steady state = 0) and were selected in areas where maximum joint stresses were expected. The dark grey colour represents monitoring properties corresponding to the adhesive while the remaining monitoring property (black shaded) corresponds to the central adherend. The EVOLVE code then allows us to look at every steady state for the maximum principal stresses recorded in the adhesive and in the adherend. This reduces the post-processing of the results quite considerably and also makes the selection of the optimum fillet shape a simpler task. Although the maximum principal stresses for the initial structure (s.s =0) were found to be either on the adhesive in contact with the upper or lower adherend, the position of this stress varies in some steady states. This means that the maximum principal stress might not occur in the monitoring properties selected. In these cases, a full finite element analysis has to be re-run for the chosen steady states. The selection of all adhesive plates as monitoring properties would prove prohibitive due to the required memory to store all stress values for all steady states.

As the stresses of the adherend elements were not included in the optimisation routine, the Passive Evolutionary Technique did not require the use of monitoring properties. The results file from the optimisation process allows the determination of a global optimum by plotting a single graph of the maximum and mean values of the driving criterion for all steady states. This is only applicable when the variable to be minimised (optimised) coincides with the driving criterion.

The results obtained from applying the Classical Evolutionary Technique showed some variation between the optimum shapes arrived at by using different mesh densities. Instead, the Passive Evolutionary Technique was very consistent for both the corse mesh and fine mesh models analysed. Furthermore, it was found that the selection of global optimum was greatly simplified by employing the Passive Evolutionary Technique. The selection of a global optimum by employing the latter technique consisted simply in producing a plot of the maximum principal stress versus each steady state of the optimisation process, straight from the results file. Therefore, the work presented in the next section corresponds to analysis carried out using the Passive Evolutionary Technique.

The aspect ratio of the elements have to be kept as constant as possible so that the effect of this variable on the fillet shape is minimised. The size of the elements greatly influences the time taken to arrive to an optimum solution. Therefore a compromise has to be made between element size, solution time and accuracy of proposed optimum shape and stress magnitudes. An alternative to obtain the final shape of the optimum fillet is to run a B-spline through the nodes of elements at the edge of the adhesive fillet. Again, the accuracy of this spline will depend on the mesh density.

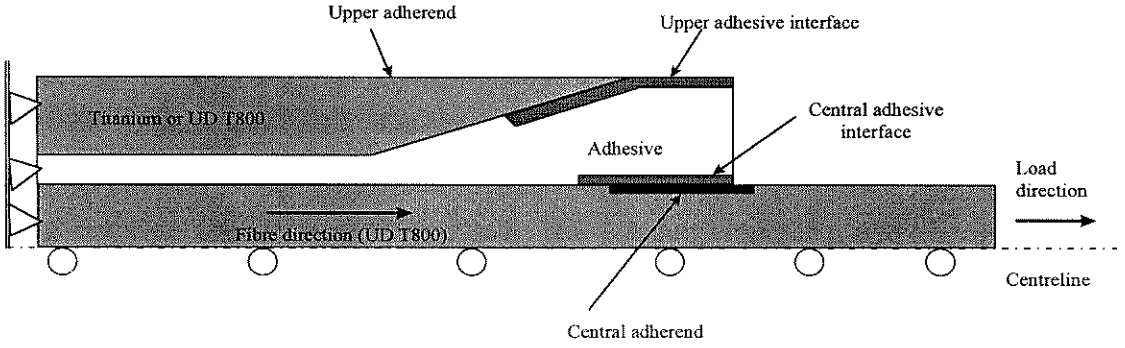

Figure 3.18: Schematic of monitoring properties for starting model (steady state=0)

A solution to this problem might be to apply the biological growth approach to the optimum plate solution so as to keep the uniform stresses along the contour. The biological growth approach [31, 32], relies on applying fictitious temperature loads based on a differential stress solution. A new finite element analysis is then run with these temperatures. The results of this FEA are incremental displacements which are to be added to coordinates of the original model. Finally, another alternative is to start with a coarser mesh and then use the optimum generated by this analysis as a starting point for a much finer mesh. This last alternative was pursued for the shape optimisation of all adhesive fillets analysed in this Chapter. The methodology consisted in firstly identifying the optimum adhesive fillet shape from a model with a coarse mesh and then using this solution as a starting point in a new optimisation run. Prior to starting the new run, the final plate solution of the coarse mesh was unevolved by three steady states to minimise the effect of the element size on the final optimum shape. The mesh was then refined locally around the fillet area by replacing every QUAD4 element by nine QUAD4 elements.

The most important feature of this structural optimisation method is that trial and error methods are effectively replaced without the need of complex mathematical formulations to be established. The shape optimisation of fillets in highly loaded bonded joints enables the designer to reduce stress concentrations which could cause premature failure at unwanted locations such as tabs during specimen testing.

3.5.4 Results derived using Passive elements

The Passive Evolutionary Technique, allows the selected properties to be chosen to drive the optimisation process. All the adherend elements were assigned passive properties so that the stresses calculated for these elements had no effect on the driving criterion employed during the optimisation process. The mean principal stress was employed as driving criterion for all models analysed. The passive element approach offers a great advantage in terms of post-processing the results. As the stresses of the adherend elements are not included in the optimisation routine, the results file from the optimisation process allows for determination of a global optimum by plotting a single graph of the maximum and mean values of the driving criterion for all steady states. This is only applicable to analysis where the driving criterion is the variable to be minimised. In the present case the objective is to minimise the maximum principal stress in the adhesive fillet. The optimisation process calculates the maximum and mean stresses; chosen as driving criterion; for all steady states (s.s) and writes these results to a file.

3.5.4.1 CFRP upper adherend, CFRP lower adherend and Young's Modulus of adhesive E=3.8 GPa

The baseline or starting model has a square ended adhesive fillet. The maximum and mean principal stresses were plotted from the result file of the optimisation program yielding the steady state with the minimum value of the maximum principal stress (global optimum).

Figure 3.19 depicts both the maximum and the mean principal stresses during the complete optimisation process pertaining to the coarse mesh model. The graph indicates, that up to s.s 80 not much stress reduction is achieved. This is due to the large overlap distance employed in the baseline model. As the overlap length decreases, the maximum principal stress decreases as well. A small plateau is reached at approximately s.s 160 where the adhesive fillet is close to its global optimum. Finally, the global optimum is reached at s.s 167. The rejection ratio at this s.s is 94.9% whereas the maximum principal stress in the adhesive is equal to 53.98 MPa. A reduction of approximately 55 % in maximum principal stress is achieved; when comparing to the baseline; by this method yielding a 45° fillet as optimum shape. The 45° fillet starts 1 element to the right of the end of the upper adherend tip/adhesive interface. The maximum principal stress in the adhesive fillet is found halfway through the fillet and also at the interface with the lower adherend. The shape of the fillet together with the stressing of the fillet for the optimum configuration is shown in Figure 3.20.

The peel stresses at the adhesive and CFRP lower adherend were also compared to the baseline values. It was found that the maximum peel stress in the adhesive was reduced from 42.69 MPa to 21.14 MPa (50 %) whereas the maximum peel stress in the carbon fibre reinforced adherend was reduced from 30.31 MPa to 18.26 MPa (40 %).

To assess the influence of the mesh size on the optimum shape of fillet and to obtain a more accurate representation of plate stresses, a finer mesh model was run. This model was created by unevolving the optimum solution of the coarse mesh model by 3 steady states and re-meshing locally the adhesive fillet by sub-dividing every QUAD4 element into 9 QUAD4 elements. The same graphs were plotted to obtain the global optimum. The graph of the maximum and mean principal stresses corresponding to the fine mesh model is shown in Figure 3.21.

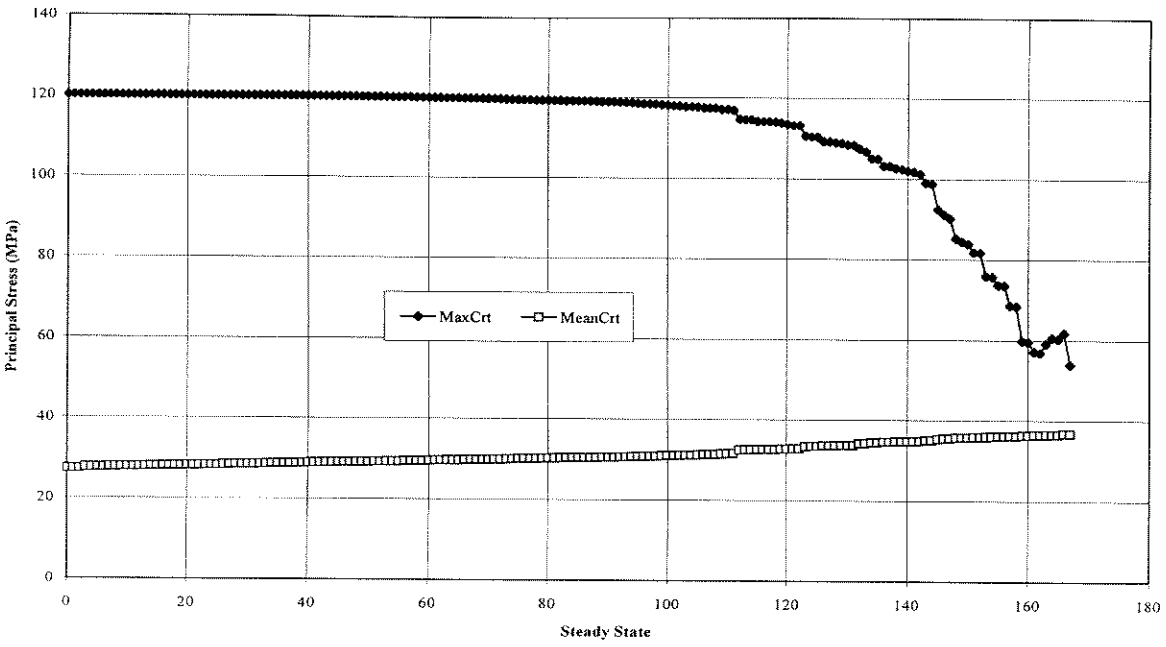

Figure 3.19: Maximum and mean principal stresses at adhesive fillet (coarse model)

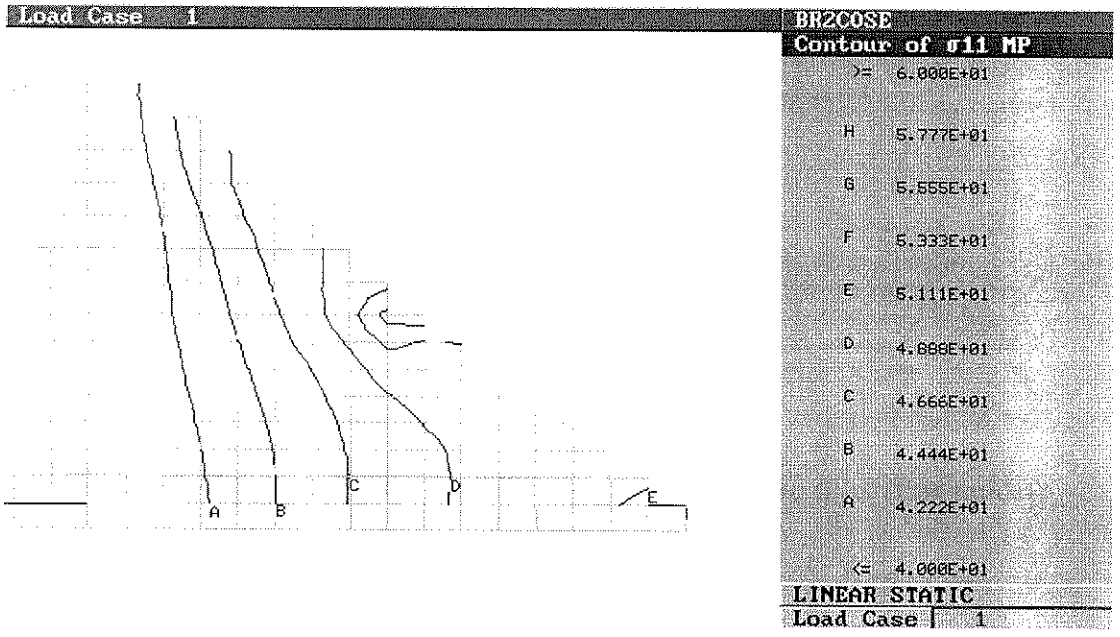

Figure 3.20: Maximum principal stress contours for optimum shape fillet at adhesive elements (coarse model)

Despite an expected increase in the magnitudes of maximum principal stress on the adhesive fillet from 53.98 MPa to 57.79 MPa, the fillet shape remained the same as for the coarse model. The maximum peel stress on the adhesive recorded a slight increase from 21.14 MPa to 22.59 MPa while the maximum peel stress in the CFRP adherend decreased slightly from 18.26 MPa to 17.41 MPa. The shape of the optimum fillet with the contours of maximum principal stress on the adhesive fillet is depicted in Figure 3.22. From this figure, it is obvious that neither the shape nor the contours of maximum principal stress were significantly affected by the finer mesh employed.

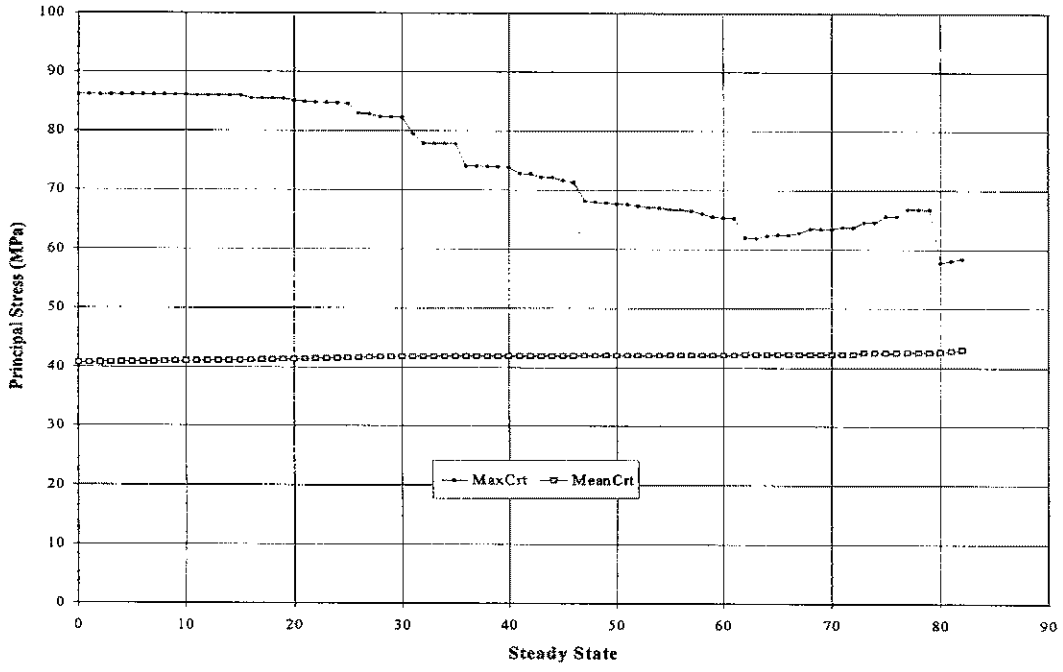

Figure 3.21: Maximum and mean principal stresses at adhesive fillet (fine model)

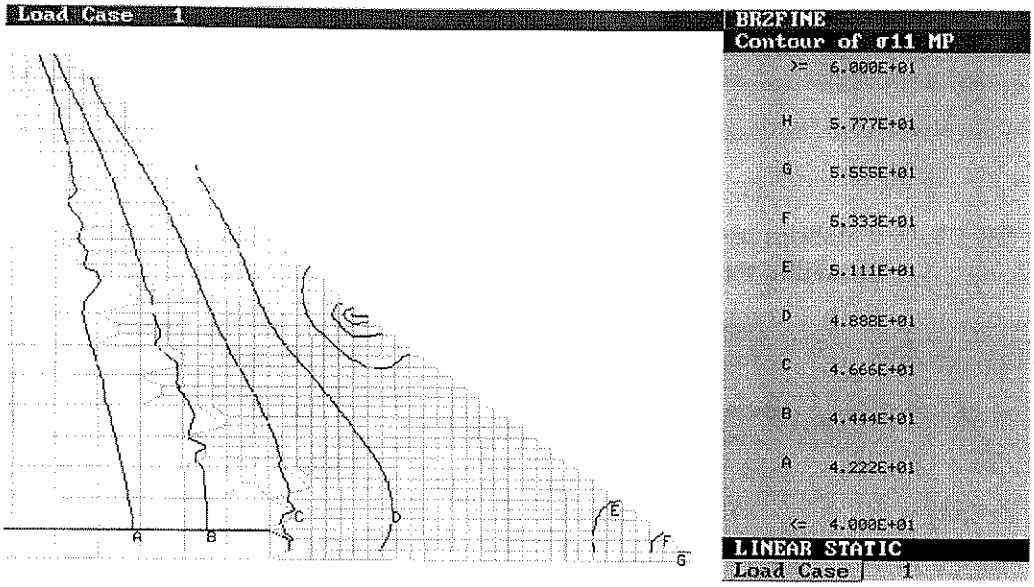

Figure 3.22: Maximum principal stress contours for optimum shape fillet at adhesive elements (fine model, upper and central adherends CFRP, $E_{adhesive}$=3.8 GPa)

3.5.4.2 Titanium upper adherend, CFRP lower adherend and Young's Modulus of adhesive E=3.8 GPa

This model was run to assess the influence of changing the upper adherend from CFRP to Titanium while maintaining the same adhesive properties (E=3.8 GPa). As the shape of fillets obtained from both the coarse mesh model and a fine mesh model were identical, the results presented for this configuration correspond to the more accurate fine mesh model. The fine mesh model was created by unevolving the optimum solution of the coarse mesh model by 3 steady states and re-meshing locally the adhesive fillet by sub-dividing every QUAD4 element into 9 QUAD4 elements. The plot of maximum and mean principal stresses shown in Figure 3.23, indicates that changing the upper adherends from CFRP to titanium results in a decrease in maximum principal stress from 57.79 MPa to 52.4 MPa (10 %). Table 3.3 shows differences between the various recorded stresses in both models. As shown on the table, reductions in maximum principal stresses and in peel stresses in both the adhesive and the central CFRP adherend were obtained by changing the material of the upper adherend from CFRP to titanium. This is believed to be due to the increase in stiffness in the through

thickness direction. This increase in stiffness helps reduce the deformation in the y-direction, thus causing a reduction in peel stresses.

Table 3.3: Comparison of maximum stresses between models with CFRP upper adherend and titanium upper adherend

Upper adherend material	Maximum Principal Stress in adhesive (MPa)	Maximum Peel Stress in adhesive (MPa)	Maximum Peel Stress in central (CFRP) adherend (MPa)
CFRP	57.79	22.59	17.41
Titanium	52.40	16.28	10.64
Difference (%)	10	38	60

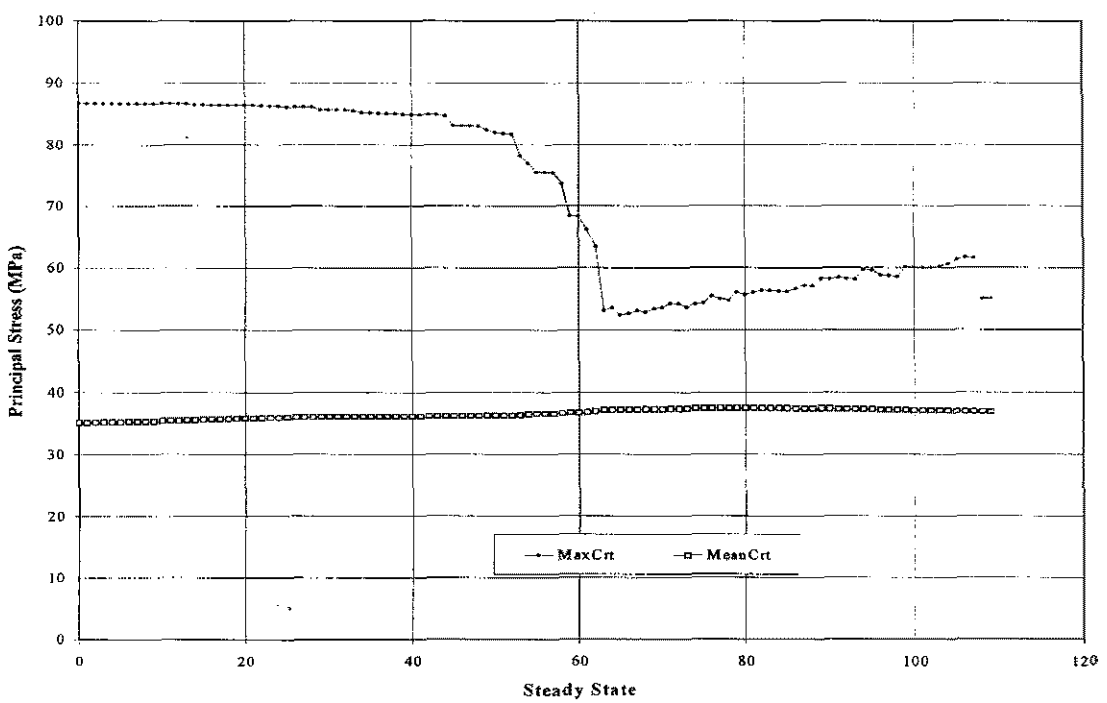

Figure 3.23: Maximum and mean principal stresses at adhesive fillet (fine model)

The contour of the maximum principal stresses and the optimum fillet shape is shown in Figure 3.24. As shown in Figure 3.24, the effect of changing the adherend material from CFRP to titanium decreased the fillet angle from 45° to 30° approximately, with a slightly lower angle close to the central adherend interface.

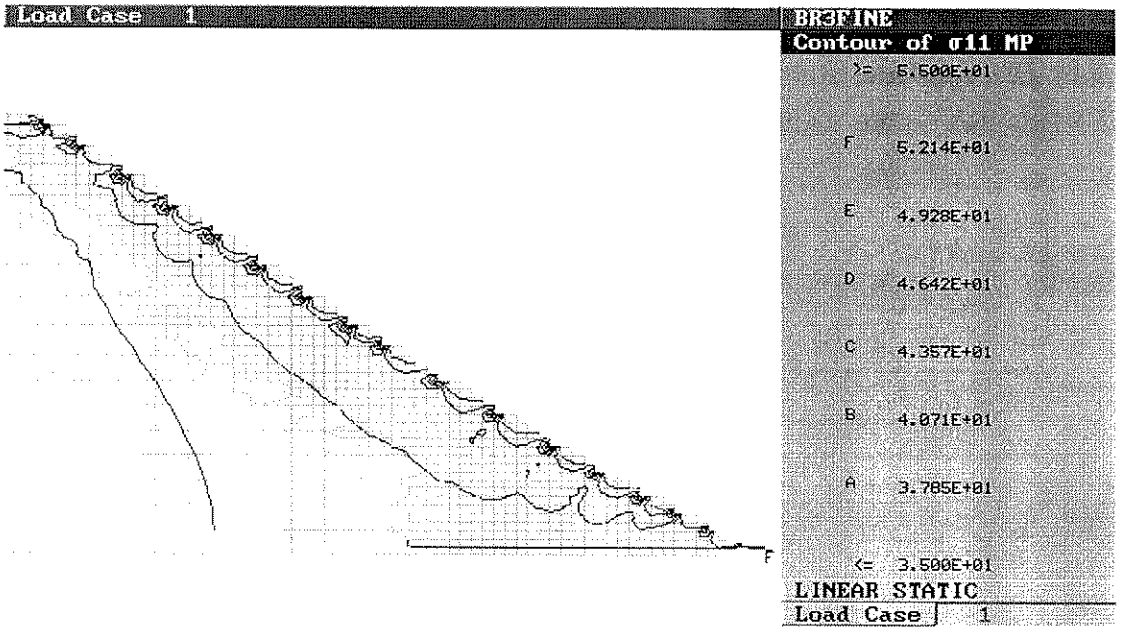

Figure 3.24: Maximum principal stress contours for optimum shape fillet at adhesive elements (fine model, upper adherend titanium, $E_{adhesive}$=3.8 GPa)

3.5.4.3 Titanium upper adherend, CFRP lower adherend and Young's Modulus of adhesive E=2.6 GPa

Once the best of the two selected materials (Titanium and CFRP) for the upper adherend was chosen, it was decided to assess the effect of reducing the adhesive stiffness by approximately 45 % to E=2.6 GPa in the model with titanium as upper adherend. The optimum adhesive fillet shapes obtained from the coarse and fine mesh models were identical. The results presented for this configuration correspond to the fine mesh model which was obtained by unevolving the optimum solution obtained from the corse mesh model by three

steady states and re-running the optimisation process. Maximum and mean principal stresses were plotted employing the result file from the optimisation run. Figure 3.25 depicts the maximum and mean principal stresses in the adhesive fillet for all steady states. The comparison between maximum principal stresses of the models with different adhesive Young's Modulus indicates that reducing the stiffness of the adhesive from a Young's Modulus of 3.8 GPa to 2.6 GPa results in a decrease in maximum principal stress from 52.4 MPa to 43.26 MPa (20 %). The contours of the maximum principal stress in the adhesive fillet at the optimum steady state and the optimum shape of the fillet are shown in Figure 3.26. The optimum fillet angle obtained for this configuration is 45°.

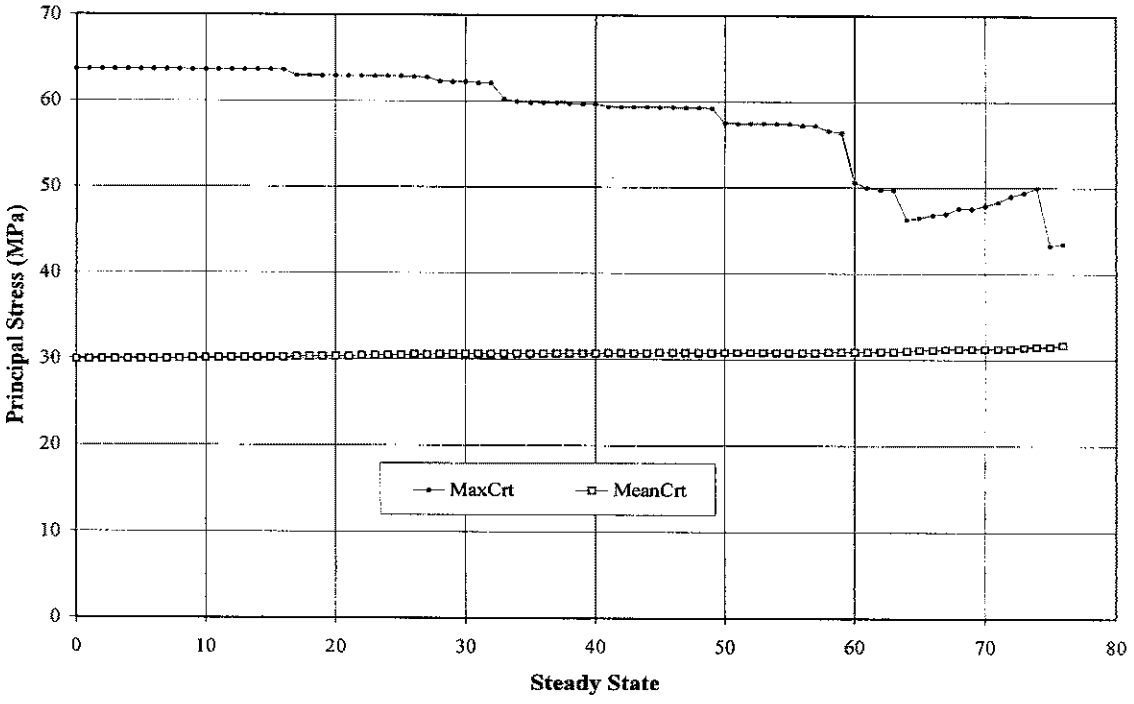

Figure 3.25: Maximum and mean principal stresses at adhesive fillet (fine model, E=2.6 GPa)

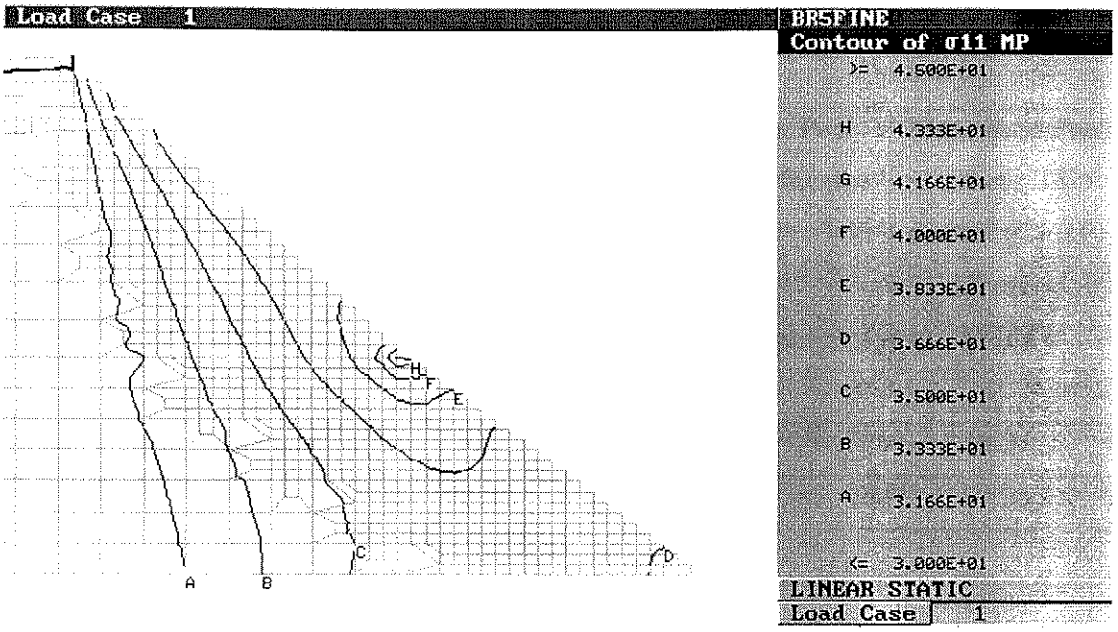

Figure 3.26: Maximum principal stress contours for optimum shape fillet at adhesive elements (fine model, upper adherend titanium, $E_{adhesive}$=2.6 GPa)

3.5.4.4 Titanium upper adherend, CFRP lower adherend and Young's Modulus of adhesive E=5.0 GPa

A third model was analysed with a stiffer adhesive. The analysis of this model allows for the construction of a trend-line of how the adhesive stresses and shape vary according to changes in adhesive stiffness. Results from the fine mesh model yielded the plot of maximum and mean principal stresses shown in Figure 3.27, and the optimum shape and contour plot depicted in Figure 3.28. Table 3.4 shows a comparison of maximum stresses for different adhesive properties, different upper adherend materials and CFRP as central adherend material. Furthermore, baseline models with peak stresses for both joint configurations are also shown in this Table. As expected, the stiffer the adhesive the larger the maximum principal stress in the adhesive. This can be simply deduced from Hooke's Law as the adhesive is assumed to be linear-elastic. Peel stresses in either the adhesive or the central CFRP adherend did not vary considerably between models.

Table 3.4: Summary of peak stresses in all models

Upper adherend material	Young's Modulus Adhesive (GPa)	Maximum Principal Stress in adhesive (MPa)	Maximum Peel Stress in adhesive (MPa)	Maximum Peel Stress in central (CFRP) adherend (MPa)
BASELINE MODELS				
CFRP	3.8	120	42.69	30.31
Titanium	3.8	98.90	42.60	30.25
OPTIMISED MODELS				
CFRP	3.8	57.79	22.59	17.41
Titanium	2.6	43.26	16.97	13.05
Titanium	3.8	52.40	16.28	10.64
Titanium	5.0	61.78	14.68	10.14

By comparing the optimum fillet shapes of the three models with titanium upper adherend and different adhesive stiffness's, we observe that as the adhesive stiffness increases, the optimum fillet angle decreases and its shape becomes more curved (changes in slope within fillet). The biggest change in optimum fillet angle occurred between the models with adhesive stiffness $E_{adhesive}$=2.6 GPa and $E_{adhesive}$=3.8 GPa with an optimum angle of 45° and 30° respectively. The difference in maximum principal stresses between the baseline models (square ended adhesive) highlight the Titanium / CFRP joint to be the best configuration to be optimised.

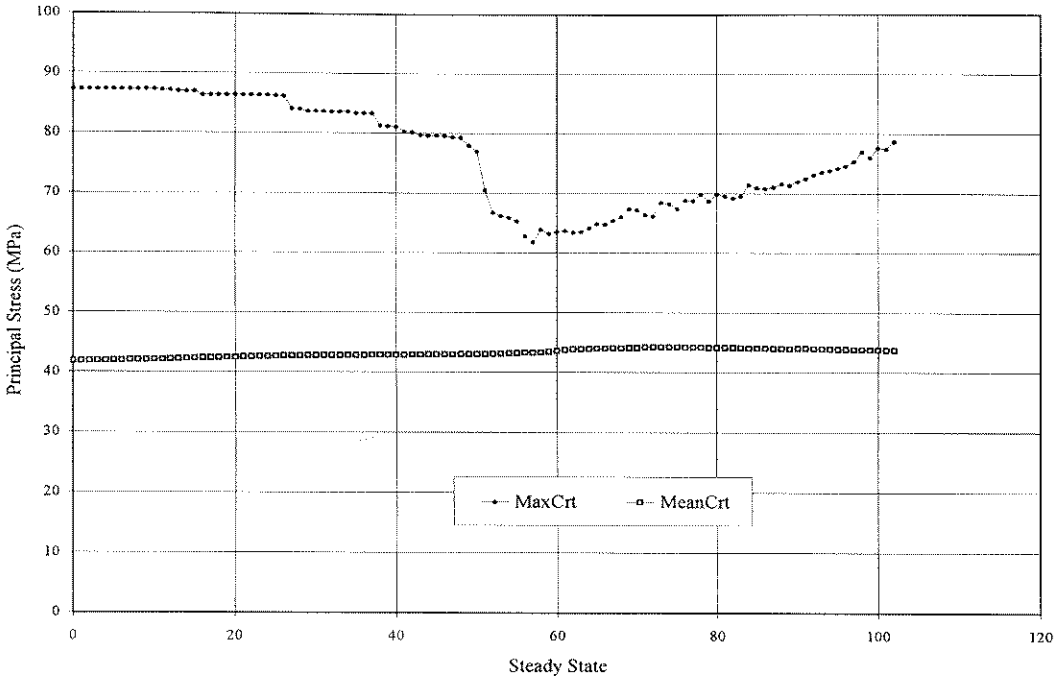

Figure 3.27: Maximum and mean principal stresses at adhesive fillet (fine model, E=5.0 GPa)

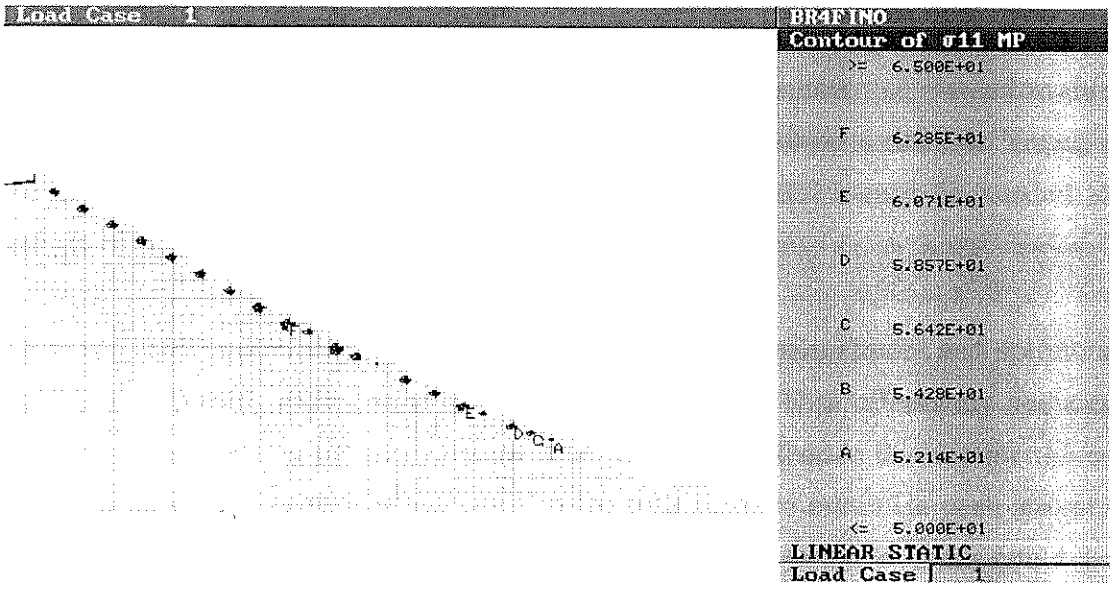

Figure 3.28: Maximum principal stress contours for optimum shape fillet at adhesive elements (fine model, upper adherend titanium, $E_{adhesive}$=5.0 GPa)

3.5.5 Discussion

The EVOLVE code was found to be effective in reducing the maximum principal stress in the adhesive for all models studied. The reduction in Maximum Principal Stress achieved with respect to the CFRP baseline model (CFRP upper and middle adherends with $E_{adhesive}$=3.8 GPa) ranged between 48 and 64 %. The peak peel stresses in the central CFRP adherend and in the adhesive were reduced by up to 66 %. A summary of all baseline and optimum solutions with their respective peak stresses is shown in Table 3.4. The table highlights the achievements in terms of stress reductions obtained by applying the Passive Evolutionary Technique. All double lap joint models had a CFRP middle adherend

The minimum principal stress in the adhesive was achieved by optimising the configuration with a Titanium upper adherend and an adhesive with a Young's Modulus of 2.6 GPa. The minimum peel stresses in the adhesive and in the central CFRP adherend were obtained with the configuration having Titanium as an upper adherend and an adhesive with a Young's Modulus of 5.0 GPa.

The maximum tension allowable of the epoxy adhesive is 40 MPa (Table 3.2). We can conclude by comparing the maximum principal stress values obtained from the optimised models, that the only optimised structure that comes close to the maximum tension allowable is the configuration with Titanium as upper adherend and an adhesive with a Young's Modulus of 2.6 GPa. Thus a further reduction of approximately 8% would be needed to ensure a margin of safety equal to one.

In order to achieve accurate solutions both in terms of stress magnitudes and optimum shape of fillets, a stepped optimisation process was proposed. This effectively reduces computation time in reaching an optimum design. The method described in this Chapter gives an excellent preliminary design tool which can be used efficiently to minimise peak stresses in bonded joints. The jagged pattern produced during the optimisation process could be smoothed out using various techniques such as the biological growth approach or spline fitting.

3.6 References

[1] Anderson, G. P., Bennett, S. J., DeVries K. L., "*Analysis and Testing of Adhesive Bonds*", pp. 11-13, 1977.

[2] Alner, D. J., "*Proceedings of the conference held at the City University 1966*", edited by Alner, D. J., pp. 108-110.

[3] Adams, R. D., edited by Mathews F.L., "*Joining Fibre-Reinforced Plastics*", Elsevier Applied Science, 1987, Chapter 5, pp. 185-226.

[4] Savla, M., "*Handbook of Adhesives Skeist 2nd edition*", pp. 434-435, 1977.

[5] Hart-Smith, L. J., "Joints", Engineered Materials Handbook on Composites, *ASM International*, Vol. 11, pp. 479-494.

[6] Volkersen, O., "Die Nietkraftverteilung in Zugbeanspruchten Nietverbindungen mit Konstanten Lashenguerschnitten", *Luftfahrtforschung*, Vol. 15, pp. 41-47, 1938.

[7] Goland, M., Reissner, E., "The Stresses in Cemented Joints", *Journal of Applied Mechanics*, Vol. 7, pp. A17, 1944.

[8] Ellis, C., "*Review of current joint analysis, design and test procedures*", CRC-AS TM 93014, pp. 1-12, 1993.

[9] Kutscha, D., Hofer, K. E. Jr., "*Feasibility of Joining Advanced Composite Flight Vehicles*", AFML-TR-68-391, January, 1969.

[10] Wolley, F., Carver, D., "Stress concentration factors for bonded lap joints", *Journal of Aircraft*, Vol. 8, No. 10, pp. 817-820, October, 1971.

[11] Adams, R., Peppiatt, N., "Stress analysis of adhesive-bonded lap joints", *Journal of Strain Analysis*, Vol. 9, No. 3, pp. 185-196, 1974.

[12] Hart-Smith, L. J., "*Analysis and design of advanced composite bonded joints*", Douglas Aircraft Company, NASA CR-2218, January, 1973.

[13] Engineering Sciences Data Unit (E.S.D.U.), "Guide to the use of data items in the design of bonded joints", Item Number 81022, July, 1981.

[14] Groth, H. L., Nordlund, P., "Shape optimization of bonded joints", *International Journal of Adhesion and Adhesives,* Vol. 11, NO. 4, October 1991.

[15] Ojalvo, I. U., "Optimization of Bonded Joints", *AIAA Journal*, Vol. 23, NO 10, pp. 1578-1582, 1985.

[16] Lerchenthal, C. H., "*Design of Bonded Lap Joints for Optimum Stress Transfer, Part 1. The Symmetrical (or double) Lap Joint*", Department of Mechanics, Technion-Israel Institute of Technology, Haifa, 1964.

[17] Cherry, B. W., Harrison, N. L., " The Optimum Profile for a Lap Joint", *Journal of Adhesion*, Vol. 2, pp 125-129, April 1970.

[18] Moore, G. J., "*MSC/NASTRAN Design Sensitivity and Optimization – User's Guide*", The MacNeal-Schwendler Corporation, 1994.

[19] Xie, Y. M., Steven, G. P., "A simple evolutionary procedure for structural optimisation", *Computational Structures,* Vol. 49, NO5, pp. 885-896, 1994.

[20] Xie, Y. M., Steven, G. P., "Optimal design of multiple load case structures using an evolutionary procedure", *Engineering Computations*, Vol. 11,1994.

[21] Querin, O. M., Steven G. P., Xie Y. M., "*EVOLVE User Guide*", Department of Aeronautical Engineering, University of Sydney, NSW, 2006, Australia, 1996.

[22] Xie, Y. M., Steven, G. P., "*A simple evolutionary procedure for structural optimisation*", Research Report, FEARC-9203, University of Sydney, 1992a.

[23] Querin, O. M., "*Evolutionary Structural Optimisation: Stress Based Formulation and Implementation*", PhD Thesis, Department of Aeronautical Engineering, University of Sydney, Australia, April, 1997.

[24] Suzuki, Kikuchi, "A homogenization method for shape and topology optimisation", *Comp. Methods Applied Mech. Eng.*,pp 291-318, 1993.

[25] Hemp, W. S., "*Michel's structural continua*", Optimum structures, Oxford, Clarendon Press, Chapter 4.

[26] Rasmussen, J., Lund, E., Birker, "*Collection of examples: CAOS optimisation system*", 3rd edition, Special Report No. 13, Institute of Mechanical Engineering, Aalbork University, Denmark, 1992.

[27] Hart Smith, L. J., edited by Mathews F. L., "*Joining Fibre-Reinforced Plastics* ", Elsevier Applied Science, Chapter 7, pp 282-299, 1987.

[28] Rispler, A. R., Steven, G. P., "Optimisation of Highly Loaded Joints", *Proceedings of the 20th Congress of the International Council of the Aeronautical Sciences*, Sorrento, Italy, Volume 1, pp. 160-166, September 8-13, 1996.

[29] Crocombe, A. D., Adams, R. D., "Influence of the Spew Fillet and other Parameters on the Stress Distribution in the Single Lap Joint", *Journal of Adhesion*, Vol. 13, pp. 141-155, 1981.

[30] Towse, A., Davies, R. G. H., Clarke, A. B., Wisnom, M. R., Adams, R. D., Potter, K. D., "The design and analysis of high load intensity adhesively bonded double lap joints", *Proc. 4th Int. Conf. On Deformation and Fracture of Composites*, Manchester, pp. 479-488, March, 1997.

[31] Mattheck, C., Moldenhauer, H., "An Intelligent Cad-Method based on Biological Growth", *Fatigue Fract. Engng Mater. Struct.*, Vol. 13, No. 1, pp. 41-51, 1990.

[32] Mattheck, C., Burkhardt, S., " A new method of structural shape optimization based on biological growth", *Int J. Fatigue*, Vol. 12, No 3, pp. 185-190, 1990.

[33] Querin, O. M., Steven, G. P., " Evolutionary structural optimisation (ESO) using a bidirectional algorithm", *Engineering Computations*, Vol. 15, No 8, pp. 1031-1048, 1998.

CHAPTER 4

STRUCTURAL OPTIMISATION OF PIN LOADED JOINTS

4.1 Introduction

The use of mechanically fastened composite joints in the manufacturing of aerospace structures has increased considerably in the last decade. This is despite the poor structural efficiency of composite bolted joints impeding their use in highly loaded primary structures. One main reason for their ongoing use is where component disassembly is required. Further advantages of using mechanical fastening are: no surface preparation is required, joint strength is unaffected by thermal cycling and high humidity and finally inspection of bolted joints is relatively simple. The disadvantages besides the low structural efficiency due to stress concentrations at fastener holes are: increased joint weight, low joint stiffness and a danger of galvanic corrosion if dissimilar materials are being joined.

The failure modes experienced by composite joints are complex and generally very different when compared with metallic joints. The main reasons for obtaining complex failure modes are the anisotropic properties and the lack of reinforcement in the through-the-thickness direction. A schematic of the different failure modes most frequently found in composite bolted joints is shown in Figure 4.1.

From the failure modes depicted in Figure 4.1, only the bearing and tension modes are desirable [2]. The remaining failure modes are considered to be premature failure at lower loads. Examples of these premature failures are large bolt bending causing pull-through failure, shear-out failures due to too short end distances or laminates with too orthotropic patterns and blocking of plies (too many plies of same orientation stacked together).

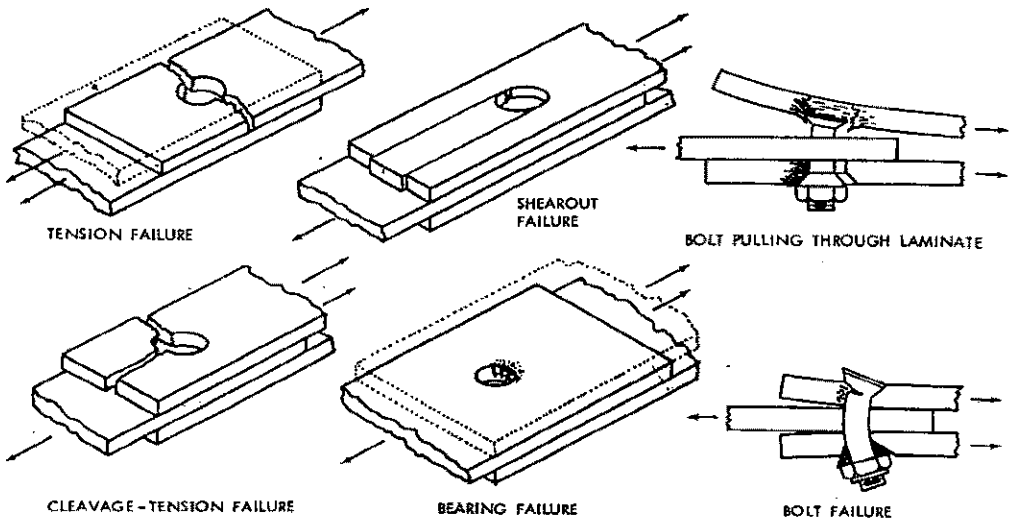

Figure 4.1: Different failure modes experienced by composite bolted joints

[1]

The parameter which influences most the distinction between bearing and tension failure modes is the width to diameter ratio (w/d). Other less influential parameters are the stacking ply sequence and the fiber pattern. Hart-Smith [2] derived empirically, curves which show the effect of changing w/d ratio on the strength and efficiency of composite joints. These curves shown in Figure 4.2, indicate that for large w/d ratios a bearing failure is obtained and that there is a point in which the failure mode changes to net tension as the width decreases or the diameter increases. This point represents the peak strength of the joint and is said to occur at a geometry associated with net tension failure or at an abrupt change in mode between bearing and tension failure. The unattainable bearing strength indicated in Figure 4.2 is mainly due to the stress concentration present at the hole boundary. This indicates that any reduction of the stress concentration factor at the boundary of the hole should increase joint strength and therefore joint efficiency.

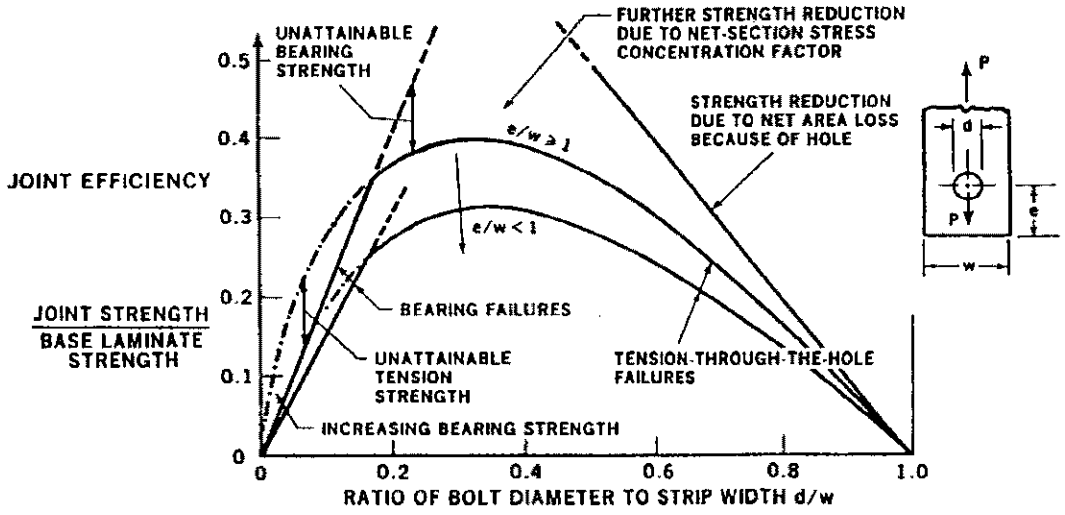

Figure 4.2: Bolted joint efficiencies for composite joints for different geometries [2]

Load bearing capacity is usually increased by thickening the base material in the joint region [3]. Experimental work by Collings [4] concluded that increasing the bolt torque increases the bearing strength. However, normal design should be based on finger tight bolts and no credit should be taken for the additional static strength developed due to the torque on the fastener [2].

Examples of methods employed in industry to reduce stress concentrations in composite joints are:

a) Incorporation of extra layers into the laminate in the holed region.
b) Local reinforcement with a stiffer fibre such as boron.
c) Local softening by using local reinforcement with a low modulus fibre (glass or aramid).
d) Adding $\pm 45^0$ fibres.
e) Incorporating layers of titanium alloy sheet.

Other additional; more recent; methods that can be found in the literature are:

a) Laminate tailoring [5].

b) Tailored fiber placement [6].

c) Use of elliptic shaped bolts [7].

d) Bonding a metallic insert in the loaded hole [8-11].

The laminate tailoring method [5] consists essentially in producing a part with different lay-ups for different regions. By doing so, the laminate can have quasi-isotropic properties around the loaded holes and more orthotropic properties in other regions. This allows the designer to have a more optimised structure by uncoupling the local bearing capacity from the influence of the laminate axial strain level. A full-scale component was tested by Eisenmann et.al. [5] showing that a 24 % increase in weight efficiency and a 62 % increase in axial strain when compared to a non tailored component could be achieved. The drawback of this method is the high manufacturing cost. This drawback is a common feature of most stress reduction methods which rely on adding extra plies of different materials around the loaded hole. A variation of this method is the TFP (Tailored Fibre Placement) [6], which is a highly automated fibre preforming process based on embroidery technology. Due to its automation this method could deliver higher strength with reduced cost increase. A study by Crothers et.al. [6] achieved a 45 % increase in bearing strength by placing fibres along load path vectors.

Of the remaining alternative methods, the elliptic shaped bolt option involves the manufacturing of purpouse built bolts and also the cutting of elliptic shaped cut-outs in the composite plates. In their paper, Wang et.al. [7] showed that by changing the circular bolt shape to an elliptical one, the bearing stresses were reduced by up to 26 % for the analysed configuration. This option could be of large benefits for repair situations when the distance from the hole to a free edge is not sufficient to enlarge the hole to remove the damage.

The remaining alternative involves the enlargement of the existing circular hole and bonding of a metal insert to increase joint strength [8-11]. This effectively reduces the degree of anisotropy round the hole. This alternative is discussed in more detail in the next section.

Bearing strength is also dependent on the clearance fit. The larger the clearance, the smaller the strength [12, 13]. This is due to the contact surface between the fastener and the base material becoming smaller as clearance distance increases thus increasing the bearing stress concentration factor. Also, a close fit between the diameter of the bolt and the inside diameter of the washer helps improving the bearing strength [3]. Joint efficiency for bearing critical laminates can also be increased by avoiding the blocking of plies and ensuring that fibre direction changes from one ply to the next. Finally, the placing of 90^{0} plies at the laminate surface should be avoided as compressive stresses at the washer in the transverse direction may cause premature failure [14].

4.2 Semi-Empirical failure models survey

Several failure models to predict joint strength have been proposed by different researchers. An extensive literature survey shows that methods vary from semi-empirical to theoretical ones. An example of a semi-empirical method used in industry is the one proposed by Hart-Smith [15, 16]. This method relies on calculated stress concentration factors for elastic isotropic materials as reference values. Corrections for orthotropy and non-linear behavior are combined into a single factor as long as both failure mode and failure location remain unchanged.

Another semi-empirical approach is one based on some characteristic length from the hole edge at which the linear elastic assumptions are valid. This approach was originally proposed by Whitney et. al. [17] with the Point Stress and the Average Stress Failure Criteria. The Point Stress approach assumes that failure occurs when the stress over some distance away from the geometric discontinuity is equal or greater than the strength of the unnotched material. The characteristic distance d_o is assumed to be a material property which does not depend on either laminate geometry or stress distribution. The Average Stress Failure Criteria assumes that failure occurs when the average stress over a certain distance a_o equals the unnotched laminate strength. This distance is also independent of both laminate and stress distribution. Niusmer et. al. [18] expanded the average stress method to compressive loading by replacing the characteristic dimension.

Fu-Kuo Chang, et. al [19-21], employed the Yamada-Sun failure criterion in conjunction with their failure characteristic curves. They codify this approach in a computer program called "BOLT". The finite element approach assumes a cosine load distribution at the hole boundary. The Yamada-Sun Criterion [22], attempts to predict failure at the laminate level rather than at the lamina level. This criterion together with the application of the "BOLT" program to predict failure of bolted joint is discussed further in the next section.

4.2.1 The use of the "BOLT" code for failure prediction

The program "BOLT" [23] is based on the assumptions of classical two-dimensional laminate plate theory and a linear stress/strain relationship. The stress analysis is performed using the finite element method and isoparametric 4-node elements. A mesh generator is employed in the program to generate the required mesh. For problems involving a single hole as studied in this Chapter, 306 elements were employed. The use of a two-dimensional code is justified by examining the effect of stacking sequence on the failure strength and mode. Existing experimental evidence by Pagano et. al. [24] and Quinn et. al. [25] shows that stacking sequence is important only when laminates are narrow or when the laminate is unrestrained laterally. Furthermore, the failure strength and failure mode appear to be unaffected by the stacking sequence when there is a slight lateral constraint on the laminate (finger tight bolt condition) [23].

The program caters for different type of joints, allows for the application of by-pass loads, and requires the input of the ply orientations, material properties and geometric configurations (w/d, e/d and l/d). The program assumes the pin and support to be rigid and a uniform tensile load applied symmetrically with respect to the centreline of the plate. "BOLT" allow only the use of symmetric laminates. The load distribution at the fastener hole is approximated by a cosine load distribution.

Once the required data is input, the stresses are calculated using the finite element method. The failure load and failure mode is calculated using the Chang-Scott-Springer failure hypothesis in conjunction with the Yamada-Sun failure Criterion. For a given

geometry and load, once the stresses are calculated, the program predicts the maximum failure load and the mode of failure. The joint is assumed to have failed when the combined stresses have exceeded a prescribed limit in any of the plies along the characteristic curve. The Yamada-Sun Criterion is based upon the assumption that just prior to failure of the laminate every ply has failed. Failure is said to occur when the following condition in Equation (4.1) is met:

$$\left(\frac{\sigma_1}{X_{1T}}\right)+\left(\frac{\tau_{12}}{X_{12}}\right)=e^2 \qquad \begin{array}{ll} \Rightarrow & e<1 \text{ no failure} \\ \Rightarrow & e>1 \text{ failure} \end{array} \tag{4.1}$$

σ_1 and τ_{12} are the longitudinal and shear stresses in a ply, respectively (where 1 is parallel to the fiber direction). X_{1T} represents the longitudinal tensile strength of the ply and X_{12} is the shear strength of a cross ply laminate with the same lay-up as the one being analysed.

The hypothesis proposed by Fu-Kuo Chang et. al. states that failure occurs when, in any one of the plies, the combined stresses satisfy an appropriately chosen failure criteria at any point on a characteristic curve which is specified by Equation (4.2). A graphical representation of the characteristic curve is shown in Figure 4.3:

$$r_c(\theta)= D/2 + R_t + (R_c - R_t)\cos\theta \tag{4.2}$$

The angle θ, measured clockwise from the x_1-x_2 axis, may range in value from $-\pi/2$ to $\pi/2$. The characteristic lengths in tension and compression R_t and R_c are determined from experimental data from the tensile and compressive strengths of notched laminates. As R_t and R_c depend on the material and lay-up configuration, the coordinates of the characteristic curve also depend on the same parameters. Joint geometry; other than through the hole diameter; and stress distribution do not affect the characteristic curve. In

many cases, Chang et. al. [23] found that the failure strength and failure mode of laminates were insensitive to precise values of R_t and R_c. This was found to be particularly true for quasi-isotropic laminates. For these laminates, approximate values of R_t and R_c should suffice for calculations. S_c represents the rail shear strength of a symmetric cross ply laminate having the same number of plies as the laminate under consideration. The predicted strength is also insensitive to values of S_c, except for laminates with more than 70 % unidirectional fibres in the loading direction. The shear-out mode is generally sensitive to the value of S_c.

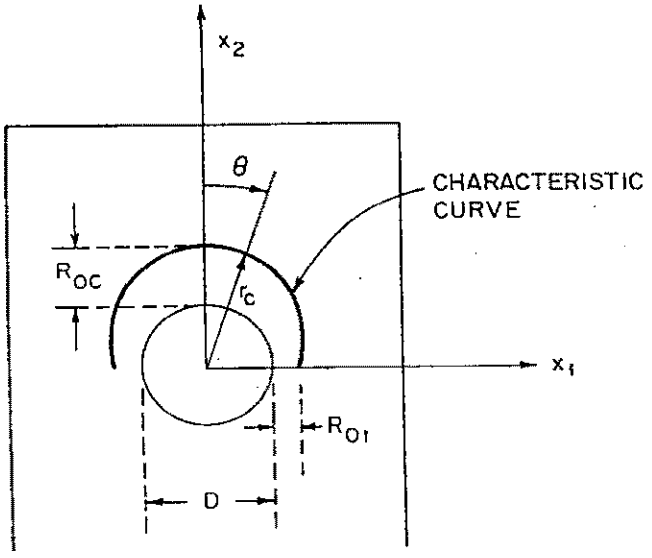

Figure 4.3: Description of characteristic curve

4.3 Increasing bearing strength by using isotropic inserts

Fibre-reinforced composite materials can be considerably weakened by the introduction of holes. This can be attributed partly to the large stress concentrations that occur in the region of geometric discontinuities and partly to a lack of plasticity. The plastic behaviour found in isotropic materials, helps in reducing the effect of stress concentrations by redistributing peak stresses. Unfortunately, this forgiving phenomenon

is not present in composite materials, at least at a macroscopic level. At a microlevel, microcracks and delaminations around bolt holes cause internal load redistribution, thus producing some softening of the material [1].

A theoretical and experimental investigation by Nilsson [8] on increasing the bearing strength of composite bolted joints, showed that by bonding a 2 mm circular metallic insert in the hole, the compressive stresses at the hole boundary were reduced by 50% and the failure load was increased by up to 55%. Nilsson showed with the aid of the finite element method that compressive stresses at the hole boundary could be reduced by bonding metallic inserts. Tensile stresses in the ligament region were also reduced by using an isotropic insert. In his work, the contact forces from the bolt were approximated as a cosine load distribution. The geometric ratios employed for the specimens were w/d=4 and e/d =2.5 and the material was Gr/Ep. The use of isotropic inserts to obtain stress concentration relief in GFRP was also studied by Herrera-Franco et. al. [9] and proved to be successful in reducing the bearing stress by 75% in the bearing region. The work by Herrera-Franco consisted in a combined experimental-theoretical program which studied the stress and strain distributions in the vicinity of single-pin lap joints in a glass-epoxy laminate. High-sensitivity Moire techniques were employed to measure the surface strains in three directions within the insert ring and in the adjacent composite plate. A comparison was made between specimens with no inserts, aluminum insert and an epoxy insert. Although stress reductions were observed with both types of insert, the aluminum insert yielded the largest stress reduction. Finally, Mirabella et. al. [11] achieved an increase in bearing strength of up to 100% by bonding a top-hat aluminum insert when compared to the no insert case.

It is clear from the work performed from these researchers that an increase in bearing strength can be achieved by placing an isotropic insert in a composite loaded hole. However, their work does not indicate what the size or shape of an optimum insert should be. As the bearing failure is related to the compressive stresses at the hole boundary, an insert could be shaped in a way so that only the compressive stresses around the hole are minimised. This would ultimately provide for an optimum utilisation of isotropic material and also the maximum possible compressive stress reduction at the hole boundary for a given insert weight. The proposed method outlined in this Chapter, aims at achieving a

stress and strain redistribution around a pin loaded hole by providing a localised plastic zone in its vicinity. To achieve a more efficient structure, it is proposed to optimise the shape of the insert by modifying the existing evolutionary structural optimisation method (E.S.O) developed by Steven et. al. [26, 27].

4.4 Modified Evolutionary Structural Optimisation Method

The proposed method aims at reducing the compressive stresses at the hole interface, at creating a redistribution of stresses and strains in the vicinity of the hole and at maximising the strength of the joint.

A finite element analysis method is proposed to optimise the shape of metallic inserts where failure mode is bearing strength. In the available evolutionary structural optimisation method described in Chapter 3, the low stressed part of material is progressively removed from a structure until an optimum is reached. A different process is suggested for optimising metallic inserts in mechanically fastened joints. Such method consists in substituting or swapping the highest stressed part of composite material into insert material step by step until an optimum is reached. This method could also be used for optimising any structure where the removal of material is not an option and where the minimisation of contact stresses is the objective of the optimisation. It allows the user to keep existing geometries intact while reducing maximum stresses in highly loaded areas.

Firstly, a finite element analysis of the desired structure is performed and the stress distribution found. A plate stress file is then set-up and using some criterion for substitution, here called Substitution Criterion (SC), the highly stressed composite material elements are substituted by insert material. The SC can be chosen for example to be the Von Mises stress. Elements will then have their properties substituted from composite material to insert material, where the Von Mises stress in the element is greater than a Substitution Ratio (SR) times the maximum Von Mises stress in the whole structure. The finite element analysis and substitution cycle are then repeated using the same SR until a steady state is reached, i.e. no more elements have their properties changed. An Evolution Rate is then introduced and subtracted to the current SR until

another steady state is reached. This process is repeated until the SR becomes equal or smaller than the Termination Criterion, which could be for example when the stress levels at the interface between composite and insert material are 30% of the maximum in the whole structure. A failure analysis could also be included within the optimisation code to detect tension type failures. This could be used as the termination criterion ensuring that the insert only "grows" when there is an increase in overall efficiency of the joint.

A flowchart of the modified ESO is shown in Figure 4.4. From the above description of the method, it is seen that two parameters need to be defined. The first is the initial substitution ratio SR_0 and the second is the evolutionary rate ER. Typical values of SR_0=99% and ER=1% have been used for the present analysis, i.e. after the first steady state has been reached, the new SR will be of 98%. The steps taken to employ the modified ESO and its mathematical representation can be seen below:

1) Set-up a dense finite element mesh of the structure to be optimised

2) Assign boundary conditions, loads and material properties.

3) Specify the optimisation criteria to be employed (For example: Von Mises maximum stress) and whether a single or multiple load case optimisation should be carried out.

4) Specify the non-design properties (elements which can not be modified) and select which property (P_{old}) should be allowed to be swapped into a different property (P_{new}). The restriction during the evolutionary optimisation is that elements are allowed to change properties only once. This restriction avoids any tendency to oscillatory solutions in which an element is changed from composite to insert and then back again to its original property.

$$P_{old} \xrightarrow{accepted} P_{new} \qquad P_{new} \xrightarrow{illegal} P_{old}$$

5) Perform a linear static finite element analysis of the structure.

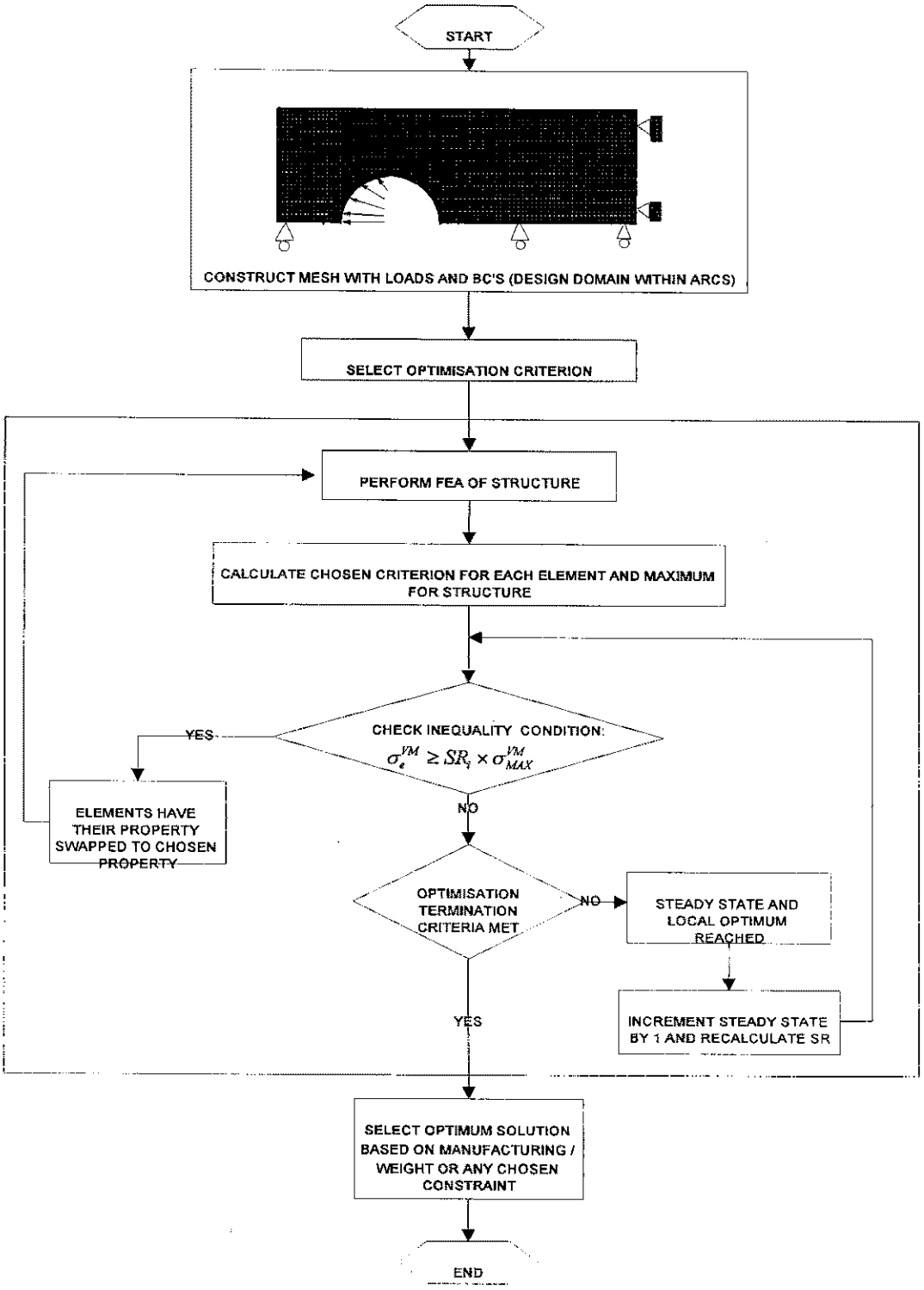

Figure 4.4: Flowchart of modified ESO

6) Compare Von Mises stress (or desired function or stress which could be edited by user) of each element σ_e^{VM} with maximum Von Mises stress present in model $\sigma_{\max}^{VM}$. The property of an element will be changed if the following inequality condition is satisfied:

$$\sigma_e^{VM} \geq SRi \times \sigma_{\max}^{VM} \qquad \text{where SRi = substitution ratio}$$

7) This criterion is used iteratively until a steady state is reached. A steady state and local optimum is said to have been reached when the above inequality condition is no longer satisfied for the current SRi. Once the steady state is reached, a negative evolution ratio is used as follows

$$SR_{i+1}=SR_i - ER$$

8) This process (steps 5 to 7) can be repeated until the desired stress ratio at the hole interface is reached or any other chosen criterion is met. For example when:

$$\sigma_e^{VM} \leq 0.3 \times \sigma_{\max}^{VM}$$

The initial substitution ratio is set to 99% so that the most stressed elements are replaced by insert material.

$$\sigma_e^{VM} \geq 0.99 \times \sigma_{\max}^{VM}$$

For an evolutionary rate of 0.01, the inequality equation after the first steady state is reached, becomes:

$$\sigma_e^{VM} \geq 0.98 \times \sigma_{\max}^{VM}$$

4.5 Single Load Case Optimisation (Geometric ratio w/d=4, e/d=2.5)

The bolt hole loading was represented by a cosine pressure distribution of the general form shown in Equation (4.3),

$$P=Pmax * \cos\theta \tag{4.3}$$

This is based on previous work by Tsujimoto et. al. [28] and appears to be a valid approximation for quasi-isotropic composite laminates. Although this approach is convenient as it reduces computational effort, care needs to be taken as Oplinger [29] has shown that this assumption can lead to serious errors in the stress distribution for certain geometries and lay-ups. A study on the effect of loading assumptions on the stress distribution at the pin/hole interface is presented in section 4.6.

The mesh employed together with the loading and kinematic constraints is shown in Figure 4.5.

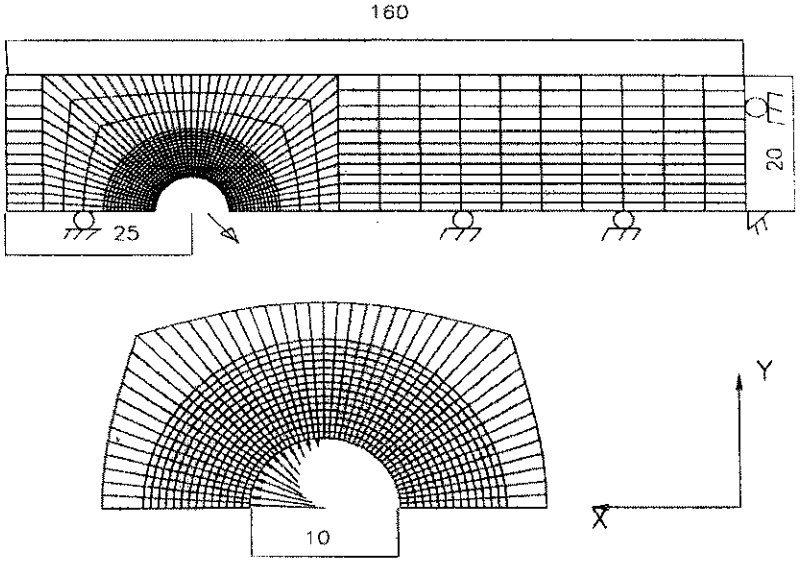

Figure 4.5: Geometry and boundary conditions of FEA model

The width to diameter ratio was 4 and edge to diameter ratio was 2.5. These ratios were chosen to allow direct comparison with results presented by Nilsson [8] and due to the fact that they should provide for a failure in bearing. The properties for the composite material chosen for this study correspond to a quasi-isotropic laminate with the stacking sequence $[90/0/90/0/-45_2/+45_2/90/0/-45/45]_S$, resulting in a laminate of 24 plies with an average thickness of 4.45mm. Failure analysis on this geometric configuration was performed with the "BOLT" program described previously in this Chapter to ensure bearing failure on the w/d=4 configuration. The following data was input to the program to calculate failure load and failure mode:

All values are in psi and in inches as the program required the input in these units.

1) One pin assumed to carry all the load (no by-pass loads)
2) Material properties of T300/934 prepreg (Hy-E3034K) were input as required

Longitudinal Youngs Modulus:	17984046 psi
Transverse Youngs Modulus:	1696882 psi
Shear Modulus:	797679 psi
Poison Ratio:	0.3
Longitudinal Tensile Strength:	230022 psi
Longitudinal Compressive Strength:	220014.5 psi
Laminate Shear Strength:	16969 psi

3) Hole diameter: 0.3937" (10 mm)
4) Width over diameter ratio: w/d=4
5) Edge over diameter ratio: e/d=2.5
6) Length over diameter ratio: l/d=16
7) Joint thickness: 0.1752"
8) Ply orientation: $[90/0/90/0/-45_2/+45_2/90/0/-45/45]_S$
9) Characteristic lengths: R_t=0.018" R_c=0.07"

The characteristic lengths were assumed to be equivalent to those of the T300/1034-C material. This material is the default on the "BOLT" program and as mentioned before should provide with a good estimate for any quasi-isotropic lay-up as the one being analysed.

The output of the "BOLT" program for this configuration and with the above data as input is as follows:

1) Failure load (P)= 6387 lb =28.4 kN
2) Bearing Strength (P/D*H)= 92604 psi = 638.5 Mpa
3) Failure mode= Bearing mode, at the angle of 14.06° with failure initiating at a 0° ply.

The reasons for using a quasi-isotropic panel are twofold. Firstly, due to the low structural efficiency of bolted joints in highly orthotropic laminates and secondly to allow for direct comparison of experimental results. For the finite element analysis, a two dimensional plane stress model using 4 node Linear Quad elements was employed and symmetry constraints were applied so as to analyse only half of the model. Material properties used in the FEA for structural optimisation purposes are presented in Table 4.1.

Properties employed for the FEA optimisation of inserts vary from those employed for the "BOLT" analysis due to the need of comparing stress concentrations with the work of Nilsson [8]. A sensitivity analysis was carried out to assess any changes in insert shape due to different material properties (composite laminate) being used on the optimisation program. The sensitivity analysis indicated that the change in insert shape was negligible as a result of employing either the T300/934 prepreg properties or the IM6/F584 prepreg properties as opposed to those presented in Table 4.1.

The substitution criterion used to achieve the two different shapes obtained, were the Von Mises stress and the Global stress in the x direction. The x direction is coincident with the load direction as shown in Figure 4.6. The global stress in the x direction

indicates that the driving criterion relates to stresses parallel to the load direction as opposed to stresses in the local coordinate of the element. The insert derived by using the global stress in the x direction as driving criterion is also referred in this thesis as "Global insert".

The stress in the x direction with respect to the global coordinate frame was chosen as it can be related directly to compressive stresses parallel to the load direction on the composite material at the interface between the pin and plate.

Table 4.1: Material properties for FEA [8]

	E_1 [GPa]	E_2 [GPa]	G_{12} [GPa]	υ_{12}
Laminae properties	138	10	3.6	0.35
Laminate properties used in FEA/ESO	52.2	52.2	19.6	0.33
Aluminum	71	71	27.3	0.3

In both cases the Termination Criterion was set to be SR=30%. The choice of SR was based on manufacturing constraints. For higher SR's, finger like structures develop behind the ligament region. These finger like structures are part of the metal insert that grows into the composite plate. The manufacturing of such "fingers" would prove very difficult. The termination criterion indicates that the magnitude of the substitution criterion (Von Mises or Global stress XX) at the interface of cut-out/insert will be smaller than 30% of the maximum driving stress on the structure.

The optimised shaped inserts (FEA mesh) obtained from the structural optimisation code EVOLVE with both substitution criterions are shown in Figure 4.6. Figures 4.7 & 4.8 depict the actual manufactured shapes of the different inserts and their location within the specimens.

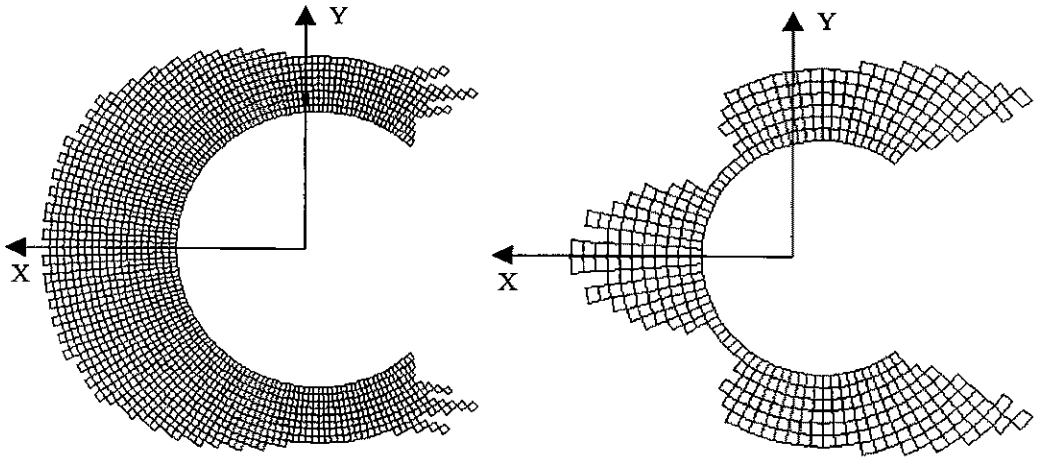

Figure 4.6: Mesh from FEA structural optimisation for both driving criterions: Von Mises stress (left), XX stress (right))

The explanation to the peculiar shape obtained for the "Global insert" is that the insert grows in regions where the absolute XX stress (i.e. compressive or tensile stress) is high. Thus composite material is converted to aluminium (insert material) in the bearing and ligament regions.

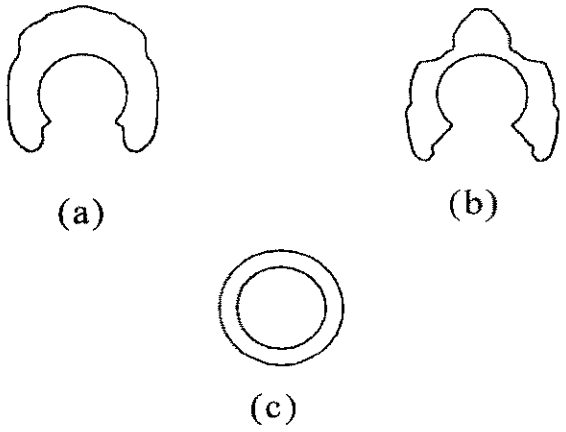

Figure 4.7: Von Mises insert (a), Global insert (b) and 2mm Circular insert (c)

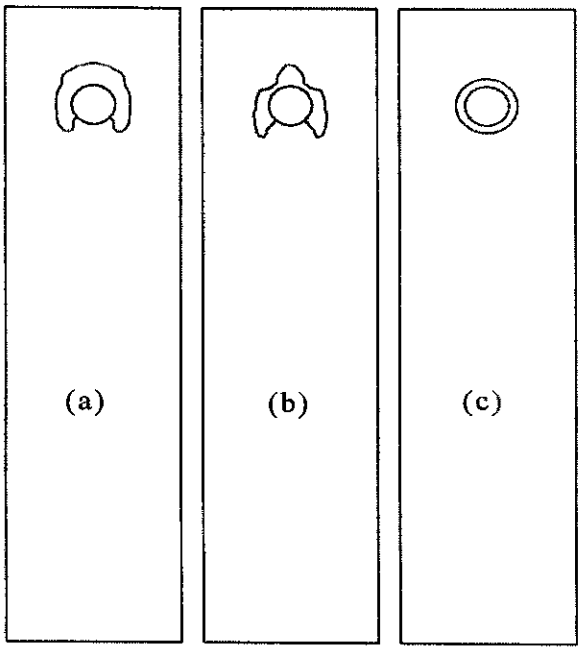

Figure 4.8: Specimens with Von Mises insert (a), Global insert (b) and 2mm Circular insert (c)

4.5.1 Optimisation results (Geometric ratio w/d=4 , e/d=2.5)

The results obtained from finite element analysis for a loaded composite hole without insert, showed that the maximum compressive stress concentration factor at the hole boundary was of -5 and occurs at $\alpha=0^{o}$ while the maximum tensile stress concentration factor was of 5.5 and occurs at $\alpha=90^{o}$. As shown by Nilsson [8], enlarging the existing hole and placing a circular ring with a wall thickness of 2mm can significantly reduce these high stress concentration factors. These stress concentration factors are then reduced to -3 at $\alpha=0^{o}$ and 2.2 at $\alpha=112.5^{o}$ respectively. The proposed method of optimising the shape of inserts achieved a further reduction in compressive stress concentration of 46% when the Von Mises stress was the driving criterion (Von Mises insert) and of 49% when the stress in the x direction with respect to the global coordinate frame was chosen as driving criterion (Global insert). The corresponding values for compressive stress concentration factors are of -1.6 at $\alpha=0^{o}$ for the Von Mises insert and

of -1.5 at $\alpha=0^{\circ}$ for the Global insert. In the case of the Global insert, the highest compressive stress concentration was of -1.67 and occurred at $\alpha=22.5^{\circ}$. The tensile stress concentration factor at $\alpha=90^{\circ}$ remained the same for the Von Mises insert and a further reduction of 25 % was achieved by the Global insert, i.e. a value of 1.67 was achieved. When compared to a composite laminate without insert, the reduction in compressive stress concentration reaches 67 %, while the tensile stress concentration is reduced by up to 70%. The Graph of the Von Mises stress distribution for all cases studied is shown on Figure 4.9. Graphs of the stress in the x direction with respect to the global coordinate frame and the radial stress distribution are depicted in Figure 4.10, while the hoop and the shear stress distributions are shown in Figure 4.11.

It is interesting to note from these graphs, that the substitution criterion used for both inserts produces an even distribution of the corresponding stress around the periphery of the loaded hole. Furthermore, the Global insert appears to be more efficient in reducing both the maximum compressive and tensile stress at the interface. In addition, the overall structure is 3% stiffer for the Von Mises insert than that with a 2mm insert or 7.3% stiffer than the no-insert configuration. The structure with the Global insert is 5.2% stiffer than that with a 2mm circular insert and 13% stiffer than a structure without insert. A comparison of the reduction of maximum compressive stress at the interface per unit mass of test specimen, shows that the optimum shape developed using the Von Mises stress as optimisation criterion is approximately 40% more efficient when compared to the 2mm circular insert. The shape developed by using the stress in the x direction with respect to the global coordinate frame as driving optimisation criterion provides a similar efficiency to that achieved by the Von Mises insert.

It is interesting to note that the Global insert has a peak Von Mises, radial and hoop stress at 45° to the load direction. This occurs due to the very small amount of insert material at this region as seen in Figure 4.6. Although all inserts increase the shear stress concentration at the composite / insert interface, the Global and Von Mises insert result in a smaller shear stress concentration when compared to the circular insert.

The aim of the shape optimisation of inserts is to reduce the high stress concentration factor present in mechanically fastened composite joints to increase the

bearing strength of pin loaded and bolted joints. The modified evolutionary procedure for structural optimisation as applied to the configuration analysed in this section shows large reductions in stress concentrations at the bearing critical area. Both optimised shape aluminum inserts obtained from the evolutionary structural optimisation package achieved a reduction in compressive stress concentration of approximately 46% when compared to a 2 mm circular insert, and a reduction of 67 % when compared to a laminate without metallic insert.

The following sections assess the effect and validity of a cosine pressure distribution representing the bolt hole loading for quasi-isotropic composite laminates. Furthermore, the effect of load distribution on the optimum shape of inserts is also analysed on the following sections.

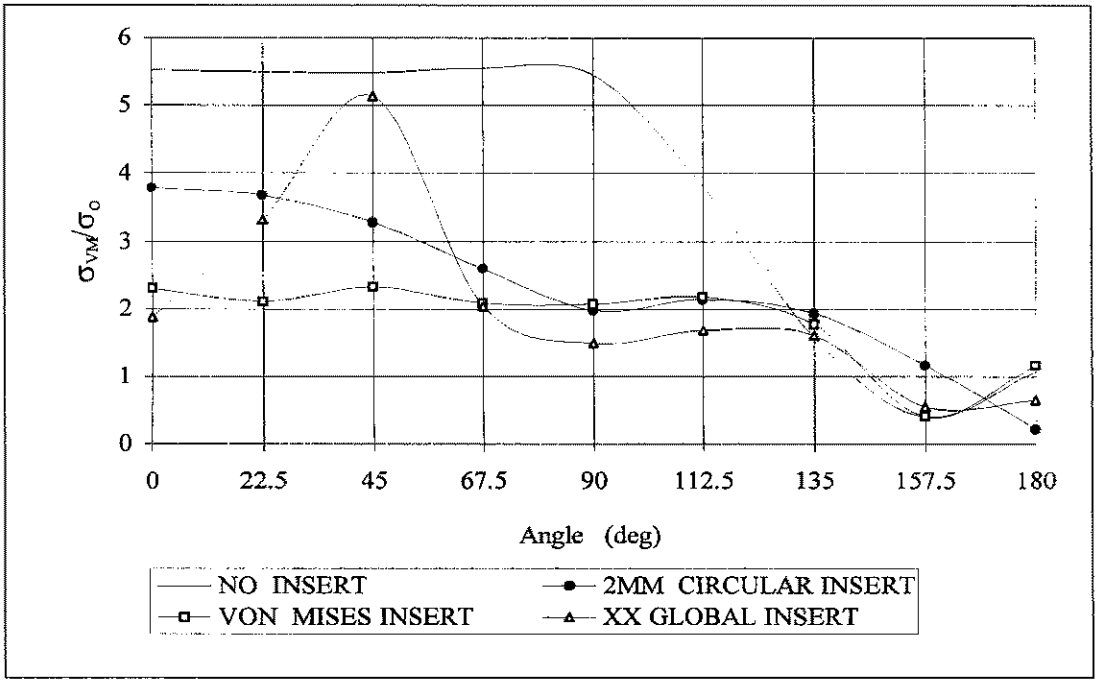

Figure 4.9: Von Mises stress distribution at interface composite/insert

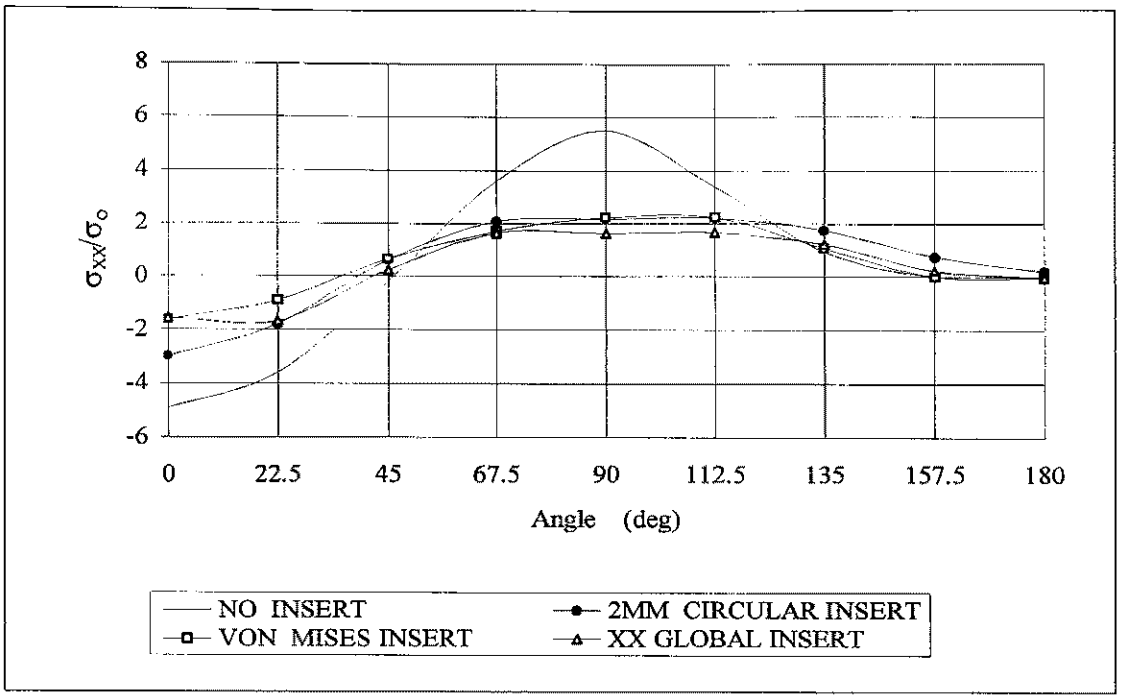

(a)

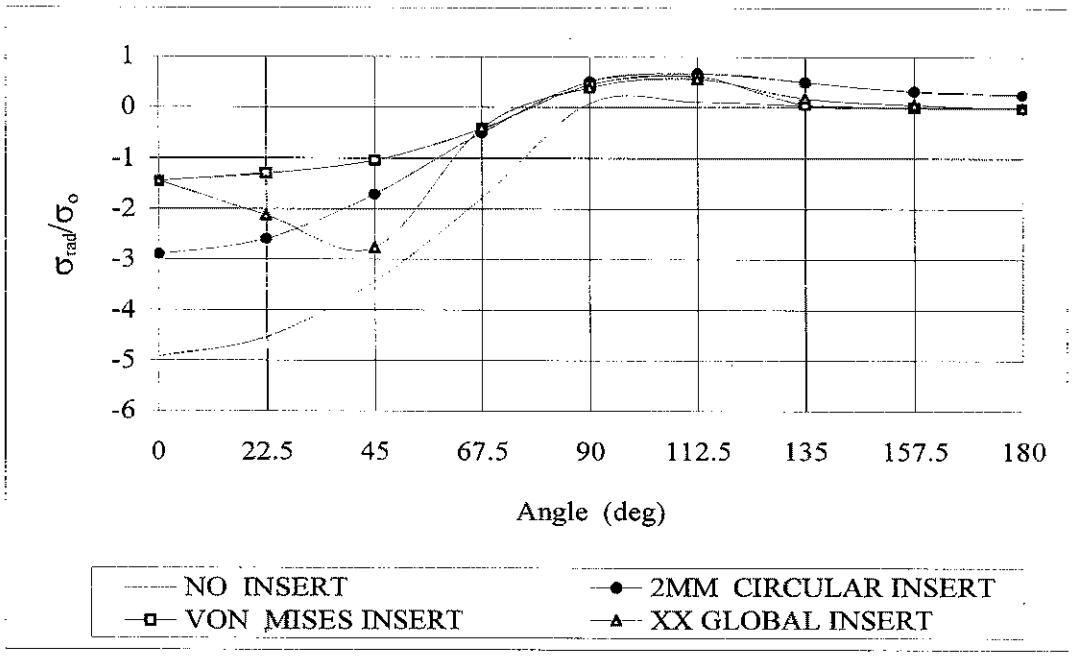

(b)

Figure 4.10: Global X (a) and Radial (b) stress distribution at interface composite/insert

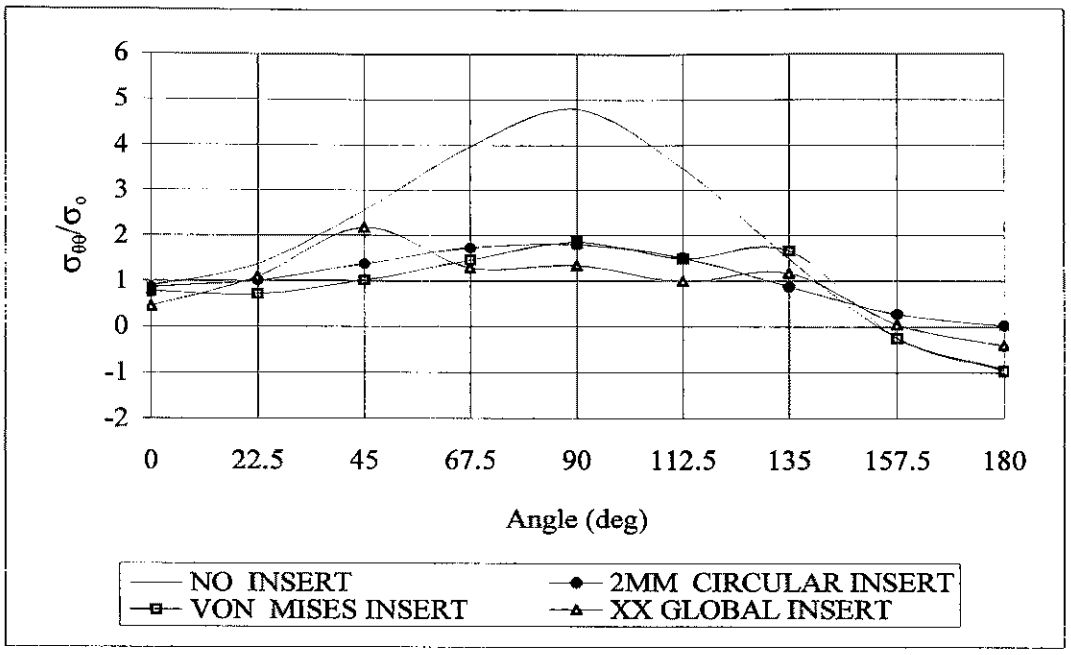

(a)

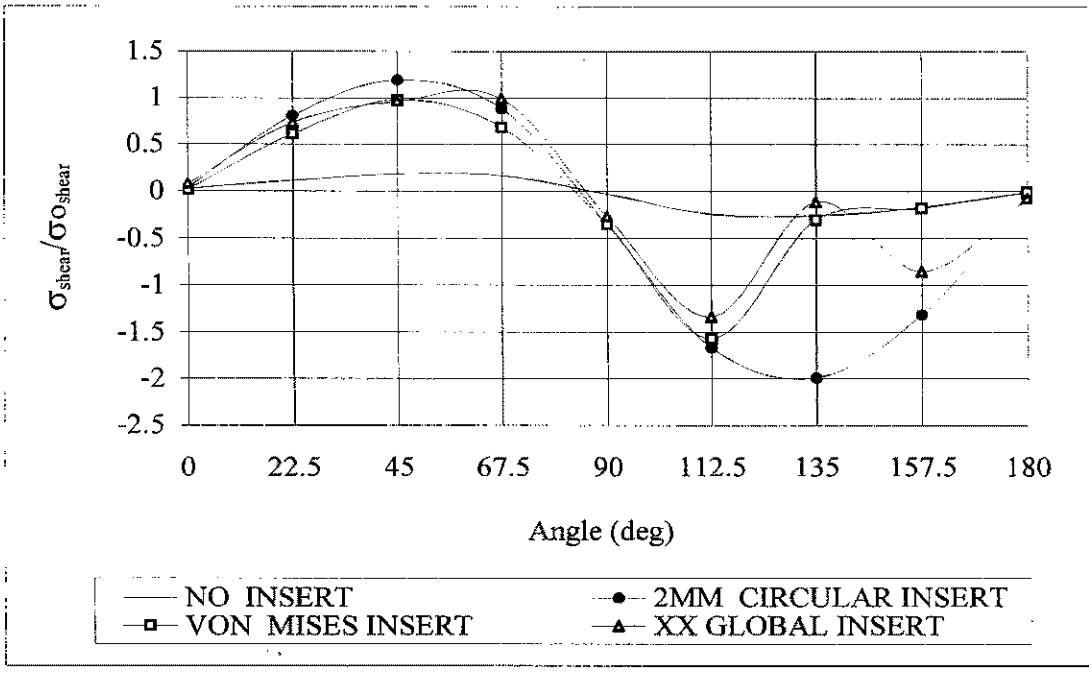

(b)

Figure 4.11: Hoop (a) and Shear (b) stress distribution at interface composite/insert

4.6 Effect of loading assumption on stress distribution at pin/hole interface

Significant amount of research has been conducted by different authors on the stress distribution around a loaded hole. The very small amount of this research relevant to this section is presented. In 1928, Bickley [30], studied the state of stress around a circular hole in an infinite elastic plate of uniform thickness subjected to prescribed in-plane tractions acting on the periphery of the hole. He provides solutions for a single force F acting on the hole at θ=0 deg which can be used to form a Green's function to prescribe radial tractions on the hole boundary. The effects of uniform radial pressures along an arc, and a traction varying cosinusoidally over half of the boundary were also analysed by Bickley. In 1970, Gould et. al. [31] of MIT employed finite element methods to compute pressure distributions as well as contact zones between bolt and plates. They also determined experimentally the radii of separation by two different methods. Their experiments correlated well to the finite element analysis carried out and lead to concluding that smaller zones of contact than those indicated in the literature are obtained in practice. The above references deal with isotropic materials but are still relevant to the work presented in this Chapter as all the analysed composite plates had lay-ups with quasi-isotropic properties.

In 1971, Waszczak et. al. [32] predicted the elastic stress distribution around a pinned joint in anisotropic structures by means of finite element methods. The effect of the pin was represented by a half cosine radial pressure distribution. In 1974, Oplinger et. al. [33] employed an interactive approach in determining the contact arc between a pin and an orthotropic panel. This non-linear problem was solved by using the least squares collocation method with a complex variables formulation of the two dimensional problem. In 1975, Ojalvo [34] concluded that accurate analysis methods require the use of displacement type boundary condition at the hole rather than an assumed radial pressure distribution and that the method must allow for a variation in contact angle of the pin on the plates. De Jong, in 1977 stated that the assumption of an infinitely rigid pin is reasonable for every laminate except the unidirectional orientation [35]. He further stated that for isotropic and a slightly anisotropic case the cosine distribution appears to be a good approximation to the actual stress distribution around a loaded hole. More recently, Xiong [36] developed an analytical method that employs an iterative scheme based on a

complex variational approach to predict failure. In addition, the analysis accounts for the flexibility of all members in the joint.

Two-dimensional anisotropic theory can be employed to derive the elastic stress distribution around a loaded hole [37]. This theory can be applied to composite laminates by combining it with classical lamination theory [38, 39].

Although the load distribution around the periphery of the hole is often assumed to vary cosinusoidally, this analysis can yield significant errors depending on material, lay-ups and geometric ratios (w/d and e/d). A study assessing this phenomenon was conducted by Oplinger [29]. De Jong [40], performed some further studies on this subject finding that a close to cosinusoidal distribution can be found in quasi-isotropic lay-ups of CFRP. This distribution can vary considerably as the degree of orthotropy increases. Furthermore, the author has found that the peak radial stress normally lies at the edge of the hole where the direction of the highest Young's Modulus of the composite plate is at right angles to the hole boundary. The tangential stress (ligament region), does not necessarily lie in the smallest net area of the plate. The location of this maximum stress can vary around the periphery of the hole depending on lay-up and geometry. De Jong [35] and Oplinger [29] also showed that stress distributions tend to become independent of geometry ratios once the w/d and e/d values are greater than 4. In all the cases above, the pin/hole contact is assumed to be frictionless. Although friction between pin and hole has some effect on the stress distribution around the hole, this effect was assumed to be negligible for the pin-loaded quasi-isotropic plates considered in this Chapter. Furthermore, the influence of pin flexibility has been studied by Hyer et. al. [41] concluding that similar results to those obtained under infinitely rigid pin assumptions are obtained when an aluminum alloy or steel pin are in contact with a CFRP plate.

The effect of the stress distribution on the laminate strength was studied by Fu-Kuo Chang [19]. In his paper, it was shown that the strengths and failure modes calculated from both a cosine load distribution and a load distribution determined by an iterative procedure; based on ensuring that all normal stresses are in compression along the contact area; agreed closely.

To assess the effect of the load distribution on the quasi-isotropic composite plates analysed on this Chapter, a study using gap elements was conducted. The distribution at the edge of the hole was obtained by running a finite element analysis of the joint to be optimised. The gap elements were assumed infinitely rigid. The same FEA model as described in Section 4.7.1 was employed. A graph comparing the cosinusoidal distribution (Equations (4.3) and (4.4)) assumed for the first configuration analysed (w/d=4) and the actual load distribution obtained by means of running a finite element analysis with gap elements is depicted in Figure 4.12. No traction was allowed at the edge of the hole thus ensuring that all normal stresses along the contact area were in compression. The load distribution obtained with this method compares very well to that presented by Agarwal [42] (Figure 4.13a) while some discrepancies were observed between the load distribution obtained and Fu-Kuo Chang's one [19] (Figure 4.13b). From the graph, the differences between the cosine distribution and the distribution obtained with the finite element analysis appear to be significant.

$$T_i = \frac{-4P}{\pi D} n_i \cdot \cos\theta \qquad (4.4)$$

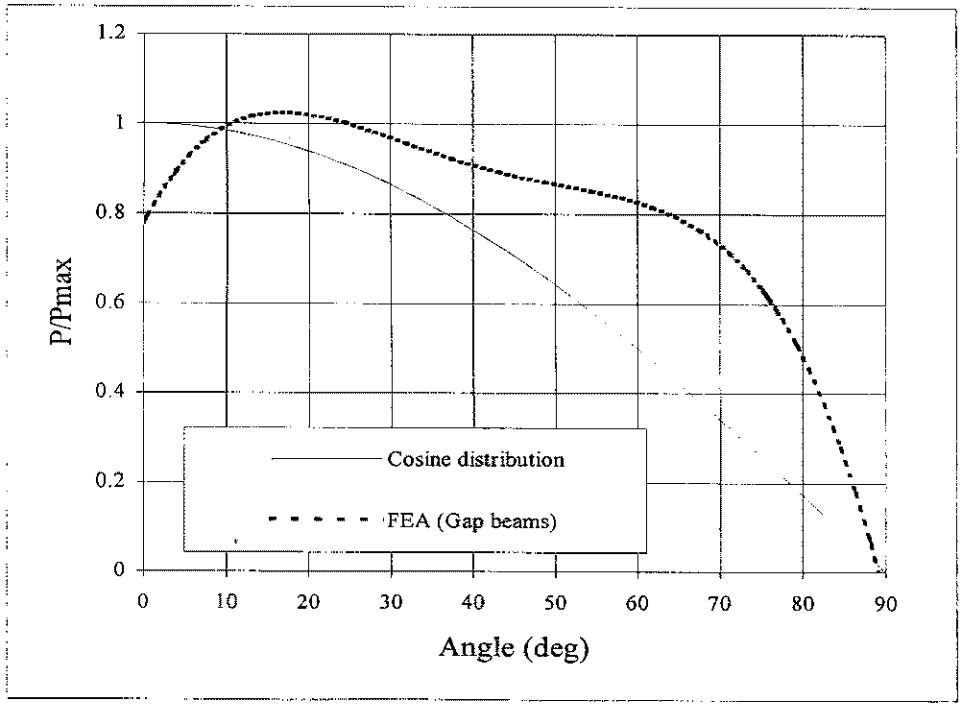

Figure 4.12: Bolt load distribution around hole

As shown in many of the referred papers, the contact zone obtained with the iterative method (FEA using gap elements) is smaller than the contact zone obtained with the cosine distribution. The gap element approach yielded a contact arc of 86.25° while the cosine distribution has a contact arc of 90° by definition.

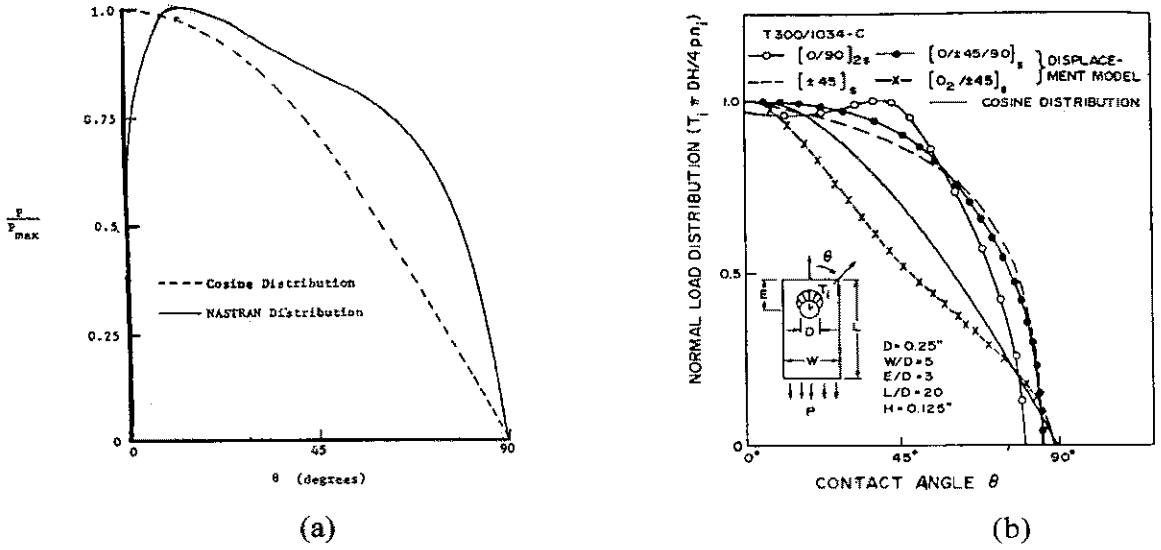

Figure 4.13: Load distribution around loaded hole as calculated by (a) Agarwal [42] and (b) Fu-Kuo Chang [19]

4.6.1 The effect of load distribution on insert shape

Initial studies conducted on shape optimisation of inserts (w/d=4 configuration) assumed a cosinusoidal distribution along the periphery of the hole based on work done by Tsujimoto et. al. [28]. As described in the preceding section a significant difference between the cosine distribution and the actual distribution obtained with finite element analysis was found. To test the effect of the difference in load distribution on the size and shape of insert, an optimisation run was carried out employing gap elements. The resulting shape and size of the insert was then compared to the same parameters obtained by running the assumed cosine load distribution. The optimum aluminum insert shape obtained employing the cosine load distribution is shown on Figure 4.14 while that one

obtained for the gap element solution is depicted in Figure 4.15. The size of the elements was identical for both models to allow for direct comparison of both size and shape. Each element has an equivalent arc representing an angle of 1.875°/element. The number of elements was compared between models along the radial lines at five different angles with respect to the loading direction to establish differences in size and shape. The results are shown in Table 4.2 and the graphical representation of the variation of insert size for different angles is depicted in Figure 4.16. The largest difference in size as a percentage occurs at approximately 60° while the smallest difference in number of elements is found at 0° (loading direction). For all angles surveyed, the number of elements hence the size of the insert was larger for the finite element analysis employing gap elements to distribute the load to the hole. The differences in size and shape were found to be significant as shown on Figure 4.16. Therefore, the shape obtained from the gap beam analysis was employed for manufacturing the optimised insert as this should result in a more accurate representation of the loading conditions at the pin / insert interface. The detailed optimisation of the w/d=11.5 configuration can be found in Section 4.7. It was also found that during the optimisation process and as the insert grew, the contact angle varied.

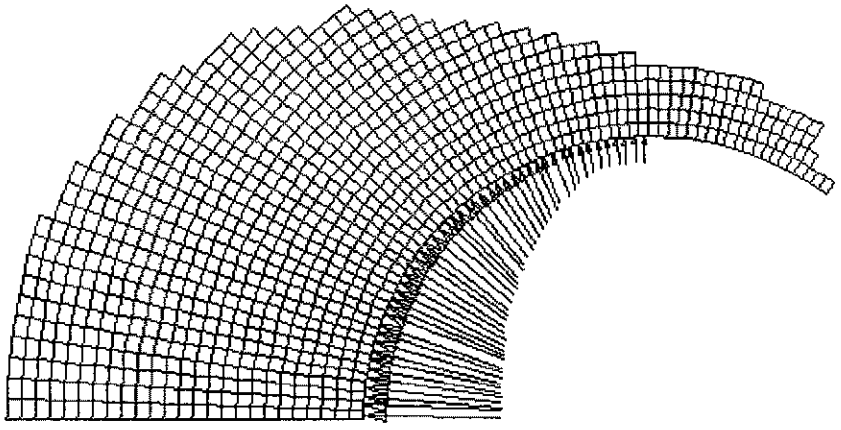

Figure 4.14: Optimum insert shape for cosine load distribution

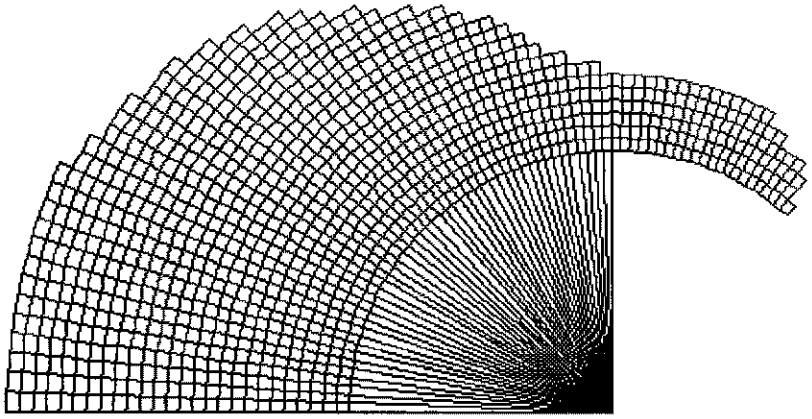

Figure 4.15: Optimum insert shape for gap element distribution

Table 4.2: Effect of loading assumption on optimised insert shape

Angle (deg)	Number of elements Cosine Load Distribution	Number of elements FEA/Gap Beam Distribution	% Difference
0	25	26	3.85
30	23	24	4.17
45	19	21	9.52
60	13	16	18.75
90	5	6	16.67

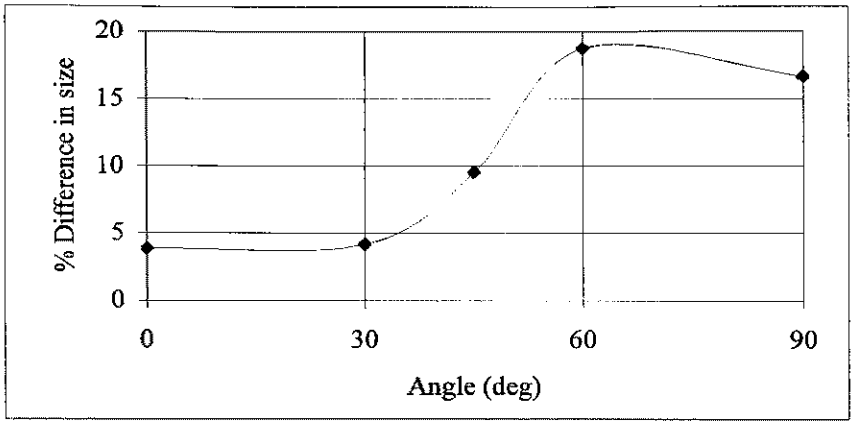

Figure 4.16: Variation of insert size for different angles

4.7 Single Load Case Optimisation (Geometric ratio w/d=11.5 , e/d=7.85)

The variation in optimum insert geometry due to the cosine loading assumptions is quite significant as shown in the preceding section. As a result of these findings the larger geometric ratio was analysed employing gap elements to distribute the load between pin and hole.

Failure analysis on this geometric configuration was also performed with the "BOLT" program described previously in this Chapter. For this configuration, the geometric ratios resulting from placing a circular insert and from the no insert condition were analysed. This was seen necessary as the analysis performed on the first geometric configuration with circular inserts showed a change in failure mode from bearing to net-tension, essentially negating the use of inserts (see Chapter 7).

The following data was input on the program to calculate failure load and failure mode for the no-insert configuration:

All values are in psi and in inches as the program required the input in these units.

1) One pin assumed to carry all the load (no by-pass loads)
2) Material properties of IM6/F584 prepreg (T5A145-F584) were input as required

Longitudinal Youngs Modulus:	18000000 psi
Transverse Youngs Modulus:	1700000 psi
Shear Modulus:	800000 psi
Poison Ratio:	0.3
Longitudinal Tensile Strength:	339000 psi
Longitudinal Compressive Strength:	230000 psi
Laminate Shear Strength:	13600 psi

3) Hole diameter: 0.551" (14 mm)
4) Width over diameter ratio: w/d=11.43
5) Edge over diameter ratio: e/d=7.86
6) Length over diameter ratio: l/d=27
7) Joint thickness: 0.1437"
8) Ply orientation: $[90/0/90/0/-45_2/+45_2/90/0/-45/45]_S$
9) Characteristic lengths: R_t=0.018" R_c=0.07"

The characteristic lengths were assumed to be equivalent to those of the T300/1034-C material. This material is the default on the "BOLT" program and as mentioned before should provide with a good estimate for any quasi-isotropic lay-up as the one being analysed.

The output of the "BOLT" program for this configuration and with the above data as input is as follows:

1) Failure load (P)= 6215 lb =27.6 kN
2) Bearing Strength (P/D*H)= 78471 psi = 541 Mpa
3) Failure mode= Bearing mode, at the angle of 0° with failure initiating at a 45° ply.

The following data was modified to account for the inclusion of a metallic circular insert with an outside diameter of 22.6 mm (0.89"):

1) Hole diameter: 0.89" (22.6 mm)
2) Width over diameter ratio: w/d=7.08
3) Edge over diameter ratio: e/d=4.867
4) Length over diameter ratio: l/d=16.8

The output of the "BOLT" program for the configuration to include the circular insert and with the above data as input is as follows:

1) Failure load (P)= 8512 lb =37.9 kN
2) Bearing Strength (P/D*H)= 66573 psi = 459 MPa
3) Failure mode= Bearing mode, at the angle of 0^{o} with failure initiating at a 45^{o} ply.

Although the assumptions employed to calculate the failure load for the configuration including the circular insert might not be very accurate, they should be sufficient to reasonably predict the failure mode. The main difference lies in that the circular insert being aluminium re-distributes the load into the composite plate most probably in a way that affects the loading assumptions.

4.7.1 Finite Element Analysis

The mesh employed and kinematic constraints are shown in Figure 4.17. The loading due to the bolt was simulated by introducing rigid beam elements in the points where the contact area was known and gap elements were employed closer to the ligament region. This was found to be necessary after running the same analysis with an assumption of a cosinusoidal loading which proved that the contact area varied as the insert grew; as described in the preceding section. For the finite element analysis, a two dimensional model using 3614 four noded Linear Quad elements, 102 TRI 3 (3 node elements) and 63

beam elements (4 of which were gap elements) was employed and symmetry constraints were applied so as to analyse only half of the model. The width to diameter ratio was chosen to be approximately 11.5 and the edge to diameter ratio 7.85 to ensure a bearing type failure.

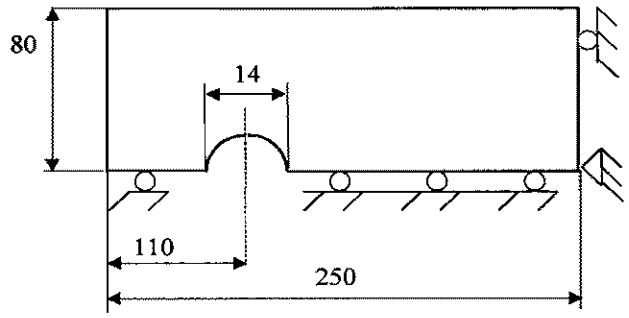

Figure 4.17: Dimensions and kinematic constraints

This was found to be necessary as earlier tests on smaller specimens failed in a net tension type failure (see Chapter 7). The properties for the composite material chosen for this study correspond to a quasi-isotropic laminate. The same material properties as used in the finite element analysis performed on the w/d=4 configuration was employed for the w/d=11.5 configuration (Table 4.1).

The substitution criterion used to achieve the optimised shape insert was the Von Mises stress. The Termination Criterion was the size of the insert. This ensured that the optimised insert weighed the same as the circular insert for which a bearing failure was calculated. Figure 4.15 previously depicted in Section 4.6.1 shows the optimised shaped insert obtained from the EVOLVE structural optimisation method employed, while Figure 4.18 depicts the actual inserts manufactured (optimum and circular insert of equivalent weight).

4.7.2 Optimisation results (Geometric ratio w/d=11.5 , e/d=7.85)

The results obtained from FEA for a loaded composite hole without insert, showed that the maximum compressive stress concentration factor at the hole boundary was -13.55 and occurs at $\alpha=0^{\circ}$ while the maximum tensile stress concentration factor was 10.7 and occurs at $\alpha=90^{\circ}$. The circular insert chosen for this configuration had a wall thickness of 4.2 mm. This ensured a w/d and e/d ratio that should result in bearing failure. An additional consideration for this joint configuration was the prediction of the maximum Von Mises stress on the aluminium inserts (optimised and circular shapes). Predictions were carried out as a result of early test specimens (w/d=4) showing significant yielding of the insert prior to failure. FEA results, indicate that maximum Von Mises stresses on the aluminium (2024-T3) inserts at the predicted failure load (27.6 kN, see Section 4.7), are well below the yield stress of the aluminium employed.

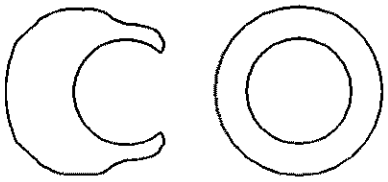

Figure 4.18: Von Mises insert (left), 4.2mm Circular insert (right)

The stress concentration factors present in the loaded composite hole without insert are then reduced to -6.2 at $\alpha=0^{\circ}$ and 2.7 at $\alpha=66.5^{\circ}$ respectively by the introduction of the circular insert. The proposed method of optimising the shape of the inserts achieved a further reduction in compressive stress concentration of 54% using the Von Mises stress as driving criterion. The corresponding compressive stress concentration factor at $\alpha=0^{\circ}$ is -4. The tensile stress concentration factor at $\alpha=90^{\circ}$ increased when compared to the circular insert by 60% but was still 140% lower than for the no insert condition. This higher stress concentration at the ligament region is acceptable, as the objective is to decrease the

compressive stresses at the composite interface where bearing failure occurs. A Graph of the Von Mises stress at the composite/insert interface is show on Figure 4.19.

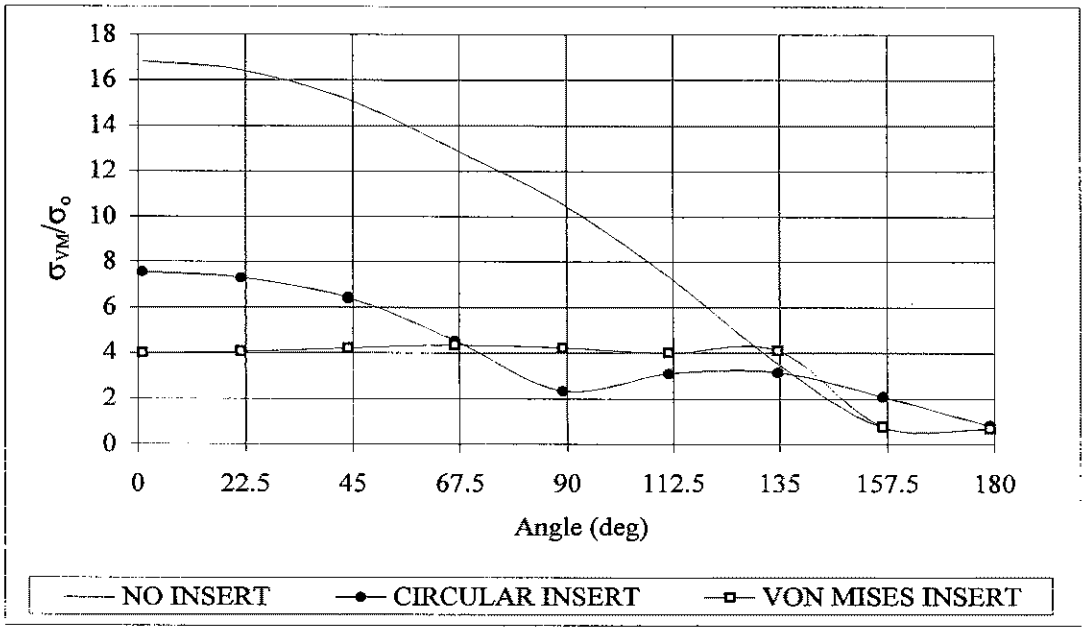

Figure 4.19: Von Mises stress distributions at interface composite/insert

When compared to a composite laminate without insert, the reduction in compressive stress concentration is larger than 230%. The Von Mises stress concentration was also reduced at the interface of composite/insert material by 89% when compared to the circular insert of equal weight.

The radial and hoop stress distributions are depicted in Figure 4.20, while the shear stress distribution is shown in Figure 4.21.

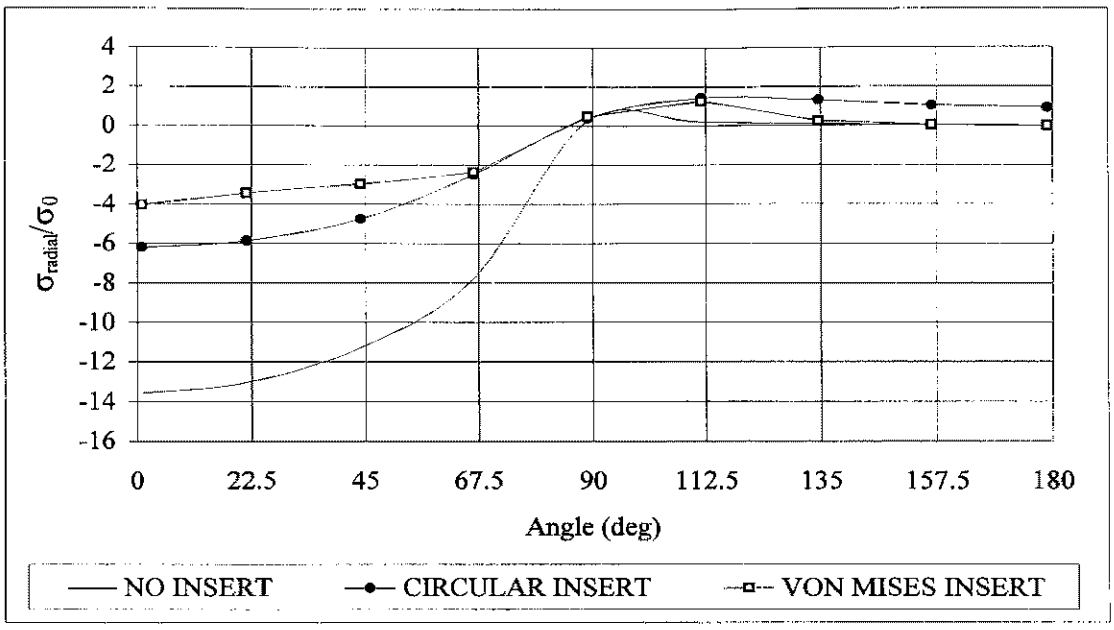

(a)

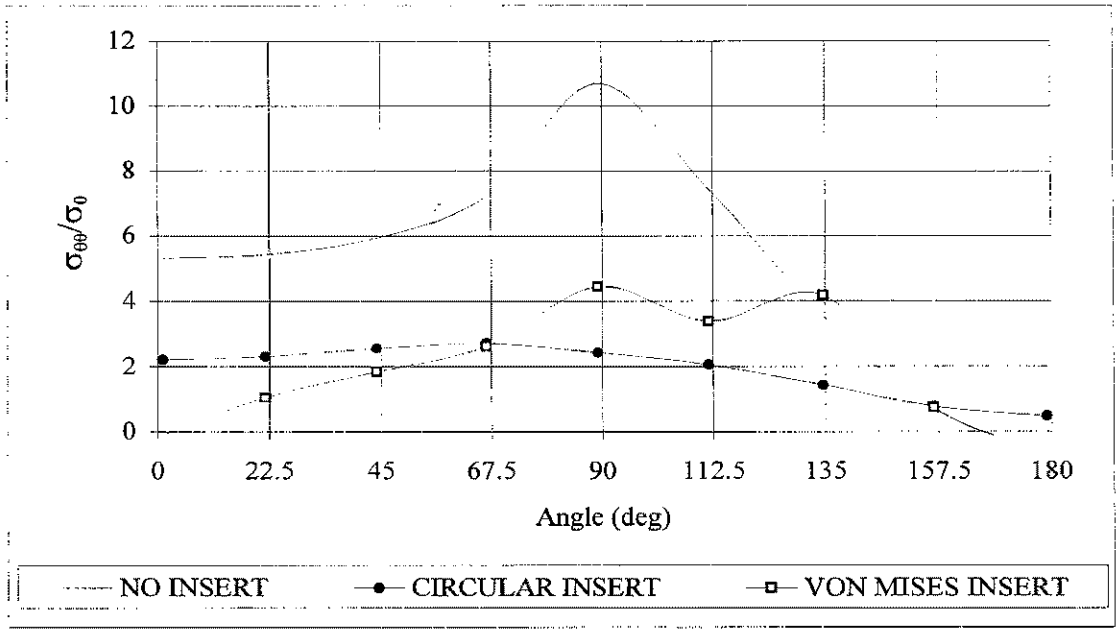

(b)

Figure 4.20: Radial (a) and Hoop (b) stress distribution at interface composite/insert

As observed for the w/d=4 configuration, it can be noted from these graphs, that the substitution criterion used for the optimised insert produces an even distribution of the corresponding stress around the periphery of the loaded hole.

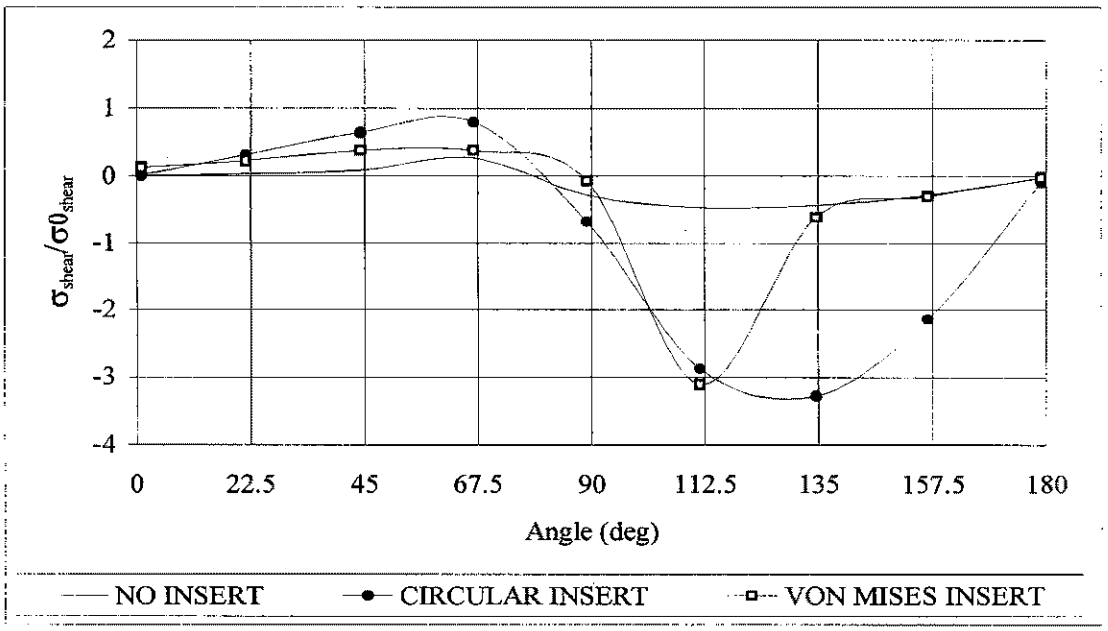

Figure 4.21: Shear stress distribution at interface composite/insert

4.8 The effect of insert material on optimum insert shape

To test the effect of the difference of insert materials on the size and shape of inserts, optimisation runs were carried out with both aluminium and steel as the insert material. Both analyses were performed employing gap elements. The resulting shape and size of the insert between the two runs were then compared at the same substitution rate (30 %). The optimum steel insert shape obtained is shown on Figure 4.22 while the optimum aluminium insert shape is depicted in Figure 4.23. Although the figures are useful to compare size and shape of the different material inserts at the same substitution rate, it does not mean that the stresses at the composite interface are equivalent. The reason is that

the element Von Mises stress is related to the maximum stress in the structure by the following equation previously described in Section 4.4:

$$\sigma_e^{VM} \leq 0.3 \times \sigma_{\max}^{VM} \qquad \text{where: SR(substitution rate)= 0.3}$$

The difference between the maximum Von Mises stress on the model with a steel insert and the one with an aluminium insert was approximately 50%; the former being greater.

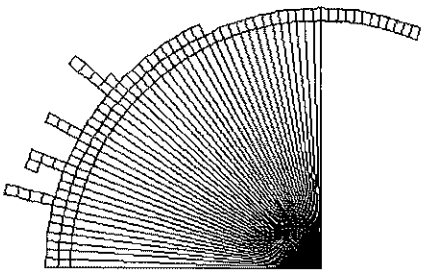

Figure 4.22: Optimum steel insert (SR=30%)

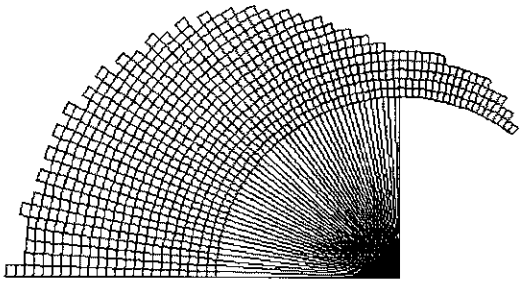

Figure 4.23: Optimum aluminium insert (SR=30%)

The optimum shape and size obtained for the model with aluminium insert and the steel insert are distinctly different. Besides of being much smaller, the optimum steel insert shape is almost circular with the exception of 4 different areas where a finger type shape developed. This shows how the difference in stiffness between the inserts influences the optimum insert shape. The stiffness of the steel insert is approximately three times greater than the aluminium (E_{steel}=210 GPa, $E_{aluminium}$=71 GPa).

As the maximum Von Mises stress varies for the steel insert and the aluminium insert there is a need to establish an additional comparison between the two models. A

more meaningful comparison can be achieved by assessing the differences between models that yield an equivalent stress at the composite interface. The evolutionary history of the optimisation run for the steel insert model was analysed, in order to select the substitution rate that provides with a similar Von Mises stress level to the aluminium optimum insert model at the composite interface. The baseline model for comparison (optimum aluminium insert) is equivalent to that shown in Figure 4.23. The substitution rate for the optimum steel insert shape which yields an equivalent Von Mises stress at the composite interface was SR=23.50%. The corresponding insert shape for this substitution rate is depicted in Figure 4.24.

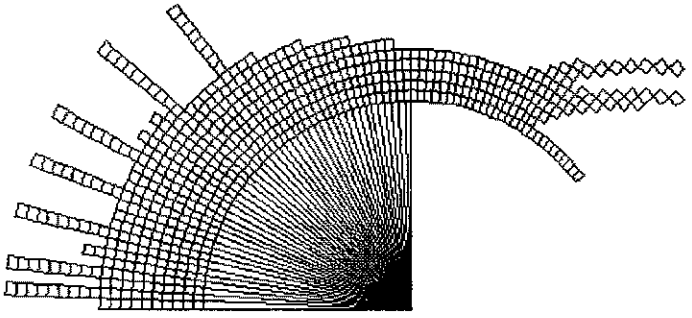

Figure 4.24: Optimum steel insert (SR=23.50%)

Although the shape resembles more closely the one obtained with the aluminium insert, the finger like shape continues to be present at different angles with respect to the load direction. The average diameter of the optimum steel insert at the bearing region; ignoring the finger like protrusions; is almost half of that of the optimum aluminium insert. At 90° to the load direction (ligament region), the number of elements is equal between the two models. It is very likely, that the finger like protrusions develop due to the large stiffness differential between the steel insert and the laminate. The stiffness ratio between the steel and the laminate is approximately 4, while the stiffness ratio between the aluminium and the composite laminate is approximately 1.4. A comparison between the

optimum steel insert (Figure 4.24) and the optimum aluminium insert (Figure 4.23), shows that the latter is a better candidate due to ease of manufacture.

4.9 The effect of joint geometry on optimum insert shape

The results obtained for the first geometric ratio analysed (w/d=4) were compared to those ones obtained for the second geometric ratio (w/d=11.5) to assess the influence of geometry on the shape and size of the optimum inserts. The only difference between the analysis performed for the first and second geometric ratios was the loading distribution assumption. The geometric ratio of w/d=4 assumed the loading to be distributed from the pin to the hole in a cosine distribution while the analysis performed on the w/d=11.5 ratio employed gap elements to distribute the load between pin and hole. The resulting shape and size of the insert between the two runs were then compared at the same substitution rate (30 %). The optimum aluminum insert shape for w/d=4 and e/d=2.5 is shown on Figure 4.25 while the optimum aluminium insert shape for w/d=11.5 and e/d= 7.85 is depicted in Figure 4.26. As the size of elements between models was dissimilar due to the different geometric ratios, no attempt is made here to compare the size of the insert at different angles. The difference in load distribution assumptions between models further hinders obtaining an accurate comparison. In general terms, the largest difference between the optimum inserts obtained from the shape optimisation of joints with different geometric ratios occurs at the ligament region.

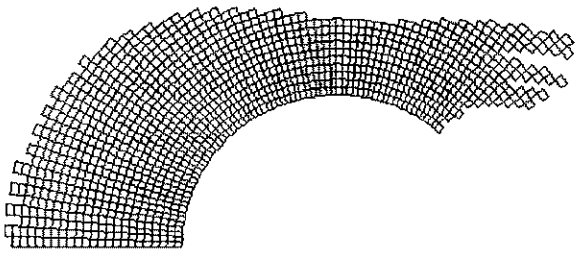

Figure 4.25: Optimum insert w/d=4

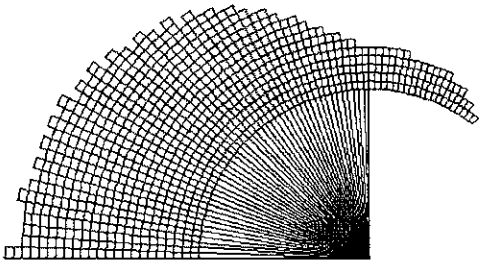

Figure 4.26: Optimum insert w/d=11.5

The joint configuration with w/d=4 conforms quite closely to half an ellipse while the configuration with w/d=11.5 is more "bubble" shaped. The transition in the shape of the insert between the bearing region and the ligament region is also smoother than the transition between these two regions in the configuration with w/d=11.5. The distribution of the insert material behind the ligament region (on the non-bearing side of the hole) is significantly different between the two configurations. There is considerably more material in this region for the w/d=4 configuration when compared to the w/d=11.5 configuration. Furthermore, a "finger" like structure developed for the w/d=4 configuration at approximately 120°. The difference in material distribution is directly related to the stress distribution for the geometry considered. Therefore, the addition of material for the w/d=4 configuration at the ligament region occurs as a result of large Von Mises stress (driving criterion for both models) values at those elements. A comparison of the Von Mises stress distribution between the no-insert configuration with both w/d=4 and w/d=11.5 can be made from Figures 4.9(a) and 4.19 respectively. This shows that while the stress concentration factor for the w/d=4 configuration is fairly constant between the bearing and ligament regions, the opposite occurs for the w/d=11.5 configuration. In the latter geometric configuration, the Von Mises stress concentration factor at the ligament region is approximately 38 % lower than at the bearing region. This explains the differences in shape and size of the optimum aluminium inserts at the ligament region and behind it. It also highlights that an indication of optimum shape of a metallic insert can be obtained from a contour plot of the chosen driving criterion.

4.10 Multiple Load Case Optimisation (w/d=11.5, e/d=7.85)

A multiple load case problem was run for one pin-loaded joint configuration using similar procedures to those employed for single load case optimisation problems. Only one geometric configuration was analysed consisting in a w/d=11.5 ratio and an e/d=7.85. The bolt hole loading in either direction was represented by a cosine pressure distribution equivalent to that employed for the single load case optimisation (w/d=4, Section 4.5). The two load cases employed were equivalent and opposite in directions. The cosine load distribution assumption had to be employed for multiple load case optimisation due to the software's inability of employing different sets of gap elements for each load case.

Properties, boundary conditions and mesh were the same as for the single load case optimisation of pin-loaded joints.

For the multiple load case optimisation of inserts, an "or" operator between load cases was used as any element which has a high stress concentration on any of the load cases should be swapped to insert material. Therefore, the procedure described in Section 4.4, Item 6 needs to be modified as follows:

6_{modified}) Compare Von Mises stress (or desired function or stress which could be edited by user) of each element and for each load case (LCi) $\sigma_e^{VM}{}_{\text{LCi}}$ with maximum Von Mises stress present in model $\sigma_{\text{max LCi}}^{VM}$. The property of an element will be changed if the following inequality condition is satisfied for either load case:

$$\sigma_e^{VM} \geq SRi \times \sigma_{\max}^{VM}$$

The substitution criterion used to achieve the optimum shape shown in Figure 4.27, was the Von Mises stress. This Figure also depicts pictorially the two load cases employed. The forces from Load Case 1 are applied along the edge of the hole with the smallest edge margin while the opposite applies to Load Case 2. The termination criterion was set to be SR=30%. The termination criterion indicates that the Von Mises stress at the composite/insert interface for either load case will be 30 % of the maximum Von Mises stress in the whole structure for the respective load cases.

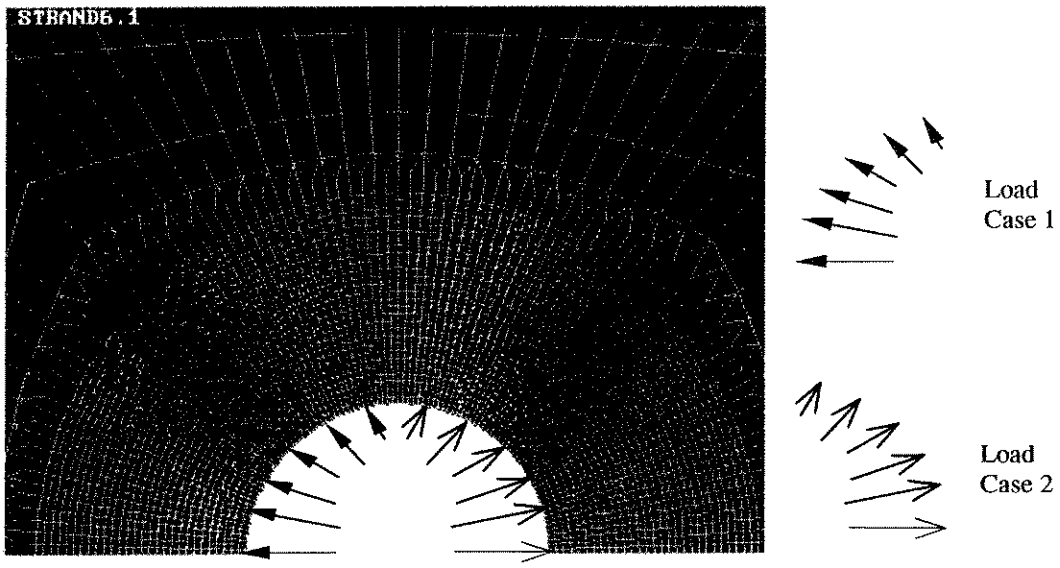

Figure 4.27: Multiple load case optimum insert shape

4.10.1 Multiple Load Case Optimisation results (Geometric ratio w/d=11.5, e/d=7.85)

A comparison of radial, hoop, shear and Von Mises stresses at the composite interface was made for both load cases employed during the optimisation procedure. The stresses which are more relevant to a bearing induced failure are the radial and Von Mises stresses. These stresses varied by only 0.5 % between load cases 1 & 2 for the no insert configuration. The maximum radial and Von Mises stress concentrations occur at 0° and 180° for load cases 1 & 2 respectively. A larger variation between load cases stress results of up to 15 % is found for both insert configurations (circular and Von Mises insert). The radial and Von Mises stress concentrations are larger for the second load case. This is applicable for all configurations analysed. The following comparisons are all based on the largest stress concentrations obtained for the second load case. The maximum Von Mises stress concentration factor at the hole boundary was –16.8 while the maximum radial stress concentration was -13.7. They both occur at α=180°. These stress concentration factors are reduced to –6.8 and –5.90 respectively by the introduction of a circular insert of 5.8 mm wall thickness. The optimum insert shown in Figure 4.27; which has an equivalent mass when compared to the circular insert; further reduces the Von Mises stress concentration at the composite/insert interface to -4.9 and the radial stress concentration to

4.5. The largest stress concentration magnitudes for the insert configurations still occur at 180°. A graphical representation of the Von Mises stress concentration for both load cases 1 & 2 is shown in Figure 4.28 and Figure 4.29 respectively.

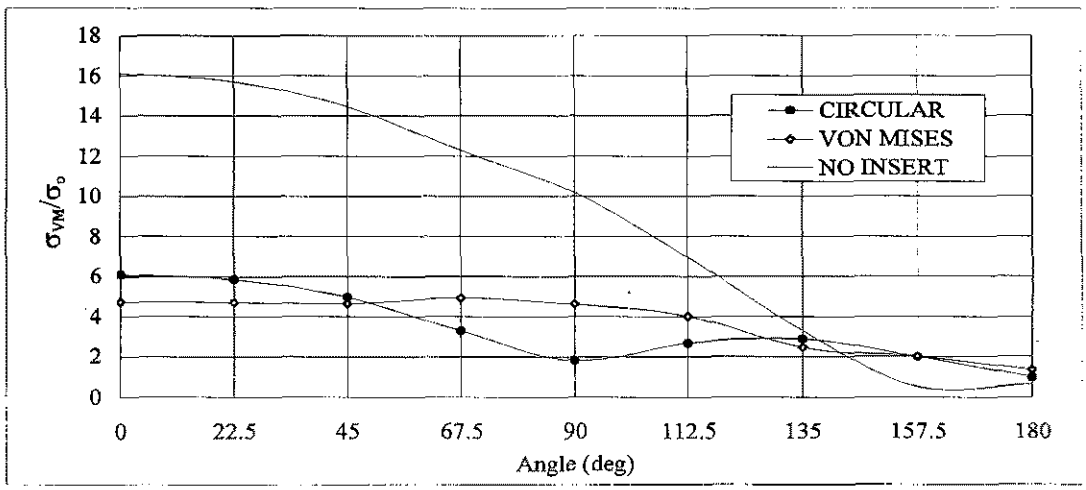

Figure 4.28: Von Mises stress distributions at interface composite/ insert for load case # 1

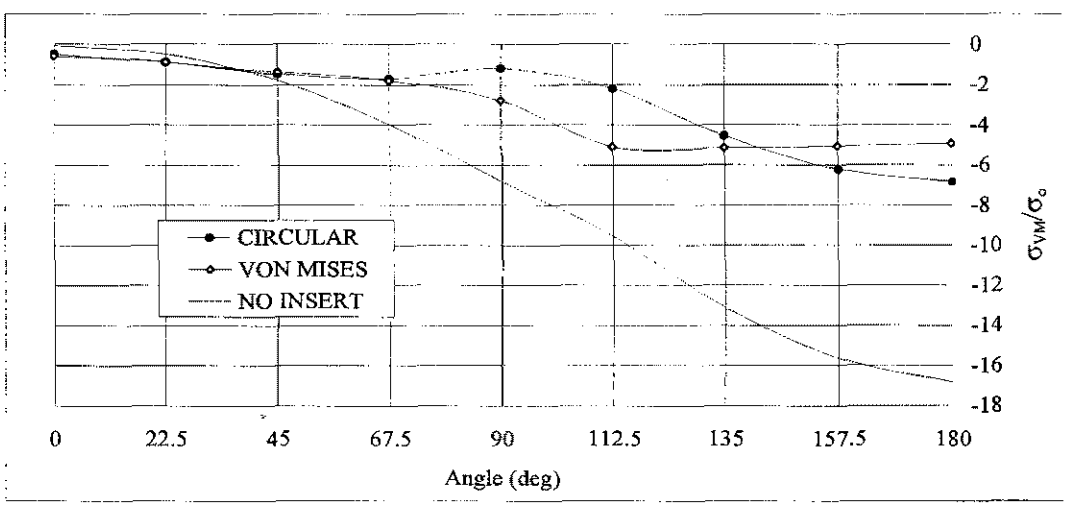

Figure 4.29: Von Mises stress distributions at interface composite/ insert for load case # 2

These graphs show how large reductions in Von Mises stress concentrations are achieved for both load cases by the introduction of metallic inserts; in particular the optimally shaped insert. Similar reductions in stress concentration magnitudes are shown in Figures 4.30 & 4.31; which depict the radial stress distributions for load cases 1 & 2 respectively.

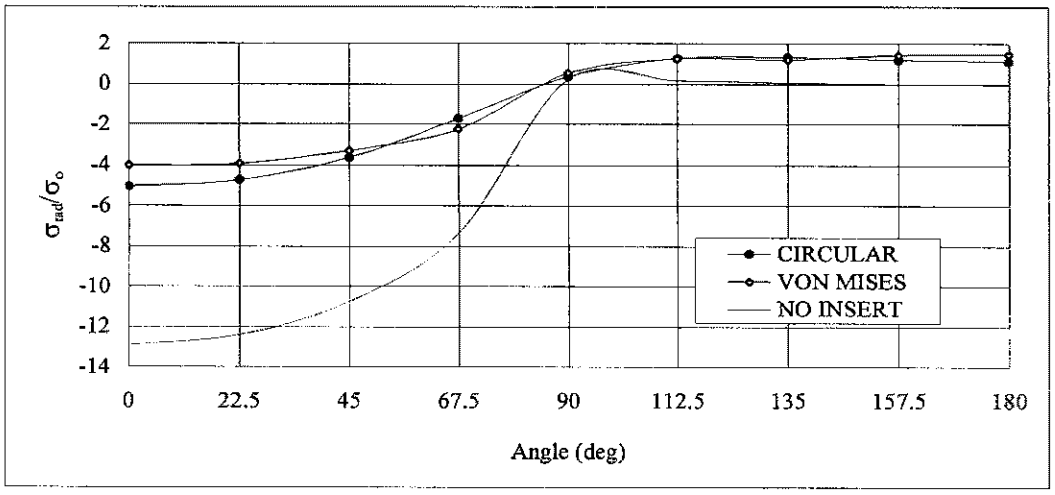

Figure 4.30: Radial stress distributions at interface composite/ insert for load case # 1

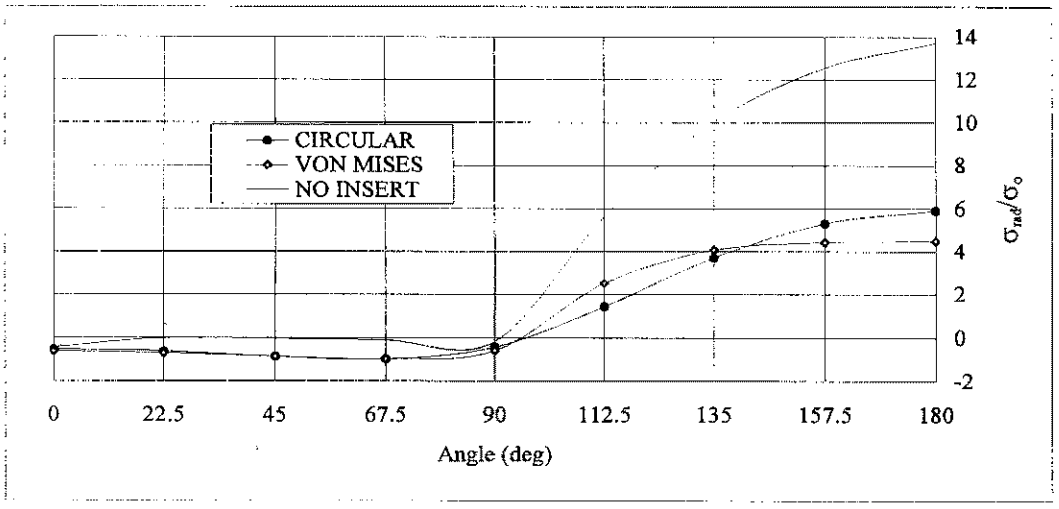

Figure 4.31: Radial stress distributions at interface composite/ insert for load case # 2

The hoop stress distributions for load cases 1 & 2 are shown in Figures 4.32 and 4.33, while the shear stress distributions for these load cases are depicted in Figures 4.34 and 4.35.

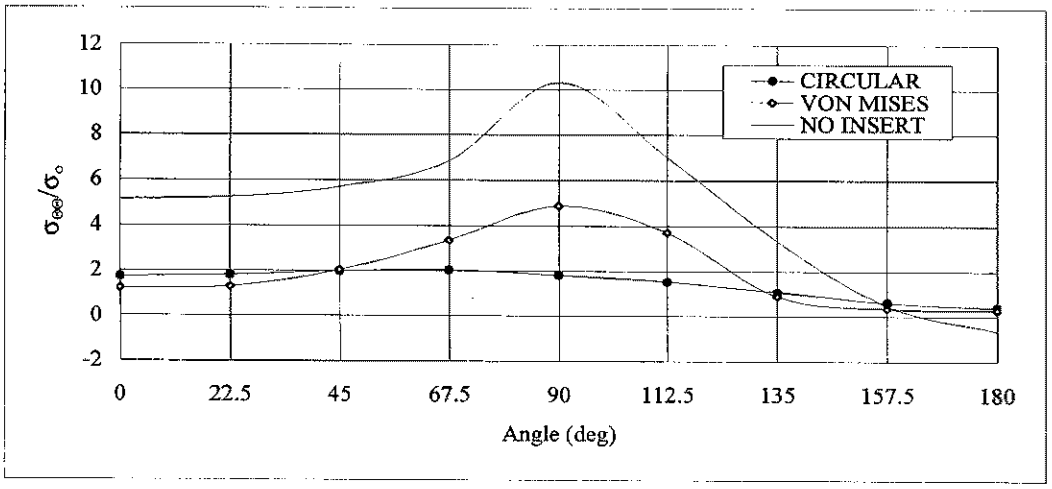

Figure 4.32: Hoop stress distributions at interface composite/ insert for load case # 1

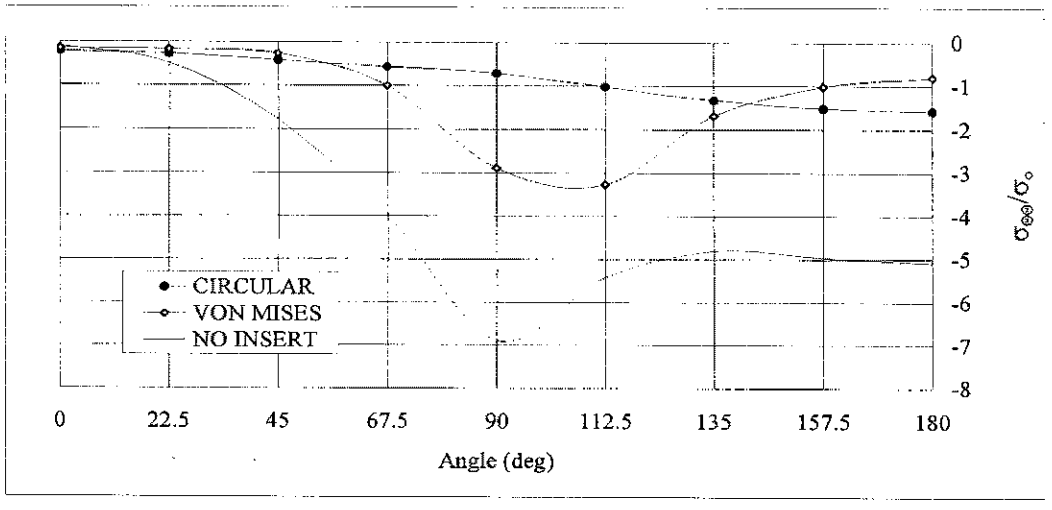

Figure 4.33: Hoop stress distributions at interface composite/ insert for load case # 2

Hoop stress concentrations are reduced for both load cases with either the circular or Von Mises inserts. The largest reductions occur at the ligament region (90°). The hoop stress concentration factor is reduced by up to 50 % for load case 1 and 60 % for load case 2 with the addition of the Von Mises insert. A larger reduction is achieved with the circular insert. This is expected, since the inserts are optimised for bearing critical failures, thus they do not provide any gain in structural efficiency for net-tension type failures. The reductions in hoop stress concentrations achieved by the use of circular inserts are 80 and 90 % for load cases 1 and 2 respectively.

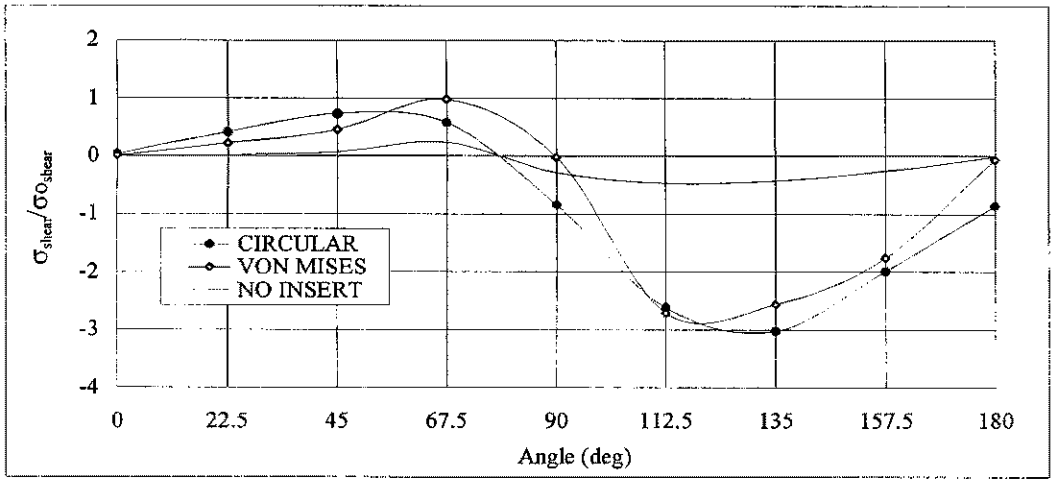

Figure 4.34: Shear stress distributions at interface composite/ insert for load case # 1

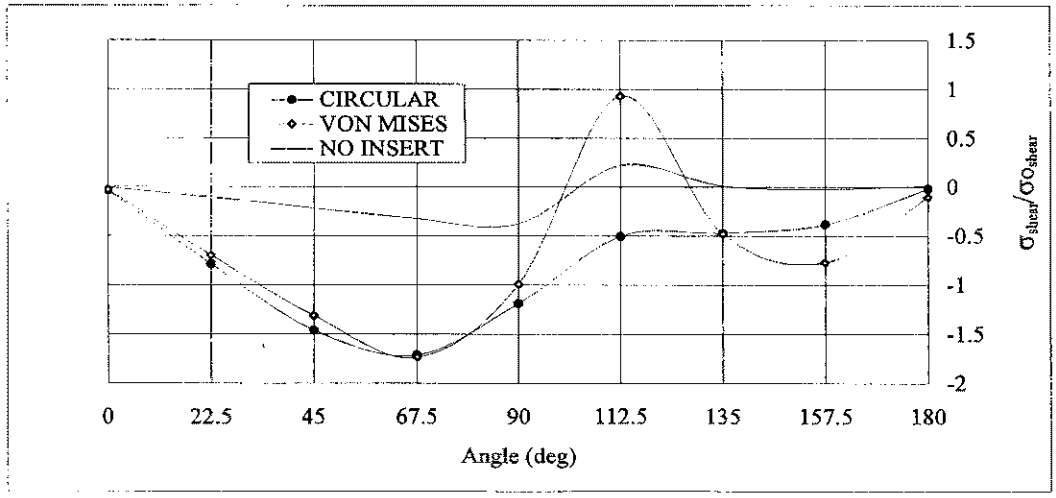

Figure 4.35: Shear stress distributions at interface composite/ insert for load case # 2

The shear stress concentrations are largely increased for both load cases 1 & 2 with the addition of either a circular or the Von Mises insert. This is due to most of the load being transferred at the interface between the insert and the composite material. Since the inserts have been targeted for bearing critical joints, the significant increase in shear stress concentration should not affect or cancel out the increase in joint strength due to the very large reductions in radial, Von Mises and hoop stress concentrations.

4.11 Multiple Hole Optimisation

Two different multiple hole optimisation problems were run for the pin-loaded joint configurations using similar procedures to those employed for single load case optimisation problems. The first geometric configuration analysed consisted in two holes in series. The w/d and e/d ratios remained at 11.5 and 7.85 respectively. A pitch of 4d was introduced between the two holes in series. The dimensions, boundary conditions and hole numbering for this configuration (two holes in series) are shown in Figure 4.36. The second geometric configuration analysed consisted in three holes in parallel. The pitch between the three holes in parallel was also 4d. The remaining geometric ratios were as follows:

a) w/d= 12
b) e/d=7.85
c) q/d=2.0 (side distance ratio)

The hole diameter was 14 mm for all cases. Dimensions, constraints and hole numbering for the three hole in parallel configuration are shown in Figure 4.37. The ratios employed for both series and parallel hole configurations were chosen to minimise any interaction effect between holes and also to reduce edge effects. Fu-Kuo Chang et.al [21] suggest the following guidelines for hole pitch and edge distances by which the failure load is not affected significantly:

a) by the proximity of two holes in parallel when the distance between two holes (pitch) is larger than 3D.

b) by the proximity of two holes in series when the distance between two holes (pitch) is larger than 2D.

c) by the edge when the distance between the edge and the hole is greater than 3D.

d) by the proximity of side when the distance between the hole and the side is larger than 2D.

These results were derived from analysis performed on quasi-isotropic graphite-epoxy composite laminates.

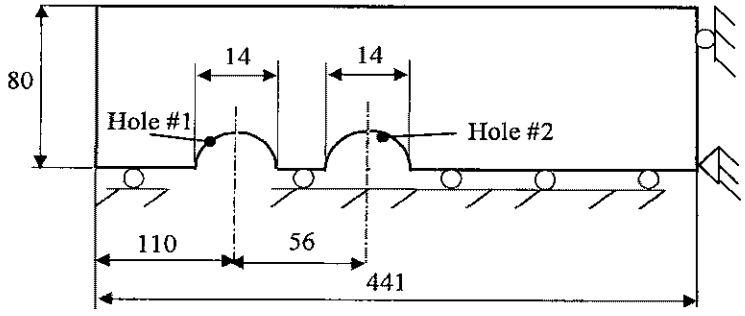

Figure 4.36: Dimensions and boundary conditions for two holes in series

The bolt hole loading was simulated at both holes by introducing rigid beam elements in the points where the contact area was known and gap elements were employed where the contact zone was undetermined (around the ligament region). This helped determining the active gap elements around the ligament region. Once this was established, the optimisation run was performed employing rigid beam elements only. The use of gap element during the optimisation run would significantly slow down the analysis as every time an element is swapped from composite to insert material, the matrixes would have to be re-assembled and the gap beam checking would have to be repeated until convergence was achieved.

Properties and boundary conditions were the same as for the single hole optimisation of pin-loaded joints. The mesh densities were similar to the ones employed for single hole optimisation. Composite plates are assumed to be pin-jointed to infinitely rigid plates.

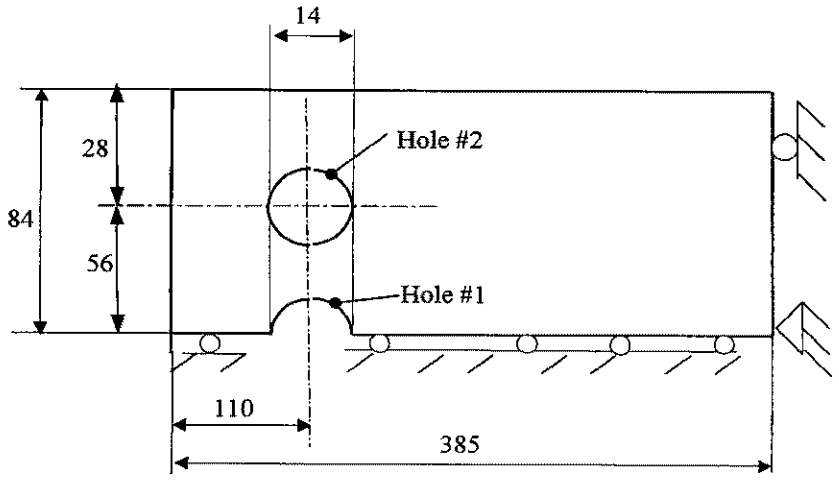

Figure 4.37: Dimensions and boundary conditions for three holes in parallel

The substitution criterion used to achieve the optimum insert shapes for both the series and parallel configurations was the Von Mises stress. Figure 4.38 depicts the optimally shaped inserts for the two holes in series configuration for holes 1 & 2.

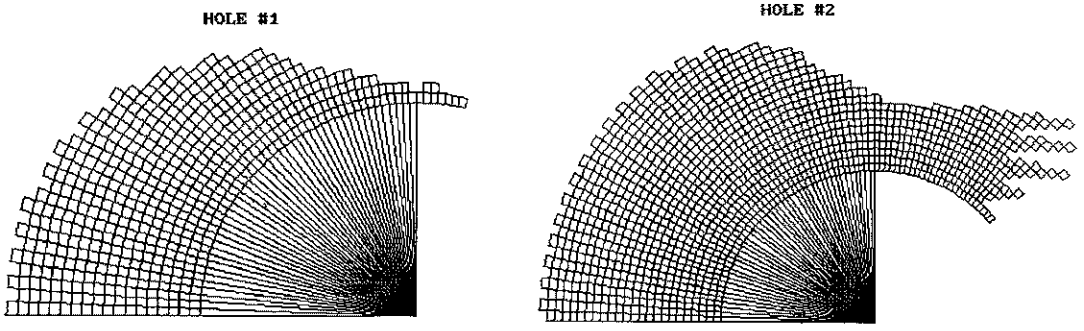

Figure 4.38: Optimally shaped inserts for two holes in series configuration

The optimally shaped inserts at holes 1 & 2; for the three holes in parallel configuration; are shown in Figures 4.39 & 4.40 respectively. Due to symmetry considerations the third hole is equivalent to hole 2.

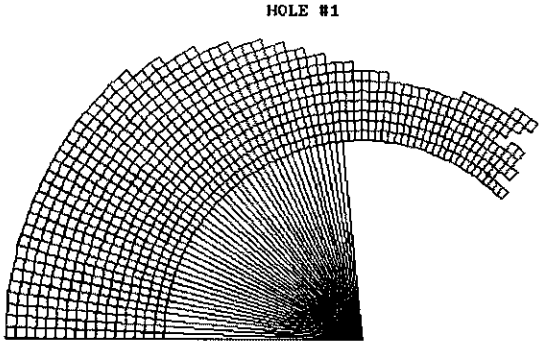

Figure 4.39: Optimally shaped insert for three holes in parallel configuration -Hole #1

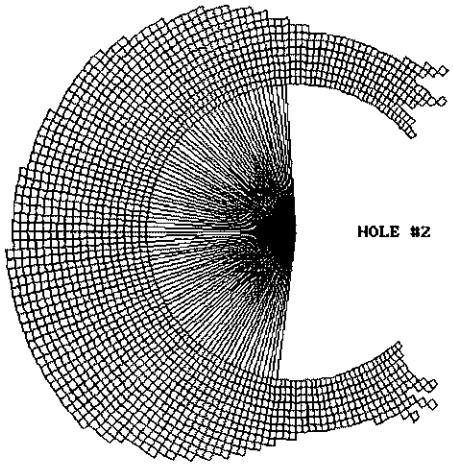

Figure 4.40: Optimally shaped insert for three holes in parallel configuration -Hole #2

The termination criterion in all cases was set to be SR=30%. The termination criterion indicates that the Von Mises stress at the composite/insert interface for both holes will be 30 % of the maximum Von Mises stress in the whole structure.

4.11.1 Results of two holes in series optimisation

The stresses which are most relevant to a bearing induced failure are the radial and Von Mises stresses. A comparison of radial stress distribution for the no-insert and optimum insert configurations at the composite interface of holes # 1 & # 2 is shown in Figure 4.41. The Von Mises stress distribution for both configurations (with and without insert) at the two holes in series is shown in Figure 4.42. The maximum radial and Von Mises stress concentrations occur at 0° for both holes # 1 & # 2. The radial and Von Mises stress concentrations; for the no-insert configuration; are approximately 20 % larger for hole # 2 when compared to hole # 1. The modified EVOLVE method applied to both holes redistributes the load in the joint and yields an equivalent stress concentration at holes # 1 & # 2. Up to 70 % reduction in radial and Von Mises stress concentrations is achieved at the composite/insert interface.

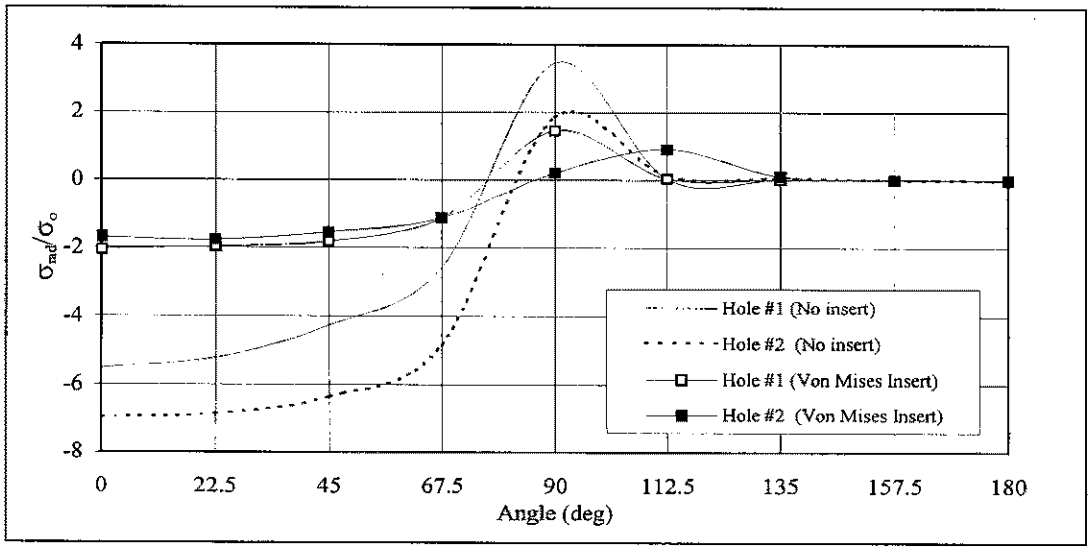

Figure 4.41: Radial stress distributions at interface composite/ insert for holes # 1 & # 2

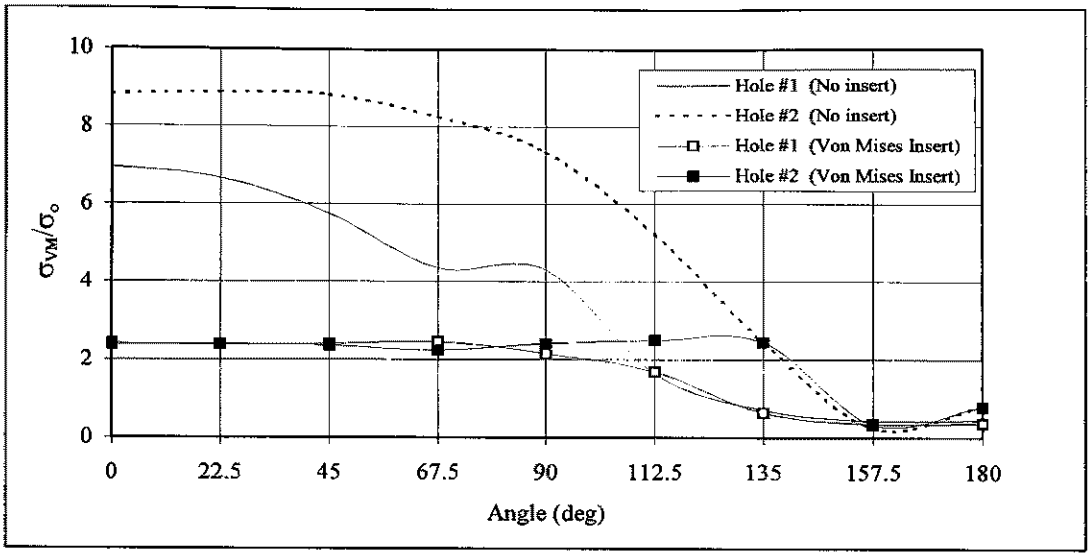

Figure 4.42: Von Mises stress distributions at interface composite/ insert for holes # 1 & # 2

4.11.2 Results of three holes in parallel optimisation

The radial stress distribution for the no-insert and optimum insert configurations at the composite interface of holes # 1 & # 2 is shown in Figure 4.43. The Von Mises stress distribution for both configurations (with and without insert) at the three holes in parallel is shown in Figure 4.44. As for the two holes in series, the maximum radial and Von Mises stress concentrations occur at 0^o for both holes # 1 & # 2. For the three holes in parallel, the magnitudes of radial and Von Mises stress concentrations; for the no-insert configuration; is very similar for holes #1 and # 2. Up to 63 % reduction in radial and Von Mises stress concentrations is achieved at the composite/insert interface of holes # 1 and # 2.

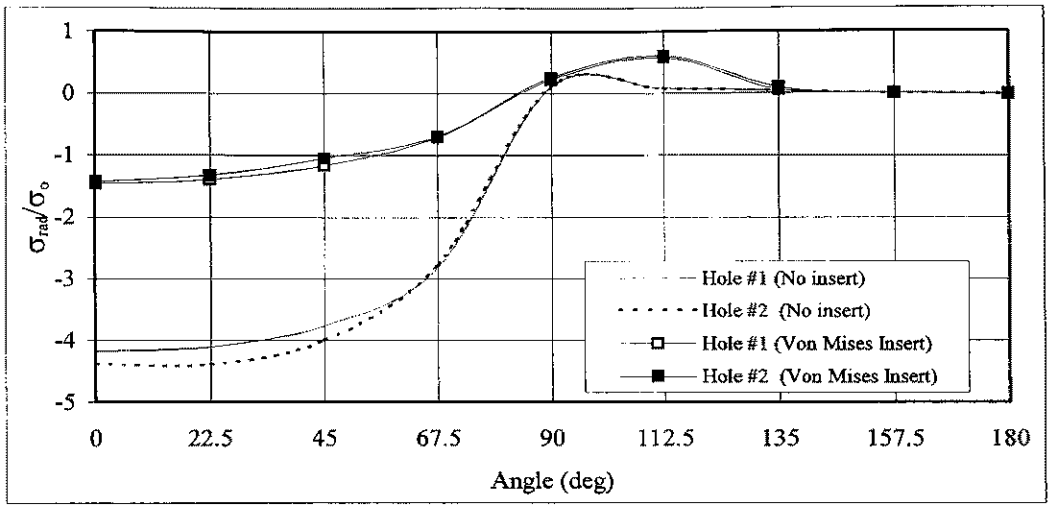

Figure 4.43: Radial stress distributions at interface composite/ insert for holes # 1 & # 2

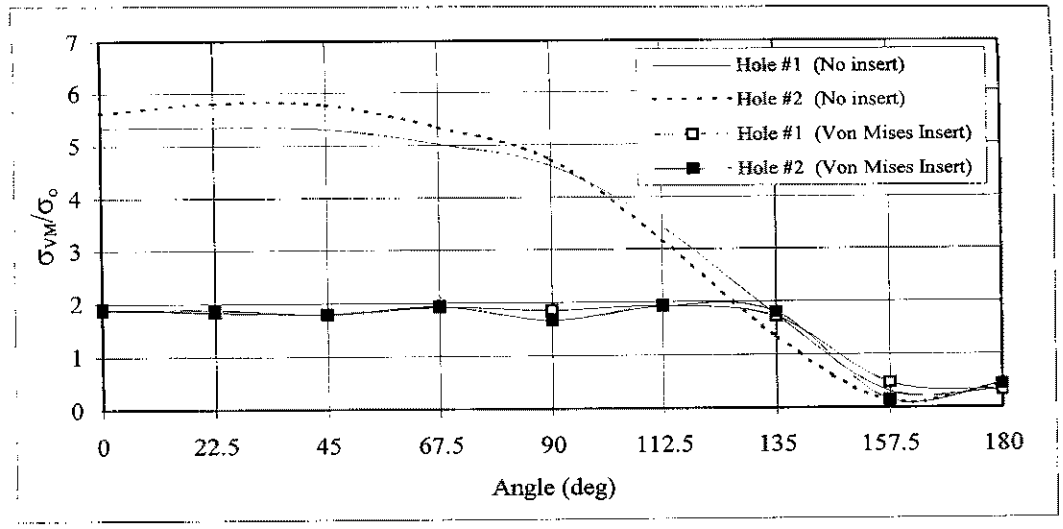

Figure 4.44: Von Mises stress distributions at interface composite/insert for holes # 1 & # 2

Although there is no significant difference between the no-insert configuration stress concentrations of holes # 1 & # 2, the optimum inserts redistribute the stress concentrations more uniformly between the three holes.

4.12 Discussion

Several procedures can presently be employed to improve the strength of composite joints under loaded hole conditions. Most of these procedures are based on the incorporation of extra layers into the laminate in the holed region and although they are successful in improving the strength of the laminate, manufacturing costs are usually greatly increased. This confines such procedures to critical applications such as highly loaded lugs. Other procedures such as the incorporation of 45 deg fibres in the vicinity of the hole or local reinforcement with a stiffer fibre such as boron are also costly. The suggested method of incorporating an optimally shaped insert into a laminate could prove cost effective if such insert could be co-cured within the laminate. Furthermore, the inserts could incorporate a washer from both sides to avoid delamination around pin loaded holes.

The 40 % (w/d=4) to 55 % (w/d=11.5) improvement in the capability of the optimised inserts in reducing the maximum compressive stress at the interface per unit mass of test specimen clearly shows the potential of this procedure.

The effect of the adhesive on the failure mode of specimens was evaluated during the testing program presented in Chapter 7. The experimental results showed no adhesive failure in any of the tests performed with inserts. Furthermore, although the hoop and shear stresses are significant in the ligament region, it is not expected that they will provide debonding of the inserts. The reason for this is that most of the load is transferred in shear and not in tension. This justifies the exclusion of the adhesive from the optimisation process.

The work presented in this Chapter shows that the optimisation procedure proposed could be successfully applied to both multiple load cases and on multiple holes. In fact, multiple optimisation criterion where more than one substitution criterion is employed, could also be performed following the same concept.

4.13 References

[1] Hart-Smith, L. J., "Joints", Engineered Materials Handbook on Composites, *ASM International*, Vol. 11., pp 479-494.

[2] Matthews, F.L (editor), "Joining Fibre Reinforced Plastics", *Elsevier Applied Science*, Essex, 1987.

[3] Herrington, P. D., Sabbaghian, M., "Effect of radial clearance between bolt and washer on the bearing strength of composite bolted joints", *Journal of Composite Materials,* Vol. 26, No. 12, pp. 1826-1843, 1992.

[4] Collings, T. A., "The strength of Bolted Joints in Multi-Directional CFRP Laminates," *Composites*, Vol. 8, No. 1, pp. 43-55, January 1977.

[5] Eisenmann, J. R., Leonhardt, J. L., "Improving Composite Bolted Joint Efficiency by Laminate Tailoring", Joining of Composite Materials, *ASTM STP-749*, K.T. Edward, Ed., American Society for Testing and Materials, pp. 117-130, 1981.

[6] Crothers, P.J., Drechsler, K., Feltin, D., Herszberg, I., Bannister, M., " The Design and Application of Tailored Fibre Placement", *Proceedings of ICCM11*, Gold Coast, Australia, Vol. 1, pp 600-610, 14^{th}-18^{th} July 1997.

[7] Wang, J. T., Lotts, C. G., Davis, D. D. Jr., "Analysis of Bolt-Loaded Elliptical Holes in Laminated Composite Joints", *Journal of Reinforced Plastics and Composites*, Vol. 12, pp 128-138, February 1993.

[8] Nilsson, S., "Increasing Strength of Graphite/Epoxy Bolted Joints by Introducing an Adhesively Bonded Metallic Insert", *Journal of Composite Materials*, Vol. 2, pp. 642-650, 1989.

[9] Herrera-Franco, P. J., Cloud, G. L., " Strain-Relief for Composite Fasteners-An Experimental Study", *Journal of Composite Materials*, Vol. 26, pp. 751-768, 1992.

[10] Rispler, A. R., Steven, G. P.," Shape optimisation of Metallic Inserts in Composite Bolted Joints ", *Proceedings of PICAST 2-AAC 6*, Vol. 1, pp 225-229, Melbourne, March 20-23, 1995.

[11] Mirabella L., Galea, S. C., " An Experimental Investigation into the use of Inserts to enhance the static performance of thin composite bolted lap joints", *Proceedings of ICCM-11*, Vol. 6, pp 148-157, Gold Coast, Australia, July 14-18, 1997.

[12] Chen, W. H., Lee S. S., Yeh, J. T., "Three dimensional contact stress analysis of a composite laminate with bolted joint", *Composite Structures* Vol. 30, 1995.

[13] Camanho, P. P, Matthews, F. L., " Finite element analysis of mechanically fastened joints in CFRP", *Proceedings of ICCM-11*, Vol. 6, pp 139-147, Gold Coast, Australia, July 14-18, 1997.

[14] Arnold, W. S., Marshall, I. H., Wood, J., " Optimum design considerations for mechanically fastened composite joints", *Composite Structures*, Vol. 16, p85-101, 1990

[15] Hart-Smith, L. J., "*Mechanically-fastened joints for advanced composites-Phenomenological considerations and simple analyses*", Douglas Aircraft Company Paper DP6748A, November 1978.

[16] Hart-Smith, L. J., "*Bolted joints in graphite-epoxy composites*", Douglas Aircraft Company, NASA Langley Report CR-144899, NASA, Washington DC, USA, January 1977.

[17] Whitney, J. M., Niusmer, R. J., "Stress Fracture Criteria for Laminated Composites Containing Stress Concentrations", *Journal of Composite Materials*, Vol. 8, pp 253-265, 1974.

[18] Niusmer, R. J., Labor, J. D., "Applications of the Average Stress Failure Criterion: Part II- Compression", *Journal of Composite Materials*, Vol. 13, pp 49-61, January 1979.

[19] Chang, F. K., " The Effect of Pin Load Distribution on the Strength of Pin Loaded Holes in Laminated Composites", *Journal of Composite Materials*, Vol. 20, pp 401-408, July 1986.

[20] Chang, F. K., Scott, R. A., Springer, G. S., "Failure of Composite Laminates Containing Pin Loaded Holes- Method of Solution", *Journal of Composite Materials*, Vol. 18, pp 255-278, May 1984.

[21] Chang, F. K., Scott, R. A., Springer, G. S., "Design of Composite Laminates Containing Pin Loaded Holes", *Journal of Composite Materials*, Vol. 18, pp 279-289, May 1984.

[22] Yamada, S. E., Sun, C. T., " Analysis of Laminate Strength and Its Distribution", *Journal of Composite Materials*, Vol. 12, pp 275-285, July 1978.

[23] Chang, F. K., Scott, R. A., Springer, G. S., "*Strength of Mechanically Fastened Composite Joints*", Air Force Wright Aeronautical Laboratories, Technical Report AFWAL-TR-82-4095, June 1982.

[24] Pagano, N. J., Pipes, R. B., "The Influence of Stacking Sequence on Laminate Strength", *Journal of Composite Materials*, pp. 50-57, 1971.

[25] Quinn, W. J., Mathews, F. L., "The Effect of Stacking Sequence on the Pin-Bearing Strength in Glass Fibre Reinforced Plastics", *Journal of Composite Materials*, Vol. 11, pp. 139-145, 1977.

[26] Xie, Y. M, Steven, G. P., "A simple evolutionary procedure for structural optimisation", *Computational Structures*, Vol. 49,NO 5, pp. 885-896,1994.

[27] Xie, Y. M, Steven, G. P., "Optimal design of multiple load case structures using an evolutionary procedure", *Engineering Computations*, Vol. 11, 1994.

[28] Tsujimoto, Y., Wilson, D., " *Elastoplastic Failure Analysis of Composite Bolted Joints*", Centre For Composite Materials, Univ. of Delaware, CCM-85-09.

[29] Oplinger, D. W., *Proceedings of the 4th Conference On Fibrous Composites in Structural Design*, Plenum Press, NY, USA, 1980.

[30] Bickley, W. G., "*The Distribution of Stress Around a Circular Hole in a Plate*", Royal Society of London, Vol. 227 A., pp. 383-415, July, 1928.

[31] Gould, H. H., Mikic, B. B., "*Areas of Contact and Pressured Distribution in Bolted Joints*", NASA CR 102866, N70-41982, June, 1970.

[32] Waszczak, J. P., Cruse, T. A., "Failure Mode and Strength Prediction of anisotropic Bolt Bearing Specimens", *Journal of Composite Materials*, Vol. 5, pp. 421-425, 1971.

[33] Oplinger, D. W., Gandhi, K. R., "Analysis Studies of Structural Performance in Mechanically Fastened Orthotropic Laminates", *Proceedings of 2nd Conference on Fibres, Composites and Flight Vehicle Design*, AFFDL-TR-74-103, pp. 811-842, September, 1974.

[34] Ojalvo, L., "Survey of Mechanically Fastened Splice Joint Analyses", *Fourth Army Materials Technology Conference*, 1975.

[35] De Jong, T., "Stresses Around Pin Loaded Holes in Elastically Orthotropic or Isotropic Plates", *Journal of Composite Materials*, Vol. 11, pp. 313-331, July, 1977.

[36] Xiong, Y., "An Analytical Method for Failure Prediction of Multi-Fastener Composite Joints", *International Journal of Solids and Structures*, Vol. 33, pp. 4395-4409, 1996.

[37] Lekhnitskii, S. G., "*Theory of elasticity of an anisotropic body*", Mir Publishers, Moscow, USSR, 1981.

[38] Agarwal, B. D., Broutman, L. J., "Analysis and Performance of Fiber Composites", Wiley, NY, USA, 1980.

[39] Jones, R. M., "Mechanics of Composite Materials", Scripta Book Co., Washington DC, USA, 1975.

[40] De Jong, T., Vuil, H. A., Report LR-333, Aerospace Department, Delft University of Technology, The Netherlands, 1981.

[41] Hyer, M. W., Klang, E. C., VPI-E-84-17 (CCMS-84-02), Virginia Polytechnic Institute and State University, Blacksburg, Virginia, USA, 1984.

[42] Agarwal, B. L, "Static Strength Prediction of Bolted Joint in Composite Material", *AIAA Journal*, Vol. 18, NO. 11, pp 1371-1375, November, 1980.

CHAPTER 5

TEST PANEL PREPARATION OF PIN LOADED JOINTS

5.1 Introduction

This chapter details the manufacturing process employed for the production of flat composite panels, with different geometry cut-outs, for the two batches of specimens tested as described in Chapter 4. Different cutting techniques were investigated to produce the cut-outs with different shapes. Water jet cutting was chosen due to both tolerance requirements and surface finish. The aluminium inserts required were manufactured by wire cutting. This allowed for a closer tolerance and the production of 6 inserts in a single wire cut operation by stacking 6 aluminium plates which were pre-welded at the edges. The size of the composite panels employed for the first batch of specimens was different to that used for the second batch of specimens due to different width over diameter ratios (w/d) and edge distance over diameter ratios (e/d) being required. Furthermore the testing configuration of the first batch of specimens required the use of tabs for attaching the specimen to the test rig whereas the second batch of specimens were bolted to two end steel plates to attach them to the Instron Testing Machine.

5.2 Panel Geometry

The first batch panels were manufactured with an overall dimension of 160 x 40 mm. The w/d employed for the first batch of specimens was 4 while the e/d ratio used was 2.5. The hole loaded by the pin was of 10 mm in diameter. To ensure no slippage of specimens during testing, glass fibre tabs were employed. The tabs were tapered with an approximate angle of 10^{o}. The overall length of the tabs was 72 mm. Photographs of a side view of the tab arrangement and the different geometry cut-outs are shown in Figure 5.1. Four different configurations were manufactured. The smallest circular cut-out shown in Figure 5.1 is 10 mm in diameter and does not carry a metallic insert. The remaining

configurations carry different shape inserts as derived in Chapter 4. All inner diameters of the remaining inserts were 10 mm. The test specimens with their bonded metallic inserts and ply direction reference are shown in Figure 5.2. Details regarding panel lay-up and cure cycles employed are discussed in Section 5.3.

The dimensions for the second batch panels were 385 x 160 mm. The w/d employed for this batch was 11.43 while the e/d ratio was 7.86. The hole loaded by the pin in this case was of 14 mm in diameter. To attach the test specimens to the test rig, 2 rows of 10 mm diameter holes (9 in total) were drilled on the specimens at locations matching an existing test rig. Three different configurations were manufactured. The sizes and shapes of the metallic inserts were different to the ones employed for the first batch of specimens. One of the cut-outs was 14 mm in diameter and carried no metallic inserts. Another circular cut-out of 22.6 mm in diameter was water jet cut and a metallic insert of 14 mm inner diameter was bonded to the cut-out. The third configuration carried what is described as Von Mises insert in Chapter 4. A schematic drawing showing overall dimensions, hole positions and ply direction reference is shown in Figure 5.3.

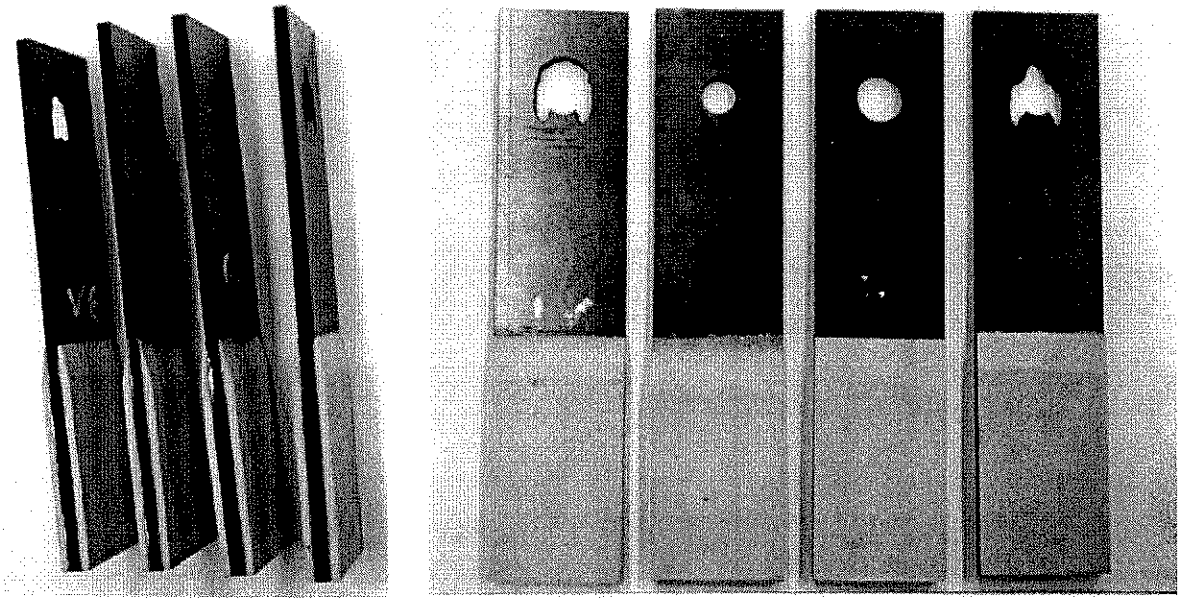

Figure 5.1: Tabs and cut-outs geometry's

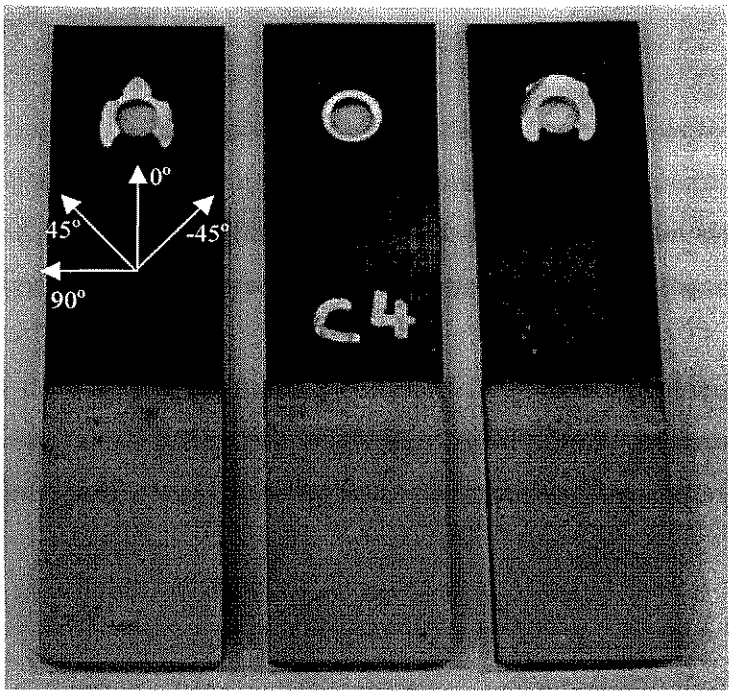

Figure 5.2: Test specimens with different insert shapes

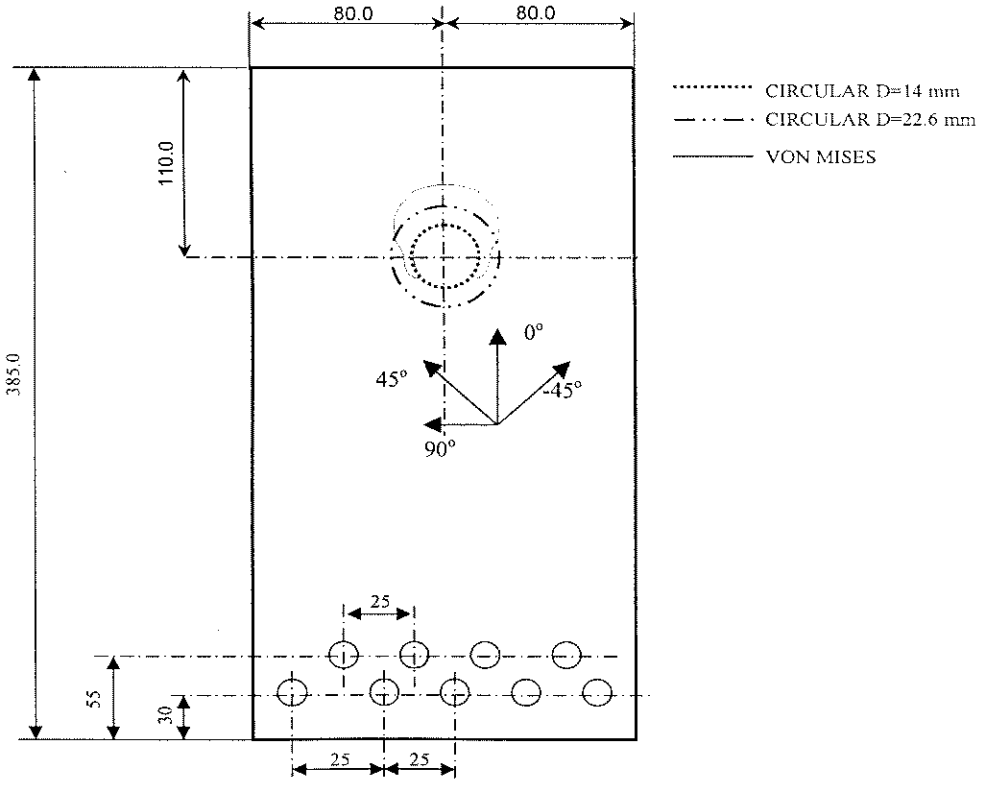

Figure 5.3: Schematic of 2nd batch specimens

5.3 Lay-Up, Materials and Cure Cycles

Two types of unidirectional pre-impregnated tapes (prepreg) were employed for the different batches manufactured. The first batch of specimens was manufactured from Hy-E 3034K – Thornel T-300 (12K) fibres in Fiberite 934 epoxy resin with a 177° C cure temperature. The cure cycle employed for this material is shown in Figure 5.4.

The second batch of specimens was manufactured from T5A145-F584 – Hercules IM6 (12K) fibres in Hexcel F584 epoxy resin (uni-directional prepreg tape) with a 177 °C cure temperature. The base cure cycle used for these specimens is shown in Figure 5.5.

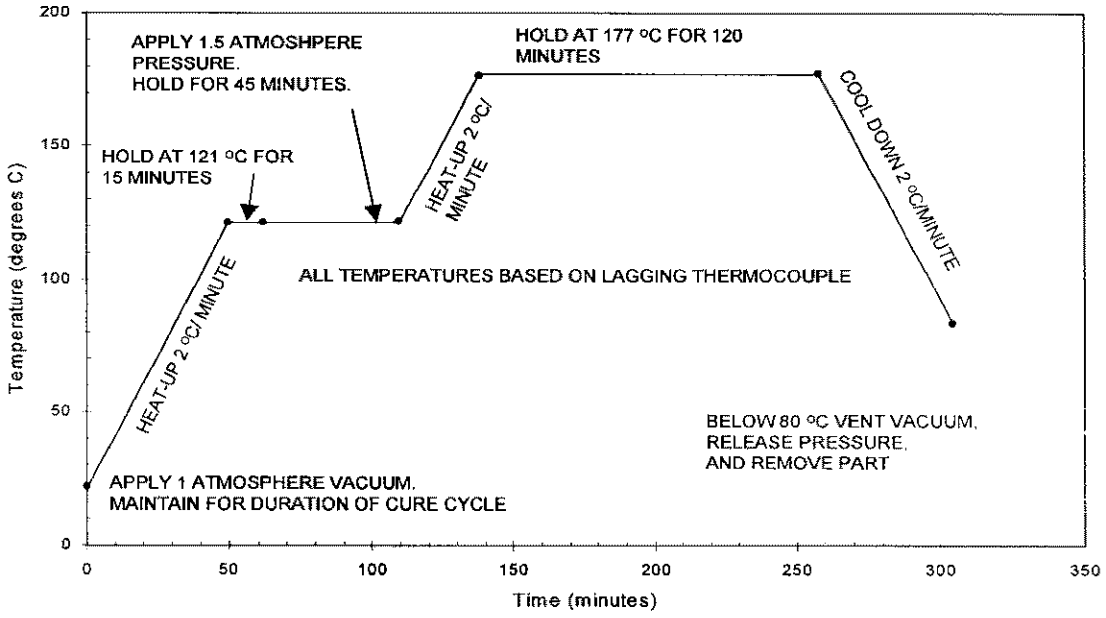

Figure 5.4: 177 °C Cure Cycle for Hy-E3034K – Thornel T300/Fiberite 934 Prepreg

The following parameters were modified on the base cure cycle to cater for the specimen thickness.

a) Vacuum debulk (0.8 atmosphere) every 10 plies.
b) The pressure specified for thick laminates is 5.8 atmoshpere.

c) Dwell at 65 °C for 1 hour.

d) Dwell at 120 °C for 2 hours.

e) Dwell at 135 °C for 1 hour.

f) Dwell at 150 °C for 1 hour.

g) Cure and complete cycle as shown in base cure cycle.

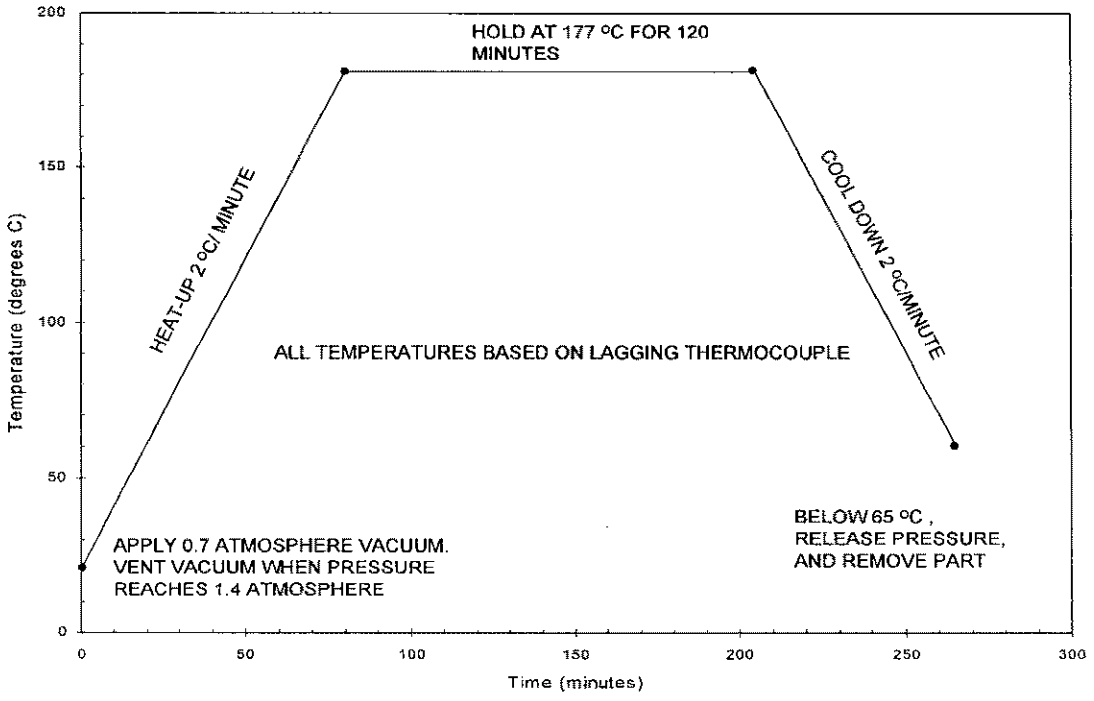

Figure 5.5: 177 °C Cure Cycle for T5A145-F584 – Hercules IM6/Hexcel F584 Prepreg.

5.4 General fabrication procedures

The ply lay-up for both batches of specimens consisted of 24 plies and is detailed below:

$$[90/0/90/0/-45_2/+45_2/90/0/-45/+45]_S$$

A metal caul plate was employed in all specimens to keep the panel thickness constant. For the first batch of specimens, panels of overall dimensions of 500 x 360 mm were cured and then cut to specimen size by means of a diamond saw. The edges were then ground to ensure they were parallel to each other. Water was employed during the grinding process for cooling purposes and to protect the grinding wheel.

The second batch of specimens was cured as panels of overall dimensions of 510 x 400 mm and cut into specimen size using water jet cutting technology.

The use of laser-beam cutting was considered but found to be unacceptable for panel thicknesses of approximately 4 mm and above [1]. Instead water jet cutting was chosen for producing all cut-outs. The main advantage of water jet cutting is that no additional operation is required to achieve a smooth finish at the edges. The rule of thumb which needs to be followed when employing this technology is that the quality of cut improves with increasing nozzle pressure, increasing nozzle orifice diameter, decreasing transverse speed, and decreasing material thickness and hardness [2]. The water jet cutting process consists in water moving through a nozzle; which contains a sapphire orifice; and exiting as a coherent cutting stream. The diameter of the cutting stream ranges between 0.08 and 0.3 mm. Sapphire is used for the nozzle due to its good erosion resistant properties.

Various alternatives were available to manufacture the metallic inserts. CNC machining was considered but found to be very time consuming and difficult to perform due to the required tolerances and the size of the inserts. Casting could become a good alternative if a very large quantity were to be manufactured. Extrusion of the desired shapes could also prove to be a cheap and efficient alternative of producing a large quantity of inserts. The chosen alternative was to have the metallic inserts wire cut. Although a relatively expensive alternative, a very good part was obtained with the desired tolerance in a small time frame and without the need to invest a large amount of capital. Furthermore, stacking the desired number of aluminium plates in order to obtain the same number of inserts reduced the cost. This resulted in one wire cut operation yielding six inserts of the particular shape. The three different shapes of inserts analysed for the first batch of specimens tested can be seen in Figure 5.6. The inner diameter of these inserts

was 10 mm. These inserts were made out of non-aircraft quality aluminium. The weights of the different inserts were dissimilar.

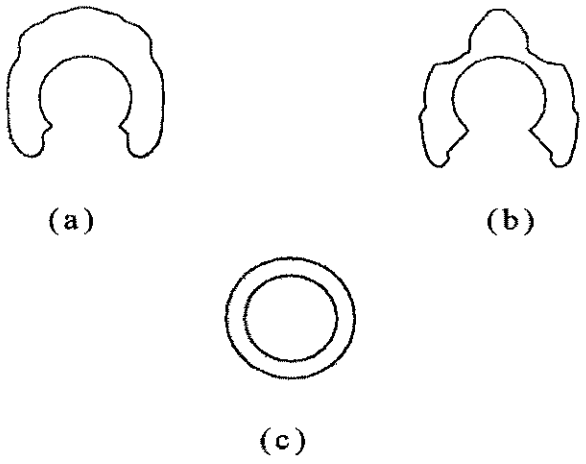

Figure 5.6: Von Mises insert (a), Global insert (b) and 2mm Circular insert (c)

Two different shapes of inserts were analysed and manufactured for the second batch of specimens. The inserts were made out of Aluminium 2024-T3. The different shapes are depicted in Figure 5.7. The inner diameter for these inserts was 14 mm. The outer diameter of the circular insert employed for the second batch of specimens was calculated using an average weight of the wire cut optimised inserts to ensure both the optimum and circular inserts would have the exact same weight. This allows for a direct comparison without the need to normalise the results with respect to the weight of the inserts.

The shapes of all inserts were obtained by producing a DXF (drawing exchange format) file from the final FEA solution. The coordinates of the points forming the contours were then joined as splines and divided in arcs and lines using a CAD package. The DXF files were used by the numerically controlled wire cutting machine to manufacture the inserts.

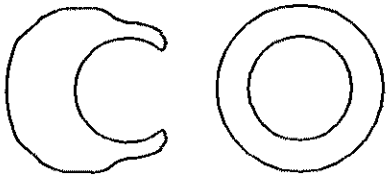

Figure 5.7: Von Mises insert (left), 4.2mm Circular insert (right)

All aluminium inserts were adhesively bonded to the composite panels with HYSOL EA9330.3; an adhesive that possesses high peel and shear strength.

5.5 References

[1] Falzon, B. G, "*An investigation into the buckling and postbuckling behaviour of hat-stiffened composite panels*", PhD Thesis, December, 1995.

[2] Schwartz, M. M., *Composite Materials Handbook*, McGraw-Hill Book Company.

CHAPTER 6

EXPERIMENTAL PROCEDURE (PIN-LOADED JOINTS)

6.1 Introduction

This chapter details the methodology employed for the testing of pin-loaded specimens with different w/d (width/diameter) ratios. Resistive strain gauges were employed to measure strains at various locations on the test specimens. The data acquisition system consisted in Labview Software coupled to a SCXI 4 Channel Isolation Amplifier with excitation. The readings obtained were then stored and processed on a personal computer. The set-up employed for the second batch of specimens did not employ any strain gauging. Instead, the photostress method was used to acquire full strain fields at insert / composite interface. The test fixture for the photoelastic testing was different to that employed for the other specimens. The reason for this was that the photostress method requires shining light onto the surface of the specimens (coated region). This required the use of 2 specimens per test, loaded through the inside with two steel plates and a pin.

6.2 Test fixtures

Test fixtures were designed and built for all w/d ratios. The test fixtures had the appropriate stiffness to ensure deflections of fixtures under expected loads would be negligible when compared to specimen displacements. The fixture employed for testing first batch specimens consisted in two rectangular plates of 140 x 60 x 6 mm steel plates with two holes of 20 and 10 mm diameter. An integrated washer of 22 mm in diameter was machined into the steel plates to ensure lateral constraint would be confined to an optimum area of 2.2 D [1]. A pin of 10 mm diameter was employed on the specimen side to load the composite specimens while a second pin of 20 mm diameter connected the two steel plates to the Instron machine fitting as shown in Figure 6.8.

The test fixture manufactured for the second batch of specimens consisted of two steel plates of 200 x 180 x 4.5 mm with two holes of 20 and 14 mm diameter holes. The integrated washer on this test fixture had a diameter of 30.8 mm to ensure a 2.2 D ratio was maintained for better clamping conditions [1] in case a bolted configuration was desired. A pin of 14 mm diameter was employed to load the composite specimens. The other side of the loading plates were loaded through a 20 mm pin. A schematic of the test set-up and a photograph showing the arrangement of loading plates and photoelastic equipment is shown in Figures 6.9 & 6.10 respectively.

6.3 Strain gauges specifications and installation

Strain gauges are commonly used in mechanical testing and measurements. The type of strain gauge used for the tests performed in this thesis is the bonded-resistance strain gauge, which consists of a grid of very fine foil or wire. The electrical resistance of the grid varies linearly with the strain applied to the device. The strain is measured as a change in resistance. Because strain measurements require detecting relatively small changes in resistance, the Wheatstone bridge circuit is generally used. The Wheatstone bridge circuit consists of four resistive elements with a voltage excitation supply applied to the ends of the bridge. Strain gauges can occupy one, two, or four arms of the bridge, with any remaining positions filled with fixed resistors. Figure 6.1 shows a configuration with a half-bridge strain gauge consisting of two strain elements, R_{G1} and R_{G2}, combined with two fixed resistors, R_1 and R_2 [2].

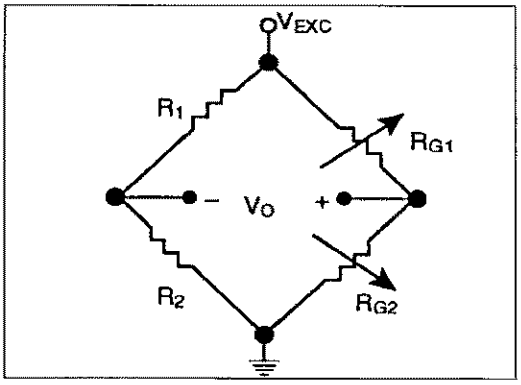

Figure 6.1: Half-Bridge Strain Gauge Configuration [2]

With a voltage, V_{EXC}, powering the bridge, the data acquisition system measures the voltage across the bridge:

$$V_O = \left(\frac{R_{G2}}{R_{G1} + R_{G2}} - \frac{R_2}{R_1 + R_2} \right) \times V_{EXC} \tag{6.1}$$

When the ratio of R_{G1} to R_{G2} equals the ratio of R_1 to R_2, the measured voltage V_O is 0 V. This condition is referred to as a *balanced bridge.* As strain is applied to the gauges, their resistance values change, causing a change in the voltage at V_O. Full-bridge and half-bridge strain gauges are designed for maximum sensitivity by arranging the strain gauge elements in opposing directions [2]. For example, the half-bridge strain gauge in Figure 6.1 includes an element R_{G1}, which is installed so that its resistance increases with positive strain, and an element R_{G2}, whose resistance decreases with positive strain. The resulting V_O responds with a sensitivity that is twice that of a quarter-bridge configuration.

Some signal conditioning products have voltage excitation sources, as well as provisions for bridge-completion resistors. Bridge completion resistors should be very precise and stable. Because strain-gauge bridges are commonly slightly unbalanced, some signal conditioners provide for null offsets, a process in which once can adjust the resistance ratio of the unstrained bridge to balance the bridge and remove any initial DC offset voltage. Alternatively, this offset voltage can be measured and used in a compensation routine.

The gauges used in the testing of all pin-loaded joints were TML Strain Gauges manufactured by Tokyo Sokki Kenkyujo Co. Ltd. The nominal gauge type was a Copper-Nickel foil gauges of length 2 and 5 mm mounted on an epoxy base with a coefficient of thermal expansion of $11 \times 10^{-6}/^{\circ}C$. Foil gauges were used because of their superior quality over wire gauges. The nominal resistance and gauge factor for this type of gauge were $120 \pm 0.3\,\Omega$ and 2.14 respectively. Tests were carried out under ambient temperature conditions (20 °C) to minimise temperature effects on the gauge resistance.

Back-to-back strain gauges were used to measure bending and far field surface strains on the w/d=4 specimens.

6.4 Photoelastic Technique

Full-field strains around the loaded region were quantitatively and qualitatively assessed by the Photostress Method. PhotoStress is a full-field technique for accurately measuring surface strains to determine the stresses in a part or structure during static or dynamic testing. This method is known in the literature as the birefringent coating method.

Firstly, a special strain-sensitive plastic coating is bonded to the test part. The adhesive used for bonding the coating onto the part contains aluminium powder in order to obtain high reflectivity. For plane surfaces, pre-manufactured flat sheets are recommended due to their constant thickness and also because they can be cut to size and bonded directly to the test part.

Secondly, as test or service loads are applied to the part, the coating is illuminated by polarised light from a reflection polariscope. When viewed through the polariscope, the coating displays the strains in a colorful, informative pattern which reveals the overall strain distribution and pinpoints highly strained areas. With an optical transducer (compensator) attached to the polariscope, quantitative stress analysis can be performed. Permanent records of the overall strain distribution can be made by photography or by video recording. This technique is ideal to accurately measure peak stresses and determine stress concentrations around holes and also at interfaces between inserts and composite materials.

6.4.1 Fundamentals of polarised light

Luminous rays are electromagnetic vibrations similar to radio waves. An incandescent source emits radiant energy which propagates in all directions and contains a whole spectrum of vibrations of different wavelengths (frequencies). A portion of this

spectrum, wavelengths between 400 and 800 nm, is useful within the limits of human perception.

The vibration associated with light is perpendicular to the direction of propagation. A light source emits a train of waves which contain vibrations in all perpendicular planes. However, by the introduction of a polarising filter P (Figure 6.2), only one component of these vibrations will be transmitted (that which is parallel to the privileged axis of the filter). Such an organised beam is called polarised light. If another polarising filter *A* is placed in its way, complete extinction of the beam can be obtained when the axes of the two filters are perpendicular to one another.

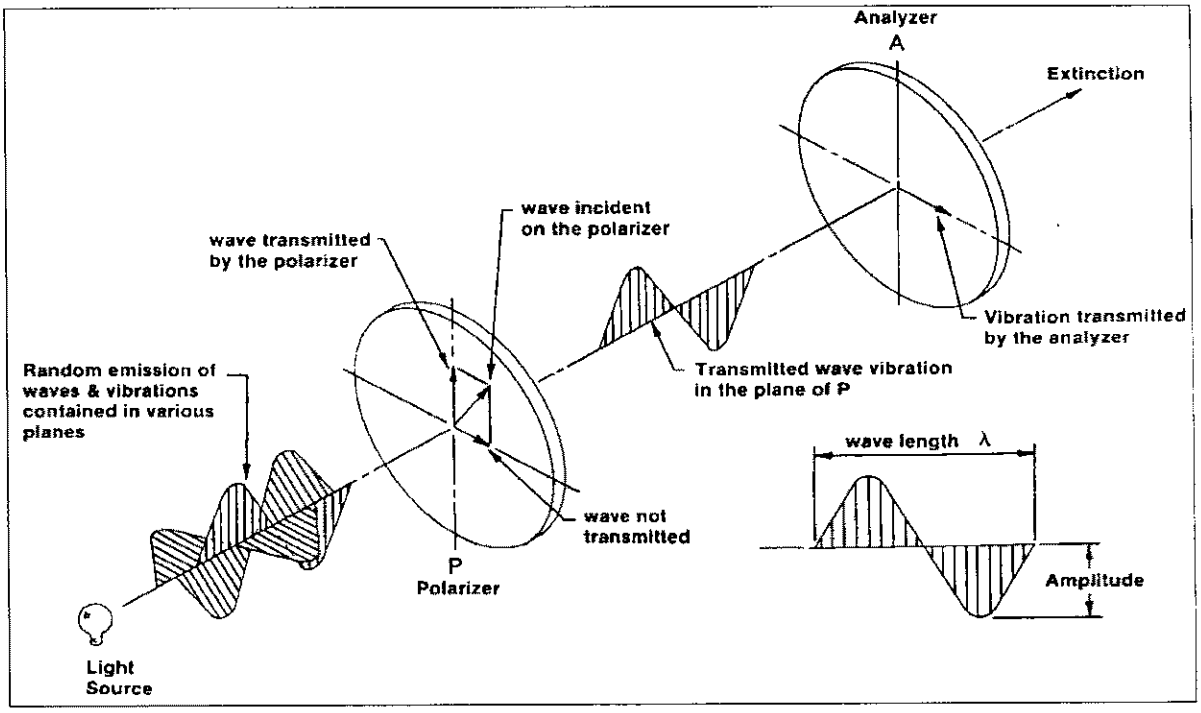

Figure 6.2: Polarisation of light [4]

Light propagates in a vacuum or in air at a speed *C* of 3 x 10^{10} cm/ sec. In other transparent bodies, the speed *V* is lower and the ratio *C/ V* is called the index of refraction. This index is constant in a homogeneous body regardless of the direction of propagation or

plane of vibration. However, in crystals the index depends upon the orientation of vibration with respect to index axis. The change in index of refraction is a function of the resulting strain.

When a polarised beam *a* propagates through a transparent plastic of thickness *t*, where X and Y are the directions of principal strains at the point under consideration, the light vector splits and two polarised beams are propagated in planes X and Y (see Figure 6.3). If the strain intensity along X and Y is ε_x and ε_y, and the speed of the light vibrating in these directions is V_x and V_y, respectively, the time necessary to cross the plate for each of them will be t / V, and the relative retardation between these two beams is:

$$\delta = C\left(\frac{t}{V_x} - \frac{t}{V_y}\right) = t(n_x - n_y) \qquad \textbf{(6.2)}$$

where: n = index of refraction

Brewster's law established that: "The relative change in index of refraction is proportional to the difference of principal strains", or:

$$(n_x - n_y) = K(\varepsilon_x - \varepsilon_y) \qquad \textbf{(6.3)}$$

The constant K is called the "strain-optical coefficient" and characterises a physical property of the material. It is a dimensionless constant usually established by calibration or given by the manufacturer in the case of pre-manufactured flat sheets. Combining the expressions above, we have:

$$\delta = tK(\varepsilon_x - \varepsilon_y) \qquad \text{in transmission} \qquad \textbf{(6.4)}$$

$$\delta = 2tK(\varepsilon_x - \varepsilon_y) \qquad \text{in reflection} \qquad \textbf{(6.5)}$$

(light passes through the plastic twice)

Consequently, the basic relation for strain measurement using the birefringent coating technique is:

$$(\varepsilon_x - \varepsilon_y) = \frac{\delta}{2tK} \tag{6.6}$$

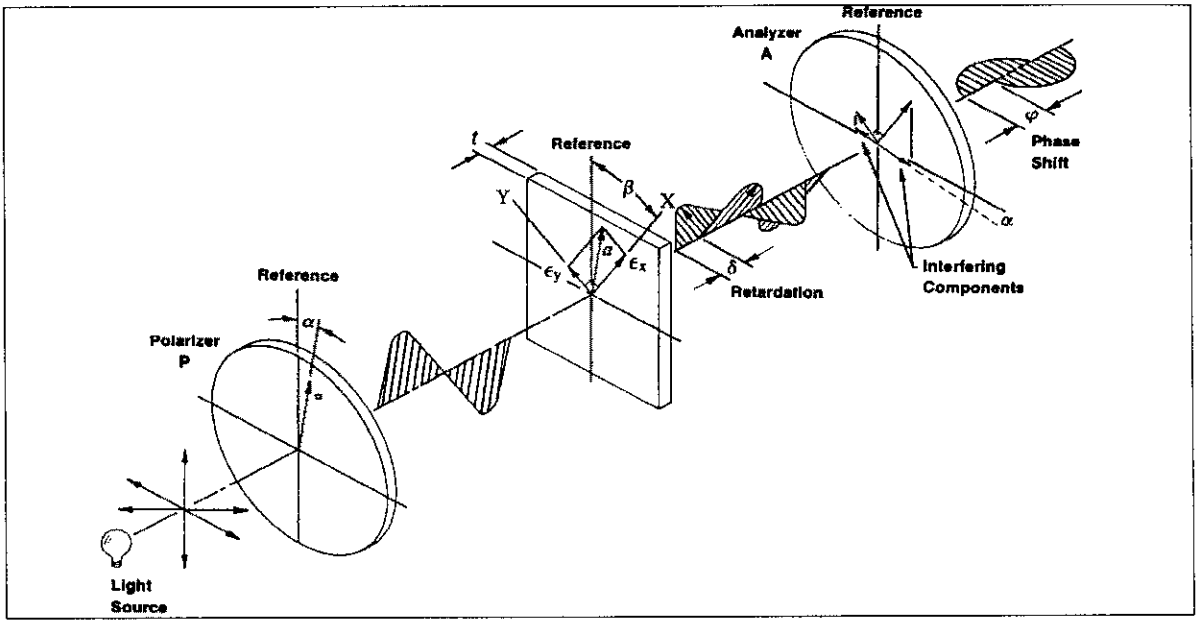

Figure 6.3: Plane polariscope [4]

Due to the relative retardation δ, the two waves are no longer in phase when emerging from the plastic. The analyser A will transmit only one component of each of these waves (that parallel to A) as shown in Figure 6.3. These waves will interfere and the resulting light intensity will be a function of both δ and of the angle between analyser and principal strain direction $(\beta - \alpha)$.

In the case of a plane polariscope, the intensity of light emerging will be:

$$I = a^2 \sin^2 2(\beta - \alpha) \sin^2 \frac{\pi\delta}{\lambda} \tag{6.7}$$

The light intensity becomes zero when $(\beta-\alpha)=0$, or when the crossed polariser/analyser is parallel to the direction of principal strains. Thus, a plane polariscope set-up is used to measure the principal strain directions.

Adding optical filters known as quarter-wave plates in the path of light propagation produces circularly polarised light, and the image observed is not influenced by the direction of principal strains. The intensity of emerging light thus becomes:

$$I = a^2 \sin^2 \sin^2 \frac{\pi\delta}{\lambda} \tag{6.8}$$

In a circular polariscope, the light intensity becomes zero when $\delta = 0$, $\delta = 1$k., $\delta=2$k...., or in general:

$$\delta = N\lambda \tag{6.9}$$

where N is 1, 2, 3, etc.

This number N is also called fringe order and expresses the size of δ. The wavelength corresponding to white light is:

$$\lambda = 575\ nm \tag{6.10}$$

The retardation is then simply described by N.

Once $\delta = N\lambda$ is known, the principal strain difference is obtained by:

$$(\varepsilon_x - \varepsilon_y) = \frac{\delta}{2tK} = N\frac{\lambda}{2tK} = Nf \tag{6.11}$$

where the *fringe value, f,* contains all constants, and N is the result of measurements.

For more comprehensive reading on the topic of polarised light the following references will be found useful [3, 4 and 5].

6.4.2 Birefringent coating method: Equipment set-up

The birefringent coating method requires the use of a reflection polariscope to observe and measure the surface strains on the photoelastically coated specimen. The 030 Series Modular System (Figure 6.4) from the Measurements Group (Vishay) was employed for all photoelastic measurements. The telemicroscope seen in the photograph was not available (optional accessory). For a complete description and specifications of the 030 Series Modular System refer to the manufacturer's Bulletin S-134.

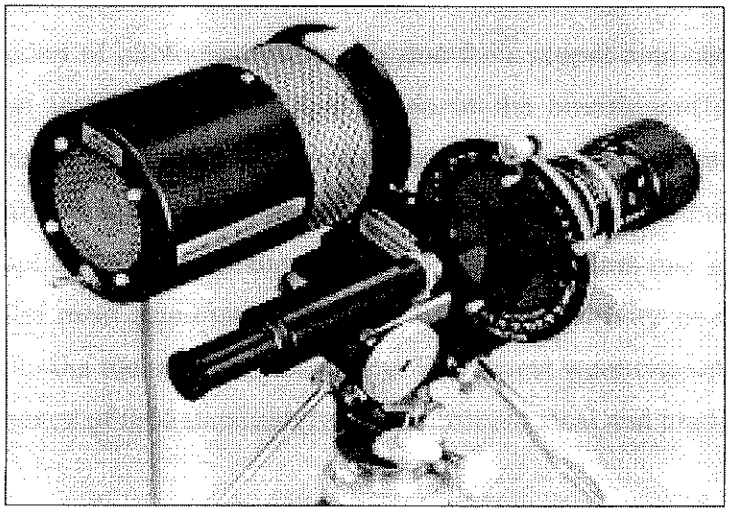

Figure 6.4: 030 Series Modular Reflection Polariscope (with optional telemicroscope)

A schematic showing the set-up for measuring statically loaded specimens is depicted in Figure 6.5.

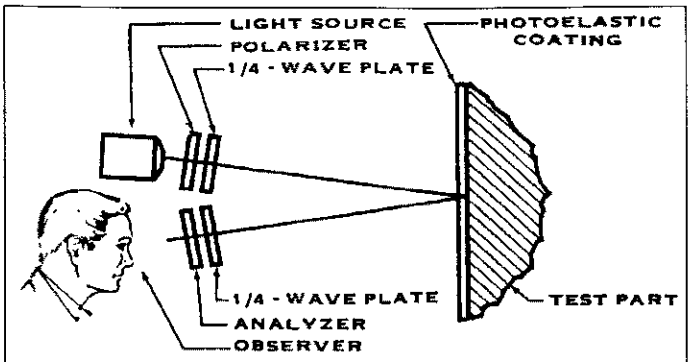

Fig. 5 — Schematic representation of reflection polariscope.

Figure 6.5: Schematic of measurement using a reflection polariscope [4]

6.4.3 Selection of photoelastic coatings

The selection of photoelastic coatings and their proper application to the specimens are fundamental to the successful application of the birefringent coating method. The coatings are carefully controlled formulations of resins blended to provide known and repeatable photoelastic properties. A systematic procedure was followed in order to select the most appropiate coating for the analysis of strain patterns and magnitudes close to a loaded hole. The most important parameter was the sensitivity of the coating as this is closely related to the measurement accuracy. Flat sheets were chosen due to their uniform thickness (tolerance of 0.06 mm) and their uniform physical and photoelastic properties.

6.4.3.1 Determination of required sensitivity

As the sensitivity of the photoelastic coating is directly related to the measured strains, its correct determination is of paramount importance. The basic equation (6.11) indicates that the sensitivity depends mainly on the sensitivity of the coating (f) and on the sensitivity of the polariscope system for determining the fringe order (N). The equipment available allowed for a maximum of four fringes to be detected by employing the null balance compensation method. The expected strain levels were determined with the aid of finite element analysis for the three types of specimen configurations (no insert, circular

insert and von mises (optimised) insert. The following equation (6.12) was employed to determine the required coating sensitivity.

$$f = \frac{\varepsilon_1 \varepsilon_2}{N} = \frac{\gamma_{MAX}}{N} = \frac{\text{expected strain level}}{\text{max. number fringes desired}} \tag{6.12}$$

After the coating sensitivity has been determined, the type and thickness of the photoelastic coating can be calculated from (13).

$$f = \frac{\lambda}{2tK} \tag{6.13}$$

For ease in selecting the adequate coating type and its thickness, a parametric plot is available from the manufacturer of photoelastic coating material [6]. Entering this plot with the desired coating sensitivity yielded a high sensitivity plastic coating with K ranging between 0.08 and 0.15 and of 2 mm thickness approximately. From the available pre-manufactured flat sheets, a PS-1 Sheet of 2.05 mm thickness was chosen. The properties for the chosen coating are shown in Table 6.1. The chosen coating has a sensitivity of 960 με/m.

Table 6.1: Physical and optical properties of PS-1 photoelastic coating

Strain Optical Coef. K	Elongation (%)	Elastic Modulus E (GPa)	υ	Thickness		Max. Usable Temperature (°C)
				(mm)	Tolerance	
0.15	5	2.5	0.38	2.05	± 0.06	150

6.4.3.2 Reinforcing effects of coating

The reinforcing effect of the PS-1 coating material employed for all pin-loaded specimens tested was considered to be negligible. The reinforcing effect is usually negligible for plane-stress problems, where the load is applied on the plane of the panel and also for membrane stresses produced with little or no bending [6].

6.4.4 Coating Installation

The installation of the coating can be divided into four operations:

1. Coating preparation
2. Surface preparation
3. Adhesive preparation
4. Bonding procedures

The flat sheets (254 x 254 mm) were cut in 9 equal squares of 85 mm sides. The edges of each square were then beveled as shown on Figure 6.6 to avoid edge effect which could distort the fringe and isoclinic patterns. Furthermore, clearance holes were drilled in the coating to ensure that the pin would not come into contact with the coating.

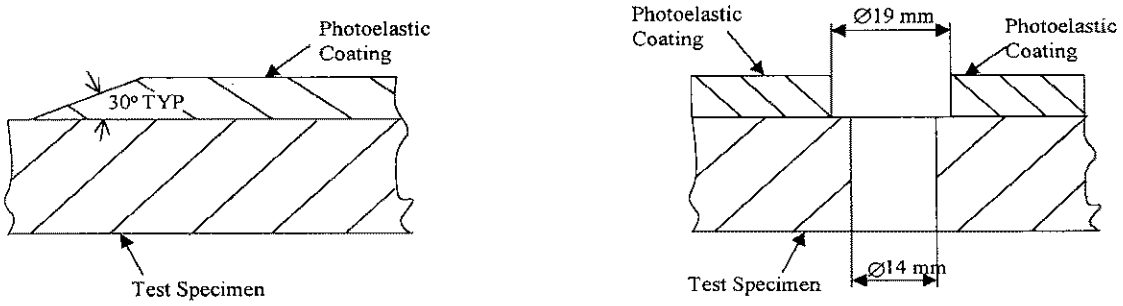

Figure 6.6: Bevelling and clearance on photoelastic coating

Contact between coating and pin has to be avoided due to possible local distortion of the fringes at the point of contact. Figure 6.6 shows the actual clearance between the hole in the specimen and the coating sheet.

After the squares of photoelastic coating were cut, both sides of the coating were degreased and cleaned by using isopropyl alcohol. The area of the specimen where the photoelatic coating is bonded was lightly sanded and cleaned with acetone. This ensures a good adhesion between coating and test item.

The PC-1 Bi-Pax adhesive was selected for bonding the coating to the specimens. After mixing the adhesive, the specimen was coated with an adhesive layer of approximately 1 mm thickness. A thin coating of adhesive was applied to the edges of the photoelastic coating to provide for a seal against moisture absorption. Finally, the photoelastic coating was placed on the specimen and left to cure for 24 hours at room temperature.

6.4.5 Fringe generation and interpretation

As the load is applied to the test item, fringes start to appear first at the most highly stressed points on the specimen. When the load is further increased, new fringes start shifting the original fringes towards the less stressed region. The fringes retain their identity as the loading is increased and they are also continuous, ie they do not merge with one another. Each band represents a different degree of birefringence corresponding to the underlying strain in the test part. Each band will have a unique colour which identifies the fringe order everywhere along that band.

The birefringent coating method usually employs white light for full-field interpretation of fringe patterns. White light is composed of all wavelengths in the visible spectrum. Therefore, the relative retardation which causes extinction of one colour does not generally extinguish others. As the colours are extinguished the observer sees the complementary colour. These complementary colours make up the visible fringe pattern in white light. The relationship between colour, relative retardation and fringe order is shown in Table 6.2. Because of simultaneous multiple extinction of colors, the second-order tint

of passage is fainter than the first, and falls in the transition area between red and green fringes. The last transition easily detectable under white light occurs when pink is extinguished producing a pink/green colour. The zero-order fringe is represented by the black colour.

Summarising, the difference in the principal strains, or the maximum shear strain in the surface of the test part, can be obtained by simply recognising the fringe order and multiplying it by the fringe value of the coating (960 με/m).

Table 6.2: Isochromatic Fringe Characteristics

Colour	**Approximate Relative Retardation (nm)**	**Fringe Order N**
Black	0	0
Gray	160	0.28
White	260	0.45
Pale Yellow	345	0.60
Orange	460	0.80
Dull Red	520	0.90
Purple (Tint of Passage)	575	1.00
Deep Blue	620	1.08
Blue-Green	700	1.22
Green-Yellow	800	1.39
Orange	935	1.63
Rose Red	1050	1.82
Purple (Tint of Passage)	1150	2.00
Green	1350	2.35
Green-Yellow	1440	2.50
Red	1520	2.65
Red/Green Transition	1730	3.00
Green	1800	3.10
Pink	2100	3.65
Pink/Green Transition	2300	4.00
Green	2400	4.15

6.4.6 Principal Strain directions

The principal strain directions are measured with respect to an axis of symmetry or reference line. The selection of a convenient reference is straightforward in the case of the pin-loaded specimens. The vertical axis of symmetry was selected for all specimens.

By rotating the reflection polariscope analyser, complete extinction of light can be achieved. As a result of this procedure, black lines called isoclinics are obtained. An example of an isoclinic and the equipment set-up to measure the principal strain directions is shown in Figure 6.7.

The isoclinics are lines where the principal stresses have a constant inclination. The isoclinics can be plotted by rotating both the polariser and analyser in angular increments (e.g 15°). These lines can then be combined into one graph.

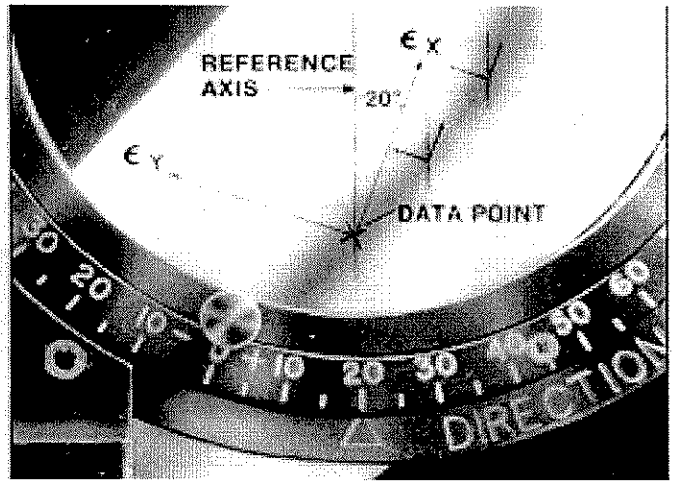

Figure 6.7: Measurement of principal strain directions by employing a reflection polariscope [4].

The following rules apply to the construction of isoclinics:

a) Isoclinics of all parameters must pass through isotropic points. Isotropic points are points where the difference of principal stresses is zero.
b) An isoclinic of one parameter has to coincide with an axis of symmetry if such an axis exists.
c) The parameter of an isoclinic which intersects a free boundary is determined by the slope of the boundary at the point of intersection.
d) Isoclinics of all parameters pass through points of concentrated load.

The thickness of the isoclinic depends on how rapidly the principal strain directions change. The narrower the line the more rapid the principal strain directions change from point to point. Finally, the isoclinics can be employed to construct an isostatic diagram. Isostatic lines possess the property of being tangent to the principal strain direction. Therefore, the information they provide can be helpful in determining the stress or load path through the tested item.

6.5 Test set-up

Test specimens with w/d =4 (1^{st} batch of specimens) were tested in an Instron 1195 machine fitted with a 50 kN load cell. An Instron 5567 testing machine with a 30 kN load cell was used for the photoelastic analysis performed on the second batch of specimens with w/d=11.5. Typical specimen dimensions for all batches of specimens are described in Section 5.2 of Chapter 5.

The set-up employed for the first batch of specimens tested with a width/diameter ratio equal to 4 is shown in Figure 6.8. Specimens were tested both under finger tight pressure and under pinned conditions. An integrated washer was machined into the rectangular loading plates to provide for the contact area between the plate and the test specimens. The diameter of this raised washer was 2.2 D which is a commonly recommended ratio for clamping area [1] in composite bolted joints. The specimens were loaded in double shear as shown in Figure 6.8. Strain gauges for the first batch of specimens were bonded to both sides of the test items to determine in-plane loading. The tests were performed in an Instron 1195 (50 kN load cell) machine under displacement control at 0.1 mm/min. Load, displacement and strain readings for all strain gauges were

continuously monitored using both Instron software and Labview coupled to a SCXI 4-Channel Isolation Amplifier with excitation.

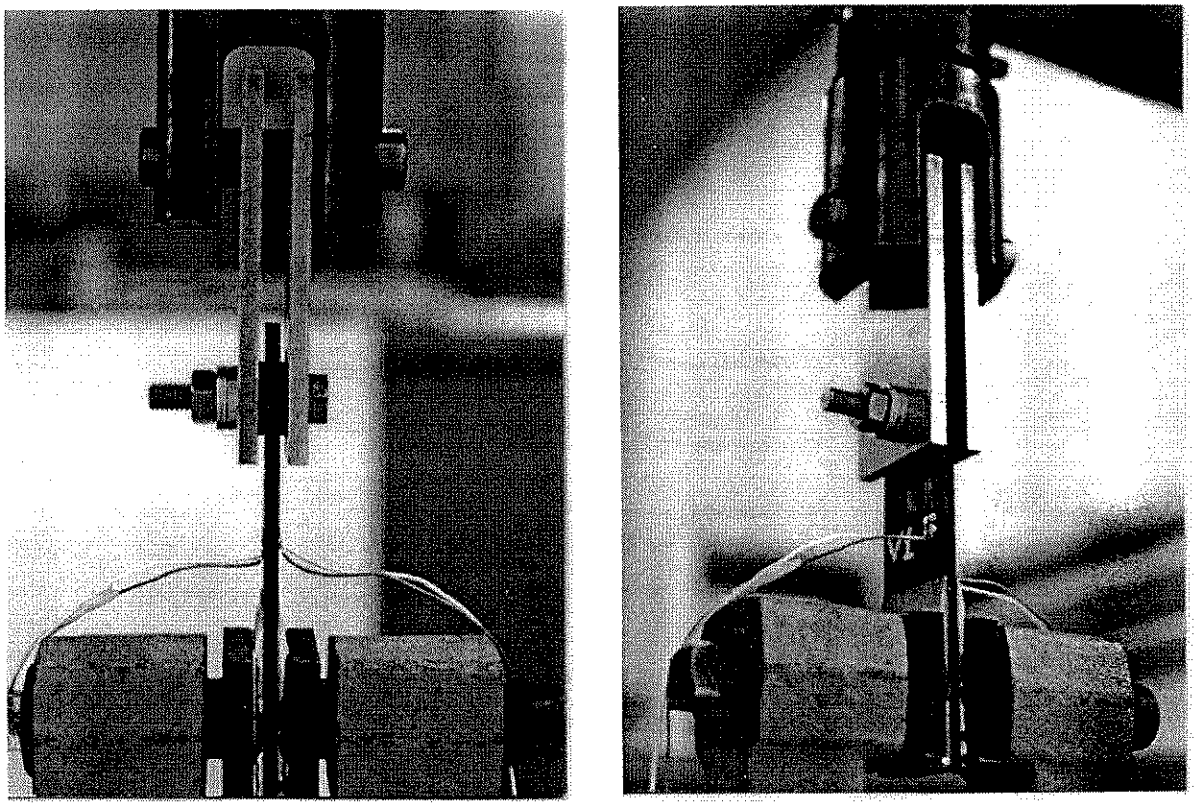

Figure 6.8: Photograph of experimental set-up used for 1st batch of specimens (w/d=4)

The second batch of specimens (w/d=11.5) were not strain gauged and results were obtained by photography and video recording strain patterns on the photoelastic coating placed around the pin loaded region on the specimen. The testing machine employed in this case was an Instron 5567 (30 kN load cell) and the displacement rate used was 0.5 mm/min. To accommodate the new w/d ratio of the specimens, a new test fixture (see Section 6.2) was designed and built. This test fixture had also an integrated washer on the loading plates to allow for clamping of the loaded hole if desired. A different set-up to the one used for the first batch of specimens was employed. The difference was that the loading plates had to be placed on the inner side of the specimens as shown in a schematic on Figure 6.9. The reason for this requirement was that the light had to be shined directly into the pin-loaded region and the reflection of this light had to be analysed with a

reflection polariscope. As a result of the required testing configuration, two specimens were tested simultaneously back to back. Photoelastic measurements were only taken from one of the specimens. A photograph of the set-up showing the Instron testing machine and the recording equipment employed is shown in Figure 6.10.

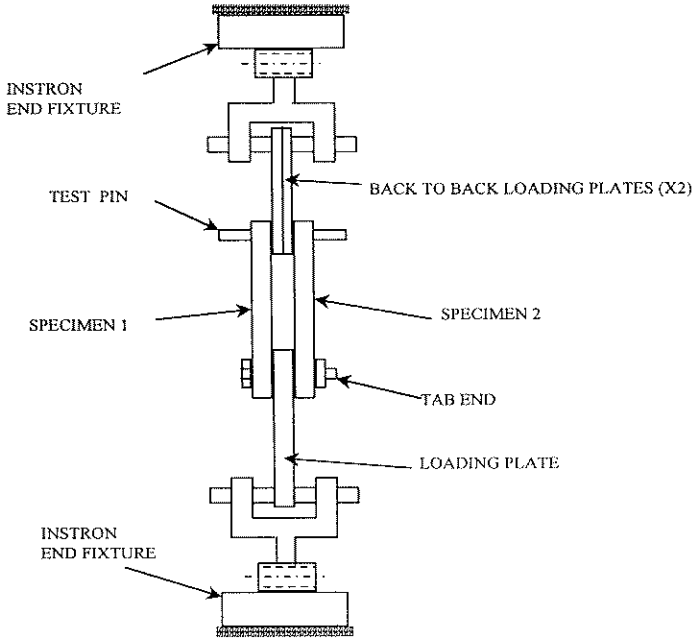

Figure 6.9: Set-up of test fixture for photoelastic analysis

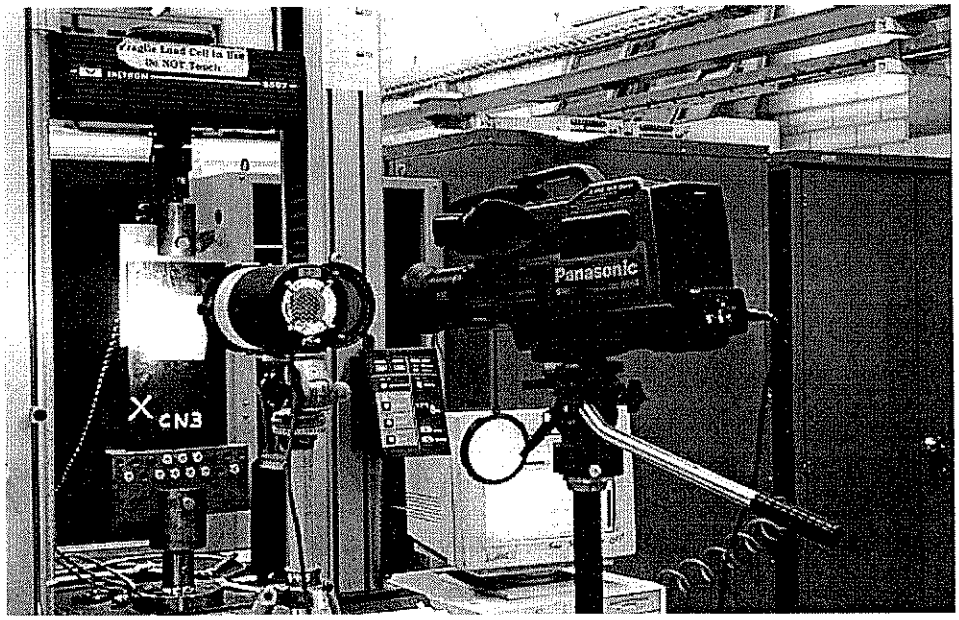

Figure 6.10: Photograph of photoelastic measurement set-up for 3rd batch of specimens (w/d=11.5)

6.6 References

[1] Rispler, A. R., Steven, G. P., "Shape Optimisation of Metallic Inserts in Composite Bolted Joints", *Proceedings of the 2nd Pacific International Conference on Aerospace Science & Technology*, Melbourne, Australia, Vol. 1, pp. 225-230, March 20-23, 1995.

[2] Application Note 048, National Instruments, July 1993.

[3] Kuske, A., Robertson, G., "*Photoelastic Stress Analysis*", 1974.

[4] Technical Note TN-702-1, Measurements Group, 1989.

[5] Dally, J. W., Riley, W. F., "*Experimental Stress Analysis*", McGraw-Hill Book Company, 1965.

[6] Tech Note TN-704-1, Measurements Group, 1978.

CHAPTER 7

ANALYSIS OF PIN LOADED JOINTS TEST RESULTS

7.1 Introduction

This chapter presents the results obtained from testing different pin and bolted joint configurations to assess the benefits of employing metallic inserts in highly loaded joints. The description of both specimen dimensions and test configurations has been given in Chapters 5 and 6. Two distinctive tests were performed. The first batch of specimens with a w/d=4 were tested under finger tight conditions and under pin loaded conditions while the second batch of specimens with a w/d=11.5 was tested under pin loaded conditions only, whilst employing the photoelastic test set-up described in Chapter 6. The change in configurations was a result of the first batch of testing yielding net tension and shear-out type failures instead of the desired bearing type failure mode. Furthermore, the second batch of specimens was tested employing photoelastic measurement techniques to be able to obtain a quantitative and qualitative comparison of stresses in close proximity to the composite/metallic insert interface. The results obtained for the w/d=4 configuration are then compared to predictions employing the "BOLT" computer program [1] described in Chapter 5. Photoelastic measurements on specimens with w/d=11.5 are compared to finite element analysis predictions of maximum shear strains at the insert / composite interface.

7.2 Test results of Geometric configuration w/d=4

The total number of tested specimens for this configuration was 19. Of these 19 specimens, 11 were tested under finger tight conditions while 8 were tested under pin-loaded conditions. Table 7.1 shows the maximum, minimum and average failure loads obtained for the finger tight configuration as well as the average far field strain at failure.

Table 7.1: Test results of finger tight configuration specimens w/d=4

Type of specimen	Number of specimens tested	Average Maximum Load (kN)	Average Strain recorded at failure (με)	Maximum Load (kN)	Minimum Load (kN)
No inserts	3	32.18	3651.90	33.22	30.87
Circular inserts	3	29.46	3352.13	29.94	28.92
Von Mises inserts	2	29.31	3456.13	30.31	28.31
Global inserts	3	27.58	3352.13	28.82	24.33

From this table we observe that the metallic inserts had a negative effect on the failure loads. Specimens with no inserts, were in average 8.5% stronger than specimens with any type of insert.

The failure mode on the specimens with no insert was net-tension while specimen with optimised inserts failed in a combined shear-out net tension failure mode. The failure mode experienced by the specimens with circular inserts was shear-out. This indicates that the inclusion of inserts on the specimens tested under finger tight conditions which were designed to increase bearing strength could not do so, as the failure mode on specimens without inserts was net-tension. No indication of bearing failure was present in any of the specimens tested under finger tight conditions. Furthermore, the specimens with aluminium inserts show significant yielding of the insert at failure. The aluminium employed for the manufacturing of the inserts was a non-aircraft quality aluminium.

Typical failed specimens for each type of tested joint are shown in Figure 7.1. The inclusion of the insert also diminished both the effective composite net tension section and the edge margin distance. This is most probably the cause of the reduced shear-out / net-tension failure experienced by the specimens with metallic inserts. Due to large yielding experienced by the optimised inserts, the adhesive employed for bonding the insert to the composite specimen failed below the ligament region. The circular inserts experienced less

yielding when compared to the "optimised" inserts and the failure mode in these specimens was shear-out only.

Typical load versus far field strain curves obtained from finger tight tests for the circular insert, Von Mises insert and the specimens with no insert are shown in Figure 7.2. The specimens with "Global inserts" tested under finger tight conditions behaved very similarly to the specimens with "Von Mises" inserts and therefore are not shown. The graphs indicate a change of slope for the "Von Mises" insert specimens at approximately 10 kN.

Global insert Von Mises insert No insert Circular insert

Figure 7.1: Typical failed test specimen for all joint configurations (finger tight)

At this load it is believed that the aluminium inserts started yielding. As the yielding was contained in-plane of the specimens; ie lateral constraint was imposed by the loading plates; the adhesive used for bonding the inserts to the composite specimens failed in tension.

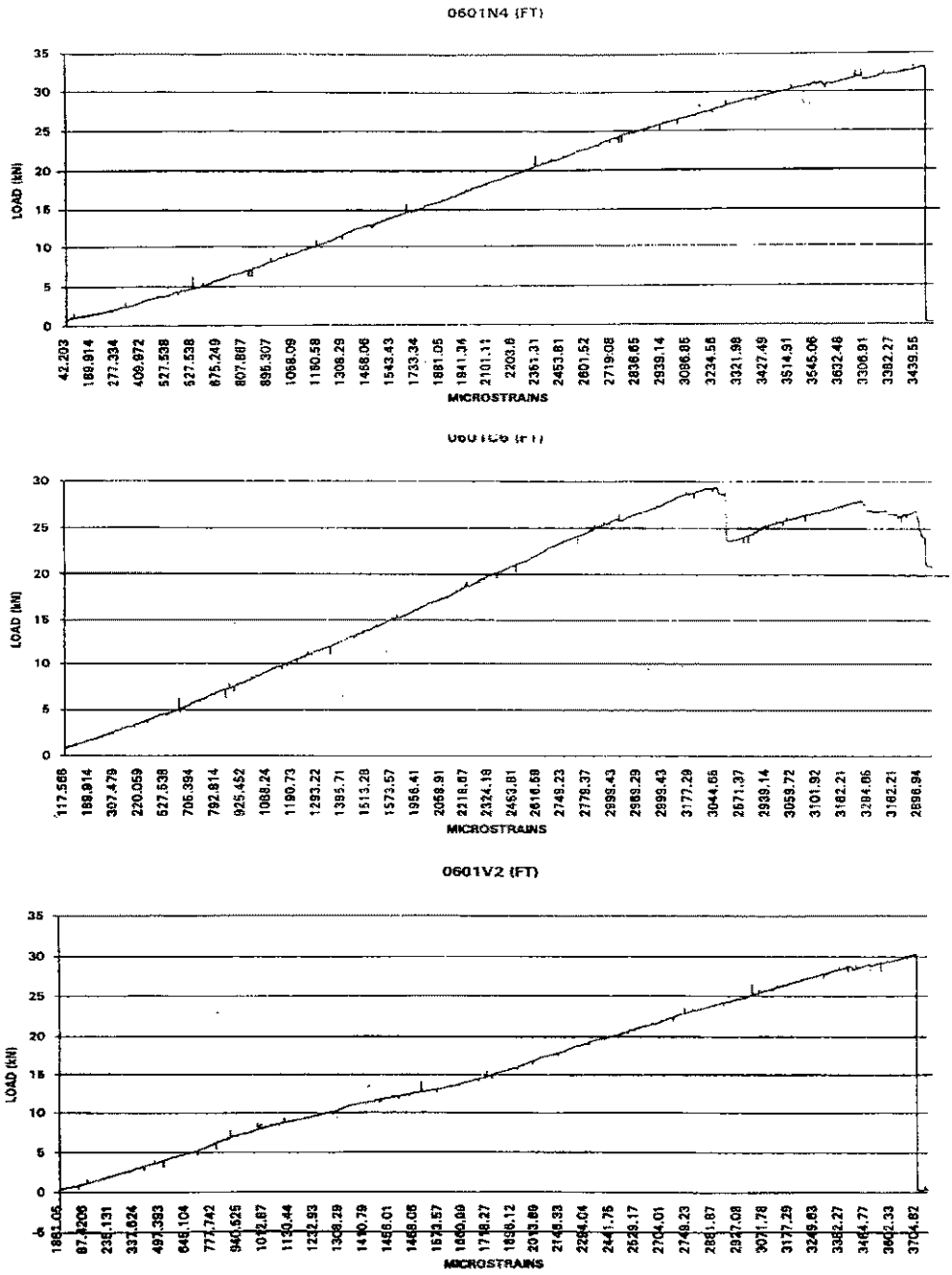

Figure 7.2: Typical load versus far field strain curves for different tested configurations under finger tight conditions; (a) no insert, (b) circular insert, (c) Von Mises insert

(poor quality of picture due to data lost on hard disk crash)

The pin-loaded specimens behaved quite differently when compared to the finger tight specimens. Table 7.2 shows the maximum, minimum and average failure loads obtained for the finger tight configuration as well as the average far field strain at failure.

Table 7.2: Test results of pin-loaded configuration specimens w/d=4

Type of specimen	Number of specimens tested	Average Maximum Load (kN)	Average Strain recorded at failure (με)	Maximum Load (kN)	Minimum Load (kN)
No inserts	1	26.16	2999.43	26.16	26.16
Circular inserts	2	26.08	2925.58	29.11	23.06
Von Mises inserts	2	30.21	3462.16	31.70	28.72
Global inserts	3	28.04	3186.33	30.19	26.71

As expected, the strength of specimens with no inserts decreased for the pin-loaded condition. The failure mode also changed from being net-tension to bearing. The average failure load for the no insert pin-loaded configuration was approximately 20% lower than for the no insert finger tight condition. The specimens with circular inserts presented a similar behaviour with an 11% lower failure load under pin-loaded conditions. In this case, the failure mode changed from shear-out to bearing.

Both specimen configurations with "optimised" inserts ("Von Mises" shape and "Global" shape) under pin-loaded conditions, showed the opposite behaviour to that shown by the circular insert and no insert configuration under the same conditions. Although only marginally stronger than their finger tight counterparts; between 1 and 3 %; the optimised inserts performed better under pin-loaded conditions. The "Global" and the "Von Mises" insert shape configuration yielded an increase in strength of 7 % and 15 % respectively. when compared to the no insert configuration under pin-loaded conditions.

All specimens tested under pin-loaded conditions failed in bearing. Typical failed specimens for each tested configurations are shown in Figure 7.3. The increase in ultimate strength achieved as a result of bonding the "optimised" inserts for the pin-loaded configuration shows that when the failure mode on specimens with no inserts is bearing, strength can be improved by the addition of an optimised insert. Typical load versus far field strain curves obtained from finger tight tests for the circular insert, Von Mises insert and the specimens with no insert are shown in Figure 7.4. The specimens with "Global inserts" tested under finger tight conditions behaved very similarly to the specimens with "Von Mises" inserts and therefore are not included. The graphs indicate a significant amount of yielding on both the circular insert and the optimised insert ("Von Mises" insert configuration) at the same level as for the specimens tested under finger tight conditions; ie at approximately 10 kN. At this load it is believed that the aluminium inserts started yielding. The yielding in this case was not contained in-the plane of the specimens as there was no lateral constraint around the loaded hole. This provided some local plasticity thereby relieving stress at the composite interface.

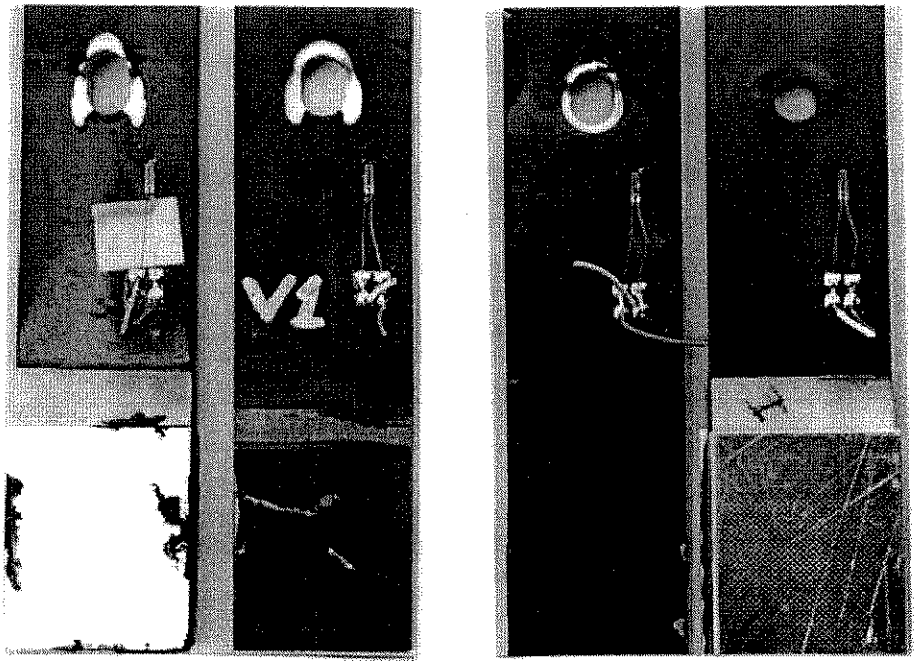

Global insert Von Mises insert No insert Circular insert

Figure 7.3: Typical failed test specimen for all joint configurations (pin-loaded)

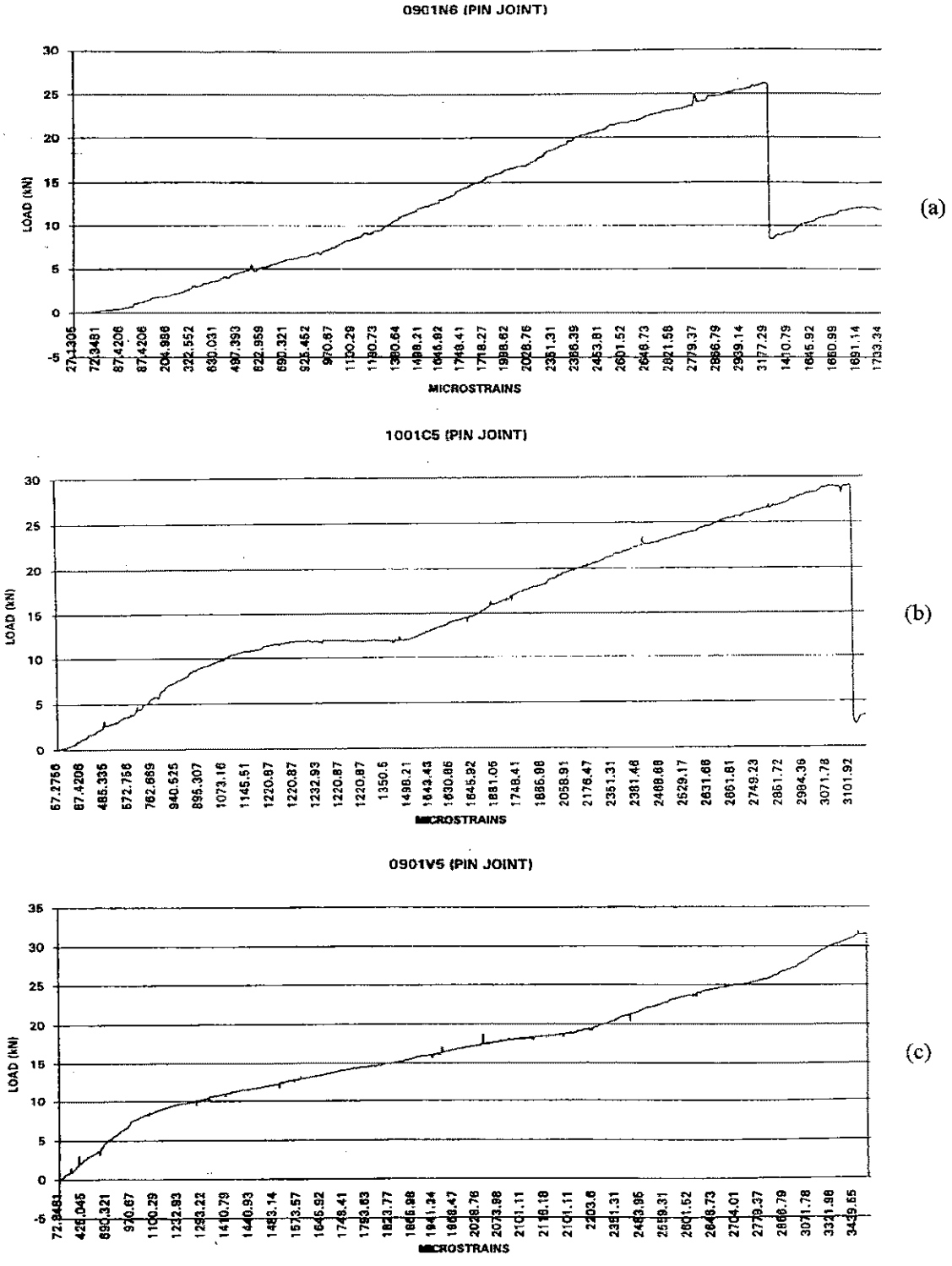

Figure 7.4: Typical load versus far field strain curves for different tested configurations under pin-loaded conditions; (a) no insert, (b) circular insert, (c) Von Mises insert

(poor quality of picture due to data lost on hard disk crash)

None of the specimens tested under pin-loaded conditions showed failure of the adhesive at the inserts / composite interface. If we assume bearing failure to occur at 4 % elongation; as normally used in design calculations; the effect of the inserts on bearing strength is counterproductive. This is most likely due to the type of aluminium employed for the manufacturing of the inserts. This indicates the importance of limiting the onset of yielding on the insert material by ensuring that yielding starts at a load at least 20 % larger than the failure load of specimens with no inserts. Following the above guidelines will ensure that the metallic inserts are beneficial to the joint strength.

Thin aluminium plates were bonded to the glass fibre tabs after experiencing some difficulties due to slippage of the specimens in the Universal Testing Machine. The aluminium plates minimised slippage and no further difficulties were encountered during testing.

7.3 Correlation of Failure Load /Mode of w/d=4 configuration test results

The testing of the first batch of specimens highlighted the need of ensuring bearing failure on specimens with plain holes to ensure the joint efficiency could be improved by adding metallic inserts. This resulted in failure analysis being carried out to determine optimum joint configuration and to ensure the inserts could contribute to increase the joint efficiency. Fu-Kuo Chang's et.al code "BOLT" [1] was employed to carry out failure analysis on all configurations. The capabilities and assumptions employed on this code are described on Chapter 4.

The required input includes ply properties, orientations, geometry, characteristic lengths, strengths of each ply and shear strength of cross ply laminates. Characteristic lengths were assumed to be equivalent to the ones used by default on the "BOLT" program (T-300/1034-C, quasi-isotropic lay-up). This should be sufficiently accurate as it is shown in the literature [2], that for quasi-isotropic lay-ups the failure load and mode are insensitive to precise values of characteristic lengths both in tension and compression. The

output consists on the failure load, failure mode, bearing strength, location of failure initiation and failed ply group.

The material properties employed in the analysis correspond to the Hy-E 3034K prepreg which was employed for the manufacturing of the first batch of specimens (configuration w/d=4). The correlation of pin-loaded test results with failure analysis predictions using "BOLT" are shown in Table 7.3.

Table 7.3: Comparison of test results to prediction using "BOLT" computer code

Type of specimen	Average Maximum Load TEST (kN)	Actual Failure Mode TEST	Failure load "BOLT" Prediction	Failure mode "BOLT" prediction	Angle of Failure Initiation "BOLT"
No inserts	26.16	Bearing	28.41	Bearing	14°
Circular inserts	26.08	Bearing	29.59	Tension	90°

The maximum difference between prediction and test results was of 12 % for the circular insert configuration. The prediction of failure indicates that failure occurs at the 0° ply. The change of predicted failure mode for the circular insert configuration did not correlate well to the pin-loaded case. Such failure mode was observed for the finger tight specimens where the no insert configuration failed in net-tension at 90° while the circular insert configuration failed in shear-out. The explanation for this could be related to the yielding of the aluminium insert. In the finger tight configuration, the specimens with circular insert had the lateral support provided by the raised washers on the loading plates which restricted the amount of yielding. Any yielding had to be kept in plane which coupled with the effectively reduced edge margin resulted in shear-out failure. This was not the case for the pin-loaded configuration where a much larger amount of out-of-plane yielding was observed on the aluminum insert.

The geometric ratios employed for the failure analysis conducted on the no-insert configuration were w/d=4 and e/d=2.5. For the circular insert configuration, it was assumed that the outside diameter of the metallic insert was equivalent to the actual hole diameter of the joint. This yielded an effective w/d=2.86 and an e/d=1.78.

The analysis lead to an increase in w/d from 4 to 11.5 for the second batch of specimens and also an increase in e/d from 2.5 to 7.9. The large increases in joint dimensions were not only a result of ensuring bearing failure on specimens with no insert. The increase aided also in simplifying the construction of the metallic inserts and resulted in simpler full fringe identification by means of photoelastic analysis as described in the next section.

7.4 Test results of Geometric configuration w/d=11.5 (Photoelastic Testing)

The total number of tested specimens for this configuration was 5. These 5 specimens were tested initially up to 10 kN and after unloading them they were re-tested up to 25 kN. All specimens were tested under pin loaded conditions as shown in Figure 6.9 on Chapter 6. It is to be noted, that since the specimens were tested in pairs; back to back due to the photoelastic set-up requirements; each specimen would see half the total load recorded. Figure 7.5 depicts a typical load v displacement curve for all tested specimens. No differences were observed in the stiffness between specimens with inserts and specimens with no inserts. Only one of the specimens (CN4) tested failed during testing. The specimen had no insert and a crack developed at approximately 20 kN. This specimen was c-scanned prior to testing together with all other specimens and a small delamination around the hole was detected. All specimens were c-scanned prior and after testing to assess any damage which might have developed during testing and could not be identified through the load v deflection graphs. The only specimen that showed increase damage when compared to scans performed prior to testing was the CN4 specimen which failed during testing. The load-displacement graph of the failed CN4 specimen is shown in Figure 7.6.

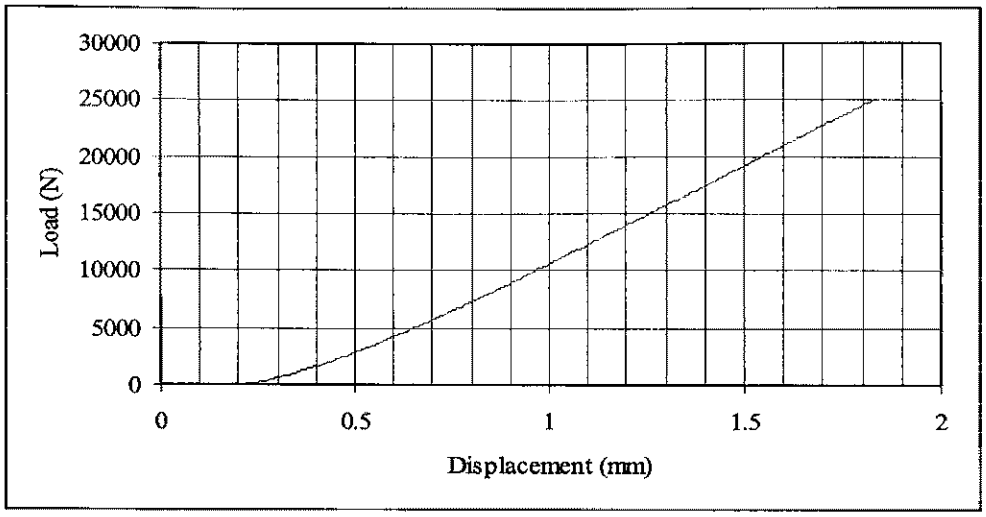

Figure 7.5: Typical load-displacement curve for all tested specimens

The most significant parameters which needed to be determined in order to establish correlation with the finite element analysis and to proof the concept of strain reduction at the composite interface by the use of metallic inserts, were the maximum fringe and the full field strain at the composite interface. The maximum fringes calculated with the aid of a polariscope for the specimens tested up to 10 kN are tabulated in Table 7.4. A pictorial representation comparing the isochromatic fringe patterns for these specimens with and without inserts is shown in Figure 7.7.

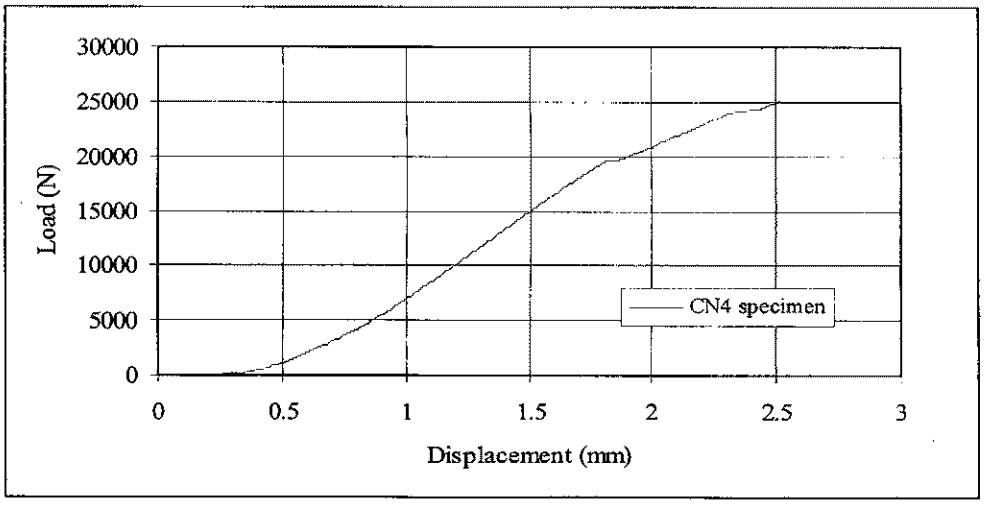

Figure 7.6: Failed specimen (CN4)

Table 7.4: Maximum fringes calculated for specimens tested up to 10 kN

SPECIMEN NAME (fringes measured at specimen marked with **bolt** font)	LOAD RECORDED (kN)	DISPLACEMENT RECORDED (mm)	MAX. FRINGE ORDER ESTIMATE	COLOUR OF MAX. VISIBLE FRINGE	CONDITION PRIOR TO TEST N=no damage SD=significant delamination ID=insignificant delamination
CN1	10	0.86	4.15 visible	green	ID
CN2			~ 6 extrapolated		N
CN3	10	1.19	4.15 visible	green	N
CN4			~ 6 extrapolated		ID
CI1	10	0.928	4	pink/green	N
CI2					N
CI3	10	1.394	3-4		N
CI4					SD
VM4	10	0.976	1.63-1.82	Orange-rose red	N
VM5					N

Nomenclature: CN = specimens with no inserts CI = with circular inserts
VM = specimens with Von Mises inserts

The required clearance between the pin and the photoelastic coating (see Section 6.4.4 in Chapter 6) hindered the obtention of a precise fringe value at the actual pin/composite interface for the specimens with no inserts. For these specimens, the visible fringe value 2.5 mm away from the interface was extrapolated to the pin position by using linear regression analysis. The extrapolated fringe magnitude at the pin/composite interface should be smaller than the actual magnitude as the fringes tend to bunch up closer as the distance to the point of contact decreases. This should yield the smallest improvement of

strain relief due to the metallic inserts thus providing with a pessimistic estimate on percentage of strain relief.

The amount of strain relief obtained with the circular inserts was of approximately 35 % when compared to the no-insert configuration. The optimised inserts (Von Mises insert configuration) yielded an even larger strain reduction at the composite interface. The percentage reduction achieved by the use of bonded Von Mises inserts was approximately 70 % when compared to the no-insert configuration. The reduction of strain concentration by employing an optimised insert was of 55 % when compared to the circular insert configuration. The isochromatic fringe patterns shown in Figure 7.7 can be correlated to the fringe magnitudes displayed on Table 7.4 by referring to the colour-fringe relationships on Chapter 6.

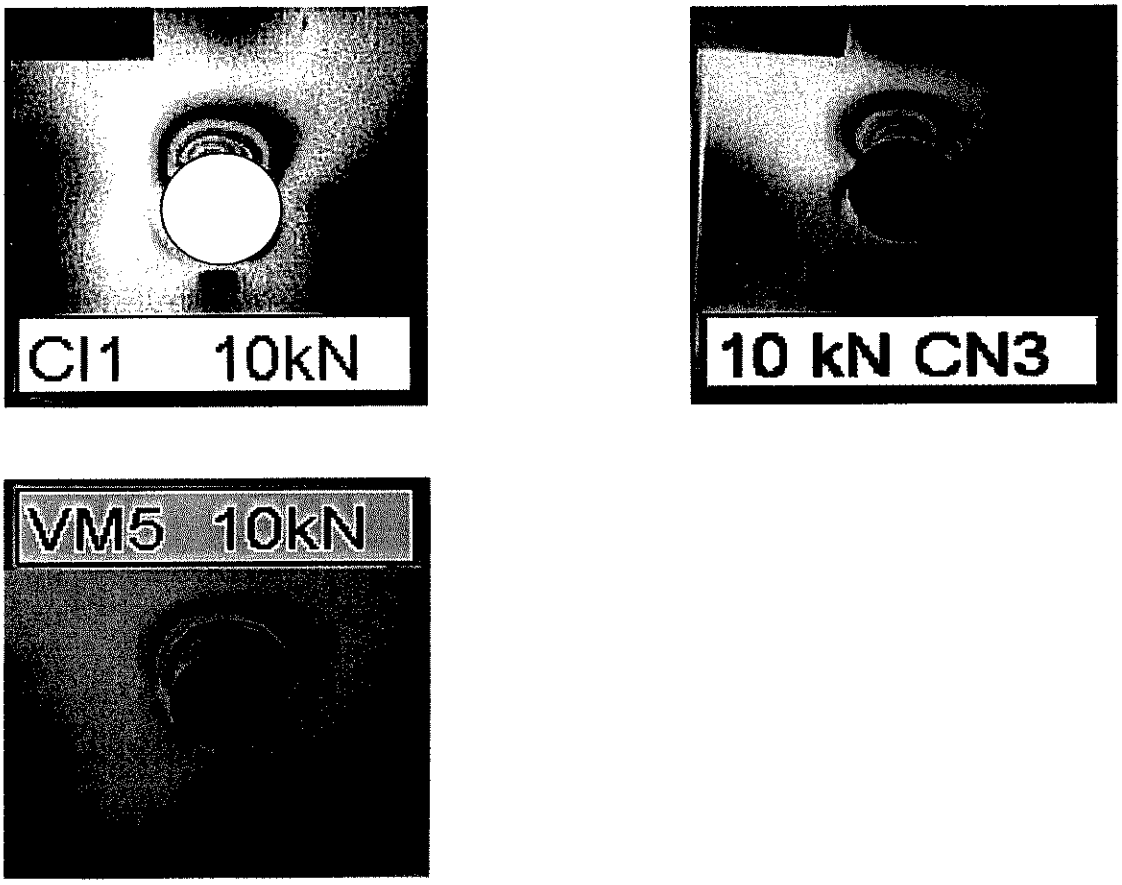

Figure 7.7: Isochromatic fringe patterns for 10 kN loading

The circular shading on the CI1 specimen represents the actual size of the circular insert while the dark line shown on specimen VM5 represents the actual shape and size of the Von Mises insert. The superposition of these lines on the photographs aid in comparing fringe magnitudes at the composite interface between different specimens.

A monochromator was also employed for some of the photographs taken during testing. The monochromator is a filter which helps in determining the number of fringes by transmitting only a narrow band of wavelengths. Specifically, the Model 036 interferential monochromator employed has a bandpass of 10 nm at the tint-of-passage wavelength of 575nm. As the magnitude of relative retardation along any fringe is an integral multiple of the wavelength (λ, 2λ, 3λ, etc.), the rays are 180 degrees out of phase, and the mutual cancellation produces extinction of the light producing a black band along fringes with a wavelength multiple of 575 nm. The photographs obtained with the aid of the monochromator filter are shown in Figure 7.8.

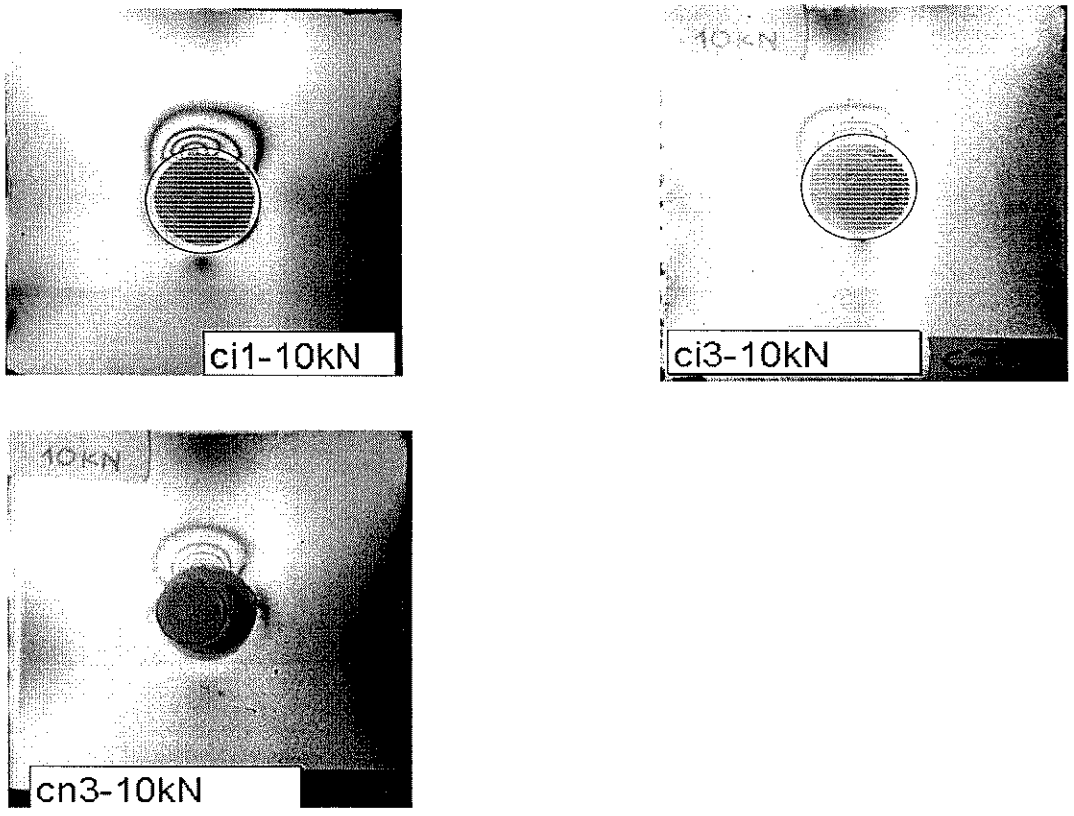

Figure 7.8: Monochromatic fringe patterns for 10 kN loading

Each black band depicted on the photographs correlates to one (1) fringe; ie fringe order = number of black bands. Unfortunately, the photograph corresponding to the Von Mises Insert did not reproduce. Nevertheless, the fringe orders can still be obtained from the isochromatic photographs on Figure 7.7.

Furthermore, isoclinics for each type of specimens were also obtained to ascertain principal strain directions. The reference for the measurement of isoclinics is the axis of symmetry (vertical) of the specimens. The isoclinics recorded for a typical specimen with no insert are shown in Figure 7.9 while those recorded for the circular insert configuration are depicted in Figure 7.10.

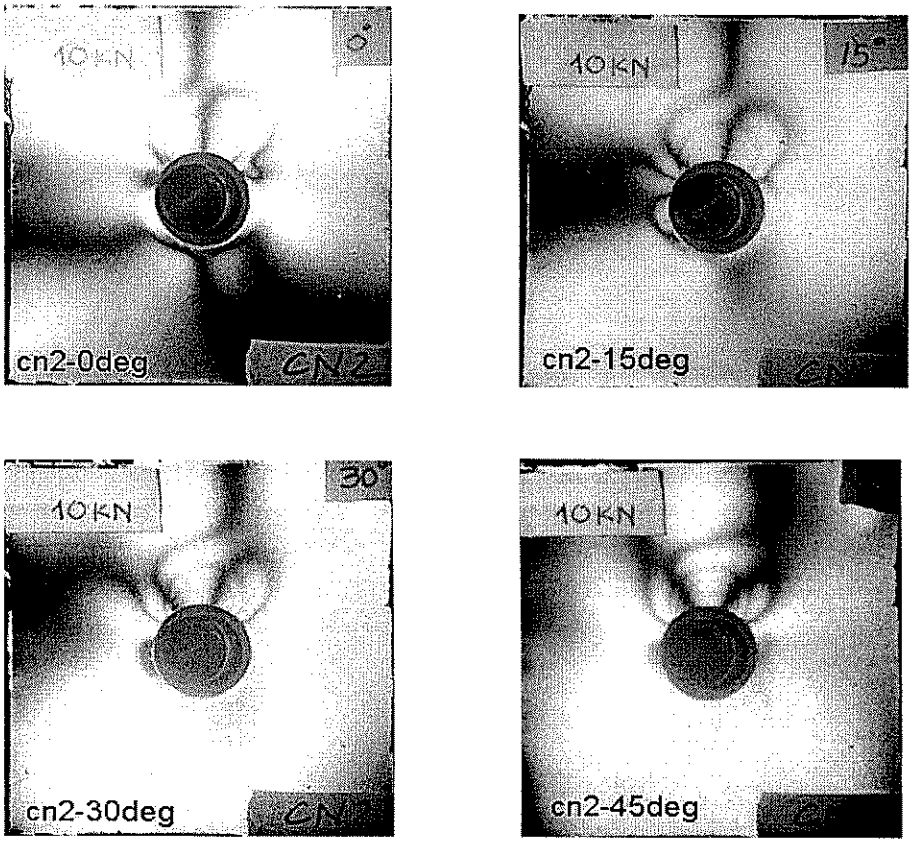

Figure 7.9: Isoclinics for no-insert configuration recorded at 15° intervals (0-45°)

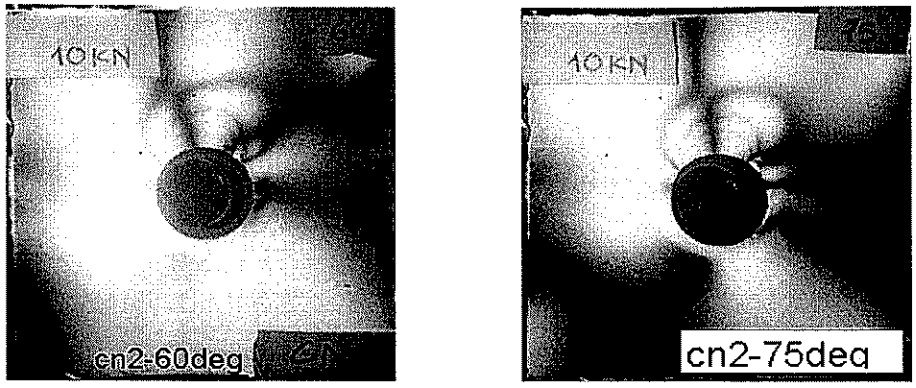

Figure 7.9: Isoclinics for no-insert configuration recorded at 15° intervals (60-75°)

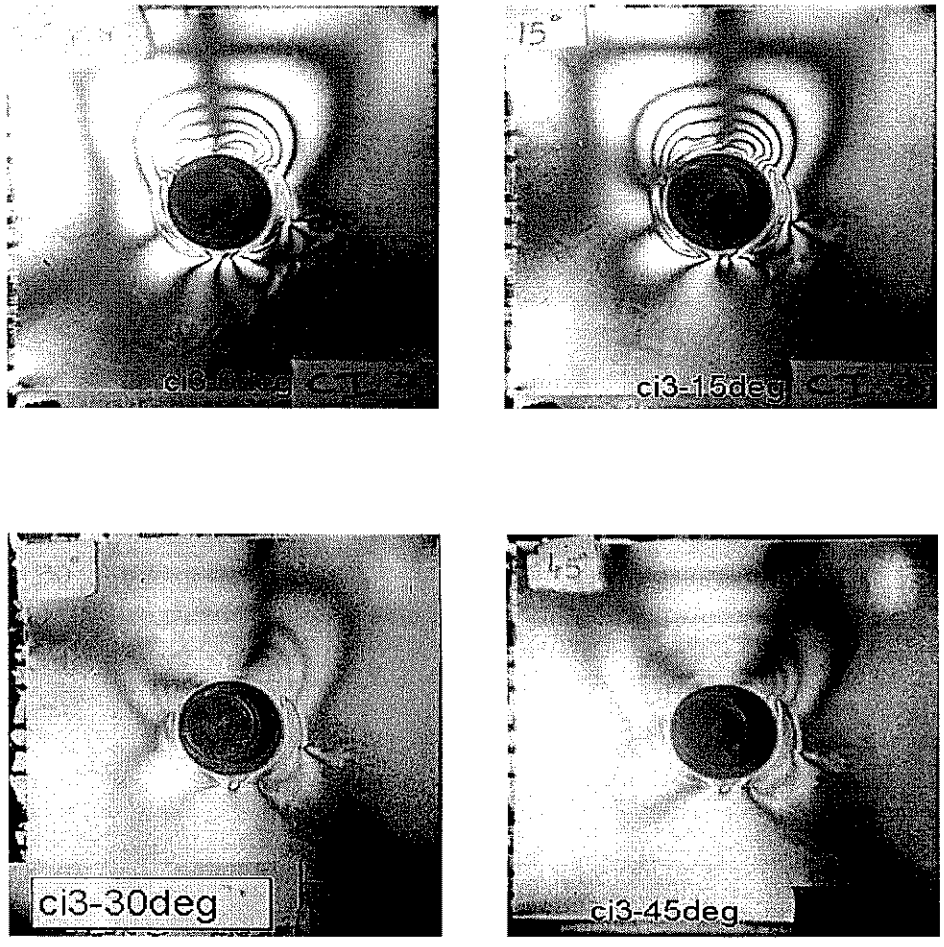

Figure 7.10: Isoclinics for circular insert configuration recorded at 15° intervals (0-45°)

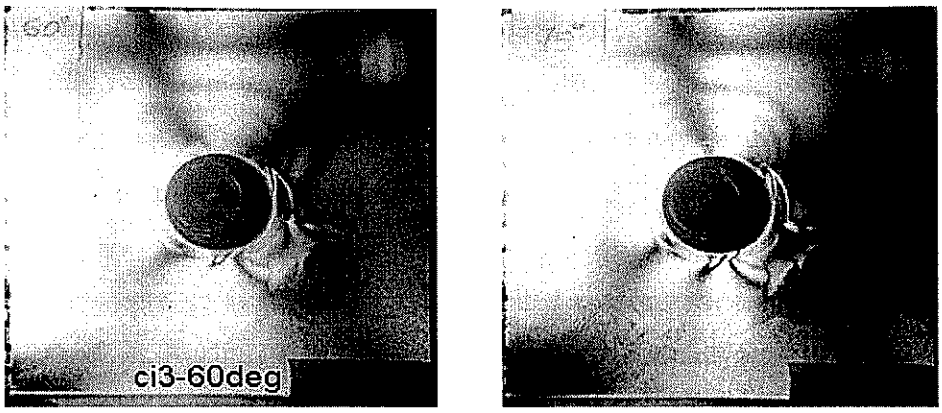

Figure 7.10: Isoclinics for circular insert configuration recorded at 15° intervals (60-75°)

Finally, the isoclinics recorded for a typical specimen with optimised insert (Von Mises insert) are shown in Figure 7.11.

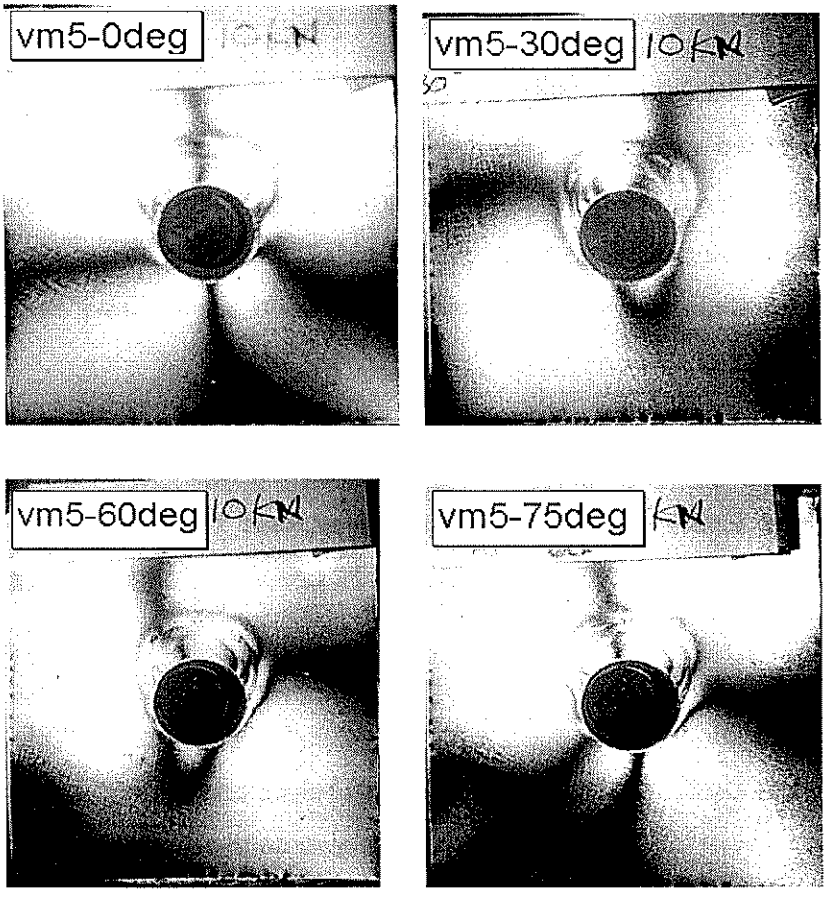

Figure 7.11: Isoclinics for optimised insert configuration recorded at different intervals

If the isoclinics are narrow and sharply defined, it means that the directions of ε_x and ε_y vary rapidly from one location to the next. On the other hand, isoclinics forming broad black lines or areas in indicate that ε_x and ε_y vary slowly in that region. The isoclinics recorded indicate that the direction of ε_x and ε_y vary more rapidly for the no-insert configuration than for the remaining configurations with inserts. The flow of stress around the loaded hole appears to be similar for all tested configurations. This should be expected as the method of loading the specimens remains constant across all specimens. The significant difference which can be noted is that the bonding of inserts produce a local distortion of principal strain directions at the interface between the aluminium insert and the composite plate. This is more markedly seen for the Von Mises insert configuration where the local distortion is clearly visible at the interface. It appears that the direction of the principal strain at the interface of the optimised insert tends to become tangent to the curvature defined by the insert. This could indicate the presence of shear transfer through the adhesive employed for bonding the insert to the composite plate.

All five specimens tested up to 10 kN were re-tested up to 25 kN; after unloading; to assess non-linear effects, specifically on the isochromatic patterns and magnitudes. The maximum fringes calculated with the aid of a reflection polariscope for the specimens tested up to 25 kN are tabulated in Table 7.5. A pictorial representation comparing the isochromatic fringe patterns for these specimens with and without inserts is shown in Figure 7.12.

All recorded fringe orders were double checked employing a high resolution video recorder. The tape was played back several times and fringe orders were obtained for different loads in addition to the 10 and 25 kN load.

The photographs obtained with the aid of the monochromator filter for specimens tested up to 25 kN are shown in Figure 7.13. Although the monochromatic photograph corresponding to the Von Mises Insert did not reproduce, the fringe orders can still be obtained from the isochromatic photographs on Figure 7.12.

Table 7.5: Maximum fringes calculated for specimens tested up to 25 kN

SPECIMEN NAME (fringes measured at specimen marked with **bolt** fond)	LOAD RECORDED (kN)	DISPLACEMENT RECORDED (mm)	MAX. FRINGE ORDER ESTIMATE	COLOUR OF MAX. FRINGE	CONDITION PRIOR TO TEST N=no damage SD=significant delamination ID=insignificant delamination
CN1	25	1.855	>> 6	Undetectable	ID
CN2				very pale	N
CN3	25	2.5	> 11	Undetectable	N
CN4				very pale	ID
CI1	25	1.8	~ 7	very pale	N
CI2					N
CI3	25	2.32	6	very pale	N
CI4					SD
VM4	24.5	1.84	4.15	Pink/green	N
VM5					N

Nomenclature: CN = specimens with no inserts CI = with circular inserts
VM = specimens with Von Mises inserts

The amount of strain relief obtained with the circular inserts for the 25 kN loading was larger than 35 % when compared to the no-insert configuration. The optimised inserts (Von Mises insert configuration) yielded more than 63 % as strain reduction at the composite interface. The reduction of strain concentration by employing an optimised insert was larger than 31 % when compared to the circular insert configuration. Due to the large amount of fringes, it is very difficult to ascertain an exact value for the no-insert configuration. This pitfall is compounded with the necessary clearance between the pin and the photoelastic coating as described in Chapter 6.

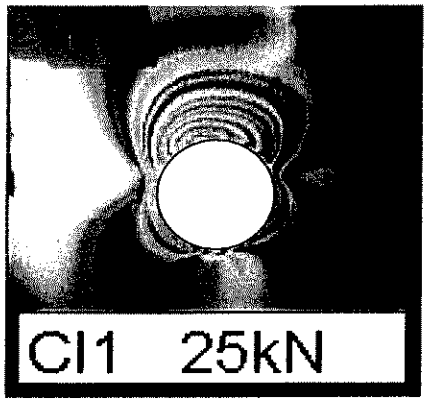

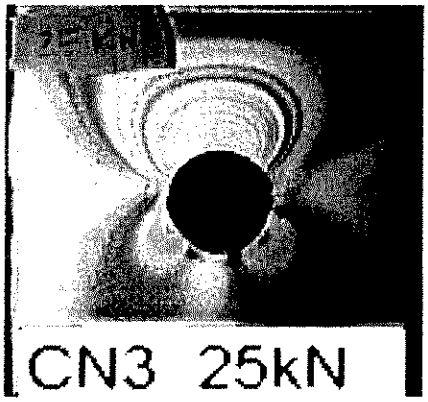

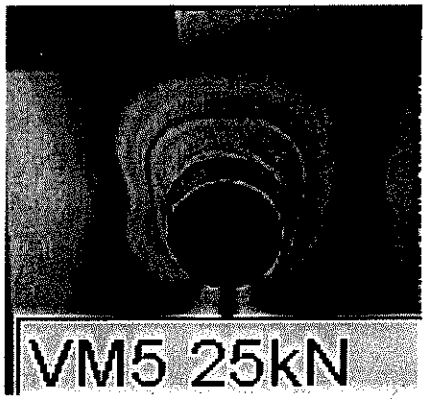

Figure 7.12: Isochromatic fringe patterns for 25 kN loading

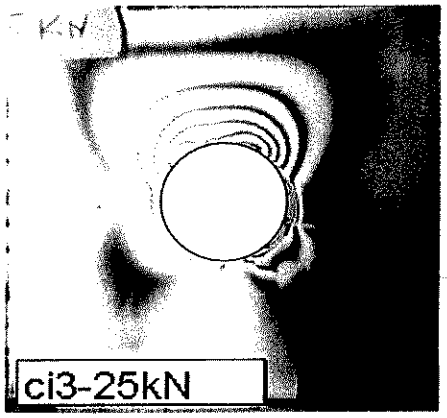

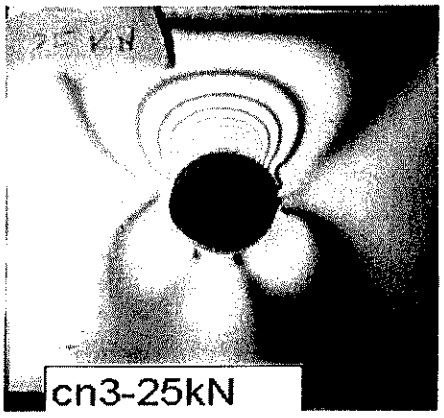

Figure 7.13: Monochromatic fringe patterns for 25 kN loading

Exact values at the pin interface were not extrapolated for this loading as the amount of fringes are bunched up together too close to each other resulting in a highly non-linear phenomenon occurring at the pin interface. Therefore all the percentages of strain relief quoted above are highly pessimistic. Due to the uncertainty and lack of accuracy of the fringe order at the pin interface, no graphs of birefringence as function of applied load were attempted. Despite the lack of graphical representation, it is clear that the maximum birefringence as a function of applied load is of a non-linear nature.

7.5 Correlation of Photoelastic Measurements to Finite Element Analysis Results

The simplest methodology to correlate the photoelastic measurements is to compare the fringe patterns and orders between the isochromatic or monochromatic photographs and the fringes obtained by running a finite element analysis. The maximum shear strain; equivalent to the fringes obtained during testing; was calculated within the finite element analysis STRAND61 by post-processing the principal strains as shown in equations (7.1), (7.2) and (7.3). The post-processing program [3], prompts for an input filename and writes results with the maximum shear strain on top, middle and bottom planes. The results are written as ε_1 to the post-processed file but they represent the maximum shear strain as calculated on Equations (7.1-7.3).

$$\varepsilon_1 = \varepsilon_{11} - \varepsilon_{22} \tag{7.1}$$

$$\varepsilon_2 = \varepsilon_{22} - \varepsilon_{33} \tag{7.2}$$

$$\varepsilon_3 = \varepsilon_{11} - \varepsilon_{33} \tag{7.3}$$

The post-processed results from (7.1) were then displayed graphically for each tested configuration. The maximum shear strain contours for the no-insert configuration are displayed 2.5 mm away from the pin loaded hole. This avoids the need to extrapolate any results for comparing fringes between test and analysis. The 2.5 mm represent the necessary clearance between the pin and the photoelastic coating as mentioned previously.

The maximum shear strain contours for the no-insert configuration are shown in Figure 7.14. The remaining plots for both the circular insert and the optimised insert configuration are depicted in Figures 7.15 and 7.16. The contours shown for both insert configurations are obtained at the aluminium insert / composite plate interface. A different amount of fringes is shown on each configuration to simplify their display.

The load applied for all the finite element models depicted in Figures 7.14, 7.15 and 7.16 correspond to the first series of tests carried out. As the load applied to the first series of tests was 10 kN and consisted on two back to back specimens being tested simultaneously, the load applied on the models corresponds to 5 kN. The models employed to calculate the maximum shear strains are identical to those employed in Chapter 4 for calculation of interface stresses for all tested configurations.

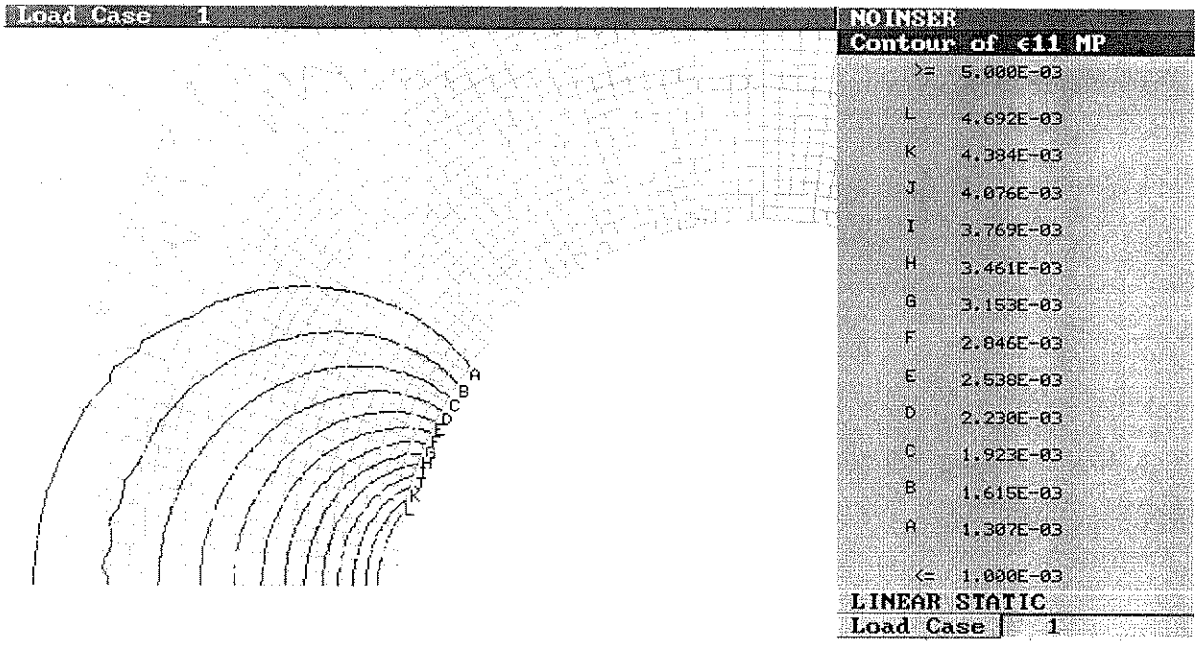

Figure 7.14: Maximum shear strain contours for the no-insert configuration

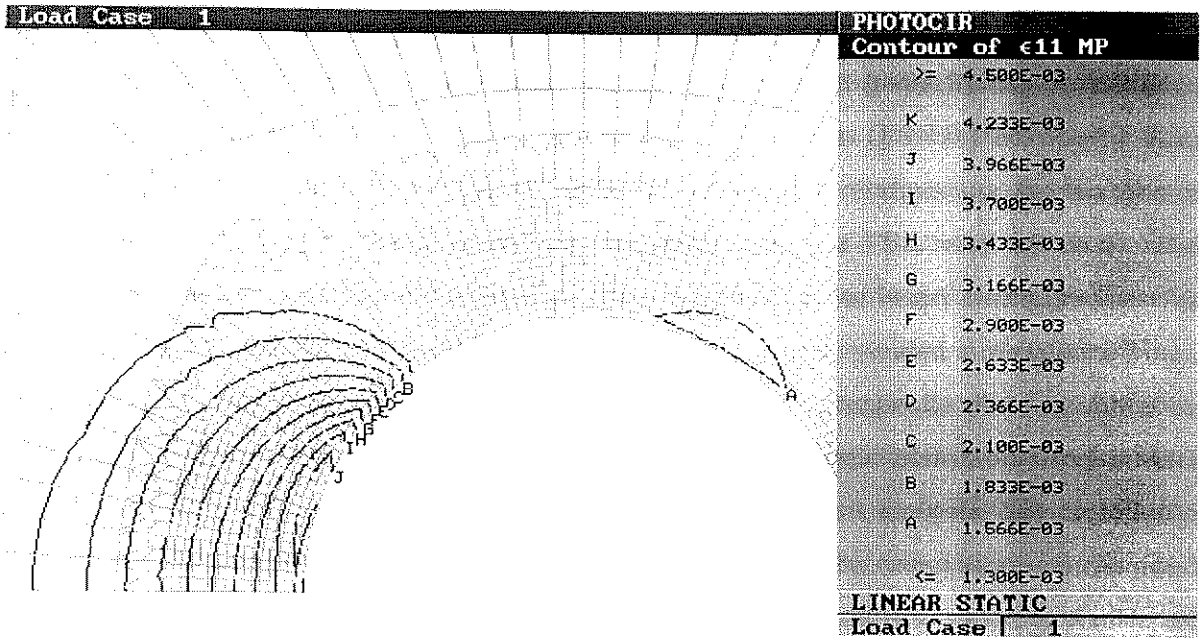

Figure 7.15: Maximum shear strain contours for the circular insert configuration

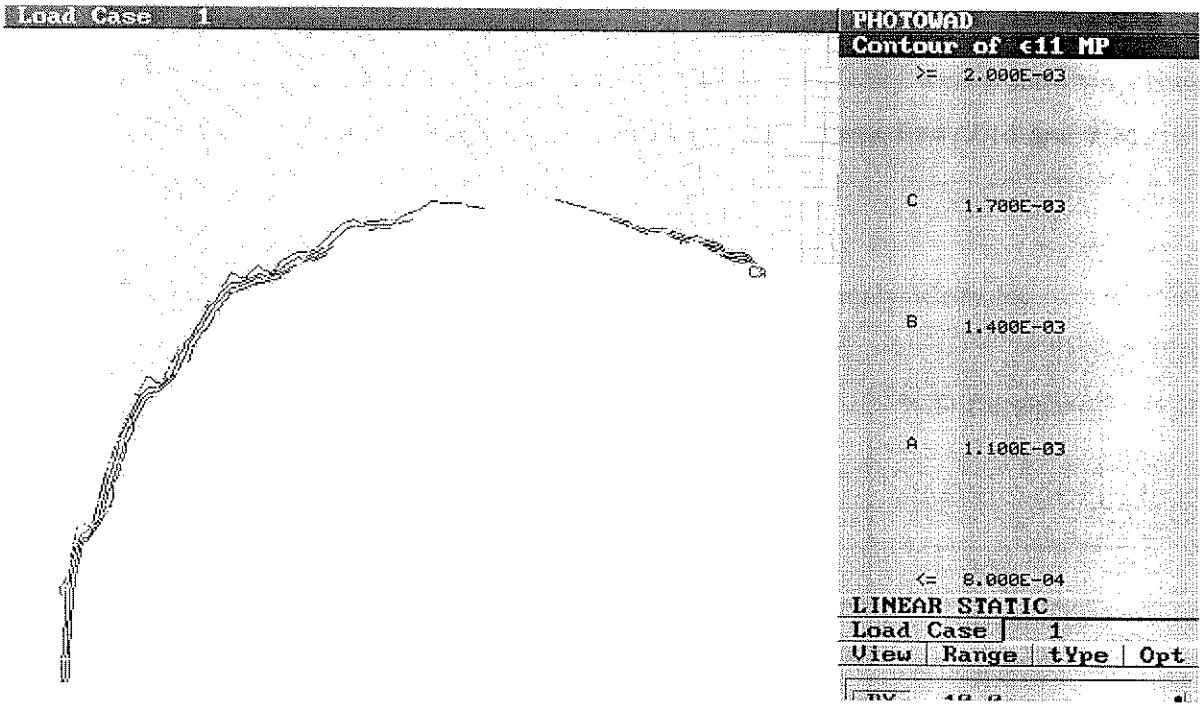

Figure 7.16: Maximum shear strain contours for the optimised (Von Mises) insert configuration

The fringes or contours of maximum shear strain displayed on the finite element results are expressed in microstrains. The photoelastic constant given by the photoelastic coating manufacturer for the coating employed on all specimens (PS-1B thickness=2 mm, "K" factor 0.15) was of "f" =960 με / fringe. Based on this relationship, the maximum fringe order obtained for the no-insert configuration from the FEA was 4.9 at 0°. The maximum fringe order (maximum birefringency) for the circular insert configuration was again at 0° with a magnitude of 4.4. Finally, the optimised insert yielded a maximum fringe order of 1.8 evenly distributed along the aluminium insert / composite plate interface. A tabular comparison is made in Table 7.6 between the photoelastic measured fringe orders and the maximum shear strains obtained from the finite element analysis. For correlation purposes, values corresponding to test results were averaged. The correlation is quite good considering the accuracy of photoelastic measurements. It is interesting to note that in all cases, the predicted magnitudes for maximum shear strain at the interface (whether close to the pin or at the composite / insert interface) were larger than those obtained by testing. It is likely that the larger predicted maximum shear strain values are a result of using the given fringe value of coating given by the manufacturer instead of the one obtained by calibrating the coating. Furthermore, the accuracy between predicted and test results increased significantly for the optimised insert. The patterns also correlate very well when comparing the isochromatic fringe patterns depicted in Figure 7.7 with Figures 7.14, 7.15 and 7.16.

Table 7.6: Comparison between test and finite element analysis results

Type of specimens	Maximum fringe order **TEST** RESULTS	Maximum fringe order **F.E.A** RESULTS	% Difference
No inserts	4.15	4.9	15
Circular inserts	3.75	4.4	15
Von Mises inserts	1.73	1.8	4

Although no failure correlation is possible since the second batch of specimens were not tested to failure, "BOLT" code predictions are presented to give an indication on predicted failure modes and loads. The reasons for not testing the specimens to failure were twofold. Firstly, the load capacity of the INSTRON machine employed was only 30 kN. Since the specimens were tested back to back due to the photoelastic measurements requirements each specimen could be tested to a maximum of 15 kN only, compared to the minimum predicted failure load of 27.65 kN. Secondly, although it would have been interesting to assess failure, the main goal of the testing program was to correlate predictions of strain relief in the linear elastic range (operational conditions) against FEA results to proof the overall concept.

The predicted failure load for the no-insert configuration was 27.65 kN and the predicted failure mode was bearing at 0° (coincident to load direction) with failure initiating at a 45° ply. The failure load predicted for the circular insert configuration was 36.3 kN with all remaining failure parameters identical to those predicted for the no-insert configuration.

7.6 Conclusion

The results are quite conclusive in terms of strain concentration reduction achieved by the bonding of aluminium inserts in pin loaded holes. Also, results from the first batch of specimens indicate that the yield strength of the insert material is significant in determining any possible gains which could be achieved by placing metallic inserts in composite laminates.

Results from photoelastic analysis indicate that by distributing an equivalent amount of material in an optimum configuration, a larger reduction in strain concentration can be achieved. In fact, 55 % in maximum shear strain reduction was achieved with the optimised insert when comparing it to the strain concentration on the circular insert specimens. This further validates the approach in composite materials where by reducing the compressive stresses at pin loaded holes in bearing critical structures improves the efficiency of the joint. Maximum shear values are only used as a "tool" to allow for

correlation of test results to FEA predictions. The fact that the predictions of maximum shear strain values and fringe patterns were quite accurate when compared to actual test results, indicate that the remaining stresses predicted at the composite/insert interface should also be accurate (see Section 4.7.2).

This original approach could also be applied to repairs of primary structures where bearing failure has initiated and has been identified. The damaged area could be removed by enlarging the cut-out with the optimised shape after analysing and identifying all possible load paths. For a hole that is loaded in two main and opposite directions the optimum shape will approximate an ellipse with the major axis coincident with the direction of the load as shown in Chapter 4 (Multiple Load Case Optimisation).

When the direction of the principal load is not known, the best alternative is to bond a circular insert. It is further believed that the introduction of a cap (as shown on Figure 7.17) to the optimised metallic insert will further strengthen the joint by providing with a lateral constraint to the local buckling of fibres in contact with the metallic insert.

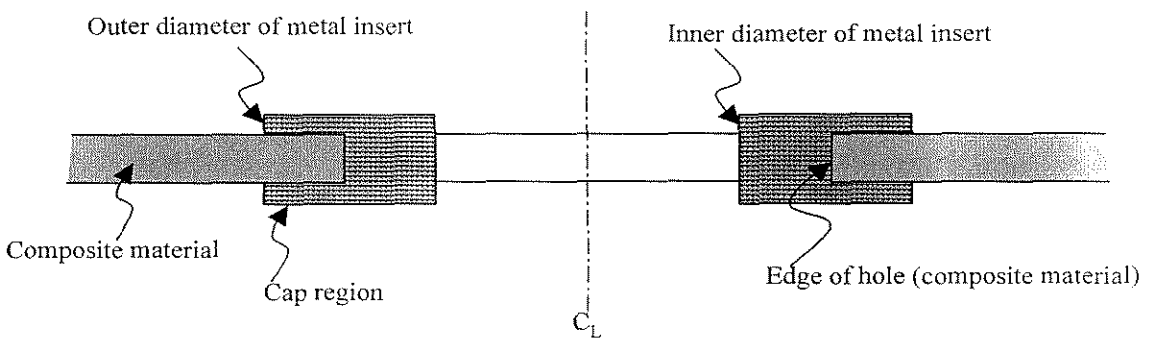

Figure 7.17: Integral metallic insert with cap

The concept of shifting and changing material properties to critically loaded regions or areas where stress concentrations limit the loading capability of highly loaded structures can be applied to numerous fields beyond aircraft structures.

The drawback is that the proposed methodology will be relatively costly due to the limited availability of water jet equipment necessary for producing the optimised cut-out shape and the requirement of wire cutting technology for the production of the optimised insert. The overall cost could be greatly reduced by the production of standard repair kits in which the inserts could be extruded. This will limit the cost to the production of the optimised shape cut-out. The alternative of employing circular inserts will be much cheaper than the optimised insert alternative but the efficiency of the joint might not be fully restored to design requirements.

7.7 References

[1] Chang, F. K., Scott, R. A., Springer, G. S., "Strength of Mechanically Fastened Composite Joints", Air Force Wright Aeronautical Laboratories, *Technical Report AFWAL-TR-82-4095*, June, 1982.

[2] Wang, J., Banbury, A., Kelly, D. W., "Evaluation of approaches for determining design allowables for bolted joints in laminated composites", CRC-ACS, 1997.

[3] Personal communication with Mr Stuart Wishart, swish@aero.aero.usyd.edu.au, 1997.

CHAPTER 8

EXPERIMENTAL EVALUATION OF COMPOSITE T-JOINTS

8.1 Introduction

Joints are best avoided due to their negative effect on structural efficiency. However, they are necessary due to production considerations and design requirements. From a manufacturing and repair viewpoint, large and complex structures are not viable to be formed in one process. This introduces the need for the joining of several components to produce the completed structure. When the components to be joined are orthogonal to each other, the transfer of load occurs in an out of plane mode. In this case, the lack of reinforcing fibres across plies results in low out-of-plane strength. This low strength is a result of the failure being dominated by the resin properties. The added stress concentrations due to joint geometry and manufacturing considerations can lower the joint efficiency even further. To increase the out-of-plane load carrying capability of these joints, it becomes imperative to fully understand their behaviour up to failure. Only then, an improved out-of-plane load transfer mechanism could be found. One of the proposed ways to increase the out of plane load transfer capacity of composite T-joints found in the literature is by adding an insert in the resin rich area [1, 2, 3]. A 3-D woven insert trialed by Lockheed has shown to increase the pull-off strength by approximately 45% [3].

Out-of-plane joints can be found both in marine and aircraft structures. Typical marine structures involving the transfer of load between two orthogonally placed plate shells are deck-to-bulkhead joints, shell-to-bulkhead and floor-to-tank-top joints [4]. Tee joints in aircraft structures are found in wing/inlet connections, integrally composite spars and in hinge/spar connections [1, 2, 5]. Figure 8.1 shows a series of out-of-plane joints used in both the aircraft and marine industries. In the current and following Chapter the term out-of-plane is referred to the plane formed by the flange as shown on Figure 8.2. That is, the loading occurs orthogonally to the plane defined by the flange of the T-section.

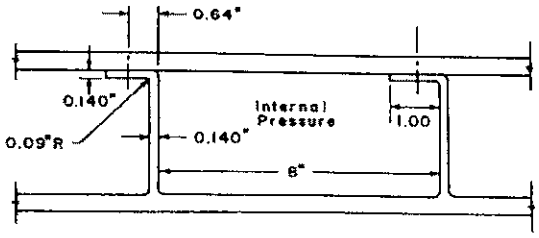

(a) Reference [2]

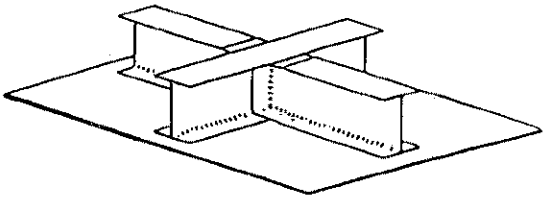

(b) Reference [3]

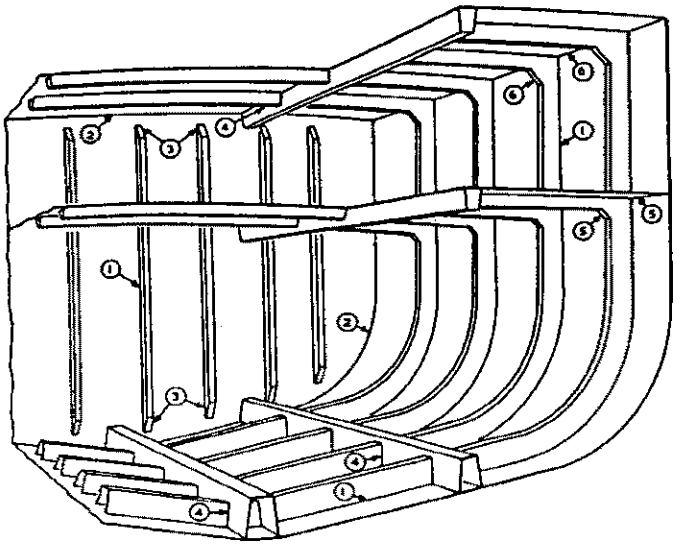

(1) Frame/shell
(2) Bulkhead/shell
(3) Stiffener ending
(4) Stiffener intersection
(5) Deck-edge (tee)
(6) Deck-edge (knee)

(c) Reference [4]

Figure 8.1: Different out-of-plane joints used in the aircraft and marine industries

The out-of-plane characteristics of composite T-sections are evaluated experimentally in this Chapter and computationally with detailed finite element analysis, in Chapter 9.

This chapter details the procedure adopted for the testing of composite T-joints. The goal of the testing program is to determine important parameters that determine out-of - plane strength of T-joints. Different types of carbon fibre inserts were placed in the resin

rich area of composite T-joints subjected to tension (pull-out) force. The main variable between the different types of inserts was their fibre orientation. The effects of the fibre orientation and size of the insert were assessed by testing all specimens to failure. A single strain gauge at the underside of the web/flange junction was employed to investigate the transfer of load between the web and flange area. Two side strain gauges were also employed to monitor in-plane loading in the first batch of specimens. Photoelastic techniques were employed on the second batch of specimens to determine highly strained regions prior to failure.

8.2 Geometry of test specimens

The dimensions of both batches of specimens tested under tensile loads are shown in Figure 8.2. The parameters for which dimensions are not given on the sketch are tabulated below on Table 8.1.

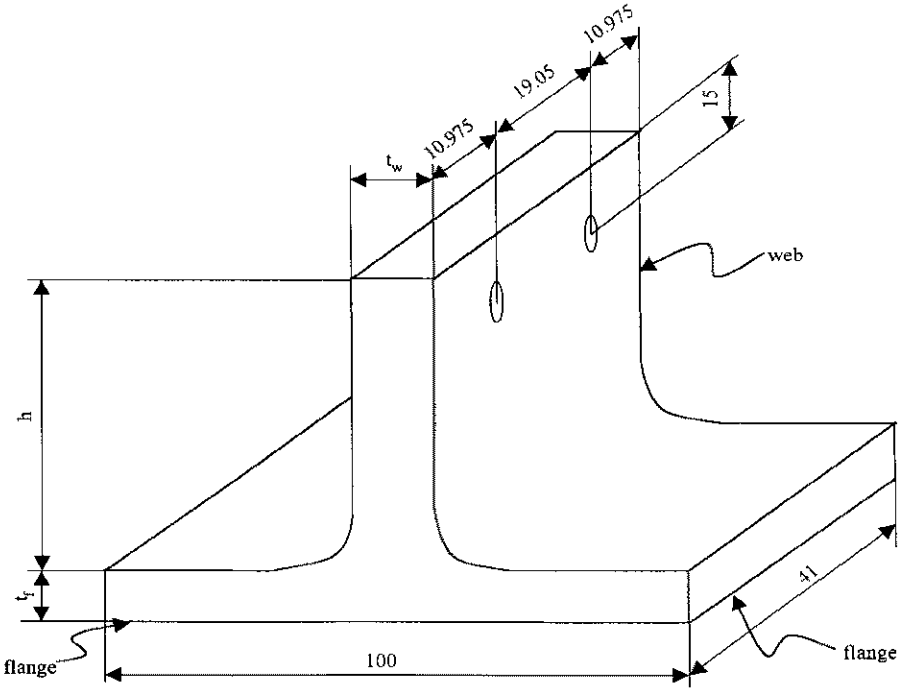

Figure 8.2: Generic specimen dimensions

Table 8.1: Specimen dimensions for all specimens

	t_w	t_f	h
	Web thickness	Flange thickness	Web height
	(mm)	(mm)	(mm)
First specimen batch			
2 mm nominal web thickness	2.15	1.7	48
5 mm nominal web thickness	5.24	3.2	48
10 mm nominal web thickness	10.45	5.85	48
Second specimen batch			
2 mm nominal web thickness	1.82	1.99	65
9.6 mm nominal web thickness	9.12	3.35	65

8.3 Lay-up and Insert Configuration

8.3.1 First batch of specimens

The ply lay-ups for different first batch specimens are given below:

2mm web thickness (14 plies across the web):

$$\left[\pm 45 / 0_3 / 90 / 0\right]_S$$

5mm web thickness (34 plies across the web):

$$\left[\pm 45 / 0_2 / 90 / 0_2 / \pm 45 / 0_3 / 90 / 0_2 / 90 / 0\right]_S$$

10 mm web thickness (68 plies across the web):

$$\left[\pm 45/0_2/90/0_2/\pm 45/0_3/90/0_2/90/0/\pm 45/0_2/90/0_2/\pm 45/0_3/90/0_2/90/0\right]_S$$

The flanges of the specimens were layed up as half the web, and then had another four plies added to the base. These plies were oriented, from the bottom as follows: [90/0/$\pm$45]. This resulted in an asymmetric lay-up in the flange region. A sketch of ply orientations and filler orientations applicable to all T joint specimens is shown in Figure 8.3.

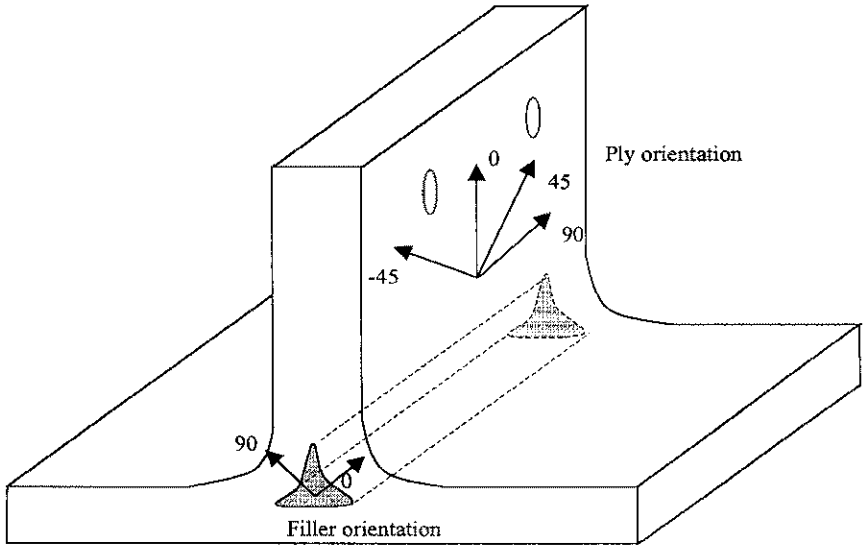

Figure 8.3: Ply and filler orientation

The detail lay-up of the 2 mm nominal web thickness specimens is depicted in Figure 8.4. The same ply referencing system was employed for both the 5 and the 10 mm nominal web thickness specimens.

Three T-joints configurations were manufactured and will be referred to as the following configurations: a) no filler, b) uni-directional filler and c) two-directional filler. Both uni-directional and two-directional filler configurations are depicted in Figure 8.5.

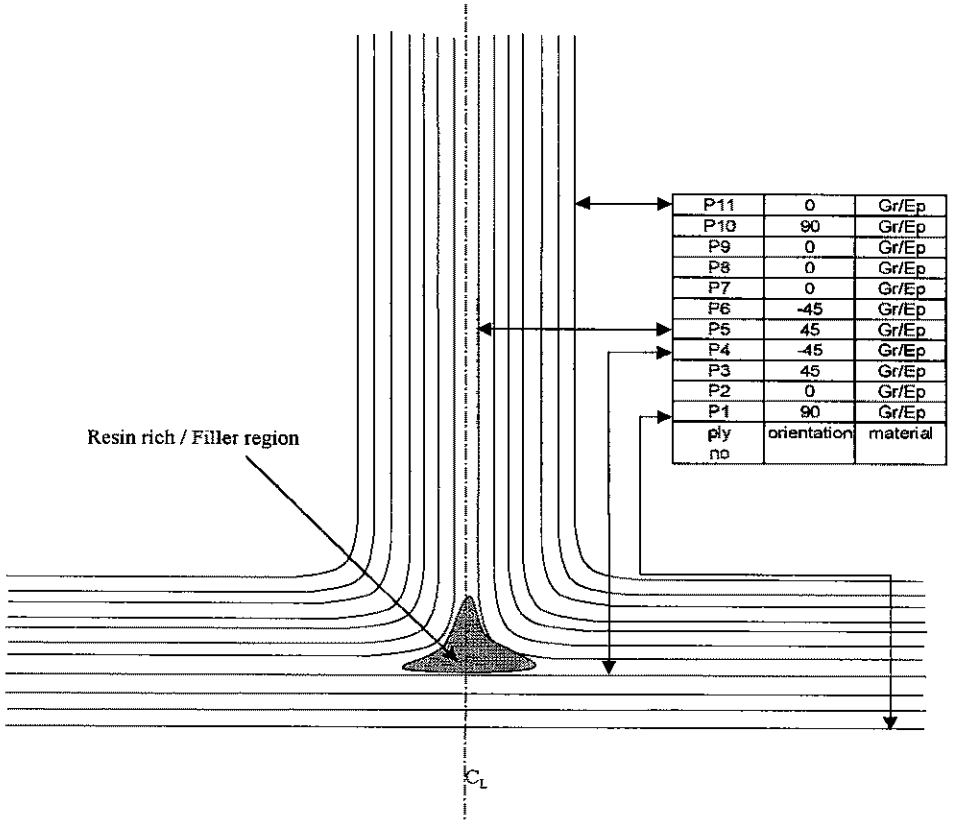

ply no	orientation	material
P11	0	Gr/Ep
P10	90	Gr/Ep
P9	0	Gr/Ep
P8	0	Gr/Ep
P7	0	Gr/Ep
P6	-45	Gr/Ep
P5	45	Gr/Ep
P4	-45	Gr/Ep
P3	45	Gr/Ep
P2	0	Gr/Ep
P1	90	Gr/Ep

Figure 8.4: Detailed lay-up of 2 mm nominal web thickness (1st batch specimens)

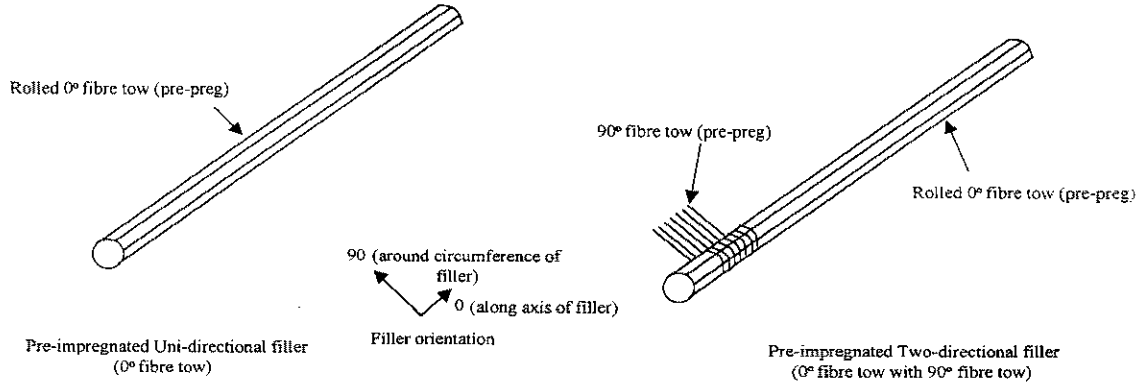

Figure 8.5: Filler configurations

8.3.2 Second batch of specimens

The ply lay-up for second batch specimens is given below:
2 mm nominal web thickness (12 plies across the web):

$$[0/90/\pm 45/90/0]_s$$

The flanges of the specimens for the second batch of specimens were layed up as half the web, and then had another eight plies added to the base. These plies were oriented from the bottom, as follows: [0/90/0/0/$^{+}_{-}$45/90/0]. This resulted in an asymmetric lay-up (14 plies) in the flange region. The detail lay-up of the 2 mm nominal web thickness specimens is depicted in Figure 8.6.

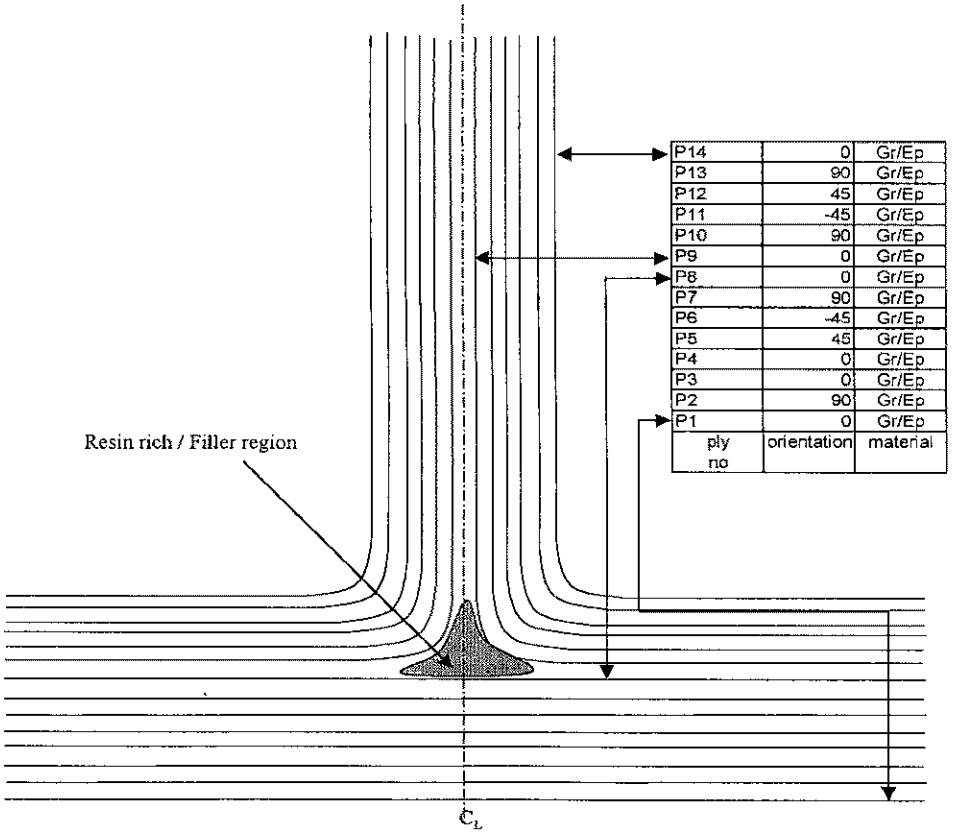

Figure 8.6: Detailed lay-up of 2 mm nominal web thickness (2nd batch specimens)

Four different T-joints configurations were manufactured within the second batch of specimens. The following configurations were employed and will be referred as follows: d) no filler, e) uni-directional filler (0 deg fibre tow), f) bi-axial filler (bi-axial carbon sleeve) and g) three-directional filler. The uni-directional filler configuration employed for the second batch of specimens was identical to that employed for the first batch of specimens (see Figure 8.5). Photographs of the two-directional and three-directional filler configurations are depicted in Figure 8.7.

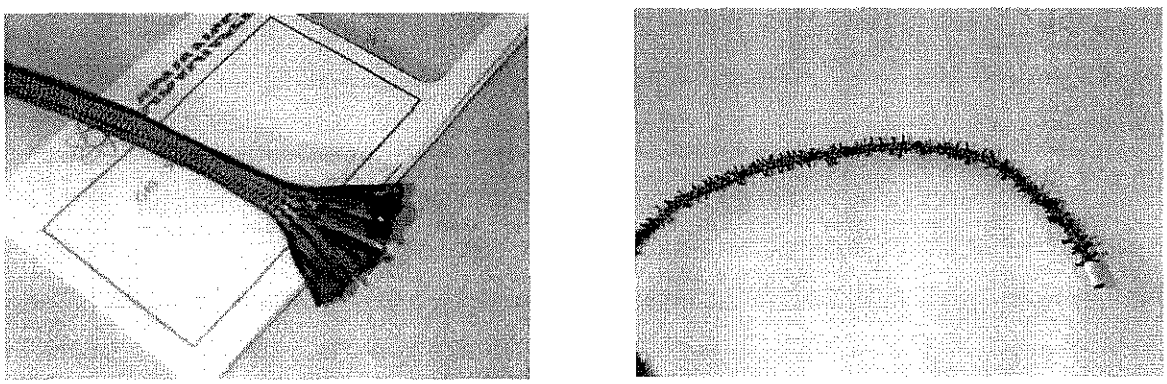

Figure 8.7: Two-directional and three-directional filler configurations

A thicker batch of specimens using the same material as the above four T-joint configurations was manufactured. These specimens had no inserts and were laid-up as follows:

9.6 mm nominal web thickness (60 plies across the web):

$[^{+}_{-}45/0/90/^{+}_{-}45/0/90/^{+}_{-}45/90/0/^{+}_{-}45/0/90/^{+}_{-}45/0/90/^{+}_{-}45/^{+}_{-}45/0/90/^{+}_{-}45/0/90]_s$

From the 60 plies, the inner 36 plies were dropped-off at the web/flange intersection. The same ply referencing system as depicted in Figure 8.3 was used for these specimens. The nominal flange thickness is 3.5 mm (22 plies) with the following asymmetric lay-up:

[$\pm$45/0/90/$\pm$45/0/90/$\pm$45/90/0/0/90/90/0/90/0/90/0/$\pm$45]

8.4 Tooling and manufacturing details

Test specimens within the first batch were made from Hy-E3034K – Thornel T-300 (12K) fibres in Fiberite 934 epoxy resin (uni-directional prepreg tape) with a 177 °C cure temperature. The cure cycle employed for the first batch of specimens is shown in Figure 8.8.

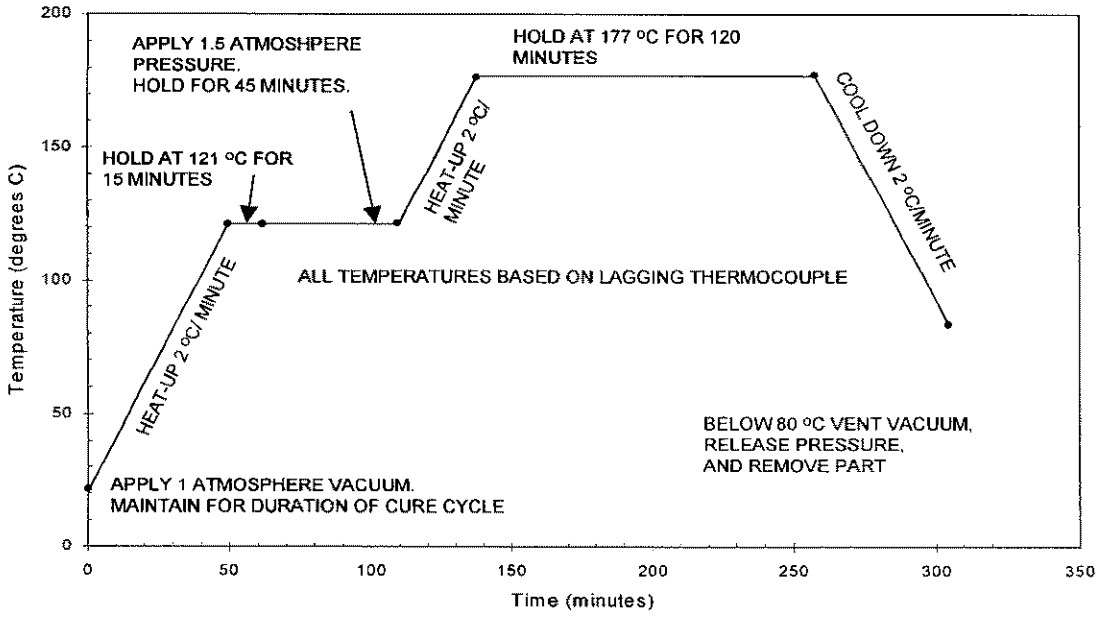

Figure 8.8: 177 °C Cure Cycle for Hy-E3034K – Thornel T300/Fiberite 934 Prepreg

The second batch of specimens were made from T5A145-F584 – Hercules IM6 (12K) fibres in Hexcel F584 epoxy resin (uni-directional prepreg tape) with a 177 °C cure temperature. The bracketed values on the material specification (12K) indicate the number of fibres in 1000s per tow. The cure cycle used for most of the second batch specimens (all 2 mm nominal web thickness specimens) is shown in Figure 8.9.

Thicker specimens (9.6 mm nominal web thickness) employed a variation of the cure cycle depicted in Figure 8.9; as follows:

a) Vacuum debulk (0.8 atmosphere) every 10 plies.
b) While the pressure for thin laminates could be varied between 3 and 6.8 atmosphere, the pressure specified for thick laminates is 5.8 atmoshpere.
c) Dwell at 65 °C for 1 hour.
d) Dwell at 120 °C for 2 hours.
e) Dwell at 135 °C for 1 hour.
f) Dwell at 150 °C for 1 hour.
g) Cure and complete cycle as per cure procedure for thin laminates.

The tooling employed for all specimens consisted of two angle irons used to lay-up half the web and flange, which were then aligned face to face with the assistance of guiding screws and placed on a flat caul plate. This enabled four specimens of a single thickness with the same filler to be produced at one time.

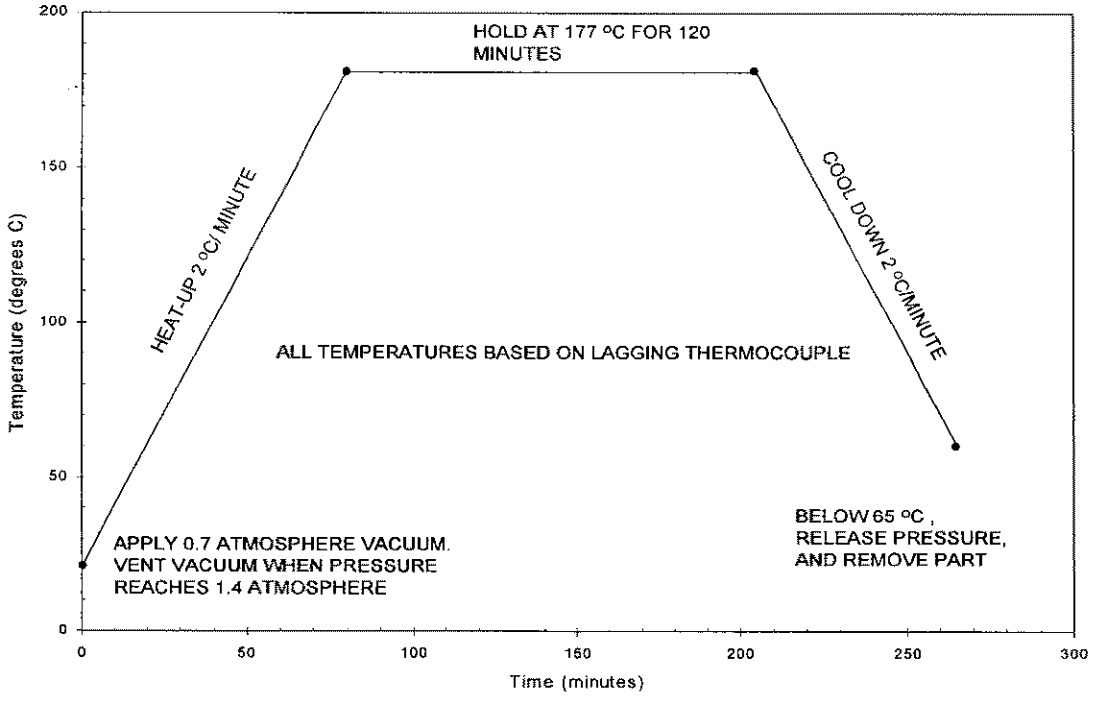

Figure 8.9: 177 °C Cure Cycle for T5A145-F584 – Hercules IM6/Hexcel F584 Prepreg.

To enable different thicknesses of webs to be manufactured from the same moulds, milled bars were chosen as spacers between the two angle irons for the various thicknesses.

8.5 Test fixture

8.5.1 Set-up and typical dimensions

Typical specimen dimensions together with strain gauges positions and pull-out test configuration are shown in Figure 8.10. Strain gauges for the first batch of specimens were bonded to both sides of the web to determine in-plane and any spurious bending out-of-plane loading post failure, and to the under side of the web/flange junction to assess load transfer to the flange. The second batch of specimens had only a single strain gauge at the under side of the web/flange junction. The two web strain gauges were omitted as it was found that the effect of asymmetric loading on the first batch of specimens was negligible.

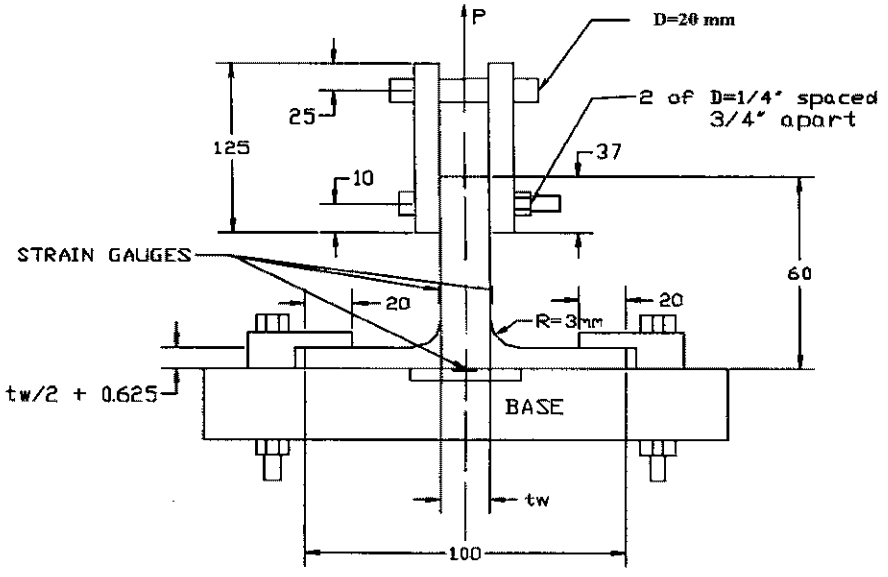

Figure 8.10: Experimental set-up for pull-out test (where t_w= 2, 5 and 10 mm for different batches of specimens).

The pull-out tests were performed in an Instron 1195 (50 kN load cell) machine under displacement control at 0.1 mm/min for the first batch of specimens and in an Instron 5567 (30 kN load cell) at 0.5 mm/min for the second batch of specimens.

8.6 Data acquisition

8.6.1 Strain gauge installation

Load, displacement and strain readings for all strain gauges were continuously monitored using both Instron software and Labview coupled to a SCXI 4-Channel Isolation Amplifier with excitation. The theoretical background to strain gauge measurements is described in Section 6.3 of Chapter 6. The positions of the strain gauges are shown on Figure 8.10.

8.6.2 PhotoStress Analysis

The photoelastic coating material was carefully selected to ensure maximum sensitivity to fringe measurements. Solid flat sheets were selected due to their uniform thickness and ease of machining. An approximate fringe value or coating sensitivity was calculated from finite element analysis performed on a T-joint with no-insert. The maximum shear strain was obtained from the above analysis and the fringe order desired was set to 4. The fringe value is calculated from (8.1). Once this value has been established, the type and thickness of the coating can be determined from (8.2).

$$f = \frac{\varepsilon_1 - \varepsilon_2}{N} = \frac{\gamma_{MAX}}{N} \tag{8.1}$$

$$f = \frac{\lambda}{2t_c K} \tag{8.2}$$

The mathematical relationship in (8.2) was plotted parametrically by the photoelastic coating manufacturer [6]. From this graph, a medium sensitivity plastic was chosen with a 2mm thickness. The strain-optic coefficient (K) for the PS-3 coating chosen was 0.02. The reinforcing effect of the coating was considered negligible due to its relative low modulus when compared to the carbon fibre prepreg. The material properties of the chosen coating are stated in Table 8.2.

Table 8.2: Material properties of photoelastic coating

Strain Optical Coef. K	Elongation (%)	Elastic Modulus E (GPa)	υ	Thickness		Sensitivity Constant to (°C)	Max. Useable Temp. (°C)
				(mm)	Tolerance (mm)		
0.02 typical	30	0.21	0.42	2.05	±0.08	40	200

A 030 Series Modular Reflection Polariscope was employed to measure stress gradients and highly stressed areas. Unfortunately, the optional telemicroscope accessory was not available. This accessory is normally employed for measurements on small parts or in regions of high stress concentration. The measurements performed on the T-sections at the web/flange intersection (small area of approximately 8x10 mm) had to be carried out by disassembling the analyser from the light source and by employing a separate electronic microscope. The polariser; which consisted in a small camera filter; had to be rotated manually until the fringes could be seen. Furthermore, to be able to shine the white light at the right angle and position, a flexible light source had to be employed. This resulted in very poor fringes that could not be assessed quantitatively. These problems where not present for the photoelastic analysis carried out on pin-loaded joints where very good quality results were obtained.

8.7 Test results and discussion of first batch specimens

A total of 17 specimens were tested for the first batch, as listed in Table 8.3.

A typical load-displacement curve for the T-joints tested is shown in Figure 8.11. The decrease in load at the end of the graph resulted from the fact that the test was conducted under displacement control. The sharp drop in load also indicates the presence of an unstable crack growth which resulted in the failure of the specimen.

Table 8.3: First batch experimental results: A - no filler, B - uni-directional filler (0 deg fibre tow) and C - two-directional filler (0 deg fibre tow wrapped with 90 deg fibre tow).

SPECIMEN NO	WEB THICKNESS (mm)	FILLER TYPE	FAILURE LOAD damage initiation load (N)	FAILURE STRAIN AT UNDER SIDE WEB/FLANGE JUNCTION (με)
T2-NF-1	2	A	1132	4339
T2-NF-2	2	A	1111	5236
T2-0-1	2	B	567	2569
T2-0-2	2	B	541	2224
T2-090-1	2	C	409	1799
T2-090-2	2	C	318	1445
T5-NF-1	5	A	1311	2713
T5-NF-2	5	A	923	2252
T5-0-1	5	B	720	1757
T5-090-1	5	C	977	1806
T5-090-2	5	C	835	2037
T10-NF-1	10	A	2330	1918
T10-NF-2	10	A	3262	2521
T10-0-1	10	B	3753	3926
T10-0-2	10	B	2967	2079
T10-090-1	10	C	3113	2055
T10-090-2	10	C	4098	2901

All specimens behaved linearly up to the presence of the first crack growth. After this event, non-linear behaviour was observed in most of the specimens. The graphs of load versus flange strain indicate a similar phenomenon to that seen on the load versus displacement graphs. The failure load, can thus be determined from either of these curves. A typical graph of the load versus strain in the under-side of the web/flange intersection is shown in Figure 8.12.

The location of the failure initiation was surprisingly similar for most of the specimens regardless of insert type and web thickness. A similar observation was reported by Pointer et.al [7], on the evaluation of T joints with different filler materials and types such as adhesive and braided inserts. The initiation of failure appears to be dominated exclusively by the resin properties and the radius at the web/flange intersection. Failure started in most of the specimens right above the "resin rich area" between the block of three 0° plies closest to the centre line. A photograph showing the failure initiation site on a specimen with t_w=5 mm (web thickness) can be seen in Figure 8.13.

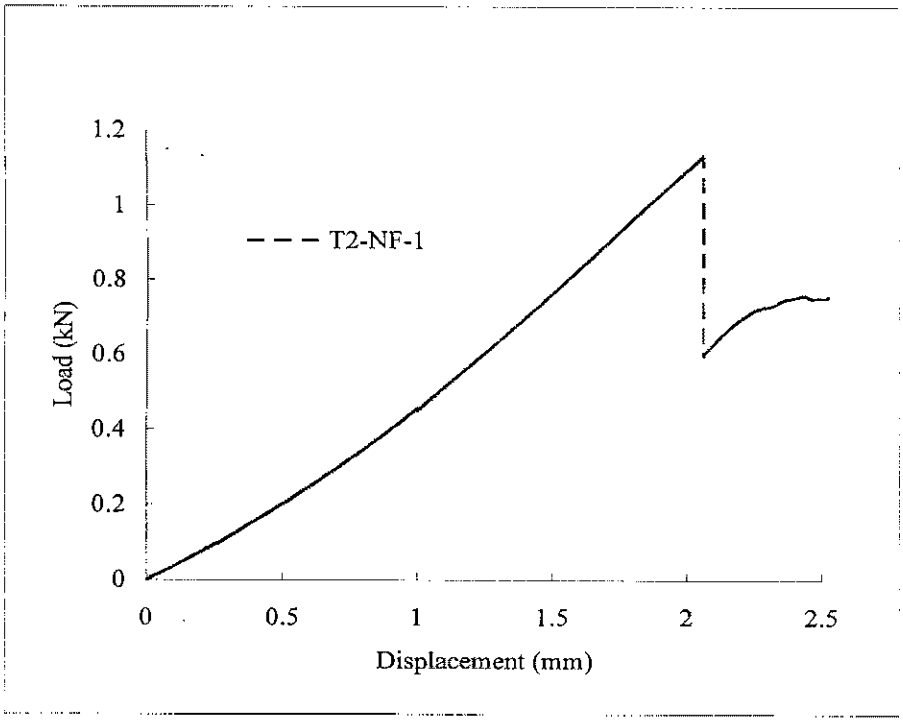

Figure 8.11: Typical load-displacement curve

Again in most of the specimens, the crack started on one side of the web only. The reason for the asymmetric failure initiation is due to the lack of perfect symmetry in the far field load. This was observed with the aid of side strain gauges; bonded to either side of the web; as a strain differential. This strain differential is shown in Figure 8.14 (Graph of Load versus web side strain). Running a finite element analysis, including some bending, assessed the effect of asymmetric loading. The results showed that the stresses at the critical elements do not vary considerably (approximately 1%). Furthermore, scatter present in the damage initiation load and in the strain reading makes difficult assessing the efficiency of the joint due to the different inserts.

The failure loads for each of the specimens tested, together with the strain readings obtained at the under side of the web/flange junction (see Figure 8.10) are listed in Table 8.3.

From this table, some important conclusions can be drawn. Firstly, for the 2 mm web, the failure load in tension actually decreases with the addition of the two types of fillers employed. Configuration B being up to 50% weaker than the no filler configuration. The weakest configuration was C with a 67% reduction in failure load.

A graphical representation showing the average strength comparison between different filler configurations is shown in Figure 8.15. A similar trend but with up to 35% reduction in failure load can be observed for t_w=5 mm (web thickness). The difference being that configuration C appears to outperform configuration B by 20%. Figure 8.16 depicts the average strength comparison for t_w=5 mm. Specimens with t_w=10 mm present an opposite trend to the remaining T-joints. In this latter case, placing both types of different inserts increases the strength of the T-joint. Configuration C appears to be the strongest (22% larger failure load when compared to the no-filler configuration A) followed closely by configuration B. A bar chart showing a comparison of average strength for t_w=10 mm is depicted in Figure 8.17.

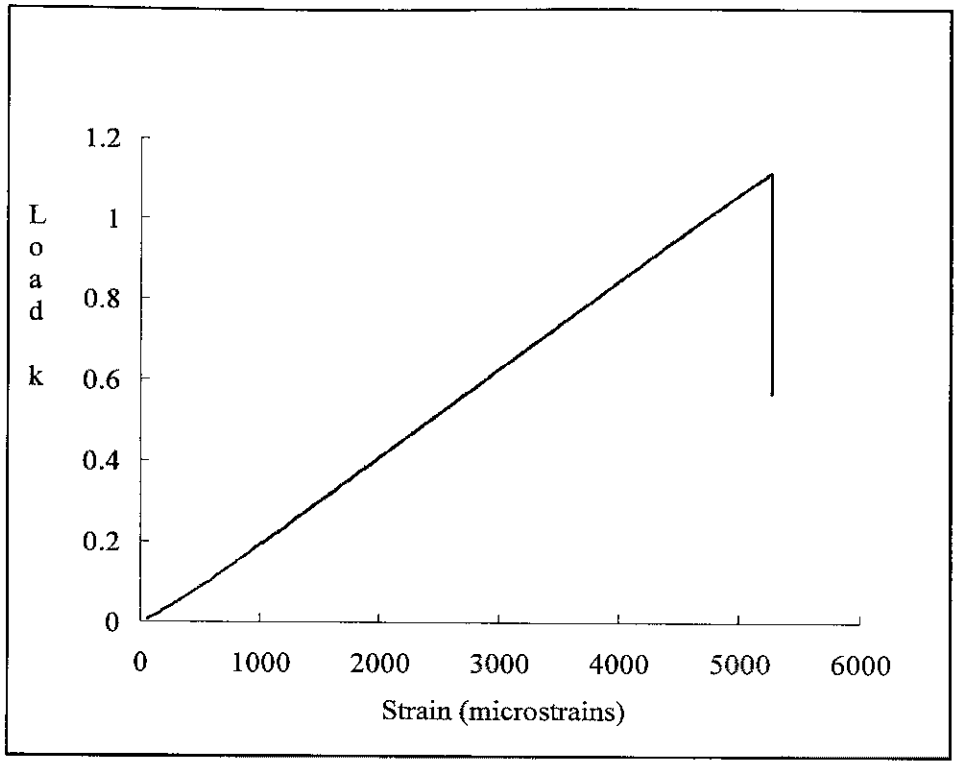

Figure 8.12: Typical load versus strain at underside of web/flange junction

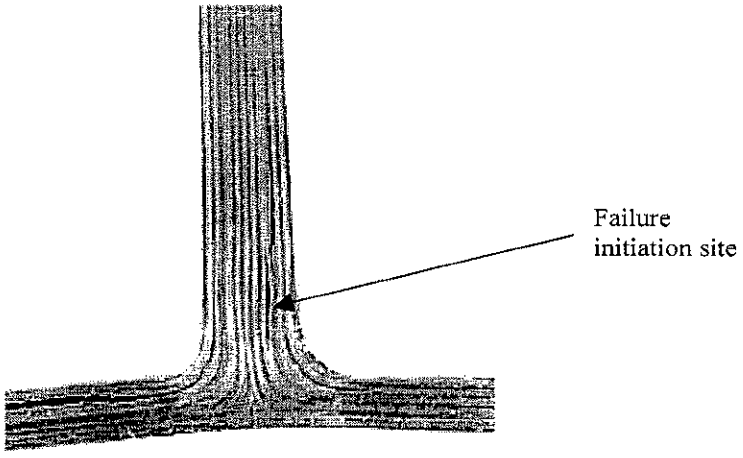

Figure 8.13: Typical failure initiation site
(photograph corresponds to T-Joint with t_w=5 mm)

The load transfer into the flange area does not appear to change with the inclusion of inserts in the resin rich region. Using linear regression analysis assessed this. A maximum discrepancy of 10% of the average strain magnitude was found.

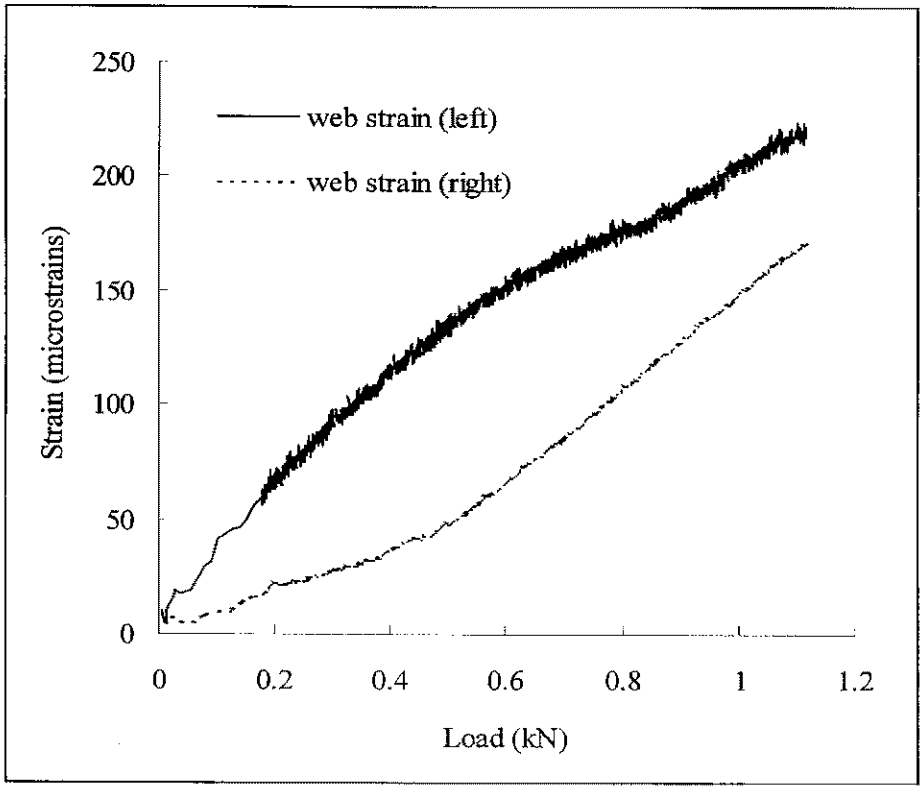

Figure 8.14: Load versus web strain at either side of web

In general, from the observation of failure initiation location across all specimens it can be concluded that the insert type had very little or no influence on the initiation site. On the other hand, the insert types appear to have a significant influence on the failure load.

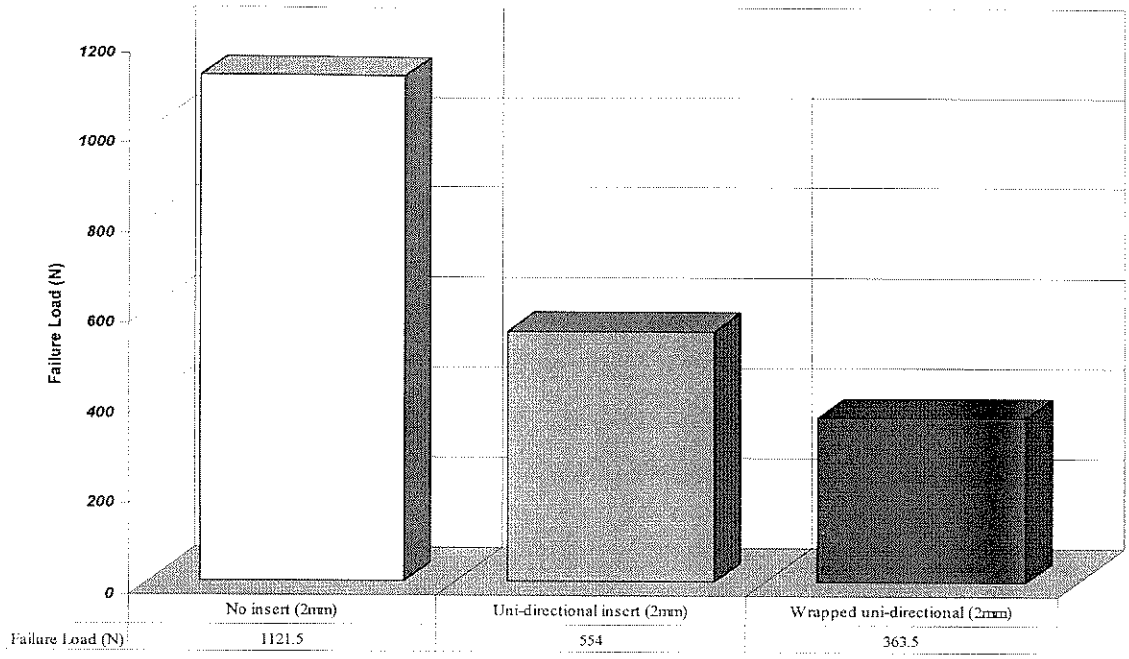

Figure 8.15: Strength comparison for different inserts (2mm nominal web specimens)

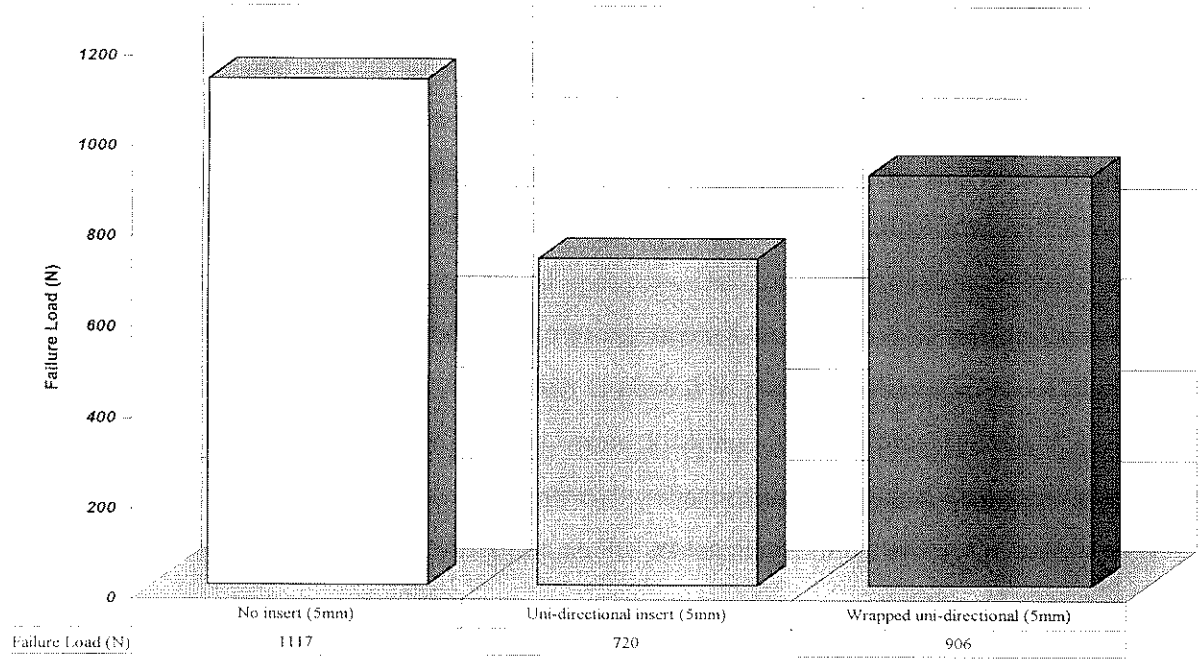

Figure 8.16: Strength comparison for different inserts (5mm nominal web thickness)

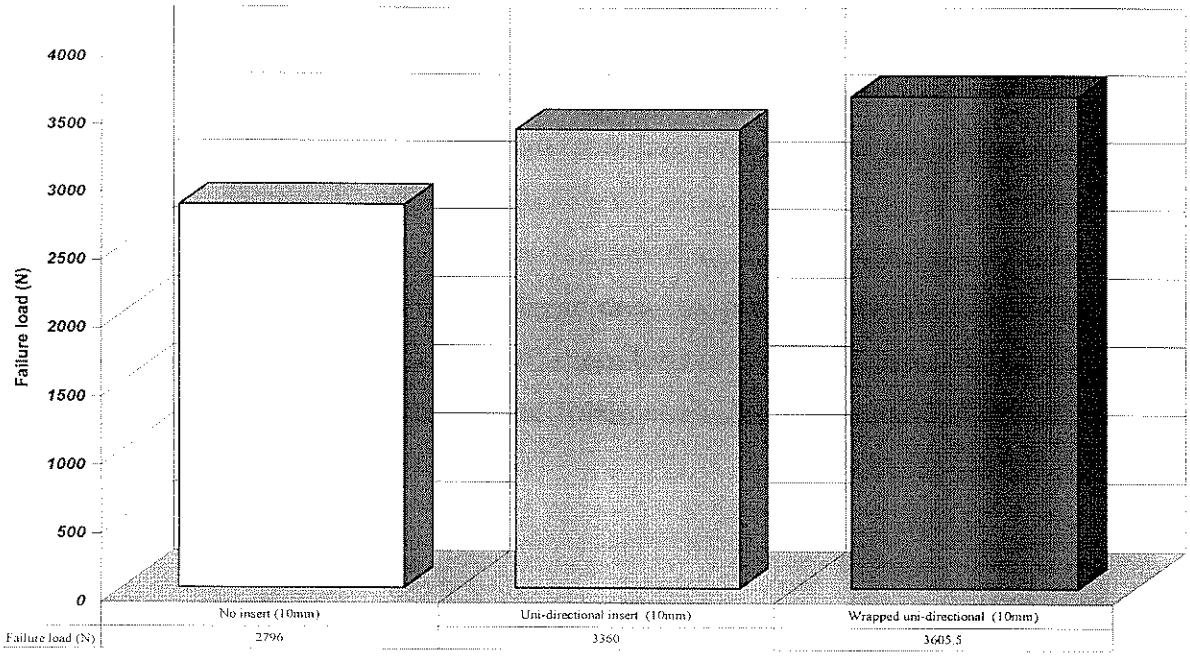

Figure 8.17: Strength comparison for different inserts (10mm nominal web thickness)

From the results listed in Table 8.3, it can be concluded that a second important variable which affects the failure load is the web thickness. It appears that for very thick sections, the addition of inserts in the resin rich area redistributes the stresses so as to delay the failure at which the web delaminates. An explanation of the above phenomenon can be found by closely examining the distorted ply geometry resulting from placing an oversized insert onto the resin rich area of specimens with t_w=2 mm and t_w=5 mm . In the specimens with no insert, the plies tend to move inwards of the T-joint filling the void at the web/flange intersection. When the insert is placed in position and later cured, the plies are restricted from moving inwards thus some kinking of the fibres around the radius occurs. This in turn produces a geometric discontinuity which creates a stress concentration and has a negative influence on the stress distribution along the web.

For thicker specimens with t_w=10 mm, the plies also tend to migrate inwards of the joint but the main difference is that the plies have a larger area in which to redistribute

themselves. Another contributing factor appears to be the height of the separation point of the two 0 ° plies which lie in the symmetry line. For t_w=2 mm and t_w=5 mm, the higher this separation point the weaker the joint. The thickest specimens show a similar trend between the two types of inserts employed. Only the no filler configuration A (t_w=10 mm), which has the lowest separation point and the lowest failure load, does not follow this trend.

Strain gauge values recorded below the web/flange intersection, provided an insight on load transfer from the web to the flange area. A performance indicator is proposed where the flange strain is divided by the failure load of the joint. These values are plotted in Figures 8.18, 8.19 and 8.20 for 2, 5 and 10mm nominal web thicknesses respectively.

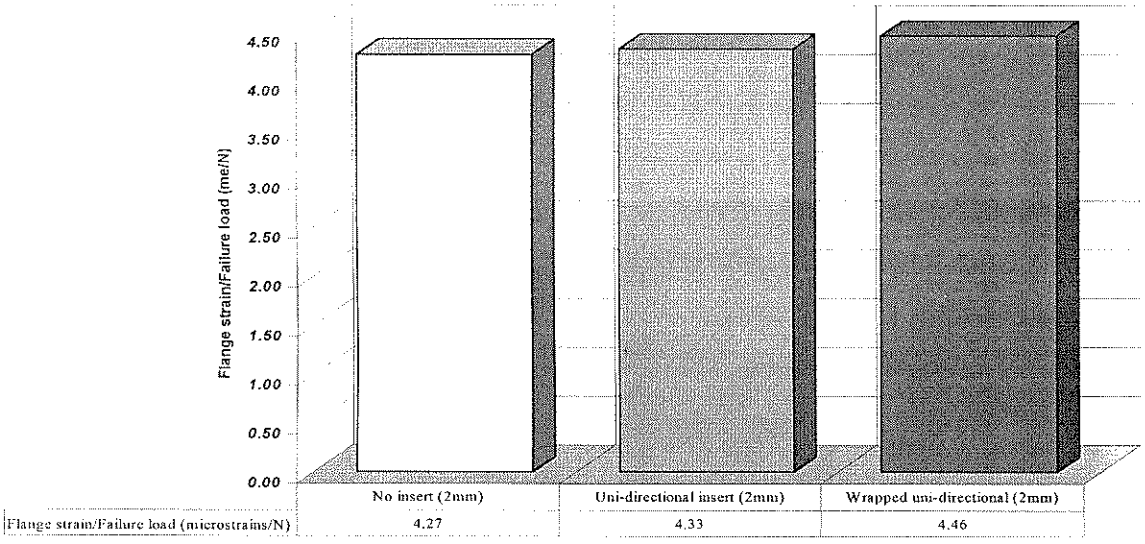

Figure 8.18: Normalised load transfer performance indicators for different inserts (2mm nominal web specimens)

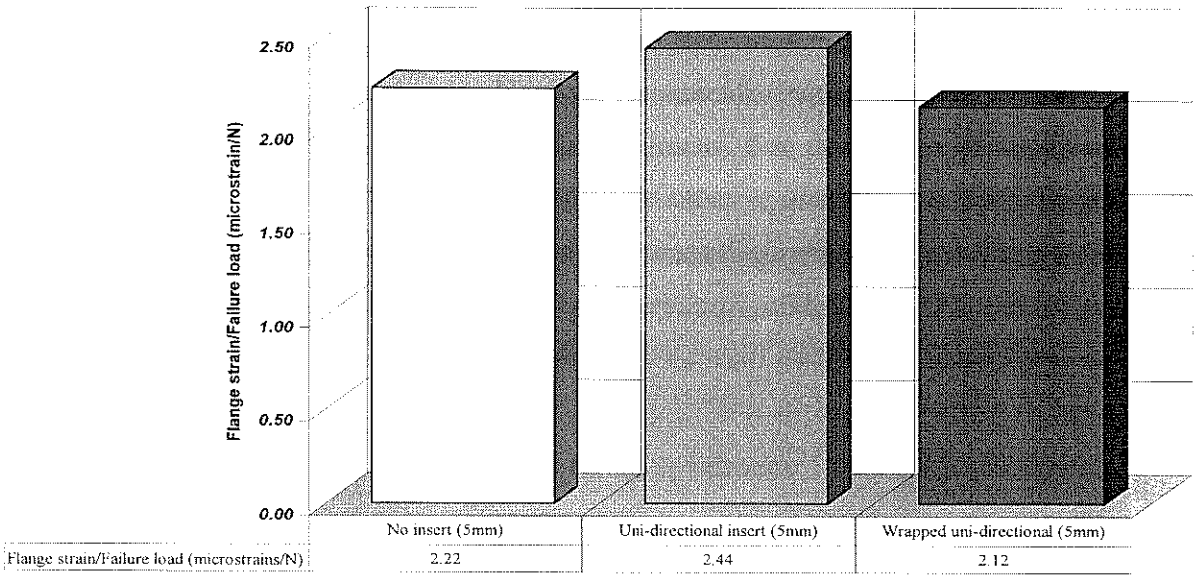

Figure 8.19: Normalised load transfer performance indicators for different inserts (5mm nominal web specimens)

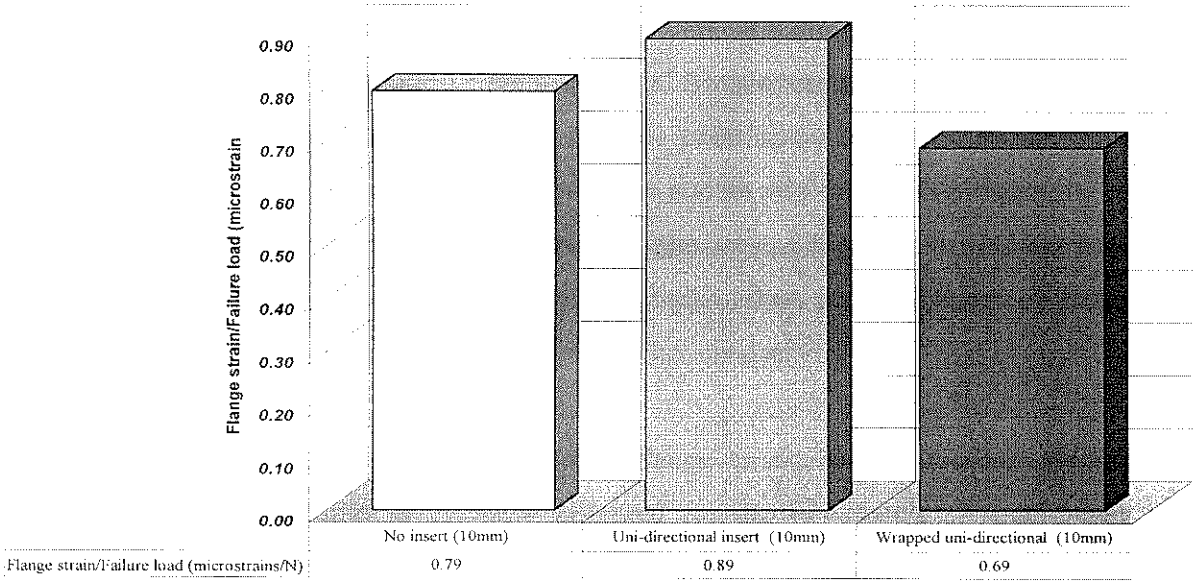

Figure 8.20: Normalised load transfer performance indicators for different inserts (10mm nominal web specimens)

The plotted value represents the induced strain per unit load at the underside of the web/flange intersection. The best performance indicatorvalue within specimens of identical web thicknesses is the smallest value for each group. From the bar chart on Figures 8.18, 8.19 and 8.20, and by comparing theses charts to the strongest specimen type within each group, the lowest normalised value coincides with the strongest joint for all web thicknesses except for the 5mm web specimens. For this group of specimens the lowest normalised value; albeit by a small difference; is obtained for the wrapped uni-directional insert configuration while the strongest configuration is the no-insert one. The second lowest value is experienced by the no-insert configuration.

8.8 Test results and discussion of second batch specimens

The second batch of specimens consisted of a total of 22 specimens. From the 22 specimens, 19 had a nominal web thickness of 2 mm while the remaining 3 had a nominal web thickness of 9.6 mm. The results for each one of this specimens including type of filler employed, failure load (damage initiation load) and failure strain measured at the under side of the web/flange intersection are shown in Table 8.4. In addition to these values, a photoelastic coating was employed to assess high strain gradients at the web/flange intersection. The small size of the specimens made it difficult to obtain good results from the applied coating. To "see" the fringes on the coating an electronic microscope had to be employed. Furthermore, the polariscope had to be disassembled so as to place the analyser in front of the microscope and an additional filter had to be placed on the path of the incident white light. Although the area of high strain gradient could be seen through the electronic microscope, photographs taken through it are of very poor quality and have therefore not being included on this chapter.

The load-displacement and load versus flange strain curves obtained from these specimens are very similar to the ones obtained for the first batch of specimens. The regions of high strain gradient were detected by employing photo-elasticity. These regions are depicted in Figure 8.21. In contrast to results observed from the first batch of specimens, the location of failure initiation varied between specimens with different insert types. It is possible that, due to the different technique employed to detect failure initiation

area (visual for the first batch and photoelasticity for the second one), the dissimilar failure areas could not be detected on the first batch of specimens. Furthermore, although the failure regions are slightly different for the second batch, the failure always initiated close to, or in, the insert region.

Table 8.4: Second batch experimental results: D - no filler, E - uni-directional filler (0 deg fibre tow), F - bi-axial filler (bi-axial carbon sleeve) and G - three-dimensional filler

SPECIMEN NO	WEB THICKNESS (mm)	FILLER TYPE	FAILURE LOAD damage initiation load (N)	FAILURE STRAIN AT UNDER SIDE WEB/FLANGE JUNCTION (με)
a1	2	D	650	3600
a2	2	D	1000	7000
a3	2	D	1000	8000
a4	2	D	740	3300
a5	2	D	880	6800
d1	2	E	1000	3750
d2	2	E	1500	6000
d3	2	E	1050	5300
d5	2	E	1220	5100
b1	2	F	880	2750
b2	2	F	940	3100
b3	2	F	1075	3100
b4	2	F	1050	3200
b5	2	F	1000	3250
c1	2	G	1200	4900
c2	2	G	1050	5000
c3	2	G	1100	5000
c4	2	G	1100	N.A
c5	2	G	1300	6600
w1	9.6	D	1100	1500
w2	9.6	D	2100	2600
w5	9.6	D	2000	2750

The failure mode observed in all specimens was delamination. This indicates a matrix dependant failure. To assess insert efficiency, several factors were plotted in bar charts.

The first three charts, Figures 8.22, 8.23 and 8.24, represent the comparison of average values of strength, stiffness and flange strain respectively. The strength comparison, based on average values, indicates that the uni-directional insert provides the strongest joint. The second strongest joint was achieved by using a three dimensional insert followed by the bi-axial insert T-joint. The weakest T-joint was obtained for the no-insert configuration. Significant scatter was observed within groups of specimens with the same type of filler. A chart highlighting the scatter in the failure load obtained within each configuration (2mm nominal web specimens) is depicted in Figure 8.25. Regardless of the scatter, the uni-directional insert is the strongest contender. The exception to this rule is the comparison between the minimum failure load obtained for the three-dimensional insert and the minimum failure load achieved by the uni-directional insert configuration. In this case (minimum failure values), the three-dimensional insert configuration is stronger. The assessment of joint stiffness (average, maximum and minimum values) showed the bi-axial insert configuration to be the stiffest T-section. The three-dimensional insert configuration was the second stiffest joint under the same comparison. Figure 8.24 indicates that the largest flange strain was generated in the no-insert configuration, followed by the three-dimensional insert configuration. The third largest flange strain was generated in the uni-directional configuration followed by the bi-axial insert configuration.

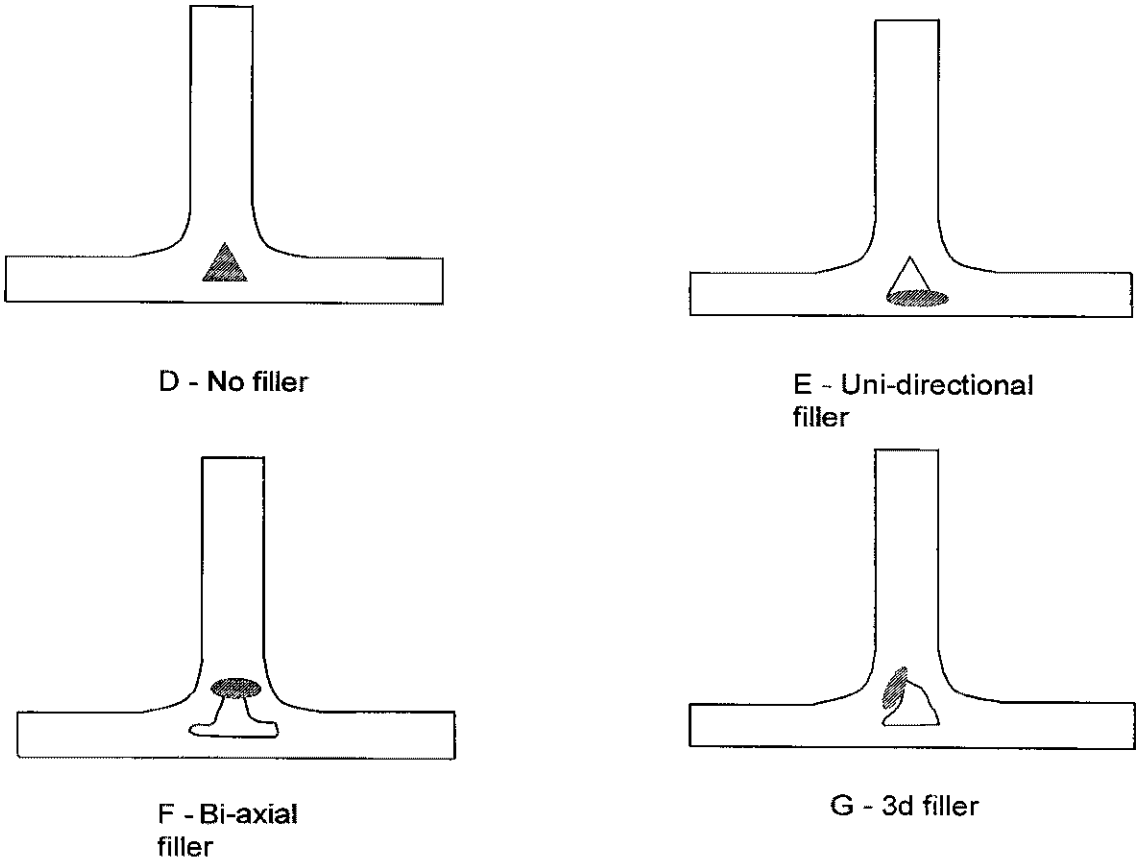

Figure 8.21: High strain gradient regions (hatched areas) detected by employing photo-elasticity.

In summary, the type and geometry of inserts had a significant effect on both strength and stiffness of T-joints. The strongest joint (uni-directional insert configuration) is one of the most flexible ones and has a relatively low flange strain value (second lowest). If the stiffness of the joint is a more important requirement, the bi-axial insert provides the best option. Furthermore, the best transfer of load to the flange area was provided by this configuration resulting in the lowest flange strain. This value was 40% lower than the second value recorded (uni-directional insert configuration) and it was also up to 50% lower than the maximum flange strain recorded (no-insert configuration). As the strain gauge recording this value is positioned right below the web/flange intersection, it provides with a good insight on load transfer from the web to the flange area.

A performance indicator can be obtained if the flange strain is divided by the failure load of the joint. These normalised values are plotted in Figure 8.26. The plotted value represents the induced strain per unit load at the underside of the web/flange intersection. Therefore, the smaller this value the better load transfer to the flange of the T-joint. That is, the load is transferred from tension in the web to bending in the flange with less bending strain. From the bar chart on Figure 8.26, the bi-axial insert configuration has the lowest ratio followed by the uni-directional insert configuration.

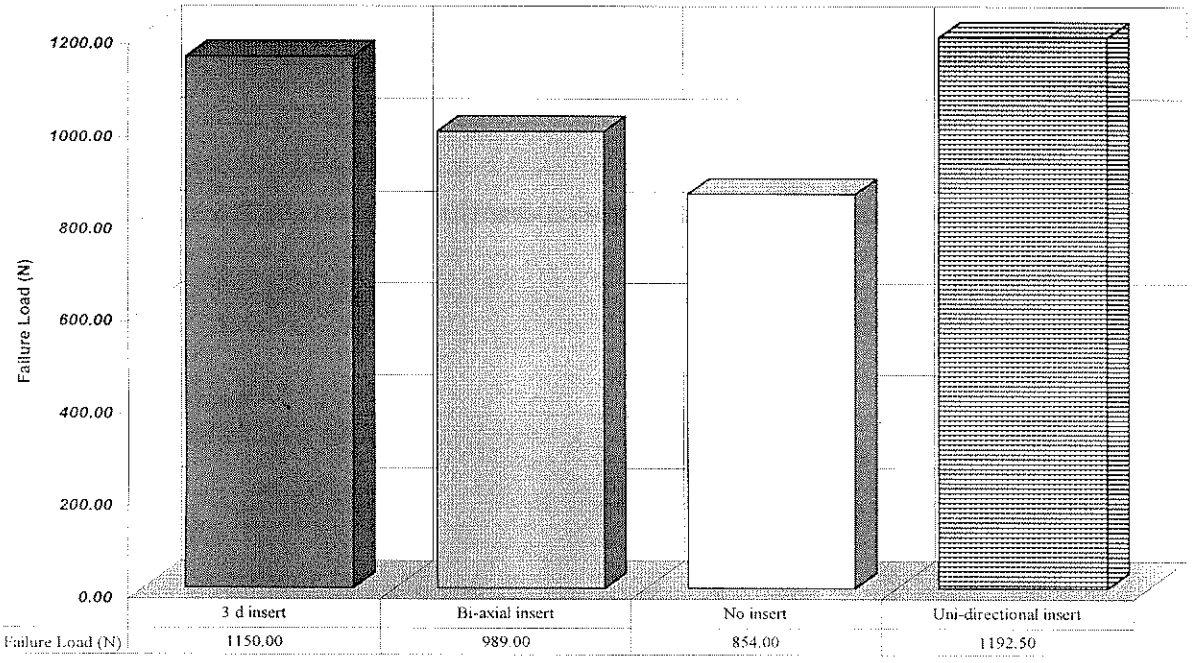

Figure 8.22: Average strength comparison for different insert types

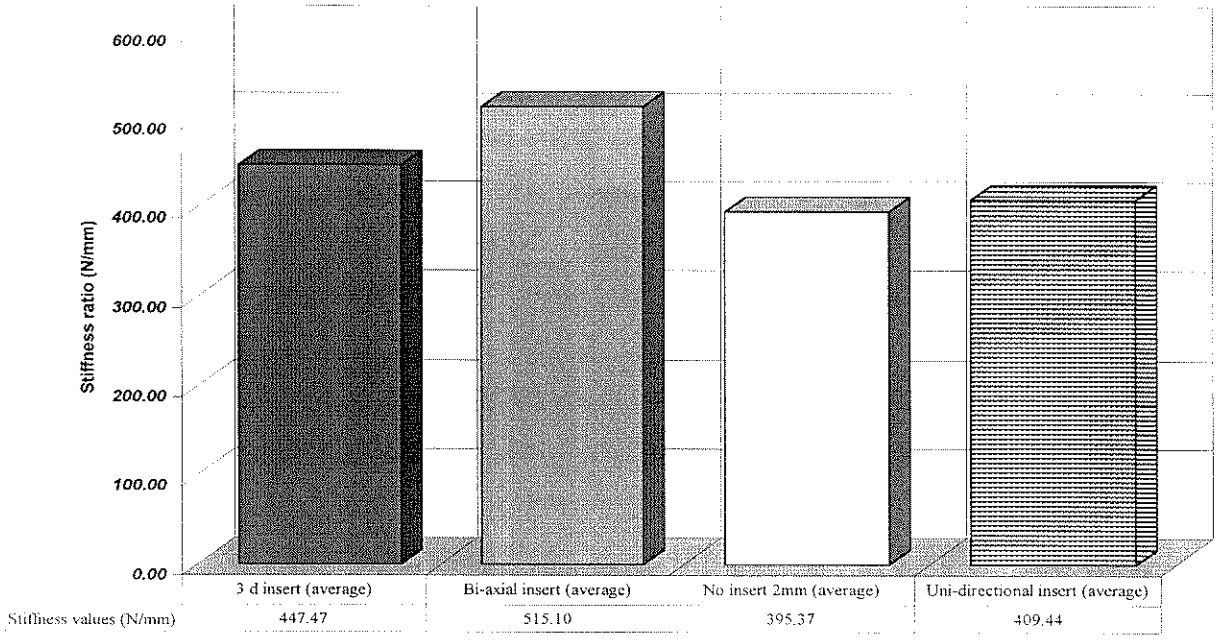

Figure 8.23: Average stiffness comparison for different insert types

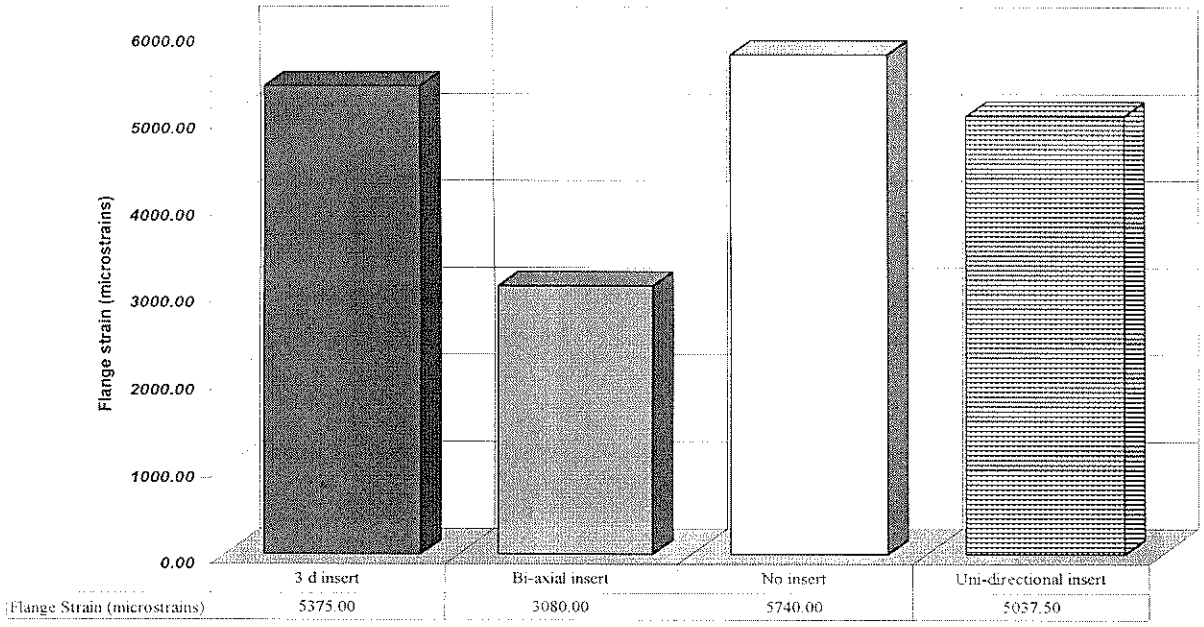

Figure 8.24: Average flange strain comparison for different insert types

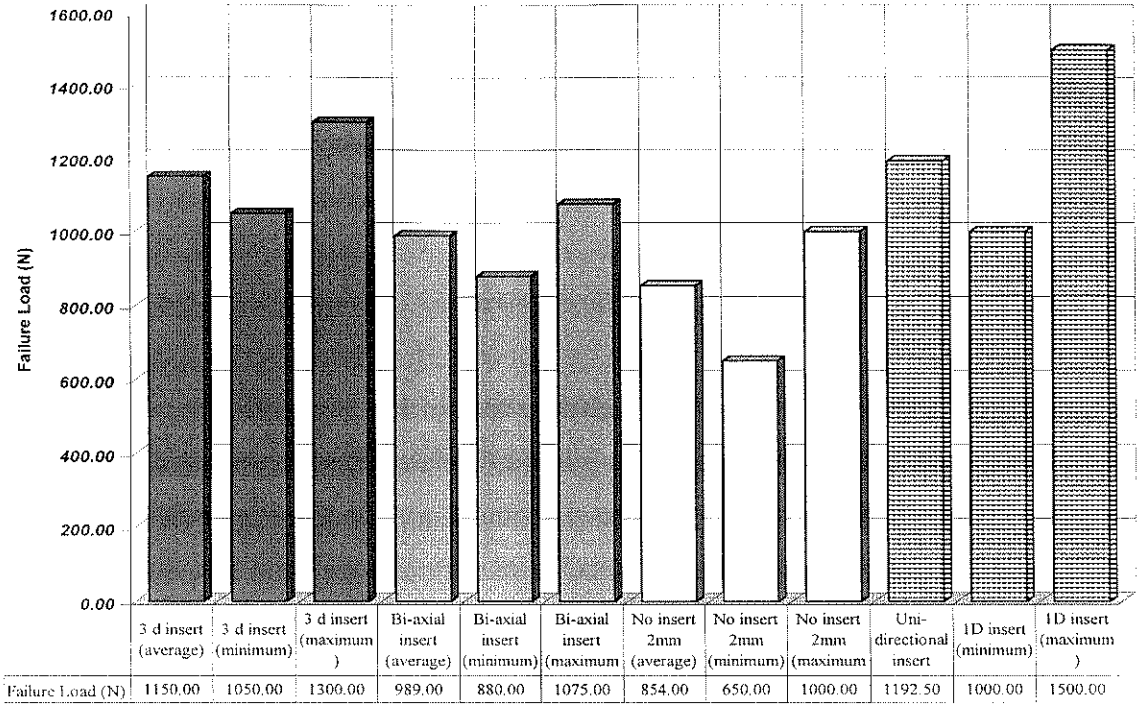

Figure 8.25: Scatter of failure load values for different inserts

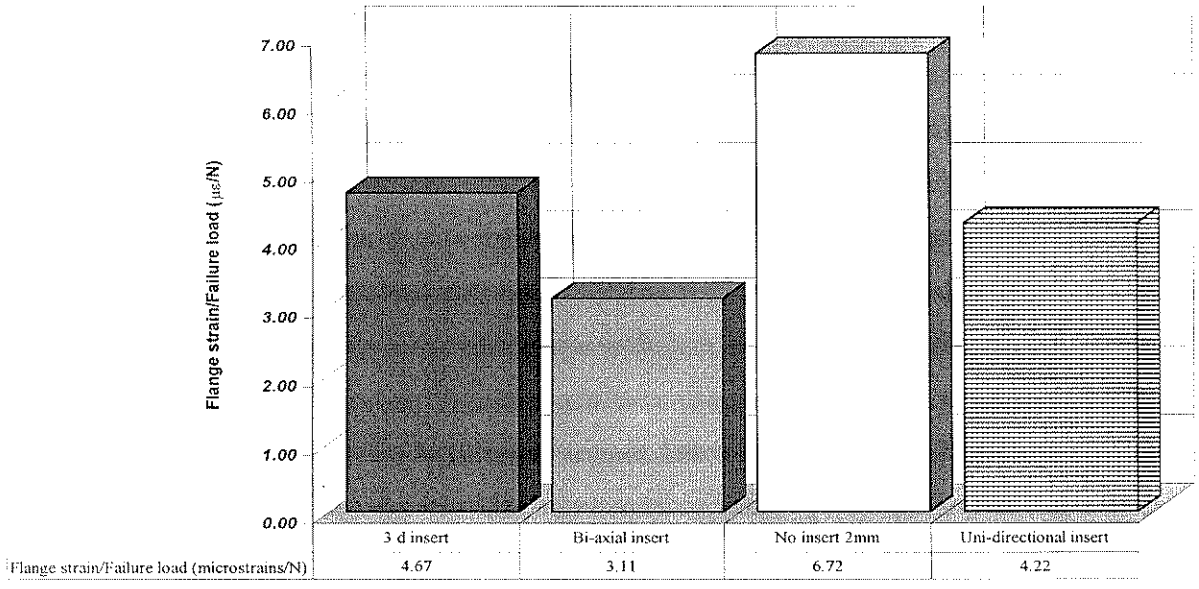

Figure 8.26: Normalised load transfer performance indicators for different inserts

Although this ratio gives a good indication as to how efficiently the load is transferred to the flange section and the effect of the insert type on load redistribution, it does not necessarily indicate which is the best T-joint configuration. For example, if the designer is after the strongest possible configuration, the T-joint with the uni-directional insert should be the chosen contender.

8.9 Conclusions

Significant differences existed between the first and second batch of specimens and the insert/ply interface of both batches. Firstly, the material (prepreg) employed for both batches was different. Secondly, the lay-up (ply orientation and number of plies at the web and flange) was also different resulting in different web and flange thicknesses as well as different ratios between web and flange thicknesses. Finally, the types of inserts employed were in general of different configurations and also different sizes. The differences in all the above parameters are described in detail in Section 8.3.

Despite of the batches of specimens being quite different from each other, some comparison can still be made in attempting to reach a general trend of behaviour as a result of employing different insert configurations and sizes.

The largest difference noted between similar specimen configurations from the first and second batch was observed on the no-insert configuration. The first batch of specimens had no void at the web/flange intersection region. The second batch of specimens presented a large gap at the intersection between the web and the flange of the specimens. This explains the large difference in failure load and also explains why the no-filler configuration while being the strongest one within the first batch of specimens, it was the weakest configuration within the second batch of specimens. The most probable cause for the large void at the web/flange intersection was excess bleeding of resin during the manufacturing of the second batch of specimens. The second difference was noted between the uni-directional insert configuration specimens manufactured within the first batch of specimens and the second batch of specimens. The difference here being the geometry of the uni-directional insert. While the first batch of specimens had over-sized

uni-directional fillers placed on the web/flange intersection, the second batch of specimens was manufactured using undersized uni-directional fillers at the same intersection. The size of the filler was deliberately changed as it was observed from the results obtained from the first batch of specimens that the placing of oversized inserts was distorting the plies next to the inserts. This was exacerbating the stress concentration problem at this location due to the added geometric discontinuity. Results from the second batch of specimens confirm this observation as it shows that the uni-directional filler configuration was the strongest one. The remaining configurations can not be compared between batches of specimens as they were distinctly different.

From the experimental results obtained from the first batch of specimens, the addition of both types of inserts employed have a detrimental effect on pull-out strength for web thicknesses of 2 and 5 mm. For thicker specimens (t_w=10 mm), this effect is reversed. The pull-out strength for the thicker specimens increased by up to 22 % with the addition of a two-directional filler. It appears that for thinner specimens, the use of inserts; when oversized; introduces geometric discontinuity's by creating kinks on the fibres which cause stress concentrations resulting in reduced pull-out strengths. This suggests that the insert design could be improved in terms of both size and shape. A larger radius connecting the web to the flange, could help to reduce these stress concentrations resulting in larger failure loads. The kinking of the fibres due to the insert placement appears to be reduced by increasing the web thickness. The larger resin rich area encountered in these specimens allow the fibers to re-accommodate themselves without kinking.

The scatter observed in results from both batches of specimens, can be attributed to the resin dominated failure mode [7, 8], together with some bending in the test specimens due to a possible lack of symmetry in the far field load. In addition, imperfections caused during manufacture are also likely to influence the amount of scatter present.

The addition of inserts in out of plane joints has to be carefully analysed for each particular case. Available literature indicates that the behaviour of laminated T-joints is very dependent on geometry and material make-up. It also indicates that the failure modes are configuration dependant and that increasing the radius of web/flange intersection increases joint strength.

8.10 References

[1] Maske, E. B., "Wing/Inlet Composite Advanced Development", AFFDL-TR-70-88, Air Force Flight Dynamics Laboratory, Wright-Patterson AFB, 1976.

[2] Gillespie, J. W., Jr., "*Evaluation of the Embedded Spar Composite Design Concept*", Master's thesis, Department of Mechanical and Aerospace Engineering, University of Delaware, Newark, Delaware, 1978.

[3] Personal communication with Techniweave Inc. on Lockheed, Fort Worth tests of Blade pull-off components, 1995.

[4] Junhou, P., Shenoi, R. A., "Examination of key aspects defining the performance characteristics of out-of-plane joints in FRP marine structures", Composites: Part A 27A, pp. 89-103, 1996.

[5] Theotokoglou, E. E., Moan, T., "Experimental and Numerical Study of Composite T-Joints", *Journal of Composite Materials*, Vol. 30, No. 2, pp. 190-209, 1996.

[6] Measurement Group Inc., *Technical Note TN-704-1*, pp. 3, 1978.

[7] Pointer, R., Awerbuch, J., Wang, A. S. D., "Evaluation of Frame/Skin Bond Strength and Durability for Advanced Composite Fuselage Crown Structures", *Proceedings of the American Society for Composites*, 9th Technical Conference, University of Delaware, pp. 833-841, September 1994.

[8] Brewer,J. C., Lagace, P. A., "Quadratic Stress Criteria for Initiation of Delamination", *Journal of Composite Materials*, Vol. 22, pp. 1141-1155, December 1988.

CHAPTER 9

FAILURE ANALYSIS OF COMPOSITE T-JOINTS

9.1 Introduction

The correlation of out-of-plane characteristics of composite T-sections by means of finite element analysis is paramount to understand the load transfer of out-of-plane joints. Several researchers have simulated the behaviour of T-joints for both aircraft and naval structures. Pointer et. al. [1] performed an analytical and experimental investigation to characterise damage initiation and progression along the frame/skin interface on a fuselage section. Plane strain analysis was conducted on the different configurations and the failure load was predicted by computing the crack-tip strain-energy release rates in terms of the applied load and crack size. The critical initiation load was predicted by applying the Griffith criteria of fracture.

Shenoi et. al. [2], developed an analytical solution to predict the failure load of a hull bulkhead joint. In this case the model was obtained by using simple beam theory. A two stage validation of the model was also carried out by comparing the finite element results with experimental values, followed by the comparison of the FEA model with the analytical model.

Gillespie et. al. [3], performed a detailed analysis on an integral composite joint. A two-dimensional finite element model with temperature dependent orthotropic material properties was employed. The model was solved using linear-elastic finite element techniques. Three different configurations of inserts were analysed including a no-insert, titanium insert and a graphite-epoxy insert configuration. The inserts were 1.5" in length and were placed parallel to the wing-skin (flange). The best correlation was achieved for the no-insert configuration where the response observed during testing was linear-elastic. Testing carried out on the other two configurations showed a bilinear load-deflection. Assuming that the initial elastic region was generated by inherent insert deformation, the

secondary stiffness was predicted by the finite element analysis fairly well. Both configurations employing inserts increased the strength of the integral joint when compared to the no-insert configuration.

Cope et. al. [4], investigated the effect of joint geometry; including different sizes and shapes of inserts; and interspar spacing on joint strength. The computational analysis was conducted by using finite element analysis and the failure load was predicted through the application of Tsai-Wu, maximum stress and maximum shear failure criteria. Application of Tsai-Wu and maximum stress failure criteria to finite element results provided with bounds to most experimental data. Use of inserts of triangular cross-section were found to introduce discontinuities in the overlap geometry which caused stress concentrations resulting in reduced ultimate strengths.

All the research found during the literature survey including the above references, assume "ideal" geometry's for the modelling of out-of-plane joints. That is, they do not account for manufacturing irregularities such as ply slippage or different compaction rates for each ply forming the laminate. The present work aims at including these parameters to increase the accuracy of failure initiation prediction as well as gaining a better insight on the load transfer in out-of-plane joints.

The first step in modelling the out-of-plane joint behaviour was to try to predict both stiffness and failure load/mode for a specimen with no insert. To this end, a three dimensional shell finite element analysis of a T-joint with no insert was performed using basic lamination theory. As the correlation was found to be poor, a two dimensional orthotropic analysis with idealised ply geometry was carried out. This analysis correlated very well both the stiffness and load transfer to the flange area. Despite of this good agreement, the failure location and failure load could not be predicted with this analysis.

To capture the microscopic behaviour at the ply level, a detailed 2-D plane strain orthotropic finite element analysis based on ply geometry obtained from an electronic microscope of a T-joint with no insert (1^{st} batch of specimens) was carried out so as to predict both the failure mode and load at which the joint would fail. The correlation between experimental and the finite element load-deflection curve shows an excellent

agreement. Furthermore, the actual ply geometry model manages to predict both the strength and the failure location accurately. The prediction for the no-insert configuration is based on interply resin failure and agrees well with experimental observations and material data.

The detailed analysis of a graphite/epoxy T-joint provided in the following section should aid in the understanding of the failure mode and load transfer mechanism of similar joints. As the specimens with different type of inserts presented a similar failure mode to the no insert configuration analysed in this Chapter, the analysis should also be valid for T-joints with graphite/epoxy inserts. The difference in failure loads between the different configurations, could be accounted for by including an effective insert property together with its detailed geometry. The inclusion of a representative insert property would require a large number of tests to be conducted on each type of insert to fully characterise each insert.

9.2 Finite element three dimensional and two dimensional orthotropic analysis

A three dimensional shell finite element analysis of a T-joint with no insert was performed using basic lamination theory. The model was assembled using 275 thin shell elements with laminate properties and 80 brick elements with isotropic properties representing the resin where the fiber volume is very low (resin rich area at web/flange intersection). The four noded thin shell element incorporates membrane-bending coupling at the element level. It has six true degrees of freedom per node. This element is only suitable for thin plate structures as it uses the Kirchhoff hypotheses for its formulation.

It was found from comparing the load versus deflection curve and strain values, that the correlation between FEA and test results was very poor. The displacement at failure was underestimated by 35 % while the strain at the underside of the web-flange junction by almost 60%. Furthermore, interlaminar failure can not be predicted with this analyis due to the fact that the resin between plies can not be included in the model. Failure prediction tools which are based on ply stresses without including interlaminar peel stresses are inadequate to accurately predict onset of failure of out-of-plane joints.

The reasons for the poor correlation can be explained by looking at the assumptions of basic lamination theory set out in Chapter 2. The assumptions which disagree with the specimen's geometry and test conditions are as follows:

a) Deformations (particularly out of plane) are large when compared to the specimen's thickness.
b) Interlaminar shear and peel strains are significant.

Due to the above disagreements with basic lamination theory, a two-dimensional plane strain orthotropic analysis was carried out to assess whether a full 3-D brick model of the T-joint was necessary to replicate both specimens geometry and out-of-plane loading.

Two different finite element models were created to simulate thin T-joints (1st batch of specimens, t_w=2.15 mm) without inserts. The T-joints with no inserts were modelled both with the actual ply geometry obtained by means of an electronic microscope and with the idealised ply geometry to assess the effect of ply geometry on both failure prediction and load versus deflection prediction.

9.3 Finite element analysis of idealised and actual ply geometry of thin T-joint with no insert

Two different finite element models were created. Both models correspond to the first batch of specimens (t_w=2.15 mm) tested in Chapter 9. The first one consisted in an idealised geometry of the plies (Figure 9.1) while the second one was constructed with the exact geometry of the plies around the resin rich area. This geometry was determined by obtaining thicknesses of individual plies at three referenced positions by means of an electronic microscope. These points were then connected using quadratic splines so as to obtain a smooth curve and continuous elements. Figure 9.2 shows the detailed mesh around the region of interest together with the reference lines employed during ply thickness measurements.

A two-dimensional plane strain analysis was performed using quadrilateral (8 and 4 node elements) and triangular elements (3 and 6 node elements) on the commercial FEA software STRAND6 [5]. The mesh employed for modelling the actual T-joint geometry consists of 1861 nodes and 648 two-dimensional elements while the idealised T-joint geometry was modelled using 1650 nodes and 584 two-dimensional elements. The T-joint was modelled using symmetry boundary conditions (Figure 9.3) so that only half of the joint needed to be modelled. The assumption of plane strain should be valid, as the width to thickness ratio is larger than 20. The properties for each angle ply were assumed to be orthotropic with transverse isotropy and were calculated employing Equations (2.7-2.9) using available material data. The thickness of the laminate is 2.15 mm at the web and 1.7 mm at the flange resulting in an average ply thickness of 0.155 mm. 0^{o} and 90^{o} plies are modelled as one row of elements. Combination $\pm 45^{o}$ plies (2 plies) are also modelled as one row of elements. The resin rich area is modelled as isotropic with net resin property values. The actual ply geometry model depicts the 4^{th} ply (90^{o}) starting from the bottom of the flange, being dispersed into the resin rich area (web/flange intersection). This re-distribution of the 90^{o} ply into the resin rich area was observed under the electronic microscope. Therefore, the quasi-triangular region formed between web and flange on the actual ply geometry model is assigned 90^{o} ply properties.

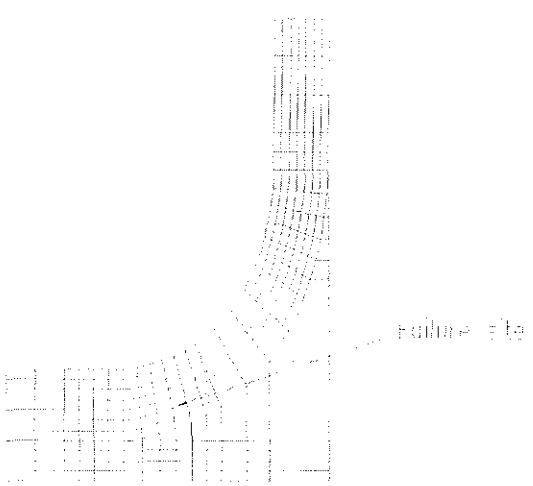

Figure 9.1: Idealised ply geometry

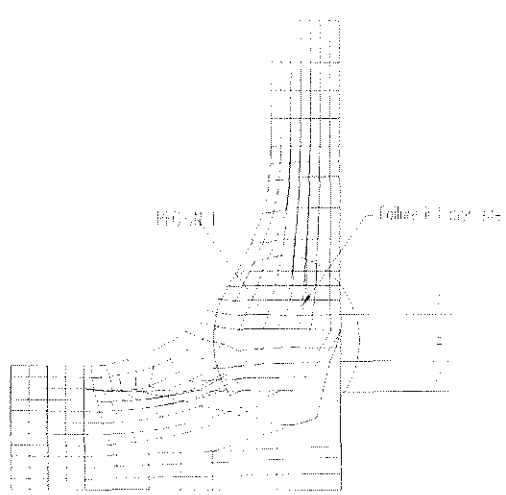

Figure 9.2: Detailed mesh of actual ply geometry model and measurement location at resin rich area

The coarseness of the mesh is required due to difficulties in meshing some of the distorted elements representing thin wedges of resin in between plies. This is particularly true for the actual ply geometry model. The "draping" capabilities of the FEA software STRAND6 [5] were employed to reduce discontinuities in the modelled fibre directions. Changes in volume fractions with changing ply thicknesses were not accounted for in the models.

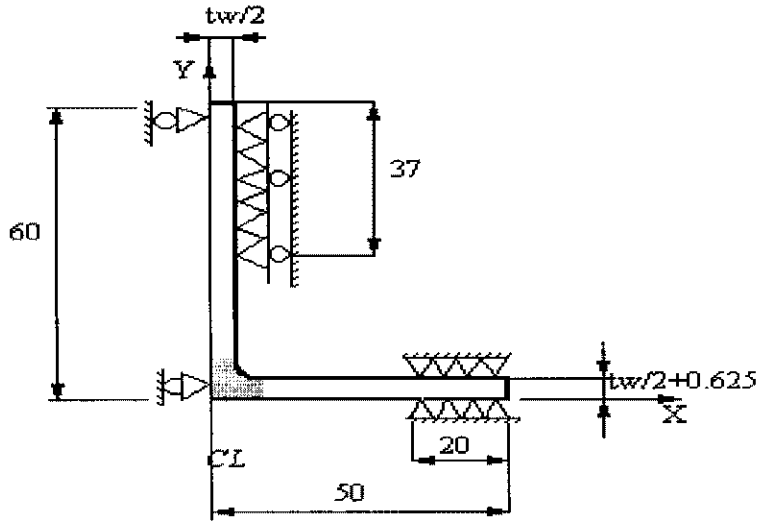

Figure 9.3: Boundary conditions for finite element analysis

(Darker area corresponds to resin rich area of interest)

9.3.1 Material properties

The material properties employed for the graphite/epoxy T300/934 uni-directional prepreg tape and the net resin were obtained from the Fiberite Materials Handbook and are listed in Table 9.1. Some of the interlaminar properties not available from the Handbook were obtained from the literature [6]. The remaining ones were assumed as follows:

$E_3=E_2$

$\upsilon_{13}=\upsilon_{12}$ } where 1,2 and 3 refer to the coordinate system shown in Figure 2.2 (Chapter 2).

The Poisson's ratios were evaluated using Betti's reciprocal law according to which transverse deformation due to a stress applied in the longitudinal direction equals the longitudinal deformation due to the same stress applied in the transverse direction [7]. Properties corresponding to the $\pm 45^{\circ}$ plies were calculated using transformation relations for engineering constants. Table 9.2, lists the actual properties as used in the finite element analysis model.

Table 9.1: Material properties

	Fiberite Hye3034K	Net resin properties (934 Epoxy Resin)
E_1 (GPa)	124	4.1
E_2 (GPa)	11.7	4.1
E_3 (GPa)	11.7	4.1
υ_{12}	0.3	0.35
υ_{13}	0.3	0.35
υ_{23}	0.6	0.35
G_{12} (GPa)	5.5	NR
G_{13} (GPa)	4.137	NR
X_{1T} (MPa)	1586	27.6
X_{1C} (MPa)	1517	27.6
X_{2C} (MPa)	275.8	27.6
$X_{2T} = X_{3T}$ (MPa)	51.71	27.6
X_{3C} (MPa)	275.8	27.6
X_{12} (MPa)	117	117

Table 9.2: Material properties as employed in finite element analysis

	0° ply	90° ply	±45° ply
E_x (GPa)	124	11.7	14.786
E_y (GPa)	11.7	11.7	11.7
E_z (GPa)	11.7	124	14.786
υ_{xy}	0.3	0.6	0.3
υ_{zx}	0.0283	0.3	0.344
υ_{yz}	0.6	0.0283	0.237
G_{yz} (GPa)	4.1	5.5	4.1

9.4 Failure analysis and correlation of test results

9.4.1 Failure criteria

Over the years, a very large number of macromechanical failure theories have been proposed. These theories were generally adapted from isotropic failure theories to account for the anisotropy of composite materials. A survey of such theories can be found in the work by Owen et. al. [8]. Some of the more commonly used criteria include the Maximum Stress theory, Maximum Strain theory, Tsai-Hill criteria and Tsai-Wu criteria. The mathematical representation of these criteria can be easily found in any composite structures textbook such as the work published by Daniel et. al. [7].

This section of the dissertation deals with prediction of failure in out-of-plane joints in which interlaminar strength of the laminate plays a vital role. The laminate failure criteria mentioned previously are not applicable to predict failure of a laminate under the action of interlaminar stresses in their original formulations. This is due to the fact that these failure criteria only include parameters related to basic lamina strengths. That is, they do not include parameters related to the interlaminar shear and interlaminar peel strengths. The reason for these parameters being excluded from a large number of the above mentioned failure theories, is that the assumptions of the classical lamination theory are normally applied. This theory states that the laminate and all its plies are in a state of plane

stress or alternatively that all the out-of-plane components are zero. This assumption can be generally satisfied for laminates under in-plane loading and in the absence of geometric discontinuity's (eg. change of ply direction or free edge of a laminate). At these discontinuity's, peel stresses tend to separate plies from each other causing delamination. Interlaminar shear stresses are also contributors in the separation or delamination of plies. The interlaminar strength of a composite material is a matrix dominated property.

Several failure criteria applicable to composite joints; where delamination can occur; can be found in the literature. These failure criteria fall within two basic approaches. The first one being the mechanics of materials approach, which essentially compares the stresses in the matrix layer between the plies against strength parameters in corresponding directions. The disadvantage of this type of approach is that strength parameters relevant to delamination type failures are not readily available.

The second approach consists in applying fracture mechanics principles for the prediction of delamination. The most commonly employed technique within this approach is the strain energy release rate method. Delamination can occur under three basic modes, peel mode (Mode I), shear mode (Mode II) and tearing (Mode III). More complex modes consist on different combinations of Modes I, II & III. The resistance to delamination growth is expressed in terms of the interlaminar fracture toughness which in turn is measured by the strain energy release rate corresponding to the three different modes of cracking (G_I, G_{II}, G_{III}).

This dissertation employs the mechanics of materials approach, due to its simplicity and the availability of strength parameters relevant to delamination type failures, such as interlaminar shear and peel strength. Another advantage of using this approach is that; in the analysed T-joints; the out-of-plane stress state is dominated by a single stress component (peel) with a small contribution from the shear stress component. This makes any method which assesses these stress components particularly attractive. The reason for the state of stress being mainly dominated by the peel stress component is that the transfer of load occurs in an orthogonal fashion (from web-to-flange). Since the in-plane stresses are negligible in comparison to the peel and shear stresses, the criteria which will be considered for the prediction of failure in the T-joint analysis will be truncated to only

include peel and shear stresses. The simplest failure criteria employed are the interlaminar peel index and the interlaminar shear index criteria. These two criteria are simply based on the interlaminar peel / shear strength of the composite material employed. A number of other failure criteria which can be found in the literature, are: modified Tsai-Wu failure criteria [9], Quadratic Delamination criteria [10], Norris criteria [11], and the tensor polynomial failure criteria [6]. This list is by no means exhaustive. In the modified Tsai-Wu failure criteria, out-of-plane stresses are the primary contributors to the prediction of failure as shown in Equation 9.1. The Quadratic Delamination criteria, is based on an average stress criteria that compares the calculated out-of-plane interlaminar stresses to their related strength. The Norris criteria has been used in assessing failure in wood while the tensor polynomial failure criteria is based on the average stress component near the free-edge region. The tensor polynomial failure criteria further assumes that the in-plane stress components do not influence the interlaminar failure. The formulation of this failure criteria is shown in Equation 9.2. The nomenclatures of all equations in this Chapter have been modified from their original formulations to standardise them to the nomenclature presented in Chapter 2.

Modified Tsai-Wu failure criteria:

$$\frac{X_{2C}-X_{2T}}{X_{2C}X_{2T}}\sigma_2+\frac{1}{X_{2C}X_{2T}}\sigma_2^2+\frac{1}{X_{12}}\left(\sigma_{32}^2\sigma_{12}^2\right)=1 \qquad \textbf{(9.1)}$$

Tensor Polynomial failure criteria:

$$\frac{1}{X_{2T}X_{2C}}\sigma_2^2+\frac{1}{X_{12}^2}\sigma_{12}^2+\frac{1}{X_{23}^2}\sigma_{23}^2+\left(\frac{1}{X_{2T}}-\frac{1}{X_{2C}}\right)\sigma_2=1 \qquad \textbf{(9.2)}$$

From the additional failure criteria presented it was decided to include for comparison reasons the Quadratic Delamination criteria and the Norris criteria only. The different criteria employed for the failure analysis of T-joints are outlined below:

(A) Interlaminar Peel Index

$$\frac{\sigma_3}{X_{2T}} \geq 1 \tag{9.3}$$

(B) Interlaminar Shear Index

$$\frac{(\tau_{13}{}^2 + \tau_{23}{}^2)^{1/2}}{X_{12}} \geq 1 \tag{9.4}$$

(C) Norris Criteria

$$\frac{\sigma_1{}^2 - \sigma_1\sigma_2}{X_{1T}X_{1C}} + \frac{\sigma_2{}^2}{X_{2T}^2} + \frac{\tau_{12}^2}{X_{12}^2} \geq 1 \tag{9.5}$$

(D) Quadratic Delamination Criteria

$$\left(\frac{\tau_{12}}{X_{12}}\right)^2 + \left(\frac{\tau_{23}}{X_{23}}\right)^2 + \left(\frac{\sigma_{2T}}{X_{2T}}\right)^2 + \left(\frac{\sigma_{2C}}{X_{2C}}\right)^2 \geq 1 \tag{9.6}$$

9.4.2 Finite Element Correlation Of No-Insert Configuration (idealised and actual ply geometries)

T-joints with t_w=2 mm and no insert corresponding to the 1st batch of tests (see Chapter 9) were analysed using the finite element method. The modelling of the thinnest T-joint should be representative of the remaining joints as all specimens (Chapter 8) presented a similar failure mode. The failure initiation site was also similar for all specimens. A linear material and geometric static analysis of the actual ply geometry was performed and found to be sufficiently accurate to simulate the displacement, failure

initiation site and mode of the actual test specimens at the failure initiation load. The strain at the under side of the web/flange junction, was also found to correlate extremely well with test results. The finite element model of the idealised ply geometry, reproduced both the displacement and strain in the flange region but failed to simulate the failure location and initiation load.

Critical resin only elements in peel and shear were selected from the FEA and analysed by applying different failure criteria based on these stresses. The elements which have a large peel or shear stress in the actual ply geometry model are shown in Figure 9.2 (elements within region 1 area). The selected elements within this region are shown in Figure 9.4. The critical stressed elements obtained from the idealised model, are indicated in Figure 9.5. The failure criteria employed, include both the linear and the quadratic type criteria such as interlaminar shear and peel strength, truncated quadratic delamination criteria and truncated Norris criteria. Table 9.3 lists selected elements sorted in ascendant order of their interlaminar tensile strength index assuming X_{2T}=51.7125 MPa for all elements (resin and plies). In Table 9.4, the elements are sorted the same way, only that resin rich pockets in between plies are given $X_{2Tresin}$= 27.6 MPa, which corresponds to the tensile strength obtained from typical net resin properties.

Both tables, also list the peel and shear stresses experienced at the selected elements, so that any failure criteria based on interply resin failure could be applied to these results. All the failure criteria employed, assume that the in-plane stress components do not influence the interlaminar failure. Tensile net resin properties were employed for Table 9.4 so as to analyse the influence on the determination of the failure initiation site.

Most of the work found in the literature, assumes the interlaminar peel strength of the composite material to drive the failure in Mode I (crack opening). Due to the considerable size of the resin rich pockets, it was decided to test this assumption and to assess whether the use of net resin properties at such resin rich areas can yield a more accurate failure prediction.

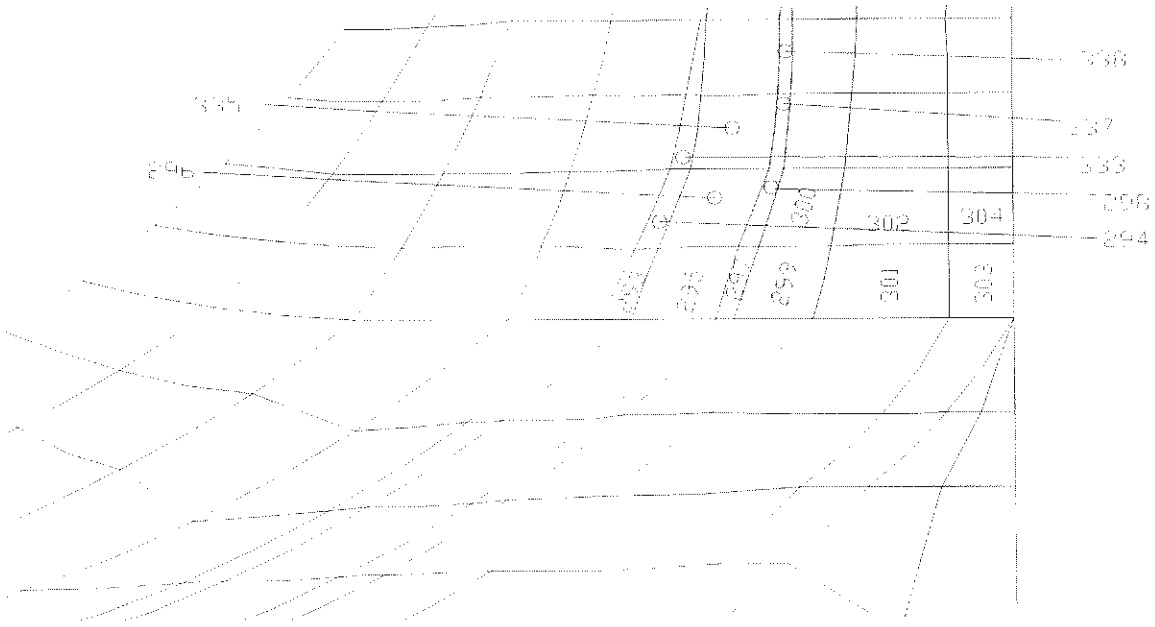

Figure 9.4: Critical elements in peel and shear (actual ply geometry)

Figure 9.5: Critical elements in peel and shear (idealised ply geometry)

Table 9.3: Finite element results at selected elements ordered in ascendant order of their Interlaminar Peel Index for $X_{2Tresin}$=51.71 Mpa

MATERIAL	PLATE NO	SIGY PEEL (MPa)	SIGXY SHEAR (MPa)	INTERLAM. PEEL INDEX	INTERLAM. SHEAR INDEX	TRUNCATED NORRIS CRITERIA & TRUNCATED QUADRATIC DELAMINATION CRITERIA
				(A)	(B)	(C)
ACTUAL	PLY	GEOMETRY		WITH	CRITICAL	VALUES
RESIN	294	35.20	-30.26	0.68	0.26	0.53
PLY LEVEL	296	37.69	-32.55	0.73	0.28	0.61
RESIN	338	38.48	-16.15	0.74	0.14	0.57
RESIN	293	38.51	-32.56	0.74	0.28	0.63
RESIN	298	41.35	-30.82	0.80	0.26	0.71
RESIN	333	42.86	-22.58	0.83	0.19	0.72
PLY LEVEL	335	44.75	-21.32	0.87	0.18	0.78
PLY LEVEL	295	45.27	-40.05	0.88	0.34	0.88
PLY LEVEL	300	45.27	-30.13	0.88	0.26	0.83
RESIN	337	48.67	-21.36	0.94	0.18	0.92
PLY LEVEL	299	53.64	-40.36	1.04	0.34	1.19
PLY LEVEL	304	55.57	-0.84	1.07	0.01	1.15
RESIN	**297**	**56.52**	**-33.59**	**1.09**	**0.29**	**1.28**
PLY LEVEL	302	57.88	-13.99	1.12	0.12	1.27
PLY LEVEL	303	65.33	4.69	1.26	0.04	1.60
PLY LEVEL	301	71.79	-15.81	1.39	0.14	1.95
IDEAL	PLY	GEOMETRY		WITH	CRITICAL	VALUES
PLY LEVEL	479	12.65	5.28	0.25	0.04	0.06
RESIN	501	13.83	-22.03	0.27	0.19	0.11
RESIN	570	18.7	-15.82	0.36	0.14	0.15
PLY LEVEL	474	20.78	-10.93	0.40	0.09	0.17
RESIN	569	21.75	-0.61	0.42	0.01	0.18
PLY LEVEL	477	25.9	-3.48	0.50	0.03	0.25
PLY LEVEL	475	34.38	-12..85	0.66	0.11	0.45
PLY LEVEL	473	38.43	-18.52	0.74	0.16	0.58
PLY LEVEL	471	38.66	-9.87	0.75	0.08	0.57

Table 9.4: Finite element results at selected elements ordered in ascendant order of their Interlaminar Peel Index for $X_{2Tresin}$= 27.6 MPa

MATERIAL	PLATE NUMBER	σ_Y PEEL (MPa)	σ_{XY} SHEAR (MPa)	INTERLAM. PEEL INDEX	INTERLAM. SHEAR INDEX	TRUNCATED NORRIS CRITERIA & TRUNCATED QUADRATIC DELAMINATION CRITERIA
				(A)	(B)	(C)
ACTUAL	PLY	GEOMETRY		WITH	CRITICAL	VALUES
PLY LEVEL	296	37.69	-32.55	0.73	0.28	0.61
PLY LEVEL	335	44.75	-21.32	0.87	0.18	0.78
PLY LEVEL	295	45.27	-40.05	0.88	0.34	0.88
PLY LEVEL	300	45.27	-30.13	0.88	0.26	0.83
PLY LEVEL	299	53.64	-40.36	1.04	0.34	1.19
PLY LEVEL	304	55.57	-0.84	1.07	0.01	1.15
PLY LEVEL	302	57.88	-13.99	1.12	0.12	1.27
PLY LEVEL	303	65.333	4.69	1.26	0.04	1.60
RESIN	294	35.20	-30.26	1.28	0.26	1.69
PLY LEVEL	301	71.79	-15.81	1.39	0.14	1.95
RESIN	338	38.48	-16.15	1.39	0.14	1.96
RESIN	293	38.51	-32.56	1.40	0.28	2.02
RESIN	298	41.35	-30.82	1.50	0.26	2.31
RESIN	333	42.86	-22.58	1.55	0.19	2.45
RESIN	337	48.67	-21.36	1.76	0.18	3.14
RESIN	**297**	**56.52**	**-33.59**	**2.05**	**0.29**	**4.28**
IDEAL	PLY	GEOMETRY		WITH	CRITICAL	VALUES
PLY LEVEL	479	12.65	5.28	0.25	0.04	0.06
PLY LEVEL	474	20.78	-10.93	0.40	0.09	0.17
RESIN	501	13.83	-22.03	0.50	0.19	0.11
PLY LEVEL	477	25.9	-3.48	0.50	0.03	0.25
PLY LEVEL	475	34.38	-12..85	0.66	0.11	0.45
RESIN	570	18.7	-15.82	0.68	0.14	0.48
PLY LEVEL	473	38.43	-18.52	0.74	0.16	0.58
PLY LEVEL	471	38.66	-9.87	0.75	0.08	0.57
RESIN	569	21.75	-0.61	0.79	0.01	0.62

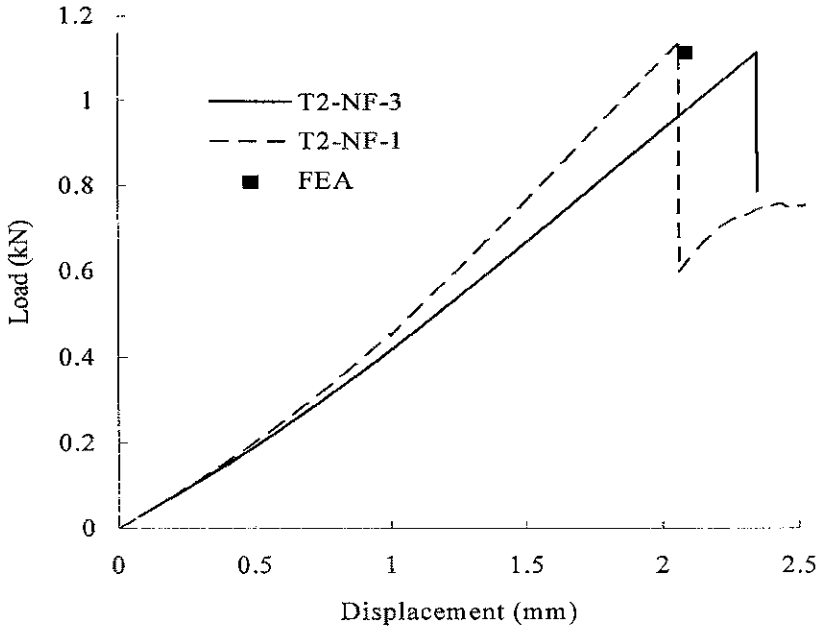

Figure 9.6: Finite element stiffness correlation

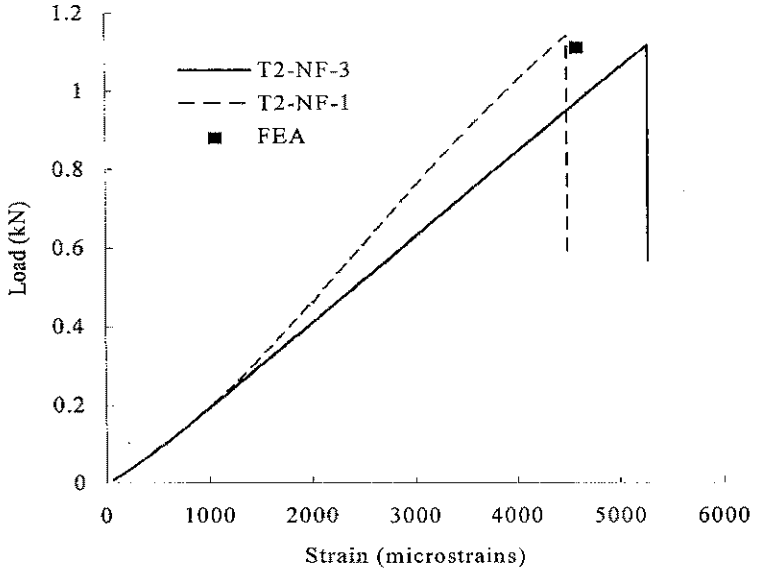

Figure 9.7: Finite element correlation of load transfer to the flange area

9.5 Summary and Conclusions

The linear-elastic finite element analysis performed on the no-insert configuration from the first batch of specimens, validated the experimental results with great accuracy and provides an excellent means to aid in the understanding of out of plane load transfer and failure initiation in T-joints. The interlaminar peel index failure based on interlaminar peel strength of the composite material proved to be the most accurate method in determining the load at which failure initiates. The determination of this load; rather than the ultimate failure load; should be more useful for design purposes as it provides a lower bound which can be used to determine joint allowables. Furthermore, the prediction of catastrophic failure should require a material and geometric non-linear analysis to account for loss of strength once failure initiates. The failure initiation site predicted with the finite element method based on actual ply geometry correlates very well to that observed during testing. The inability of the idealised ply geometry model to predict failure load and location, highlights the need of accurate geometric modelling to assess the failure of joints effectively. This work further enforces the fact that the use of net resin properties for prediction of onset of failure due to delamination is inadequate even in the presence of large pockets of resin.

The use of a quadratic type criteria proved to be unwarranted when a single state of stress is present in the joint. In these cases, the simplest approach is also the more accurate one. That is, the comparison of the local state of stress in the interply resin or matrix layer with relevant strength parameters appears to be the best approach. The finite element analysis of joints employing their detail geometry is currently not a simple task. The main disadvantage is that the measurement of ply thicknesses needs to be done under an electronic microscope. This information then needs to be post-processed by using spline fitting or similar methods to achieve an adequate mesh for the finite element analysis. This process could be automated by developing software capable of automatically generating splines from graphical pictures and of generating output to an ASCII type file readable into finite element codes.

9.6 References

[1] Pointer R., Awerbuch, J., Wang, A. S. D., "Evaluation of Frame/Skin Bond Strength and Durability for Advanced Composite Fuselage Crown Structures", *Proceedings of the American Society for Composites, 9th Technical Conference*, University of Delaware, pp 833-841, September 1994.

[2] Shenoi, R. A., Violette, F. L. M., "A Study of Structural Composite Tee Joints in Small Boats", *Journal of Composite Material*, Vol. 24, pp. 644-666, June 1990.

[3] Gillespie, J. W., Jr., "*Evaluation of the Embedded Spar Composite Design Concept*", Master's thesis, Department of Mechanical and Aerospace Engineering, University of Delaware, Newark, Delaware, 1978.

[4] Cope, R. D., Pipes, R. B., "Design of the composite spar-wingskin joint", *Composites*, pp. 47-53, January 1982.

[5] STRAND6 user manual, G+D Computing Pty. Ltd., Sydney, 1995.

[6] Kim, R. Y., Soni, S. R., "Failure of Composite Laminates due to Combined Interlaminar Normal and Shear Stresses", *Composites 86: Recent Advances in Japan and the United States*, Kawata, K., Umekawa S., Kobayashi, A.,Ed., Proc. Japan-U.S. CCM-III, Tokyo, 1986.

[7] Daniel, I. M., Ishai, O., *Engineering Mechanics of Composite Materials*, Oxford University Press, 1994.

[8] Owen, M. J., Rice, D. J., "Biaxial Strength Behaviour of Glass Reinforced Ployester Resins", Composite Materials: Testing and Design (6th Conference), *ASTM-STP 787*, Daniel, I. M. editor, American Society for Testing and Materials, Philadelphia, pp. 124-144, 1982.

[9] Tsai, S. W., Wu, E. M., "A general theory of strength for anisotropic materials", *Journal of Composite Materials*, No 5, pp. 58-80, 1971.

[10] Brewer,J. C., Lagace, P. A., "Quadratic Stress Criteria for Initiation of Delamination", *Journal of Composite Materials*, Vol. 22, pp. 1141-1155, December 1988.

[11] Nahas, M. N., "Survey of failure and post failure theories of laminates fibre reinforced composites", *Journal of Composites Technology and Research*, Vol. 8, No. 4, pp. 138-153, 1986.

CHAPTER 10

COMPOSITE HINGE DESIGN

10.1 Introduction

A composite hinge has been designed to replace an existing metallic hinge on an aircraft aileron under the Innovative Network Program (INP) from the Cooperative Research Centre for Advanced Composite Structures (CRC-ACS). The existing design consisted in an aluminium double webbed hinge which was then attached to the aileron by means of a fork fitting. The new design aims at reducing the manufacturing cost while meeting all operational requirements. The main goal of this program was to develop an optimised design of a cost competitive composite hinge fitting and validate it by the manufacture and test of a prototype. Another main goal of the program was to compare the strength of thermoplastic versus thermoset composite materials when used in a highly loaded environment.

The external geometry of the hinge was governed by the aileron's front spar. Load cases were derived from the aircraft manufacturer specifications *. Ten different load cases were considered and the most critical cases were then chosen for further analysis and testing. These load cases were obtained from a full aileron model used during the INP.

In order to reduce the number of parts and therefore the weight of the structure, the new design consisted in a single web hinge, which eliminated the need of the fork fitting. This Chapter details the analysis carried out to design the single web hinge concept.

Research carried out in the analysis and testing of highly loaded T joints presented in Chapters 8 & 9 concentrated in studying the possible failure mechanisms which could be found during testing of the composite hinge. Results of this are incorporated into the hinge design.

* For proprietary reasons, the manufacturer can not be named

10.2 Calculation of critical load case

The load cases applied to the aileron were obtained from the aircraft manufacturer and were divided into four main cases as follows:

(1) Rib Line Loads
(2) Upper Surface Suction
(3) Distributed Surface Pressures
(4) Induced Bending-Deflected

The overall assumptions employed for the derivation of the above load cases are stated on the CRC-ACS Research File [1] and are quoted as follows:

a) Loads were resolved and applied on the aileron box only.
b) All vertical load vectors were assumed perpendicular to the chord line.
c) All horizontal load vectors were assumed parallel to the chord line.
d) Balance load due to the mass balance was neglected.

The given aileron airloads were derived from the 2-D chordwise airload distributions and were then evenly distributed over the aileron surface to give total spanwise loadings. Cases (1) to (4) were combined to give the worst loading conditions on the aileron. The critical case which was chosen for the hinge analysis was the combination of cases (3) and (4). This combination of the above load cases was then resolved into aileron hinge reactions by adding the reaction of the individual load cases [1]. The largest of the calculated reactions at hinge positions (10000 N) was employed for all finite element analysis performed on the hinge. The load direction is parallel to the front spar web. This value includes a 1.5 ultimate factor. This is a safety factor commonly employed in aircraft structures as per FAR (Federal Aviation Regulations) section 25.303. Single hinge failure conditions could not be investigated due to lack of data from the aircraft manufacturer. The additional data required to do such analysis would include new induced bending parameters for each of the assumed failed hinges.

10.3 Finite element analysis of existing aluminium hinge design

10.3.1 Modelling assumptions: Two-dimensional finite element analysis of baseline design

A schematic of the existing double webbed aluminium hinge design is shown in Figure 10.1. A two-dimensional finite element analysis of this existing design was firstly conducted on the web of the hinge to obtain the load distribution of both pin loaded holes. This provided information pertaining to the load path and critically loaded sections. The two dimensional FEA on a single web (symmetry conditions) of the existing aluminium hinge was conducted under plane stress assumptions. Eight node linear elastic plate elements with isotropic properties were employed. The resultant load obtained from the critical load case was divided on two (two web design) and applied as a nodal force at the ball bearing which connects the fork fitting to the hinge.

A drawing of the fork fitting with main dimensions is shown in Figure 10.2. The fork fitting was modelled as three rigid beams connecting the centre of the ball bearing (aileron side) to either centre of the pin loaded holes in the web of the hinge (hinge side). The load was then transferred from the centre of each pin loaded hole to the periphery of the hole by means of two beam sets. These beam sets were modelled as gap elements allowed to only take compression loads. This ensured that the bolt represented by the beam elements was not allowed to "pull" (enforce traction) on the periphery of the hole.

The boundary conditions employed for the two dimensional FEA assumed clamped conditions around the flange boundary. This was thought to be conservative since it did not include any flexibility from the front spar. A flexible attachment between the front spar and the hinge should provide for less abrupt stiffness change thus reducing stress concentrations at flange spar intersection. Furthermore, any inclusion on the analysis of the spar stiffness would require the modelling of the front spar and some of the rib/skin attachments to simulate the hard point provided by the rib which is located behind the hinge.

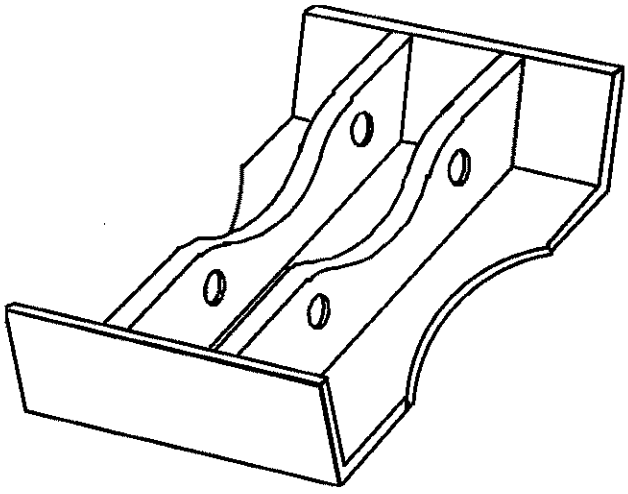

Figure 10.1: Schematic of existing double webbed aluminium hinge

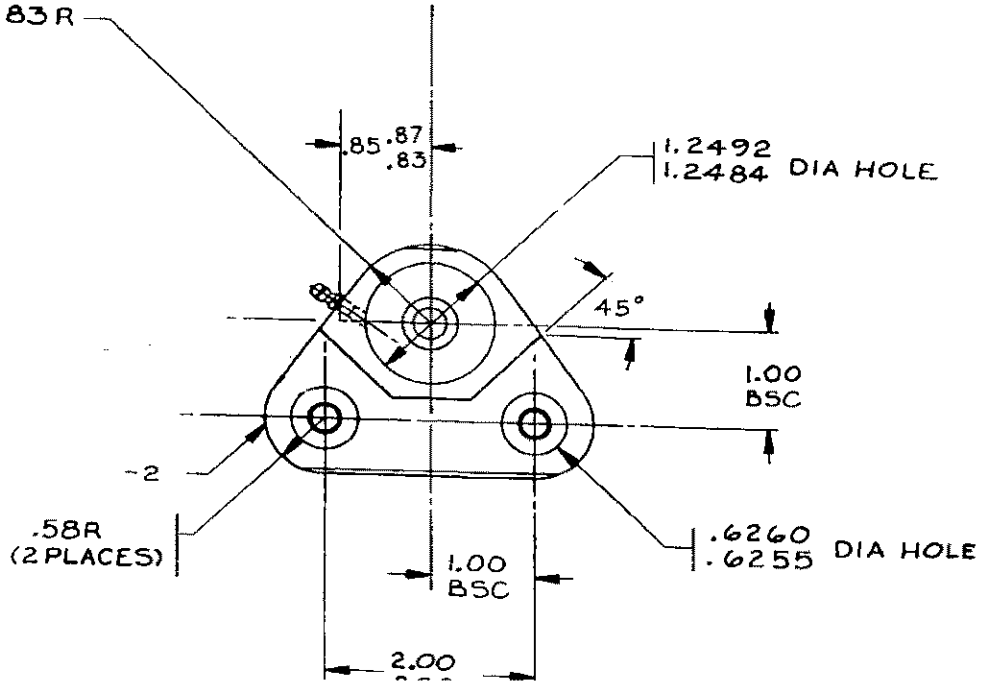

Figure 10.2: Overall dimensions of fork fitting

Figure 10.3 shows the mesh, modelling of load distribution and loading direction on the finite element model of the baseline design. A schematic of the INP baseline concept is shown in Figure 10.4. The cut-outs in the upper skin indicate the positioning of the four hinges.

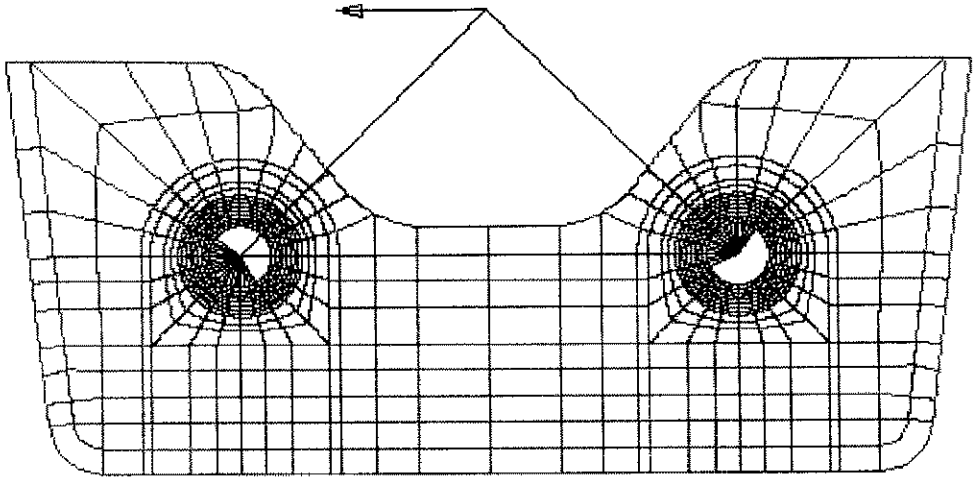

Figure 10.3: Baseline 2-D finite element model

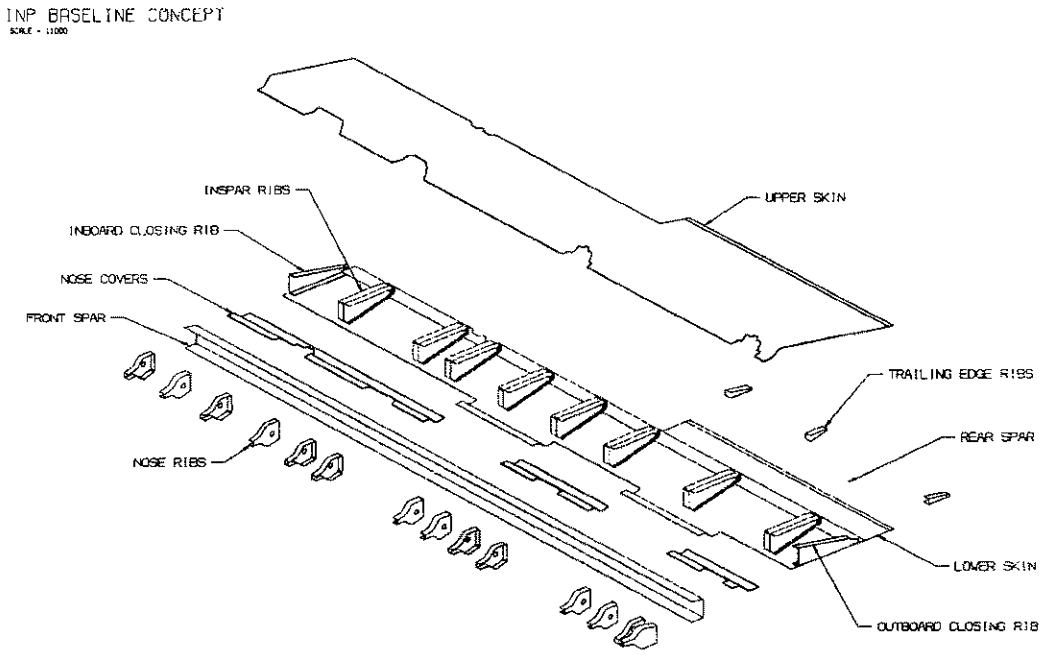

Figure 10.4: INP Baseline schematic

10.3.2 Material properties

The Young's Modulus and the Poisson's ratio of the aluminium casting 356-T6 was taken to be 71 GPa and 0.3 respectively. The yield and tensile strength for the aluminium

casting were obtained from SAE / AMS 4260D and quoted to be from section 3.6.1.2 as follows:

Tensile strength	25 ksi	(172 MPa)
Yield strength at 0.2 % offset	16.5 ksi	(114 MPa)
Elongation	1%	

The bushings employed for the pin loaded holes in the hinge web are made of beryllium and copper and are 6.35 mm thick. Material specifications for representative bearing hinge bushings indicate a tensile strength of 180 ksi (1240 MPa) with a Young's Modulus of 125 GPa and a Poisson's ratio of 0.34. The bolts connecting the hinge to the front spar of the aileron are 12 point head, 200 ksi min tensile and the self-locking nuts were 12 point, 220 ksi tensile.

10.3.3 Load path identification and critical stressed area from 2D analysis of baseline design

To identify both the load path and the most probable failure mode on the existing aluminium hinge a plot of the Von Mises stress was analysed. Figure 10.5 shows a Von Mises plot of the highest loaded region (right hole), while Figure 10.6 shows the Von Mises contour plot of the entire web section of the existing hinge design. The maximum Von Mises stress was found to be at the beryllium-copper bushing (172 MPa) while at the aluminium / beryllium-copper interface the Von Mises stress reached 83 MPa (on the aluminium). Based on these results, a safety factor of approximately 2 is obtained for the aluminium casting. From FAR sections 25.303 and 25.621 (safety factors and casting factors), the overall safety factor for a hinge casting should be 1.5*1.25=1.875. This indicates that the assumptions under which the analysis has been conducted are valid and conservative.

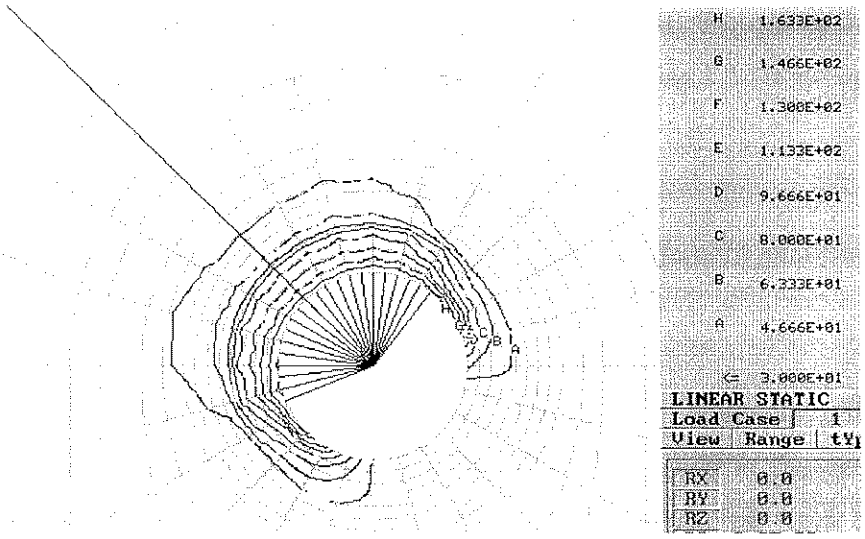

Figure 10.5: Von Mises plot of highest loaded region

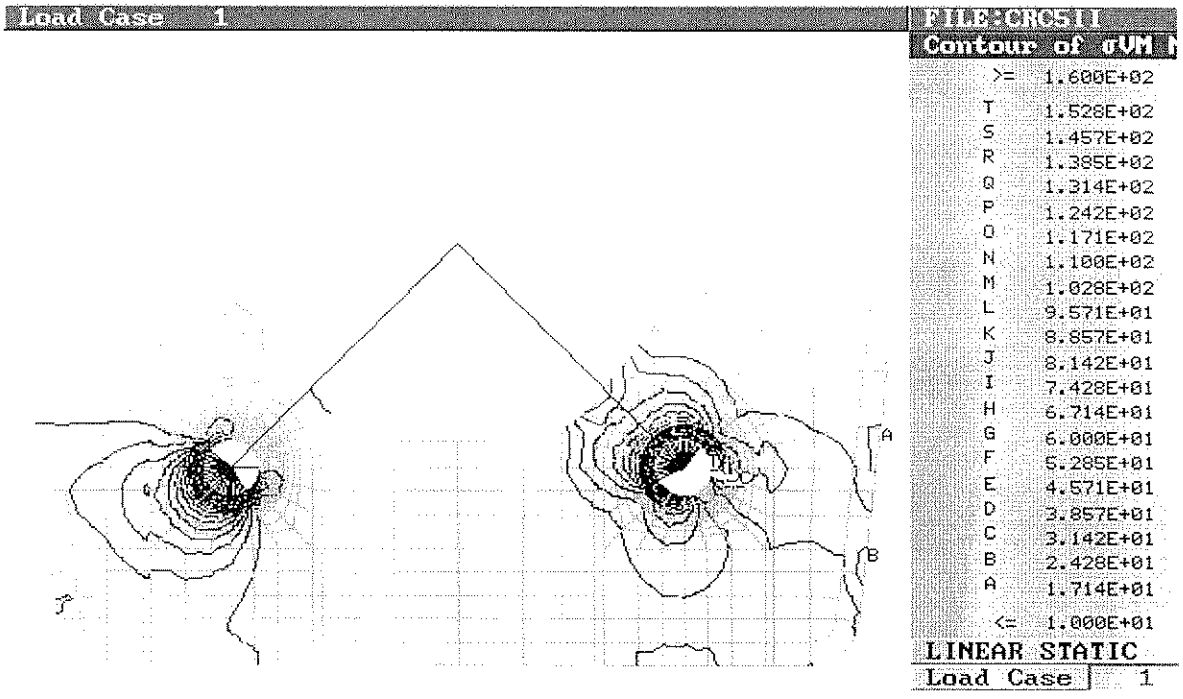

Figure 10.6: Von Mises plot of the web section

Design limit loads have been employed for all analysis due to the fact that equivalent loads were desired for both the baseline and the proposed composite designs. Ultimate

loads for both designs were different due to the dissimilar safety factors to be applied to each design. The overall safety factor for the composite hinge was 1.5 (ie no casting factor applies in this case).

10.3.4 Modelling assumptions: Three-dimensional finite element analysis of baseline design

Twenty node brick elements and fifteen node wedge elements with isotropic properties were employed. The resultant load was directly applied at the centre of each loaded hole and distributed to the periphery of the hole by placing rigid bricks (high Young's Modulus) in areas where gap beam elements were in compression. The boundary conditions employed for the three dimensional FEA assumed clamped conditions at fastener positions with symmetry conditions imposed to allow for half of the hinge to be modelled. Figure 10.7 shows the mesh on the three dimensional finite element model of the baseline design.

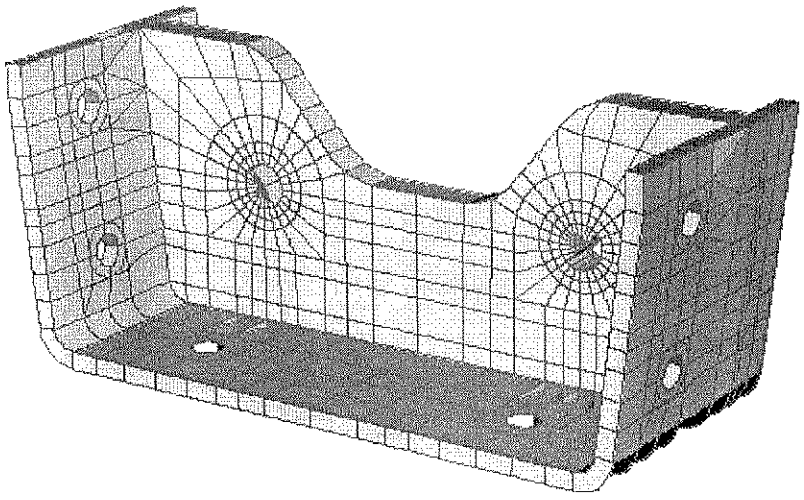

Figure 10.7: Baseline 3-D finite element model

10.3.5 Load path identification and critical stressed area from 3D analysis of baseline design

The three dimensional analysis was performed to provide additional information on the stress distribution of the baseline design. This additional information consisted mainly in obtaining the out-of-plane stress distribution and the stresses at fastener locations between the hinge and the aileron's front spar. The determination of load paths is of significant importance in achieving a more optimised design. To obtain an indication of the highly stressed and under stressed regions on the baseline design (existing aluminium hinge), a plot of the principal stress was analysed. Figure 10.8 shows a Principal stress contour plot of the highly loaded region of the existing hinge design.

As previously observed on the two dimensional finite element analysis performed on the web section of the hinge, the maximum Von Mises stress was found to be at the beryllium-copper bushing (116 MPa) while at the aluminium / beryllium-copper interface the Von Mises stress reached 57 MPa (on the aluminium). Additional high stress regions were found at most of the fastener locations where the hinge is assembled to the front spar of the aircraft's aileron.

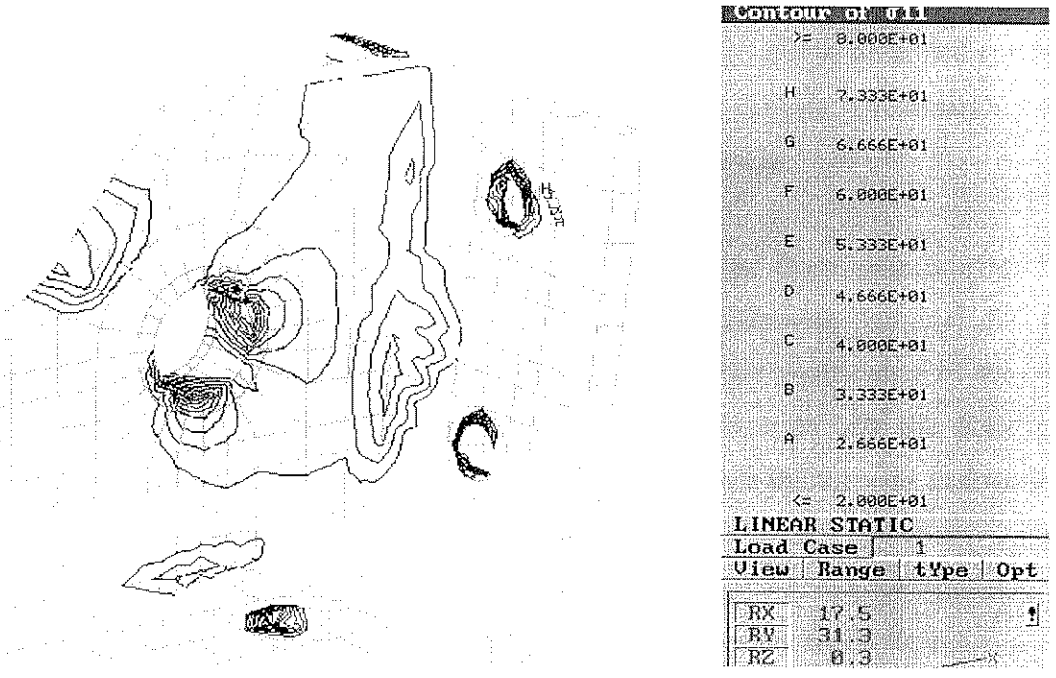

Figure 10.8: Principal stress plot of the highly loaded region on the baseline model

The significant discrepancy between the maximum Von Mises stresses obtained from the 2-D and 3-D model (approximately 45 %) is likely to be as a result of the added flexibility provided by in the 3-D model. Whereas in the 2-D model the boundary conditions assumed clamped conditions around the flange boundary, the 3-D model was only clamped at fastener locations (bolts connecting hinge to front spar). This allowed for displacement at the web/flange intersection to occur. A further reason for the discrepancies between models, could be the mesh refinement around the pin-loaded holes on the 3-D model when compared to the 2-D one. The lower maximum Von Mises stress yielded by the 3-D finite element analysis confirms that the assumption of an infinitely rigid spar results in a conservative design. Furthermore, this indicates that any sizing of the web based on 2-D assumptions and a rigid spar should result in a conservative design.

10.4 Proposed semi-optimised composite hinge design

A common approach in the aerospace industry is to reduce number of parts when optimising components. This approach was followed initially as it was seen that the fork fitting which connects the aileron to the wing could be integrated into the hinge fitting itself. This would not only reduce weight but also assembly cost. The weight in such a component is not as important due to the fact that fixed weights need to be added forward to the hinge line to achieve a balanced aileron for flutter considerations. The assembly and manufacturing cost can then be minimised by simplifying the design.

The external geometry of the hinge was governed by the front spar profile. The attachment method was to be chosen between mechanically fastening (original design), secondary bonding or a combination of the above methods. The positioning of the load pick-up point was also a fixed parameter. The above constraints left the following parameters as variables: number of webs, lay-up, flange and web thicknesses and number of parts in the hinge assembly.

The finite element analysis conducted on the existing design aided in deciding the more promising geometries by providing an insight into load paths within the hinge. After comparing a number of concepts in terms of manufacturing cost it was decided to further

develop a single web hinge concept which would reduce the number of parts on the hinge assembly from two to one (fasteners not included).

10.4.1 Modelling assumptions: Two-dimensional finite element analysis of proposed design

The sizing of the web was performed by conducting a finite element analysis on the web under the following assumptions:

a) Plane stress conditions.
b) Maximum allowable ply strain as failure criteria.
c) Material properties taken from prepreg properties (Hye3034K, see Chapter 10 for values).

The design allowables were assumed to be as follows:

ε_t =5000 με
ε_c =4000 με
γ_{xy}= 8000 με

Eight node 2D plane stress elements (632 plate elements) with orthotropic properties were employed. Ply strains were calculated using classical lamination theory. Boundary conditions and element types were identical to those employed for the analysis of the baseline design. The mesh, boundary conditions and loading distribution assumption are depicted in Figure 10.9. The crosses at nodes along the mesh boundary represent nodes fixed in all directions (x, y, z, rx, ry and rz).

The resultant load obtained from the critical load case was applied as a nodal force at the ball bearing which connects the fork fitting to the hinge. The lay-up was chosen to be quasi-isotropic in the web region as it is suggested [2] that the efficiency of highly loaded composite joints decreases for highly orthotropic lay-ups. This is particularly true around

bolt/pin loaded holes. Blocking of fibres was minimised to avoid significant reduction on bearing strength.

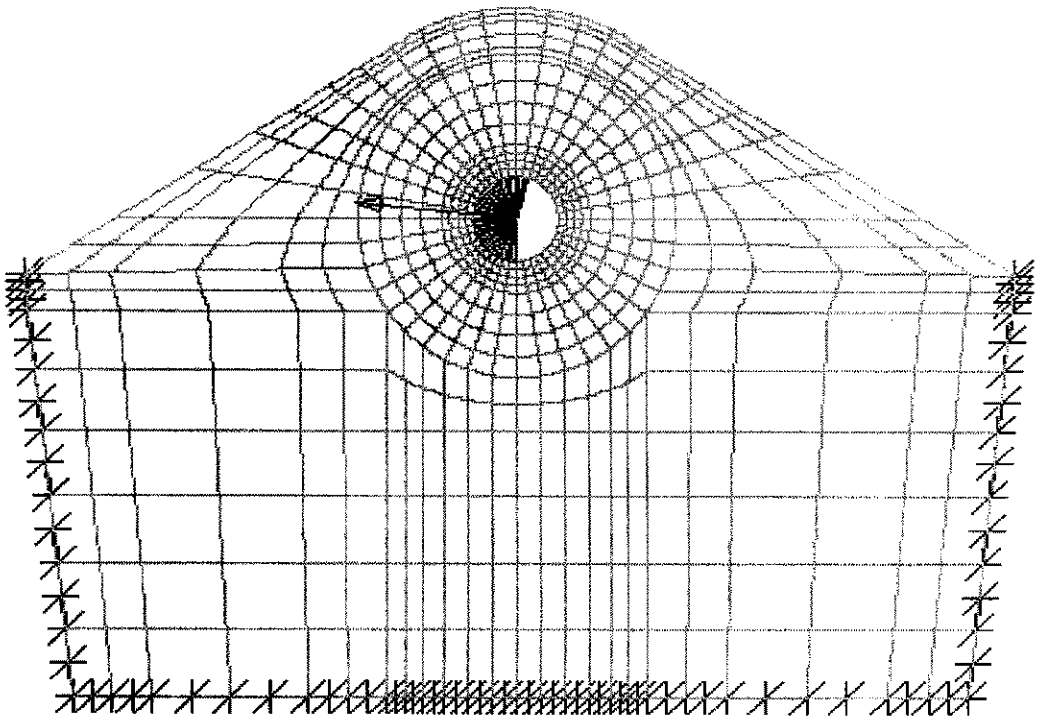

Figure 10.9: 2-D finite element model of single web concept design

Several thicknesses were trialled in an attempt to utilise material efficientlty. The resulting web thickness which met the design allowables was 12 mm and the chosen material was non-crimp fabric (ie 28 plies of non-crimp fabric resulting in an assumed cured ply thickness of 0.43 mm). The lay-up consisted in 14 plies of ± 45 and 14 plies of 0/90's as follows $(0/90/45/-45/0/90/-45/45/0/90/-45/45/0/90/-45/45/0/90/45/-45/45/-45/0/90/45/-45/0/90)_s$. The five outer plies at either side of the web continued onto the flange while 18 plies were dropped-off at the web/flange intersection. Finally, the flange section had two wrap-around plies resulting in an average flange thickness of 3.0 mm. Table 10.1, lists the actual laminate properties as used in the finite element analysis model.

Table 10.1: Laminate properties as employed in finite element analysis

	Quasi-isotropic Laminate
E_x (GPa)	47.7
E_y (GPa)	47.7
υ_{xy}	0.33
G_{yz} (GPa)	19.3

10.4.2 Modelling assumptions: Three-dimensional finite element analysis of proposed design

Once the web was sized, a 3-D finite element analysis of the hinge using plate shell elements was conducted to assess strain values at the web/flange intersection and to assess the fastening method to be employed. The FEA model only incorporates the hinge with no attempt being made to model the front spar and aileron stiffness, ie the spar is assumed to have no deflection due to hinge loads. This results in a conservative design as discussed in previous sections. It was observed during this analysis that secondary bonding of the hinge would introduce large peel stresses on the adhesive due to the rotation of the hinge with respect to the front spar of the aileron. As the most critical stress in adhesive materials is the peel stress and since the hinge is a primary structure, it was decided to mechanically fasten the hinge to the front spar.

Eight node plate shell elements (414) with four different orthotropic properties based on laminate engineering properties were employed. The different orthotropic properties were used to model the web, radius between flange and web, drop-off of plies at web/flange intersection and the flange region. The resin rich area at the web/flange junction was modelled with 20 node brick's (146). These bricks were given properties of RTM6 resin. The resultant load was directly applied at the centre of the loaded hole (position of hole corresponds to pick-up point for fork fitting) and distributed to the periphery of the hole by means of gap beam elements. These gap elements allowed to take compression loads only to ensure no traction is enforced on the periphery of the hole. The

boundary conditions employed for the three dimensional FEA assumed clamped conditions at fastener positions (see Figure 11.3 for fastener locations). Gap beam elements were placed along the flanges of the hinge to simulate the interaction between the front spar and hinge. The free end of the gap beam elements were clamped and the elements were given large stiffness to reproduce the assumed large stiffness of the front spar. A total of 510 beam elements were employed. Figure 10.10 shows the mesh and load direction of the three dimensional finite element model for the proposed design.

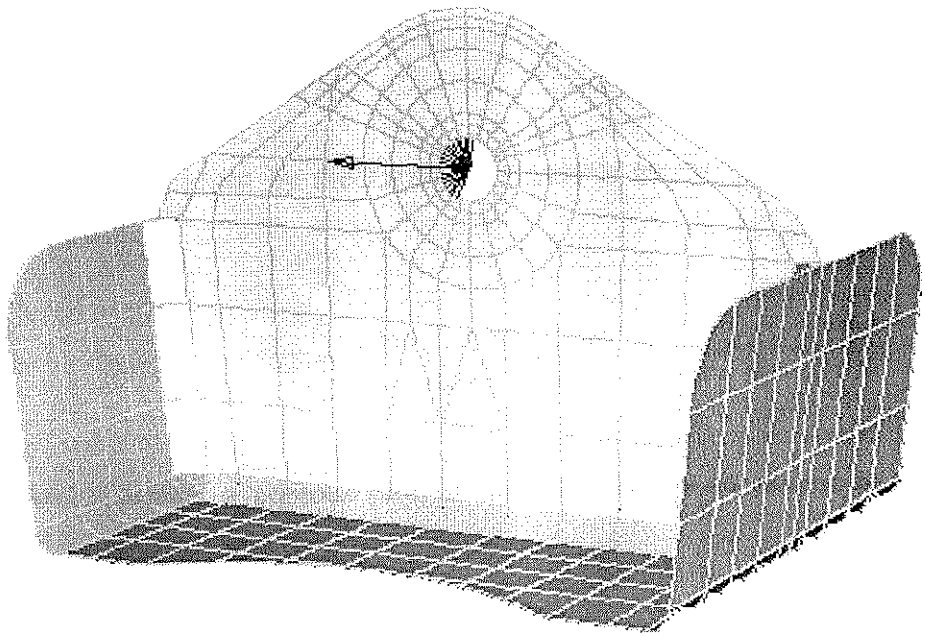

Figure 10.10: 3-D finite element model of proposed design

The smallest reserve factor in the critically stressed region (web/flange intersection in tension) was of 1.24. Reserve factors were calculated within the laminate solver of the commercial FEA software STRAND6 [3]. As mentioned previously, the maximum strain criterion was employed throughout the design process. This criterion has no interaction between the modes of failure. Therefore, the following inequalities are tested to assess whether the material has failed:

$$\varepsilon_1 < \left(\varepsilon_{1ta} = \frac{\sigma_{1t}}{E_1} \right) \tag{10.1}$$

$$\varepsilon_2 < \left(\varepsilon_{2ta} = \frac{\sigma_{2t}}{E_2} \right) \tag{10.2}$$

$$\varepsilon_1 < \left(\varepsilon_{1ca} = \frac{\sigma_{1c}}{E_1} \right) \tag{10.3}$$

$$\varepsilon_2 < \left(\varepsilon_{2ca} = \frac{\sigma_{2c}}{E_2} \right) \tag{10.4}$$

$$\varepsilon_{12} < \left(\varepsilon_{12a} = \frac{\tau_{12}}{G_{12}} \right) \tag{10.5}$$

The reserve factor given by the Laminate Solver is the highest of the five ratios calculated as follows:

$$\text{RF} = \frac{\text{Allowable Ply Strain}}{\text{Actual Ply Strain}} \tag{10.6}$$

Figure 10.11 depicts a contour plot of the principal strain around the critically stressed region.

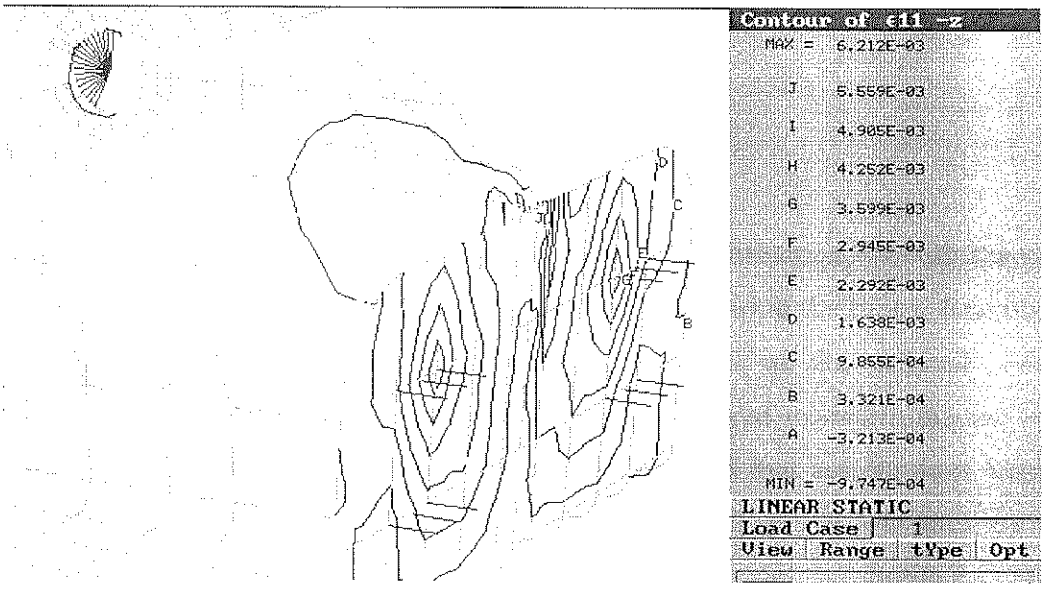

Figure 10.11: Principal strain plot of the highly loaded region on the proposed design

A deformed contour plot of the critical area is shown in Figure 10.12. Displacement values are indicated in mm in the load direction.

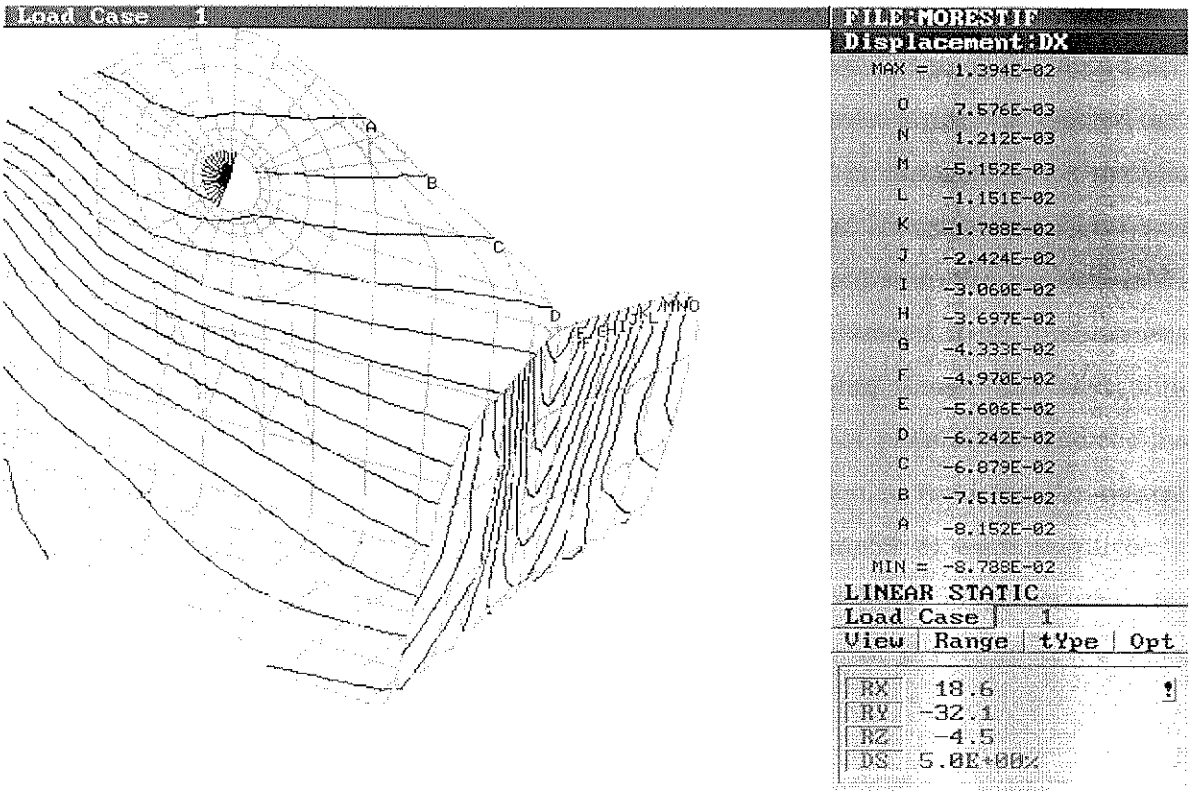

Figure 10.12: Deformed FEA plot showing highly strained region

10.5 Analysis summary

The existing design was studied in detail to gather information on both the critical features of the existing design and to identify the load path within the hinge. Running a 2-D (plane stress) and a 3-D (brick) finite element model of the original geometry accomplished this. Aircraft manufacturer's data was employed to determine the critical load case. Calculated stresses from the 2-D analysis showed that assumptions employed were conservative. This was reinforced by results obtained from the 3-D analysis which yielded lower maximum stresses when compared to the 2-D model. While the 2-D analysis indicated that the critically stressed regions where around the bearing surfaces (pin/hole

interfaces on web), the 3-D analysis showed that the largest stress concentrations would be found around the fastener holes (fasteners securing hinge flanges to front spar).

Based on the results obtained from the original design, a 2-D model of the proposed semi-optimised composite design was employed for the sizing of the web (thickness and lay-up of laminate). This approach should result in a conservative design of the web. Once this task was completed, a 3-D plate shell analysis of the composite hinge was carried out. This analysis provides with an insight on flange strains but it is expected to be poor in terms of accurately predicting critical out-of-plane (of the hinge flange plane) stresses at the intersection of the web/flange based on the knowledge gained from the analysis of T-joints in Chapters 8 & 9. Nevertheless, the in-plane strains obtained from this analysis should be valid along the radius formed between the web and flange and were thus employed for the sizing of this region (i.e. allowable drop-off of plies at the intersection between web and flange). Furthermore, the 3-D analysis was also used for the overall sizing of the flange thickness. Tests performed on T-joints (Chapter 8) were employed to determine load capability at the web/flange intersection on the hinge. The use of fillers was not attempted due to manufacturing difficulties (placing of dry fibre tows along web/flange intersection).

10.6 References

[1] CRC-ACS, Research File, CRC-AS-RF-111-001, 1993.

[2] Hart-Smith, L. J., "Joints", *Engineered Materials Handbook on Composites*, ASM International, Vol. 1, pp. 479-495.

[3] STRAND6 Reference Manual and User Guide, G+D Computing, Sydney, 1993.

CHAPTER 11

EXPERIMENTAL EVALUATION OF COMPOSITE HINGES

11.1 Introduction

This Chapter details the validation and testing program performed on thermoplastic and thermoset hinges under the CRC-ACS INP program. The main goals of the program were to validate the design cycle by testing the final components and to compare the strength of thermoplastics versus thermoset composite materials when used in a highly loaded environment. The design of the proposed hinge is covered in Chapter 10. A schematic of the existing design (2 web design) together with a photograph of the proposed single web concept design is depicted in Figure 11.1. A special purpose test rig was designed to test the hinge specimens under the worst loading case expected during operating conditions.

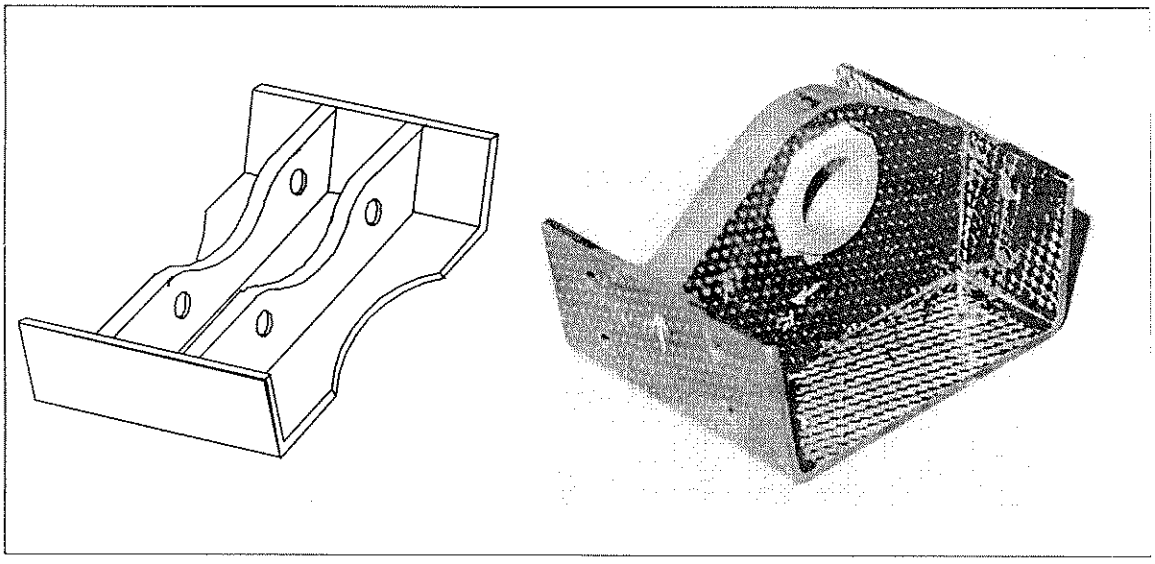

Figure 11.1: Actual aluminium hinge schematic (left) and proposed composite hinge (right)

Two different composite material systems, eg thermoset and thermoplastic composites, were used to manufacture the single web hinges. The thermoset hinges were manufactured using liquid moulding technology (RTM) and non-crimp fabrics. The thermoplastic hinges were produced from carbon fiber fabric reinforced polyetherimide (CF/PEI) using compression moulding and co-consolidation procedures [1]. Four RTM (thermoset) hinges and five thermoplastic hinges were tested to failure.

11.2 Advantages and disadvantages of thermoset and thermoplastic materials

The following advantages and disadvantages of both types of composite materials are quoted from [2]:

Advantages of thermosets:

* Low resin viscosity
* Good fibre wet-out
* Excellent thermally stability once polymerised
* Chemically resistant
* Creep resistant

Disadvantages of thermosets:

* Brittle
* Non-recyclable via standard techniques
* Must mould polymer in shape of final part---not post-formable

Advantages of thermoplastics:

* Unlimited shelf life

* Easy to handle (no tackiness)
* Recyclable
* Easy to repair by welding, solvent bonding, etc.
* Post-formable

Disadvantages of thermoplastics:

* Thermoplastics are prone to creep
* Poor melt flow characteristics

11.3 Manufacturing aspects

The thermoset hinges were manufactured using liquid moulding technology with carbon biaxial non-crimp fabrics (COTECH C-BX 440) and RTM6 resin. A summary of the manufacturing procedure for the RTM hinge is outlined below:

Firstly, the material was kitted and tackified with powdered 'B-staged' RTM6 resin. The plies were then assembled in order and heat set over wooden forming blocks under vacuum in an oven at 100^0 C for 30 minutes. After trimming the plies and closing the steel moulds, the tool was subjected to full vacuum and the resin injected at 200 kPa. Prior to this, the resin and tool were preheated to 80^0 C and 120^0 C respectively.

The thermoplastic composite hinges were produced [1] from solvent impregnated fibre fabric reinforced polyetherimide (Ultem 1000) prepreg supplied by Ten Cate Advanced Composites, the Netherlands. The carbon fabric has a 5H satin woven construction. The prepreg has a resin content of 44.1 wt.%. PEI is an amorphous polymer and has a glass transition temperature of 217 °C [3]. Because of the complex geometry of the hinge, co-consolidation (in a hot press) technique was used to manufacture the hinge, in which several components with simple geometry were first produced by compression moulding technique and then were co-consolidated in a specially designed forming mould [4]. To get fully

consolidated thermoplastic composite parts with high quality, the optimum forming conditions for this material, eg. forming temperature, holding time and forming pressure, were determined by an impregnation model developed by Hou et. al. [5]. The final void content in the thermoplastic composite hinge was less than 0.2%.

Both thermoset and thermoplastic hinges were finally trimmed to their final dimension and the holes for the fastening bolts were hand drilled. The main bush hole (load pick-up point) was drilled with a hole saw. The bush was then bonded with BR95 paste adhesive and left to cure at room temperature for over 24 hours.

11.4 Test set-up

A special purpose test rig was designed to test the hinge specimens under the worst loading case expected during operating conditions. The test set-up consisted of a hollow steel beam with two machined steel plates matching the profile of the front spar. These parts were bolted together to a larger steel plate fitted to the INSTRON testing machine. A schematic indicating loading direction with an actual photograph of the loaded hinge specimen is shown in Figure 11.2, while Figure 11.3 depicts a complete schematic of the special purpose test rig.

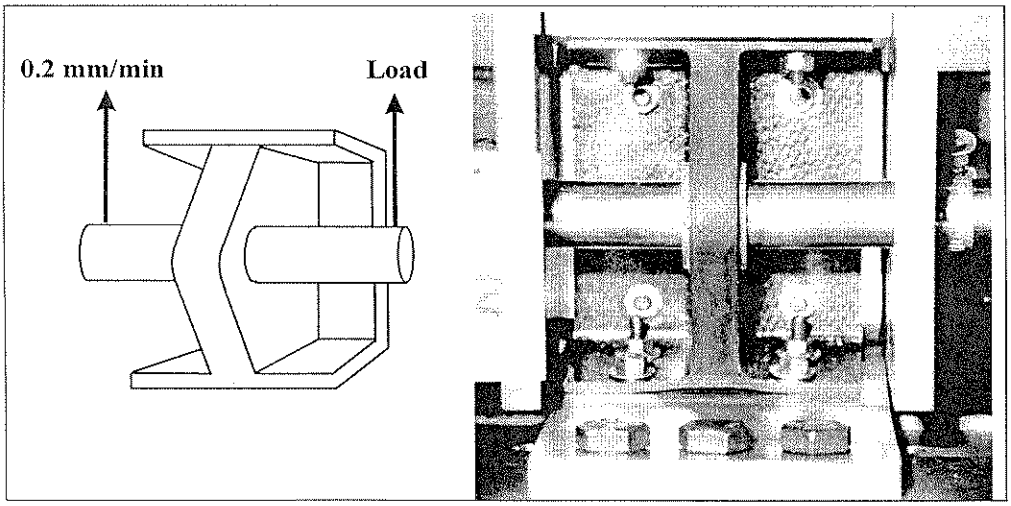

Figure 11.2: Composite hinge test set-up

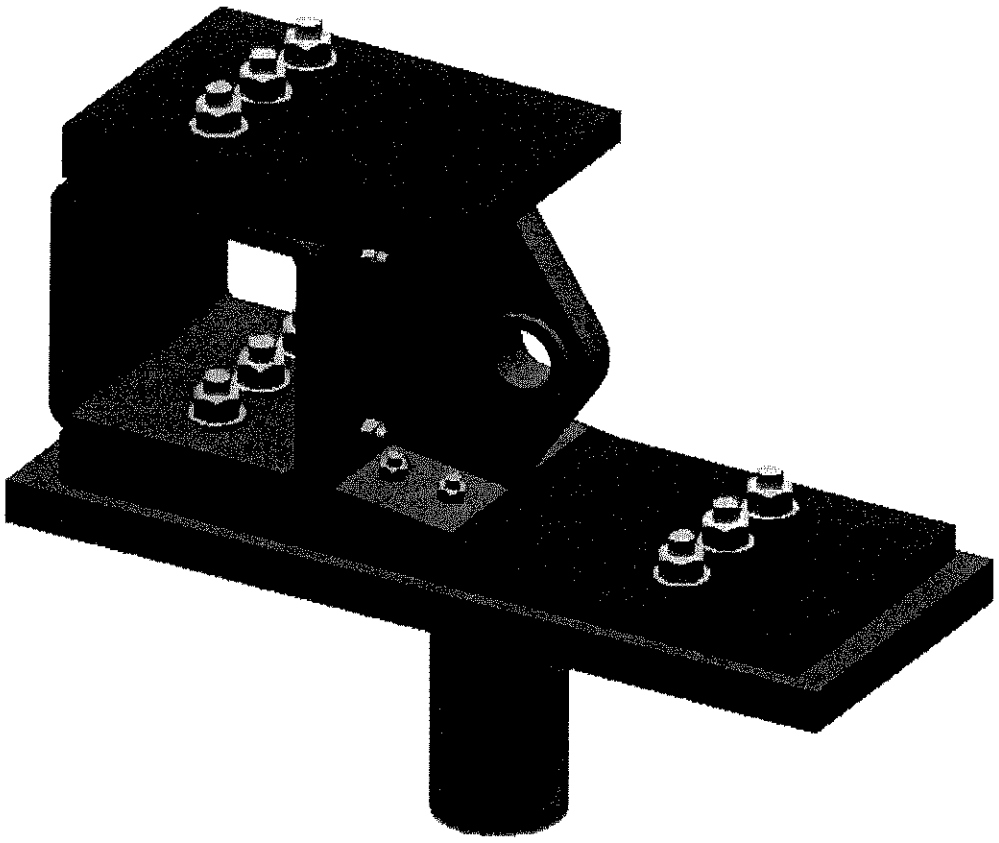

Figure 11.3: Composite hinge test rig

The tests were carried out in an INSTRON 1195 machine under displacement control at 0.2 mm/min. A load-displacement curve was obtained from the data acquisition system and the test was filmed with a SVHS video camera so as to be able to determine crack initiation/propagation.

11.5 Test results

Four RTM hinges and five thermoplastic hinges were tested to failure. A typical load-displacement curve for both thermoplastics and thermoset composite hinges is shown in

Figure 11.4. Both hinges behaved linearly up to the onset of the first crack growth in the tensile section, ie in the bottom section of the hinge being tested. After this event, non-linear behaviour was observed in both specimens. The main failure mode observed in all hinges appeared to be delamination in the tensile section (as shown in Figure 11.5), while no failure indication was observed in the compression side.

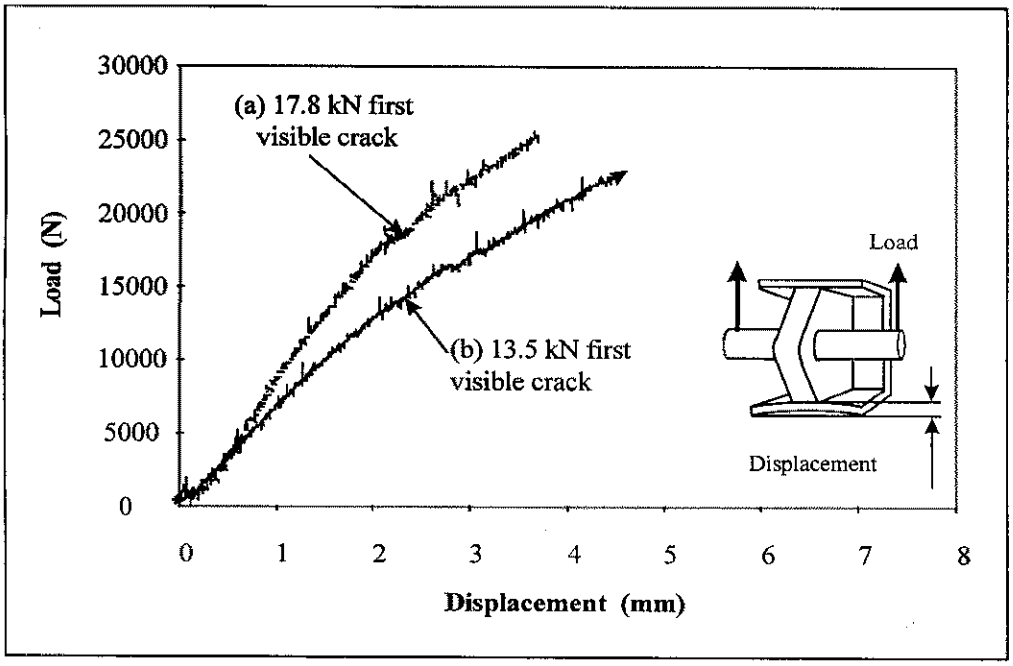

Figure 11.4: Typical load-deflection curves for (a) thermoplastic and (b) thermoset hinges

The load at which delamination started was much lower for the RTM specimens (from 9 up to 13.5 kN). Once delamination was visible to the naked eye, fibre breakage occurred close to the web/flange intersection resulting in catastrophic failure. The thermoplastic hinges delaminated at a higher load level (above 15 kN) and catastrophic failure was not observed up to the specified maximum test load of 25 kN. After the load was removed, only small delaminations could be seen in the thermoplastic hinges while the extent of failure on the RTM hinges was substantial.

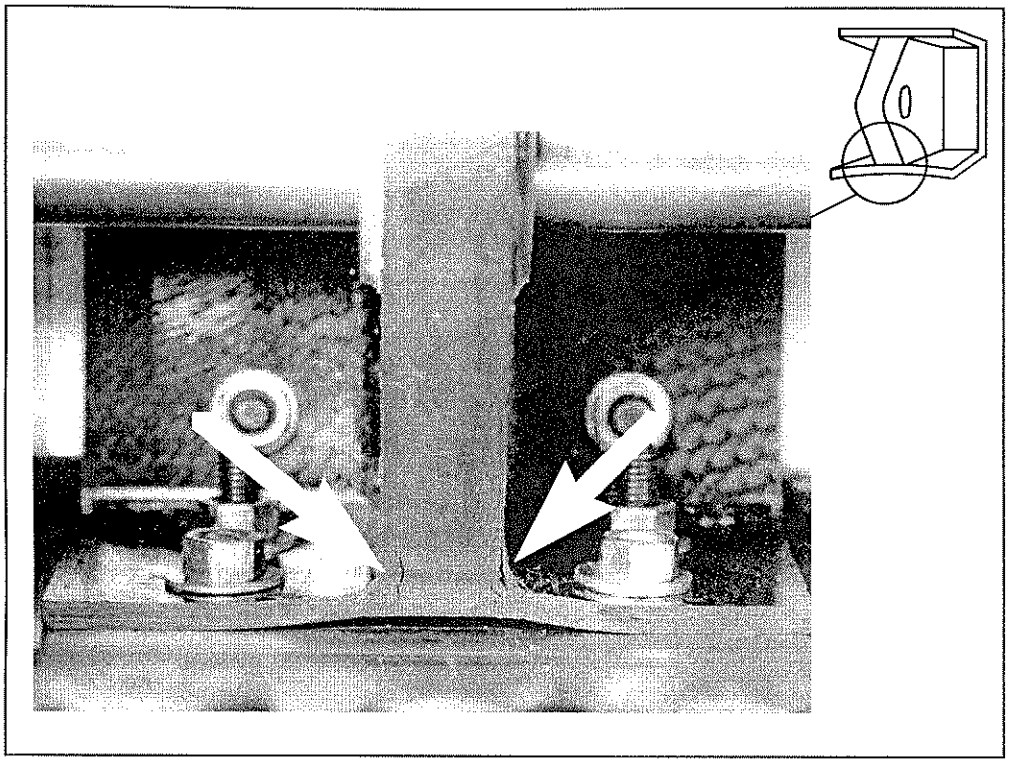

Figure 11.5: Delamination at tensile section of hinge being tested

A schematic diagram of the failure mechanisms observed during test is shown in Figure 11.6. The primary cause for delamination is due to excessive stress in the transverse direction within the matrix of a composite material. These large stresses in the tensile section of the hinge are mainly due to the out-of-plane deformation of the web/flange intersection resulting in the plies tending to pull away from the center line of the web. The failure mode observed in all hinges can aid in explaining the largest strength of the thermoplastic hinge when compared to the RTM version. Because delamination is dominated mainly by the matrix property [6], it is not surprising to see that the composite hinge made from a more toughened matrix composite system (thermoplastic) could survive a higher load than that made from a brittle matrix composite system (thermoset). The ultimate load expected during the operation of the hinge was met by the thermoplastic hinge. The initiation of failure on the thermoset hinge was just below the ultimate design load (minimum failure load recorded).

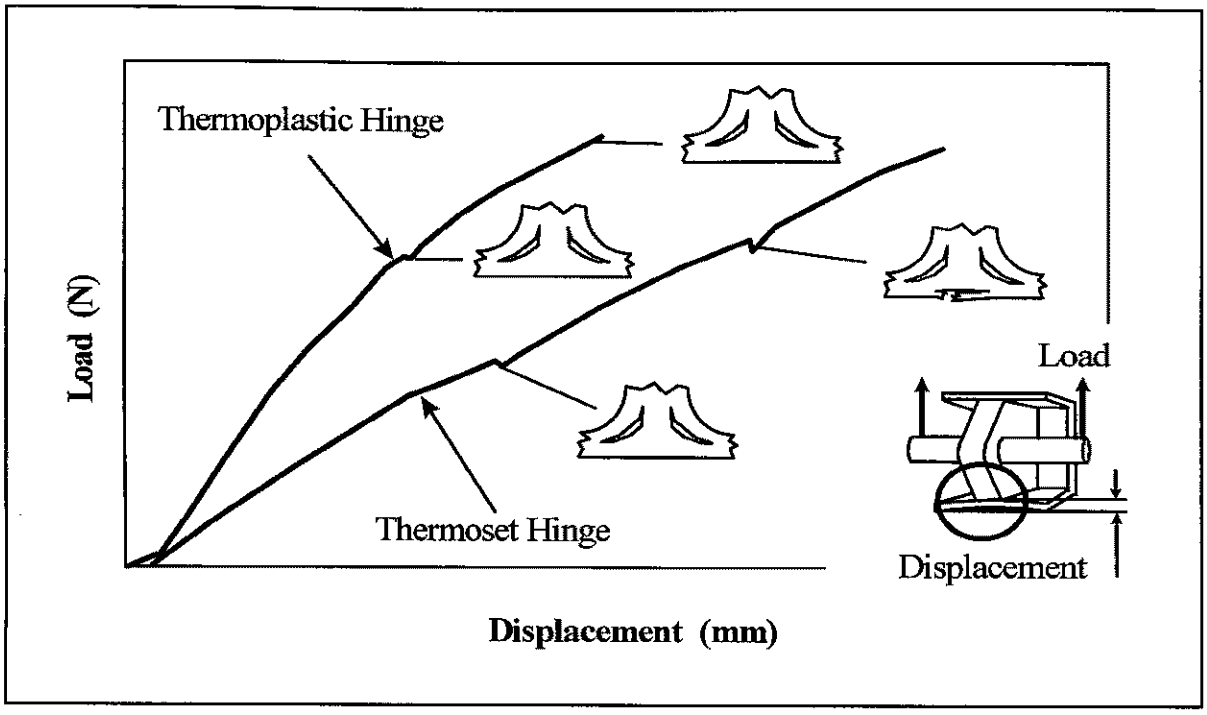

Figure 11.6: Schematic diagram of failure mechanisms in tensile section of hinge

11.5.1 Effect of web ply drop-off on hinge strength

The effect of flange thickness distribution on the hinge strength was studied using thermoplastic composite hinges [1, 7]. The flange is made up of 10 layers of CF fabric/PEI prepregs and has a total thickness of 3 mm. To obtain continuous fibre orientation in the outer side of the hinge flange as well as in the web/flange intersection, these 10 layers of prepreg were divided into two groups, namely group **a** and group **b** (as indicated in Figure 11.7). Group **a** corresponds to the build up around the web/flange intersection while group **b** forms the outer side of the flange. Two kinds of thermoplastic hinges with the same fibre orientation but with two different flange thickness distributions of **a/b** = 7/3 and **a/b** = 5/5 were tested. The results are shown in Figure 11.7. As expected, hinge with **a/b** = 7/3 flange thickness distribution delaminated at a higher load level (17.8 kN) than that of **a/b** = 5/5 (15.5 kN). The reason is believed to be due to the fact that with more continuous fibre oriented in the load

direction, the secondary tensile stresses within the matrix can be effectively reduced in the web/flange intersection.

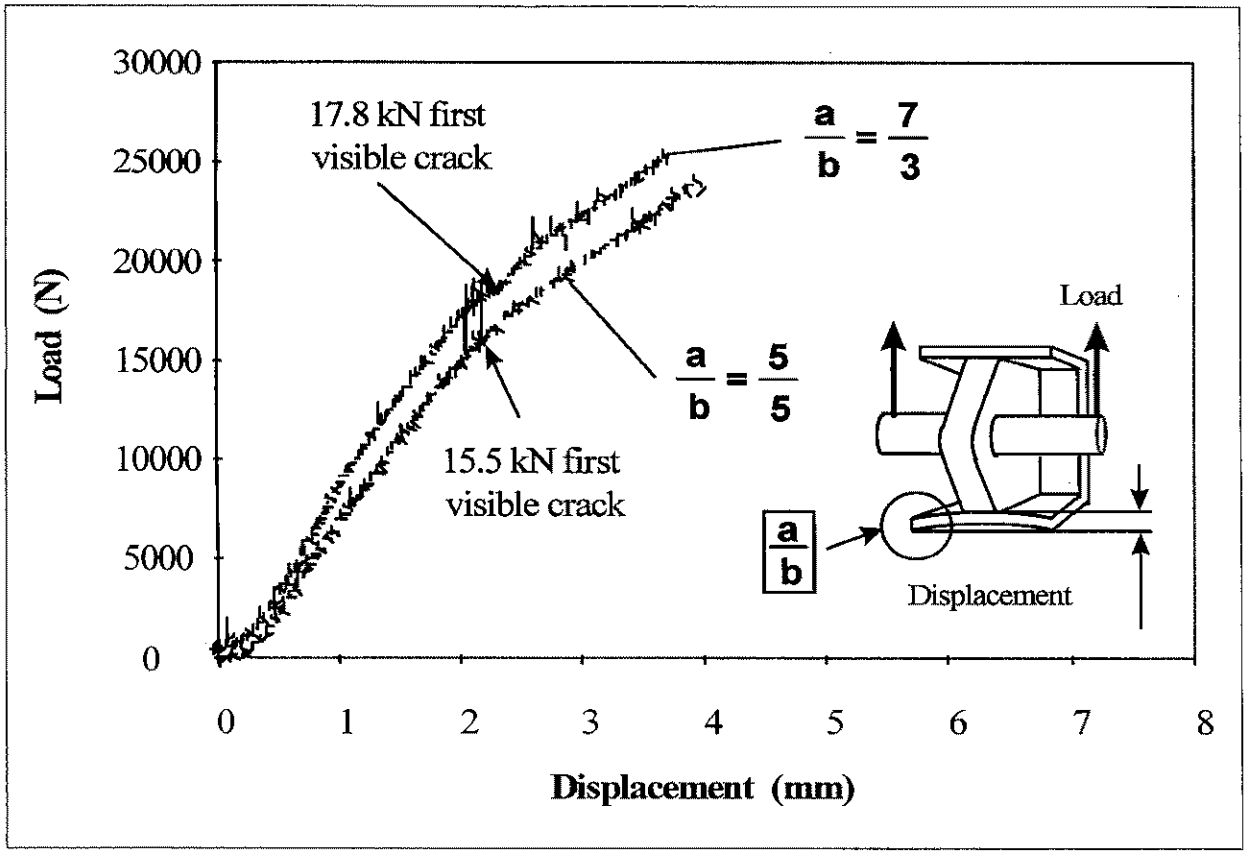

Figure 11.7: Effect of flange thickness distribution on thermoplastic composite hinge strength

11.6 Summary and Conclusions

The manufacturing cost could significantly be reduced by adopting the single web hinge concept. The overall reduction in cost would depend on recurrent manufacturing cost and expected number of hinges to be produced. The largest cost in the development of the single web hinge concept was the RTM tooling for the thermoset components and the co-consolidation moulds required for the thermoplastic hinges. The strength comparison between

thermoplastic and thermoset hinge coupons showed; as expected; that due to the failure mode being delamination, the thermoplastic hinges performed significantly better. Furthermore, if a hot-wet load enhancement factor was to be considered, the thermoplastic hinges would present a larger advantage due to the fact that their mechanical properties do not degrade as much as those of thermoset materials.

The initiation of failure in all hinges appeared to be delamination. The load at which delamination could be heard was lower for the RTM specimens. Once delamination was visible to the naked eye, fibre breakage occurred close to the web/flange intersection resulting in catastrophic failure. The thermoplastic hinges delaminated at a higher load and catastrophic failure was not observed up to a tested load of 25 kN. No visible failure could be seen in the thermoplastic hinges while the extent of failure on the RTM hinges was very large once the load was removed. The ultimate load expected during the operation of the hinge was met by the thermoplastic hinge. The initiation of failure on the thermoset hinge was just below the ultimate load (when the minimum failure load is considered).

Although the failure mode was predicted to be delamination at the web/flange intersection based on test result from T-joints conducted in Chapter 8, the load at which failure initiated could not be predicted accurately. The lack of correlation can be directly related to the large deformations observed at the web/flange intersection when compared to the predicted ones (the 3-D plate shell finite element analysis under-predicted the displacement by a factor of 10). Large displacements observed during testing can be in turn related to the difference between the assumed stiffness of the test rig and its actual stiffness. While the finite element analysis assumed the stiffness of the hinge to be negligible when compared to the test rig's stiffness, this was proven wrong by the test results which show significant deformations of the test rig during loading.

11.7 References

[1] Hou, M., Lin, Y., Mai, Y. W., "Manufacturing and Testing of Thermoplastic Composite High Load Hinge", *Proceedings of the American Society for Composites*, 12th Technical Conference, Dearborn, Michigan, pp. 1005-1014, October 6-8, 1997.

[2] Tutorial on Polymer Composite Moulding, Developed by the Intelligent Systems Lab in cooperation with the Composite Materials and Structure Centre at the Michigan State University and the Centre of Composite Materials at the University of Delaware, *http:// isl.cps.msu.edu/trp/toc.html*, 1997.

[3] Fines, R. E., Bartolomucci, J. P., "Polyether-imides (PEI)", Engineering Materials Handbooks, Volume 2, Engineering Plastics, edited by Epel, J. N. et al. Published by ASTM International, pp. 156-158.

[4] Hou, M., Lin, Y., Mai, Y. W., "Manufacturing process and mechanical properties of thermoplastic composite components", *Journal of Materials Processing Technology*, 63 (1997) pp. 334-338.

[5] Hou, M., Lin, Y., Mai, Y. W., "Optimisation of compression moulding conditions of carbon fibre fabric reinforced polyetherimide composite material", *Proceedings of the international conference on advanced materials*, Progress in Advanced Materials and Mechanics, August 12-15, 1996, Beijing, China, edited by Wang, T. C. and Chou, T. W., published by Peking University Press, pp. 97-102, 1996.

[6] Avva, V. S., Allen, H. G., Shivakumar, K. N., "Through-the-thickness tension strength of 3-D braided composites", *Proceedings of the American Society for Composites*, 9th technical conference, Newark, Delaware, published by Technomic Publishing Co., pp. 877-883, Sept. 20-22, 1994.

[7] Rispler, A. R., Hou, M., Tong, L., Steven, G. P., Ye, L., Mai, Y. W., "Design and testing of an aircraft composite hinge", *11th International Conference on Composite Materials*, ICCM 11, Gold Coast, Australia, Vol. VI: Composite Structures, pp. 158-166, July 14-18, 1997.

CHAPTER 12

CONCLUSIONS AND RECOMMENDATIONS

12.1 Conclusions for optimisation of bonded joints

This dissertation has looked in detail at the application and implementation of a heuristic optimality criteria method on bonded joints. The method is known as ESO (Evolutionary Structural Optimisation method) and consists essentially on removing the understressed material from the joint to achieve a fully stressed design. For the reduction in peak stresses on bonded joints, two areas were investigated. Firstly, the shaping of adherends to minimize peak stresses at the tip of the adhesive was researched. The problem was treated as a min-max optimisation problem where the main objective was to minimise the maximum stress on the adhesive by allowing only the adherend shape along the adhesive overlap to be modified. The results showed that the critical peak stresses can be significantly reduced for both the single and double lap joints considered. In the single lap joint the critical stresses are peel stresses which are induced by the eccentricity of the load path. These stresses were reduced by up to 36 % when compared to the baseline square ended adherends.

For the double lap joint, both the shear and peel stresses are considered to cause failure. The reason for this is that the double lap joint does not suffer from large bending moments in the adherend. The bending moments are the main cause of peel stresses at the end of the overlap. Reduction of 17 % in peak peel stresses and an 8 % on peak shear stresses were obtained in the optimisation of a double lap joint. This reduction in peak stresses on single and double lap joints will lead to an increase in joint strength and efficiency.

It has been shown in this dissertation that the redistribution of stresses on the adherend due to material removal has a large effect on the adhesive stresses. The more evenly stressed adherends result in significant stress reductions on the adhesive. The goal pursued by other researchers in attempting to achieve a uniform shear stress distribution along the adhesive is inadequate for design purposes due to creep considerations on the adhesive.

The second area investigated was the application of ESO to the search of an optimum shape fillet. This problem was again treated as a min-max optimisation problem. In this case the goal was to minimise the maximum principal stress on the adhesive. This stress was shown to cause failure in specimens with tabs. The tabs were simulated as a double lap joint with a reverse taper. The initiation of failure normally occurs at the tip of the upper adherend (reverse tapered). In this case, only elements corresponding to the adhesive fillet were allowed to evolve (could be removed). The optimisation was carried out on two different upper adherends and the best configuration (Titanium upper adherend – CFRP central adherend) was chosen for further investigation.

This investigation consisted in assessing the influence of the adhesive stiffness on the optimum shape of the adhesive fillet. Three different stiffnesses were considered to allow for a trendline to be developed. During this investigation, the concept of monitoring properties was introduced into ESO. This allows for easier tracking of the optimisation process and a faster and more efficient post-processing of results. A new optimisation technique was also developed to minimise run time of the optimisation problem. This technique consists in running the optimisation problem in a stepped fashion. It is commonly known, that the size of the elements thus the number of elements has a large influence on the time taken to arrive to an optimum solution. The stepped optimisation approach allows the user to select a relative coarse mesh to drive the design to an optimum based on the coarse mesh. This "optimum" is then unevolved by three steady states and the mesh refined locally. This desensitises the optimum solution from the element size. The problem is then restarted to obtain a new optimum solution which presents much finer detail due to the remeshing operation performed, but does not take

considerable time to run as the starting shape is much closer to the optimum solution. The use of the Classical Evolutionary Technique which considers stresses of all elements in the joint yielded some variation between the optimum shapes once the mesh densities were modified (using the developed stepped optimisation approach). Due to this variation, a newly developed capability within EVOLVE was assessed. This capability; termed Passive Evolutionary Technique; allows for the selection of desired properties from which the stresses are calculated. This technique proved very efficient. No significant variation due to change in mesh densities was observed and the post-processing was greatly simplified since the output of EVOLVE included only the stresses on the adhesive.

The results of the investigation on the effect of adhesive stiffness on optimum shape of fillet showed that as the adhesive stiffness increases, the optimum fillet angle decreases and its shape becomes more curved (changes in slope within adhesive fillet). As expected, the increase of the adhesive stiffness resulted in larger principal stresses on the adhesive fillet. The stepped optimisation approach resulted in peak stress reductions on the adhesive of up to 64 %. Peel stresses on the central CFRP adherend were also reduced by up to 66 % when compared to the starting square adhesive fillet baseline. These stresses can also result in peel failure on composite adherends. The stepped optimisation method provides with an excellent preliminary design tool which can be used efficiently to minimise peak stresses in bonded joints.

12.2 Conclusions for optimisation of pin-loaded joints

This dissertation also looked in detail into the reduction of stresses in bolted and pin-loaded joints by developing a new and modified ESO approach that does not remove elements but instead modifies their property. This approach allows material to change where high stress gradients are present. In the case of bolted and pin-loaded joints, it allows for areas of high stress concentrations where failure normally originates to be "switched" from composite to a specified metal such as aluminium. This results in an

insert "growing" into the composite material by replacing highly stressed composite material by an isotropic material in an iterative fashion. The method also allows to keep the fastener unchanged (i.e. circular shape). That is, the inner shape of the insert is kept circular while its contour is modified as the evolutionary method progresses.

During the investigation performed on the optimum shape of metallic inserts it was found that the normally assumed cosine load distribution had an effect on the optimum insert shape. Gap beam elements were employed to more accurately represent the load distribution on the loaded hole. Further investigations also assessed the effect of the material chosen for the insert and the effect of geometric ratios on the size and shape of optimum inserts. The investigations showed that the largest effect on the optimum shape of the insert was the material chosen for the insert.

The new and modified optimisation method was also successfully applied to both multiple load cases and on multiple holes problems. For a hole that is loaded in two opposite directions it was shown that the optimum shape will approximate an ellipse with the major axis coincident with the direction of the load. If the direction of the principal load is not known on a structure with multiple load cases, the best alternative is to bond a circular insert. A 40 % (w/d=4) to 55 % (w/d=11.5) improvement in the capability of the optimised inserts in reducing the maximum compressive stress at the interface per unit mass of test specimen was achieved when compared to a circular insert for the single load case problem. These stresses are largely responsible for the initiation of bearing failure on composite joints where bearing failure is the critical failure mode. The reductions in strain concentrations predicted by the finite element analysis were successfully correlated by testing pin-loaded specimens with the aid of the photoelastic technique.

The manufacturing of specimens presented challenges, in particular related to producing the optimum shape cut-outs on the composite specimens. Water-jet cutting proved to be the only alternative to produce a net optimum shape cut-out. Some delamination problems were encountered even employing the water–jet technology. The test results show that by distributing an equivalent amount of material in an optimum

configuration, a larger reduction in strain concentration can be achieved. This further validates the approach in composite materials where by reducing the compressive stresses at pin loaded holes in bearing critical structures improves the efficiency of the joint.

The concept of shifting and changing material properties to critically loaded regions or areas where stress concentrations limit the loading capability of highly loaded structures can be applied to numerous fields beyond aircraft structures. The results clearly show the potential of this procedure in the reduction of peak stresses in bolted and pin-loaded joints.

12.3 Conclusions for T-joint analysis

For out-of-plane joints a testing program was developed to assess the influence of placing different size and shape of inserts into the resin rich area normally encountered at the intersection of web and flange. The testing program yielded interesting results related to the irregularities found due to manufacturing considerations. It was found that the size of the filler has a significant effect on pull-out strength. The placing of too large fillers were found to exacerbate the geometric discontinuity (kinking of the fibres) at the web/flange junction thus increasing the stress concentration at this location. This ultimately resulted in a decrease in failure load when compared to specimens with no inserts.

A second test program confirmed this when it was found that the same type of fillers (unidirectional) but in a smaller size actually increased the pull-out strength of the T-joints. The thickness of the specimens were also found to have significant effect on pull-out strength. The thicker specimens allow for redistribution of the plies close to the filler region resulting in smaller geometric discontinuities. The larger resin rich area encountered in these specimens allows the fibres to re-accommodate themselves without kinking. It appears that for thinner specimens, the use of inserts; when oversized; introduce geometric discontinuities by creating kinks on the fibres which cause stress

concentrations resulting in reduced pull-out strengths. Scatter observed in results from all specimens, can be attributed to the resin dominated failure mode together with some bending in the test specimens due to a possible lack of symmetry in the far field load. All specimens tested suffer from a delamination type failure.

This dissertation also looked in detail into the prediction of failure in T-type joints. A linear-elastic finite element analysis performed on the no-insert configuration, successfully validated the experimental results with great accuracy. The analysis showed that the most accurate representation of the T-joint was obtained by accurately modelling the joint as a 2D plane strain problem employing orthotropic properties for each ply. Although the idealised geometry of the joint yielded good results in terms of predicting stiffness, the model was not accurate in predicting failure location and load. To achieve this, the geometry of the joint was modelled from ply thickness measurements obtained by means of an electronic microscope. Once the geometry of the T-joint was replicated on the finite element analysis, it was found that the failure initiation load and failure mode could be validated with great accuracy. The interlaminar peel index failure based on interlaminar peel strength of the composite material proved to be the most accurate method in determining the load at which failure initiates. This highlighted the fact, that the use of net resin properties for prediction of onset of failure due to delamination is inadequate, even in the presence of large pockets of resin.

The use of quadratic type criteria proved to be unwarranted when a single state of stress is present in the joint. The comparison of the local state of stress in the interply resin or matrix layer with relevant strength parameters appears to be the best approach for problems where a single state of stress is present. The work provided in this dissertation should aid in the understanding of out of plane load transfer and failure initiation in T-joints.

12.4 Conclusions for Composite Hinge Design

A further achievement of this dissertation was to successfully extend the use of composites into a highly loaded hinge. The control surface hinge fitting was manufactured using liquid moulding and dry preform technology. It was found that the manufacturing cost could significantly be reduced by adopting a single web hinge concept. Finite element analysis was employed for the design and identification of promising concepts on both the initial and final stages of the design. The initiation of failure in all hinges appeared to be delamination. The load at which delamination could be heard was lower for the RTM specimens. The thermoplastic hinges delaminated at a higher load and catastrophic failure was not observed up to a tested load of 25 kN. No visible failure could be seen in the thermoplastic hinges while the extent of failure on the RTM hinges was very large once the load was removed.

The ultimate load expected during the operation of the hinge was met by the thermoplastic hinge. The initiation of failure on the thermoset hinge was just below the ultimate load. A strength comparison between thermoplastic and thermoset hinge coupons showed; as expected; that due to the failure mode being delamination, the thermoplastic hinges performed significantly better.

12.5 Recommendations for future work

The jagged pattern produced during the optimisation process could be smoothed out using various techniques such as the biological growth approach or spline fitting. For this, a mixed technique could be developed which could see the biological growth approach to follow the shape optimisation using ESO.

The suggested method of incorporating an optimum shaped insert into a laminate could prove cost effective if such insert could be co-cured within the laminate. Furthermore, the inserts could incorporate a washer from both sides to avoid

delamination around pin loaded holes. A testing program to assess the possibility of co-curing the insert with the laminate and the effect of a washer integrated to the insert could show a further reduction of peak stresses in bolted and pin-loaded joints. The application of the original approach presented in this dissertation could be trialed to repairs of primary structures where bearing failure has initiated and has been identified. The damaged area could be removed by enlarging the cut-out with the optimised shape after analysing and identifying all possible load paths.

The finite element analysis of joints employing their detail geometry is currently not a simple task. The main disadvantage is that the measurement of ply thicknesses needs to be done under an electronic microscope. This information then needs to be post-processed by using spline fitting or similar methods to achieve an adequate mesh for the finite element analysis. This process could be automated by developing software capable of automatically generating splines from graphical pictures and of generating output to an ASCII type file readable into finite element codes.

Finally, an interesting testing program could also be developed to assess the difference in fatigue strength between the thermoplastic and thermoset hinges.

APPENDIX I

PUBLICATIONS FROM THIS RESEARCH

[1] Rispler, A. R., Steven, G. P., "Shape Optimisation of Metallic Inserts in Composite Bolted Joints", *Proceedings of the 2nd Pacific International Conference on Aerospace Science & Technology*, Melbourne, Australia, Vol. 1, pp. 225-230, March 20-23, 1995.

[2] Rispler, A. R., Steven, G. P., "Optimisation of Highly Loaded Joints", *Proceedings of the 20th Congress of the International Council of the Aeronautical Sciences*, Sorrento, Italy, Volume 1, pp. 160-166, September 8-13, 1996.

[3] Rispler, A. R., Steven, G. P., Tong, L., "*Failure Analysis of Composite T-Joints Including Inserts*", Cooperative Research Centre for Aerospace Structures Ltd.. Technical Report CRC-AS-EP 96006, October, 1996.

[4] Rispler, A. R., Steven, G. P., Tong, L., "On the Analysis of Highly Loaded Joints", *Proceedings of the International Aerospace Congress 97*, Sydney, Australia, Vol. 2, pp. 617-626, February 24-27, 1997.

[5] Rispler, A. R., Hou, M., Tong, L., Steven, G. P., Ye, L., Mai, Y. W., "Design and testing of an aircraft composite hinge", *11th International Conference on Composite Materials*, ICCM 11, Gold Coast, Australia, Vol. VI: Composite Structures, pp. 158-166, July 14-18, 1997.

[6] Rispler, A. R., Steven, G. P., Tong, L., "Failure Analysis of Composite T-Joints Including Inserts", *Journal of Reinforced Plastics and Composites*, Vol. 16, No. 18, pp. 1642-1658, 1997.

[7] Rispler, A. R., Steven, G. P., Tong, L., Wisnom, M., "Shape Optimisation of Adhesive Fillets", submitted to the *International Journal of Adhesion and Adhesives.*

[8] Rispler, A. R., Steven, G. P., Tong, L., "Photoelastic evaluation of optimised shape metallic inserts in composite materials", submitted to the *Journal of Composite Science and Technology.*